New Methods for Removal of Pollutants from Exhaust Gases

Bræstrup, Frantz Radzik

Publication date:
2009

Document Version
Publisher's PDF, also known as Version of record

Risø DTU
National Laboratory for Sustainable Energy

Ph.D. Thesis
June 2009

New Methods for Removal of Pollutants from Exhaust Gases

by

Frantz Bræstrup

Risø National Laboratory for Sustainable Energy,
Technical University of Denmark,
Fuel Cells and Solid State Chemistry Division.

Roskilde University,
Department of Chemistry and Life Sciences,
Institute Nature, System and Models.

Resumé

Forskellige typer af oxider med spinelstruktur er blevet undersøgt som mulige katodematerialer i en faststof elektrokemisk celle, til reduktion af NO og NO_2. Materiale-serier med følgende sammensætninger; $Ni_{1-x}Mg_xFe_2O_4$ $(x = 0,0; 0,3; 0,5; 0,6; 1,0)$, $NiCr_xFe_{2-x}O_4$ $(x = 0,0; 0,5; 1,0; 1,5; 2,0)$ og $MgMn_xFe_{2-x}O_4$ $(x = 0,0; 0,2; 0,4; 0,6; 0,8; 1,0)$, samt $ZnFe_2O_4$, $NiMn_2O_4$ og $MnCo_2O_4$ blev syntetiseret og karakteriseret med røntgen diffraktion, dilatometri og ledningsevne målinger. Enkelte af dem blev derudover også karakteriseret med termogravimetri, XAS og neutron diffraktion. Der blev lavet kegle-elektroder af alle materialerne og de blev efterfølgende karakteriseret med cyklisk voltammetri samt elektrokemisk impedans spektroskopi. Forholdet mellem de katodiske strømme viste, at den umiddelbare selektivitet overfor NO reduktion var meget høj, ofte med en faktor 20 eller mere. Et udvalg af de materialer, der viste størst katodisk aktivitet som kegle-elektrode, indgik som elektrodemateriale på symmetriske celler samt 3-elektrode piller. Målingerne viste at både $MgFe_2O_4$ og $ZnFe_2O_4$ kunne reducere NO_2 til NO ved katodisk polarisation og oxidere NO til NO_2 ved anodisk polarisation. Desværre lykkedes det ikke at mindske det samlede NO_x indhold i testgassen. $ZnFe_2O_4$ og $NiMn_2O_4$ blev imprægneret med BaO i et forsøg på at øge gasomsætningen over cellen. Målingerne viste at det kun havde en begrænset positiv effekt på $ZnFe_2O_4$-elektroden. Desuden reagerede BaO med $NiMn_2O_4$ hvilke gør sammensætningen ubruglig som elektrodemateriale.

$ZnFe_2O_4$ blev karakteriseret med *in situ* høj-temperature neutron diffraktion i et forsøg på at kæde ændringerne af kationsfordelingen sammen med den elektriske ledningsevne samt de dilatometriske målinger. Resultaterne viste at kationerne begyndte at flytte sig mellem de forskellige krystallografiske pladser ved temperaturer omkring 600 °C. Dette bekræftede delvist resultaterne fra ledningsevne- og dilatometrimålingerne.

XAS blev foretaget på $MgFe_2O_4$, $NiFe_2O_4$, $ZnFe_2O_4$, $NiCr_2O_4$ og $NiCrFeO_4$. Dette blev gjort for at undersøge oxidationstallet på overgangsmetallerne. $MgFe_2O_4$ og $NiFe_2O_4$ blev analyseret i forskellige gassammensætninger og resultaterne viste at oxidationstallet på Ni blev øget ved tilstedeværelsen af NO_2. Yderligere viste målingerne at NO og NO_2 adsorberede stærkt på overfladen af $MgFe_2O_4$ og derved sænkede intensiteten betydeligt.

Abstract

Different spinel-type oxides were investigated as possible cathode materials for the electrochemical reduction of NO_x gases (NO and NO_2) in an all solid oxide electrochemical cell. Three different series of spinel-type oxides, with the following composition, were analyzed: $Ni_{1-x}Mg_xFe_2O_4$ ($x = 0.0, 0.3, 0.5, 0.6, 1.0$), $NiCr_xFe_{2-x}O_4$ ($x = 0.0, 0.5, 1.0, 1.5, 2.0$) and $MgMn_xFe_{2-x}O_4$ ($x = 0.0, 0.2, 0.4, 0.6, 0.8, 1.0$). Furthermore were spinel-type oxides of $ZnFe_2O_4$, $NiMn_2O_4$ and $MnCo_2O_4$ also analyzed. The compounds were characterized with X-ray diffraction, dilatometry and resistivity measurements. Selected ones were also characterized with X-ray adsorption spectroscopy, thermogravimetry and neutron diffraction. Cone-shaped electrodes were fabricated for all of the materials and measurements were performed in different gases of NO, NO_2, O_2 and mixtures of these. Cyclic voltammetry and electrochemical impedance spectroscopy were measured in the temperature range from 300 °C to 600 °C depending on materials. Current ratios of NO over O_2 and NO_2 over O_2 showed that a number of spinels have high apparent selectivities with ratios of 20 or more.

Electrodes having the highest cathodic activity were used to fabricate symmetrical cells and 3-electrode pellets. These were used for further characterization and measurements on gas conversion. The materials used for this purpose were $MgFe_2O_4$ and $ZnFe_2O_4$ and results show that both materials can convert NO to NO_2 and back again during polarization. However, the overall NO_x level stayed almost unchanged during that process. A 3-electrode pellet with a $ZnFe_2O_4$ electrode, was infiltrated with BaO improve the activity in NO, however, the gas conversion was still very low. The effect of BaO in $NiMn_2O_4$ could not be determined as BaO reacted with the electrode materials during sintering and formed different oxides.

In-situ high temperature neutron diffraction was performed on $ZnFe_2O_4$ in order to determine the cation distribution and to understand the electronic resistivity as well as the dilatometry measurement of the material. Data were analyzed with the Rietveld refinement method and results showed that cations start to rearrange at around 600 °C which, to some extend, confirm the behaviour of the resistivity data and the dilatometry

measurement.

X-ray adsorption spectroscopy was performed on $MgFe_2O_4$, $NiFe_2O_4$, $NiCr_2O_4$, $ZnFe_2O_4$ and $NiCrFeO_4$. This was done in order to investigate possible changes in oxidation states of the transition elements. In the case of $ZnFe_2O_4$ the cation distribution was tried analyzed in order to compare the results with Rietveld refinements on high temperature neutron diffraction. Results show that it was difficult to obtain a good quality refinement without violating the bond distances with respect to reported values found by neutron diffraction and literature. $MgFe_2O_4$ and $NiFe_2O_4$ were also analyzed in different gases at 400 °C and results show that NO and NO_2 adsorb very strongly on $MgFe_2O_4$ and decreases the X-ray signal significantly. A change in oxidation state of Ni was observed in atmospheres containing NO_2.

Preface

This thesis finalizes the Ph.D. study on *New Methods for Removal of Pollutants from Exhaust Gases* which was funded by the 'Danish Council for Strategic Research, project no: 2194-05-0067. The thesis was carried out at the Fuel Cells and Solid State Chemistry Division (ABF), Risø National Laboratory for Sustainable Energy, Technical University of Denmark (DTU) in the period from 1st of April 2006 to 14th of April 2009 with scientist Kent Kammer Hansen as secondary supervisor. The work was done in collaboration with Roskilde University, Department of Nature, Systems and Models with assistant professor Dr. John Mortensen as head supervisor. All work was carried out at Risø, DTU or at the Institute for Energy Technology in Kjeller, Norway under Head of Department, Dr. Bjørn Hauback.

Acknowledgement

I wish to thank the ABF division for creating a fantastic working environment for the past three years. I have very much enjoyed my time with all of you. Special thanks goes to Vibe Simonsen, Rebecka Werchmeister, Christodoulos Chatzicheristodolou, Jonas Östby and people coming and going at the office for encouragement and good laughs during the day.

I would like to acknowledge my supervisors, Kent Kammer Hansen and John Mortensen for help and support during my thesis. Especially I would like to thank Kent for always taking his time to answer questions and discuss with me.

I would also like to thank Bjørn Hauback at IFE for helping me with the neutron diffractometer and to Dr. Bente Lebech for fruitful discussions concerning the structural analysis

of the neutron diffraction data.

I also wish to thank Emil Bjerrum-Bohr and Anne Margrethe Larsen for helping me with the final improvements of the thesis.

Finally, I would like to place a special thank to 'my three girls' at home; My wife Ida and my two daughters Anna and Elin, who always know how to make me smile and forget all worries.

Roskilde, June 2009

Frantz Bræstrup

Contents

List of Figures

List of Tables

Acronym

3E 3-Electrode

AC Alternating Current

CAS Citric-Acid Synthesis

CGO10 Cerium Gadolinium Oxide

CCP Close Cubic Packing

CPE Constant Phase Elements

CPO Cerium Praseodymium Oxide

CV Cyclic Voltammetry

DC Direct Current

EDS Energy Dispersive Spectroscopy

EIS Electrochemical Impedance Spectroscopy

EXAFS Extended X-ray Absorption Fine Structure

GNCS Glycine-Nitrate Combustion Synthesis

HC Hydrocarbons

HSA High Surface Area

LSM Lanthanum Strontium Manganate perovskite

LSA Low Surface Area

NTP Non-Thermal Plasma

O Octahedral sites

OCV Open Circuit Voltage

PVP Polyvinylpyrrolidone

RT Room Temperature

SCR Selective Catalytic Reduction

SEM Scanning Electron Microscopy

SOFC Solid Oxide Fuel Cell

T Tetrahedral sites

TG Thermogravimetry

TWCC Three-Way Catalytic Converter

UHSA Ultra High Surface Area

YSZ Yttrium Stabilized Zirconia

XANES X-ray Absorption Near Edge Structure

XAS X-ray Absorption Spectroscopy

XRD X-ray Diffraction

ZSM5 Zeolite Socony Mobile #5

Thesis Objective

This Ph.D. work was carried out as a study of new electrode materials for the selective electrochemical reduction of NO and NO_2. The method has its roots in the solid oxide fuel cell technology, where an oxide anion conducting electrolyte with electrodes on both sides acts as a reactor. Only few results on spinel-type electrode materials have been reported in literature on electrochemical reduction of NO and NO_2. Therefore, a selection of different spinel-type materials was synthesized and characterized using different methods and techniques. A few of the spinel-type materials were additionally mixed with Ba compounds in order to investigate a possible reaction route based on an electrochemical storage catalyst.

Outline of the Thesis

This thesis is divided into 7 chapters. The first chapter gives a brief introduction to the subject concerning emission of NO_x gases and methods for cleaning the flue gases. Chapter 2 describes the different materials used in this thesis, whereas chapter 3 gives an overview of the different synthesis methods as well as a description of the various characterization techniques. Chapter 4 contains the experimental part of the work and chapter 5 and 6 describe and discuss the results. Chapter 7 summarizes the results and gives some concluding remarks. Attached at the end of this thesis is the four published articles/submitted manuscripts.

Chapter 1: An introduction to the subject.
Chapter 2: A brief description of spinel-type oxides as well as the different electrolyte materials used in this thesis.
Chapter 3: An account of the different characterization methods used in this thesis.
Chapter 4: A description the experimental part of the work, including sample geometries.
Chapter 5: A presentation of the experimental results and discussions. The chapter includes published and unpublished results.
Chapter 6: A description of the results and discussions from XAS.
Chapter 7: Concluding remarks and possibilities for future work.

List of symbols

Greek Symbols

α	Expansion coefficient, [$°C^{-1}$]
α	Charge transfer coefficient
δ	Oxygen excess
η	Current efficiency, [%]
η	Over potential, [V]
ϵ	Relative electrical permittivity
ϵ_0	Permittivity of free space, [$J^{-1}C^2m^{-1}$]
γ	Inversion parameter
λ	Air/fuel ratio
λ	Wavelength, [Å]
μ	Absorption coefficient
ν	Sweep rate, [mVs^{-1}]
ν	frequency, [Hz]
χ	Molar fraction
ϕ	Phase angle, [rad, °]
ρ	Specific electrical resistance, [Ω m]
ρ	Density, [g/cm^3]
ρ	Correlation coefficient
σ	Specific conductivity, [S/cm]
σ^2	Mean-square displacement of the coordination shell, [$Å^2$]
θ	Angle of incidence of x-ray beam, [°]
ω	Radian frequency, [rad/sec]

Roman Symbols

a	Unit cell parameter, [Å]
A_m	Semi-circles in a Nyquist plot
A	Area, [m^2]
A	Atomic mass
$c*$	Initial concentration, [mol/ml]
C	Capacitance, [F]
C_g	Geometrical capacitance, [F]
C_{ne}	Near-equivalent capacitance, [F]
C_s	Stray capacitance, [F]
d	Spacing between atomic planes, [Å]
D	Diffusion constant, [m^2s^{-1}]
E	Energy of X-rays [eV]
ΔE	Energy step, [eV]
E	Electrochemical potential, [V]
E_a	Activation energy, [J/mol]
f	Frequency, [Hz]
F	Faraday's constant, 96485.3 C/mol
$\Delta G^{\ominus}$	Standard reaction Gibbs energy, [KJ/mol]
g_f	Geometrical factor
h	Planck constant, $6.62608 \cdot 10^{-34}$, [Js]
hkl	Miller indices for the Bragg reflections
i	Current, [A]
i	Exchange current, [A]
i_p	Peak height, [A]
I	Current density, [A/cm^2]
I	Intensity
j	$\sqrt{-1}$
k_B	Boltzmann's constant, $1.38066 \cdot 10^{-23}$ J/K = $8.61940 \cdot 10^{-5}$ eV/K
k	Wave number
K	Equilibrium constant
l	Length, [m]
m	Mass, [g]
M	Molar mass, [g/mol]

n	Non-negative integer
n	Constant phase element exponent
n	Number of electrons
Ox	Oxidized species Open porosity, [%]
p^{θ}	Standard pressure, [bar]
p_{O_2}	Partial pressure of oxygen, [bar]
Q	Constant phase element, [S/sec^n]
r	Radius, [m]
r	Bond length between atoms, [Å]
R	Resistance, [Ω]
R	Gas constant, 8.3145 J/(mol K)
R_{e}	Electrolyte resistance, [Ω]
Red	Reduced species
R_m	Series resistance, [Ω]
R_{p}	Agreement factor for powder diffraction profiles
S_2^0	Amplitude reduction factor
t	Time, [sec]
t	Sample thickness, [m]
T	Temperature, [°C]
T_{c}	Curie temperature, [°C]
u	Fractional oxygen coordinate
U	Voltage, [V]
U_{iso}	Isotropic displacement parameter, [Å^2]
V	Unit cell volume, [Å^3]
wR_{p}	Weighted R_{p}-factor
x	Cation-stoichiometry
Z	Atomic number
Z	Impedance, [Ω]
Z_{Re}	Real impedance, [Ω]
Z_{Im}	Imaginary impedance, [Ω]

Chapter 1

Introduction

1.1 Formation of NO_x Gases

The formation of nitrogen containing species in the atmosphere originates from a variety of different sources. The most abundant one is nitrogen, N_2 where the strong triple bond of the N≡N molecule makes it practically inert. Nitrous oxide, N_2O, is a colourless gas that is emitted mostly by natural sources, principally by bacterial activity in the soil. The gas is also used as an anaesthetic and is commonly referred to as "laughing gas." Nitric oxide, NO, is emitted by both natural and anthropogenic sources as well as from combustion processes in gasoline and diesel engines along with nitrogen dioxide, NO_2. NO_2 is also formed in the atmosphere by oxidation of NO. Other oxides of nitrogen, such as NO_3 and N_2O_5, also exist in the atmosphere, however, only in relatively low concentrations. Nitric acid, HNO_3, is an oxidation product of NO_2 in the atmosphere whereas ammonia, NH_3, is emitted mainly by natural sources.

One of the main polluting agents from internal combustion processes in diesel fired engines is NO_x ($x = 1, 2$) gases. Emission from road traffic is far the largest contributor to the NO_x formation and in 2000 the European Union road traffic was responsible for 32 % of the total NO_x formation [1]. Presently, the three-way catalytic converter (TWCC) is employed for treating gasoline engine emissions with an efficiency close to 100 %, however, the TWCC requires stoichiometric conditions to simultaneously catalyze oxidizing and reducing reactions. In diesel fired engines, air and fuel is injected separately into the combustion chamber where the air is compressed and the fuel is subsequently added for ignition. In order to improve the fuel economy, excess air (lean conditions) is used in the combustion process. This makes the TWCC unsuitable in lean burn and diesel engine applications where the exhaust contains $5 - 15$ % O_2 [2].

NO_x gases can cause serious health problems such as lungs oedemas and other respiratory problems [3, 4]. Another highly unwanted reaction is that NO_2 contributes to the formation of ozone, O_3, in the troposphere by reacting with sunlight, $h\nu$ [5] (see equations 1.1),

$$NO_2 + h\nu \rightarrow NO + O \qquad \lambda < 400 \text{ nm} \tag{1.1}$$

$$O + O_2 + M \rightarrow O_3 + M. \tag{1.2}$$

O is an oxygen radical and M is a mediator that removes excess energy from the reaction and allows the quasistable ozone to be formed. Figure 1.1 shows the NO_2 level in the troposphere over Europe and illustrated how city areas are highly exposed to the pollution. Most of the NO_2, however, is oxidized in the troposphere to nitric acid by reactions with

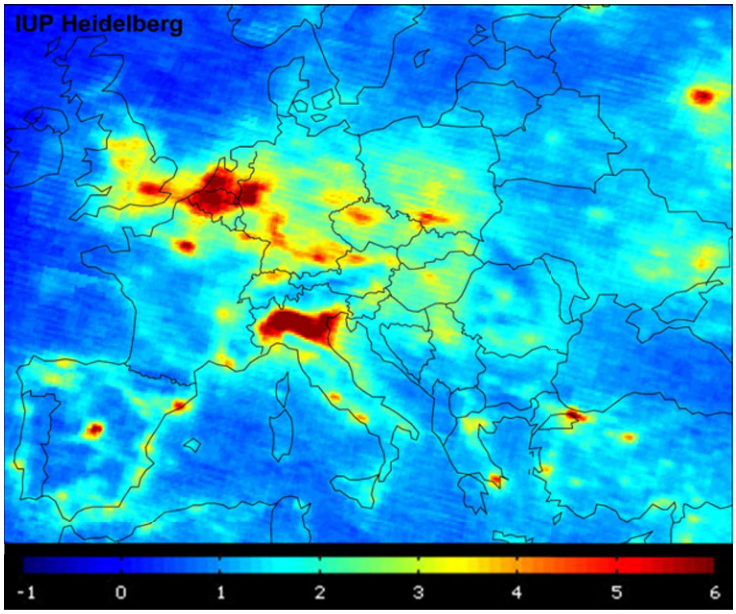

Figure 1.1: Mean vertical column density of NO_2 in the troposphere over Europe between January 2003 and June 2004. The scale is 10^{15} molecules/cm^{-2} [6].

hydroxyl radicals [7] as shown in equation 1.3,

$$NO_2 + OH \rightarrow HNO_3. \tag{1.3}$$

In the stratosphere, the rest of the NO reacts with ozone and oxygen radicals through two main NO_x cycles [5] which is shown in reactions 1.4–1.5 and 1.6–1.8.

$$NO + O_3 \rightarrow NO_2 + O_2 \tag{1.4}$$

$$NO_2 + O_2 + M \rightarrow NO + O_2 \tag{1.5}$$

1.1. Formation of NO_x Gases

$$NO + O_3 \rightarrow NO_2 + O_2 \tag{1.6}$$

$$NO_2 + O_3 \rightarrow NO_3 + O_2 \tag{1.7}$$

$$NO_3 + h\nu \rightarrow NO + O_2. \tag{1.8}$$

Pollution of NO_x therefore causes not only respiratory health problems but also leads to a depletion of ozone in the stratosphere and increasing levels of ozone at ground levels.

The main source of nitrogen in molecular NO_x, emitted from combustion processes is air. However, also aromatic nitrogen-containing compounds in the fuel (fuel nitrogen) contributes to the formation of NO_x. NO is formed through three different mechanisms during the combustion, involving oxidation of nitrogen from the air, the fuel and the reaction of nitrogen from the air with hydrocabonates followed by an oxidation [7]. However, only the oxidation of the nitrogen from the air will be described as it is the most important one. The main mechanism, known as the Zeldovich chain mechanism [8], is a thermal route which follow equations 1.9−1.11,

$$N_2 + O \rightarrow NO + N \tag{1.9}$$

$$N + O_2 \rightarrow NO + O \tag{1.10}$$

$$N + OH \rightarrow NO + H, \tag{1.11}$$

with 1.9 being the rate determining step [9]. The rate of the reactions depends on the combustion temperature and because of that, is the formation of NO_x gases lower in diesel engines than in traditional gasoline fired engines. Exhaust gas temperatures is a function of the air/fuel ratio but are typically in the range of $150 - 300$ °C (see Figure 1.2) and it contains approximately $400 - 3000$ mg/m^3 NO_x [2], of which ~ 90 % escapes the tailpibe as NO gas [10]. Diesel vehicles installed with a diesel particulate wall flow filter coated with an oxidation catalyst for soot removal will, however, have a higher NO_2/NO ratio [11]. Soot particles from diesel cars are also a major polluting agent in terms of human health. The particles are formed in the area just behind the flame front in the combustion chamber where the air fuel mixture is rich on diesel but with a low content of air [7]. However, since no experiment were made on removing soot from the exhaust of a diesel engine, no further details will be made on this subject.

The effect of air pollution from motor vehicles was recognized already in the 1950's in the US [12]. However, it was not until the US Clean Air Act of 1963 and its amendments in 1966, 1967, 1970 and 1990 that effective national programs were established. In Europe, same kind of regulations were initiated and with the foundation of the European Union, with emission standards for heavy-duty diesel trucks and bus engines (see Table 1.1).

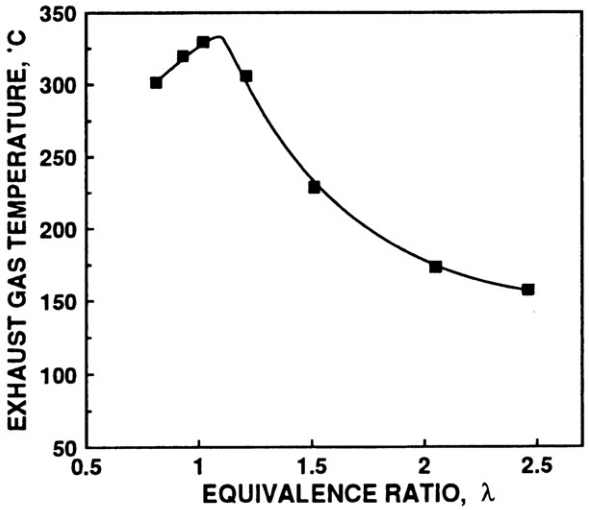

Figure 1.2: Exhaust temperatures as function of the oxygen/fuel ratio, λ.

In 2008 new regulations for the emission standards of heavy-duty diesel trucks and bus engines became effective (Euro V). New regulations concerning emission standards for diesel cars and light trucks (see Table 1.2) will come effective between September 2009 and January 2011 (Euro 5) depending on the vehicle models.

1.2 Removal of NO_x Gases

1.2.1 Catalytic Methods for Removal of NO_x Gases

The demand for reduction of NO_x emission from diesel fired engines have lead to an increased effort for finding good catalysts. The most attractive method to reduce the NO emission is through self-decomposition of NO over a suitable catalyst. However, the presence of oxygen in the exhaust gas makes it difficult to succeed. It is not the goal of this thesis to go into details on the different catalytic processes for NO reduction, however, a brief introduction of the competing technologies will be given on the subject. Catalytic removal of NO_x gases can be divided into two different approaches. One way is to make a direct decomposition of NO_x gases by a suitable catalyst and the other is selective catalytic reduction of NO_x gases with the use of a reducing agent.

1.2.2 Direct Catalytic Decomposition of Nitric Oxides

A direct thermodynamic decomposition of NO to N_2 and O_2 is always favored as the Gibbs energy, ΔG, is negative at elevated temperatures and will increase as the temperature

1.2. Removal of NO_x Gases

Table 1.1: Emission standards for heavy-duty diesel trucks and bus engines in Europe [13]. Units on the different species are given in g/kWh.

	Year	Test cycle	CO	HC	NO_x	PM[c]	smoke (m-1)
Euro I	1992[a]	ECE R-49	4.5	1.1	8.0	0.612	
	1992[b]	ECE R-49	4.5	1.1	8.0	0.36	
Euro II	1996	ECE R-49	4.0	1.1	7.0	0.25	
	1998	ECE R-49	4.0	1.1	7.0	0.15	
Euro III	2000	ESC + ELR	2.1	0.66	5.0	0.10	0.8
		ETC	5.45	0.78	5.0	0.16	
Euro IV	2005	ESC + ELR	1.5	0.46	3.5	0.02	0.5
		ETC	4.0	0.55	3.5	0.03	
Euro V	2008	ESC + ELR	1.5	0.46	2.0	0.02	0.5
		ETC	4.0	0.55	2.0	0.03	

[a] <85 kW; [b] >85 kW; [c] PM, Particulate Matter; ECE R-49: steady-state engine test; ESC, European Stationary Cycle; ELR, European Load Response test; ETC, European Transient Cycle. For type approval according to the Euro IV limit values, the emissions have to be determined on both the ETC and ESC/ELR tests.

Table 1.2: Emission standards for diesel-powered passenger cars in Europe [14]. Units on the different species are given in g/kWh.

	Year	Test cycle	CO	HC + NO_x	NO_x	PM (g/kWh)
Euro 1	1992	ECE15 + EUDC	2.72	0.97		0.14
Euro 2	1996	ECE15 + EUDC	1.0	0.70		0.08
Euro 3	2000	ECE15 + EUDC	0.64	0.56	0.50	0.05
Euro 4	2005	ECE15 + EUDC	0.50	0.30	0.25	0.025
Euro 5	2009[a]	ECE15 + EUDC	0.50	0.23	0.18	0.005[b]

[a] 2011.01 for all models;[b] proposed to be changed to 0.003 g/km using the PMP measurement procedure; PM, Particulate Matter; ECE R-49: steady-state engine test; ESC, European Stationary Cycle; ELR, European Load Response test; ETC, European Transient Cycle. For type approval according to the Euro IV limit values, the emissions have to be determined on both the ETC and ESC/ELR tests.

decreases [15]. Equation 1.12 shows the reaction of the direct decomposition of NO as well as the Gibbs energy at 400 °C,

$$\mathrm{NO} \rightarrow \frac{1}{2}\mathrm{N_2} + \frac{1}{2}\mathrm{O_2},\ \Delta\mathrm{G} = -82\ \mathrm{kJmol^{-1}}. \tag{1.12}$$

However, kinetics show that the activation energy is high (3.8 eV) [16] and therefore a suitable catalyst is needed in order to lower the activation energy barrier.

The catalysts can be divided into three different types: *Metals*, *metal-zeolites* and *metal-oxides*. The most promising metals are Pt in combination with different transition metals [17]. The reaction is believed to follow the scheme shown in equation 1.13 [18],

$$\mathrm{NO_{gas}} + \square \rightleftarrows \mathrm{NO_{ads}} \tag{1.13}$$

$$\mathrm{NO_{ads}} + \square \rightleftarrows \mathrm{N_{ads}} + \mathrm{O_{ads}} \tag{1.14}$$

$$\mathrm{N_{ads}} + \mathrm{N_{ads}} \rightleftarrows \mathrm{N_{2,gas}} + 2\square \tag{1.15}$$

$$\mathrm{O_{ads}} + \mathrm{O_{ads}} \rightleftarrows \mathrm{O_{2,gas}} + 2\square, \tag{1.16}$$

where NO adsorb, (ads), on an active site, □, on the surface of the catalyst and form species of N and O, which then desorb into gaseous, (gas), N_2 and O_2. The desorption of oxygen is not only the rate determining step but also the critical step that makes the catalytic process difficult. At temperatures below $\sim$ 500 °C, the desorption of oxygen on Pt becomes very slow and eventually blocks the surface for further decomposition of NO (commonly referred to as self-poisoning). Other metals show similar behaviour [4]. Since the exhaust temperature is typical below 300 °C, direct decomposition of NO over metal-catalysts are therefore only useful in low oxygen containing atmospheres at high temperatures.

Metal-zeolites have shown some interesting behaviour for catalytic decomposition of nitric oxides and much work have been published regarding this [19–22]. The first zeolite compound that showed a high and steady state decomposition of NO was Cu-ZSM5 [23, 24]. It is believed that the active sites are found on Cu^+, however, mechanisms for NO reduction are still under debate. Working temperatures are on the other hand still too high in order for the catalyst to be used for decomposition of nitric oxides in mobile diesel engines.

Metal-oxides have showed high activity towards decomposition of NO, with MnO_x and CuO being the most important ones [17, 25]. A large number of publications [26–29], have suggested that perovskites also could act as good catalysts. They have gained much interest because of their oxygen vacancies and redox properties of different transition

metals, which seems to be the main mechanisms that affect the activity of the catalysts. However, working temperatures are still much too high to be used for mobile diesel engine applications. Only few results on direct decomposition of NO_x over spinel-type oxides have been reported. Haneda *et al.* found that NO could be reduced over Co_3O_4 catalyst at 600 °C, however, in the presence of 5 % O_2 the activity decreased significantly.

1.2.3 Selective Catalytic Reduction (SCR) of Nitric Oxides

Selective catalytic reduction (SCR) has shown the most promising results, compared to the direct catalytic decomposition of nitric oxides. The reduction of NO_x is archived by adding a reducing agent to the exhaust gas and letting it react with the NO_x over a suitable catalyst.

HC-SCR is a technique that uses hydrocarbons (HC) to reduce the NO_x gases. The HC is either added to the exhaust gas by injecting extra fuel in front of the converter or by changing the air/fuel ration in such a way that unburned fuel escapes the combustion process in the cylinders. Zeolites (H-mordenite and Cu-ZSM5), metals (Ag/Al_2O_3,) and metal-oxides (ex. SnO_2) are some of the used catalysts [1], with the activities dependent on the chemistry of the HC. However, activities seems to decrease very fast when temperatures drops below 300 °C. Pt deposited on an Al_2O_3 support has shown capable to work a lower temperatures, however, the activity window is relatively narrow and the process has a tendency to produce large amounts of N_2O. A Na-modified form of the Pt/Al_2O_3 catalyst [30] have, however, showed that the activity window could be opened up. Combining that with a high temperature catalyst, the technique seems promising although, one would still need to find a suitable catalyst that would work below 200 °C [1] before it could be commercialized. Adding H_2 to the HC-SCR process have showed good results over the Ag/Al_2O_3 catalyst by increasing the activity below 200 °C [31]. Storage of H_2 is, on the other hand, a problem especially if the technique should be used in the transportation sector, however, it has been suggested that diesel fuel could act as a source for hydrogen [1].

Several experiments [32–36] have been made on converting NO_x and soot simultaneously in the presence of excess O_2 but activities are still low. Drouet *et al.* [37] found that non-stoichiometrical Ni-Cu manganates were highly active for reduction of NO by CO at temperatures down to 300 °C, however, working temperatures are still to high. Ni-Ga spinel has also been reported as a possible catalyst for NO reduction with C_3H_6 as the reducing agent, however, results showed that the activity below 400 °C dropped to zero.

Nonthermal Plasma (NTP)- assisted catalysts: NTP is in general any plasma which is

not in thermodynamic equilibrium, either because the ion temperature is different from the electron temperature, or because the velocity distribution of one of the species does not follow a Maxwell-Boltzmann distribution. NTP - assisted catalysts is a technique that originally was developed with the purpose of producing ozone [38]. Later, the technique was used for different kinds of large scale industrial applications. The treatment of NO_x gases in diesel exhaust from passenger vehicles and trucks has recently become an important issue [39, 40]. NTP has high potentials in combination with an appropriate catalyst and the technique has shown high activities in the temperature range of 150 - 500 °C. The technique has also showed some promising results when sulphur is present in the fuel [41]. However, problems still need to be solved concerning the power source in combination with the chemistry and the amount of reducing agents needed to operate with a sufficient level of gas conversion. The effective fuel penalty of NTP is around 6 % [42].

Ammonia/Urea-SCR is properly the must promising technique for the transportation sector that exists for the time being and it have gained much attention over the last few years. Ammonia-SCR have been tested for stationary industrial applications since the 1970s with much success in reducing up to 90 % of the NO_x [43] emission over a range of different operating conditions. However, ammonia is both toxic and corrosive and more difficult to handle from a storage point of view. Therefore, urea ($(NH_2)_2CO$) is often used instead of ammonia in the transportation sector and it has shown to function effective in a diverse range of truck engines (the effective fuel penalty is around $3 - 5$ % [42] which is acceptable for most applications). The catalysts used depend much on the operation temperature. Pt is used for low-temperature applications, whereas V_2O_5, WO_3, TiO_2 and different zeolites are used at higher operation temperatures [1,44]. Different layered clays, such as smectites, montmorillonites and hydrotalcites [44, 45] have also been considered as possible catalysts for reduction of NO_x. The Urea-SCR technique still has several problems to overcome. The freezing temperature of an aqueous urea solution is around -11 °C, which will cause problems in many countries during winter times. Storage of urea is also one of the disadvantages with the mobile SCR-technology. Urea must be carried on board in a tank, which places some requirements on packing the substance. Moreover, systems must be designed to prevent unreacted urea to escapes out of the tailpipe of the vehicle as well as N_2O formation.

NO_x storage catalyst is a technique where the NO in the exhaust gas is oxidized to NO_2 over a catalyst and stored under lean conditions as a nitrate in oxide material. Then, after a short period of time (approximate 1 minute), the engine is switched to run under rich fuel conditions which reduces the nitrates and thereby releases N_2 (and CO_2 + H_2O).

Typical catalysts are Pt and/or Pd and the storage material is Ba- or Sr-compounds. Figure 1.3 illustrates the principles behind a NO_x storage catalyst. One of the disadvan-

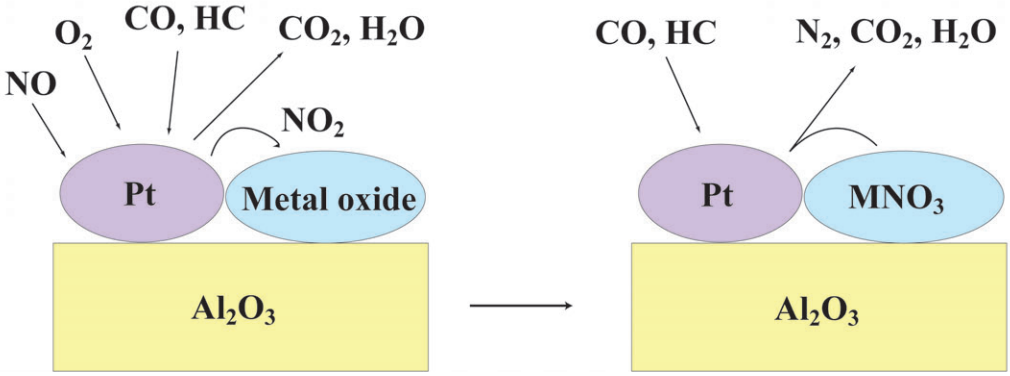

Figure 1.3: Principles behind the NO_x storage catalyst. The engine runs under lean periods which oxidize NO over Pt and store it as nitrates. The engine is then switched to run under rich periods which regenerate the metal oxide [1].

tages with the storage catalyst is its high affinity to sulphur compounds in the exhaust gas which results in a blocking of the active sites. Desulfation, however, can be achieved to some extend if the temperature is increased [46]. Problems with sulphur-poisoning may, however, be diminished just by waiting for new fuel regulations to effectuate. In the European Union (Euro IV) a maximum of 50 ppm sulphur in diesel fuel have been standard since 2005 for most highway vehicles and in 2009 (Euro V) diesel with an ultra low sulphur content of maximum 10 ppm will be used as the new standard [47]. North America and other countries like Australia have made similar standards with a maximum of $10 - 15$ ppm sulphur in diesel fuel [48]. Thermal deactivation is also a big problem as well as the use of precious metals. The width of the temperature window is also relative narrow compared to the operation conditions in mobile diesel engines and especially low-temperature activities may present a problem. The technology is therefore not ready for a full scale commercialisation.

1.2.4 Electrochemical Reduction of NO_x

Electrochemical reduction of NO_x gases was purposed already in 1975 by Pancharatnam *et al.* [49] over an all solid state cell. The NO_x gases are reduced at the cathode following the overall equations 1.17 and 1.18:

$$2e^- + NO \rightarrow \frac{1}{2}N_2 + O^{2-} \tag{1.17}$$

$$4e^- + NO_2 \rightarrow \frac{1}{2}N_2 + 2O^{2-}. \tag{1.18}$$

The oxygen ions, O^{2-}, diffuses through an electrolyte and O_2 is formed at the anode. Figure 1.4 illustrates the concept behind the technique. A drawback is that O_2 also can be reduced at the cathode which will lead to a higher consumption of current (equation 1.19).

$$4e^- + O_2 \rightarrow 2O^{2-}. \tag{1.19}$$

On way of trying to solve this problem is to find a suitable electrode material which can do a selective reduction of NO_x gases. NO and NO_2 are thermodynamically less stable than O_2, with the energy level of the antibonding orbitals located at a lower energy level than the corresponding antibonding orbitals of O_2 [15]. Therefore, by adjusting the potential

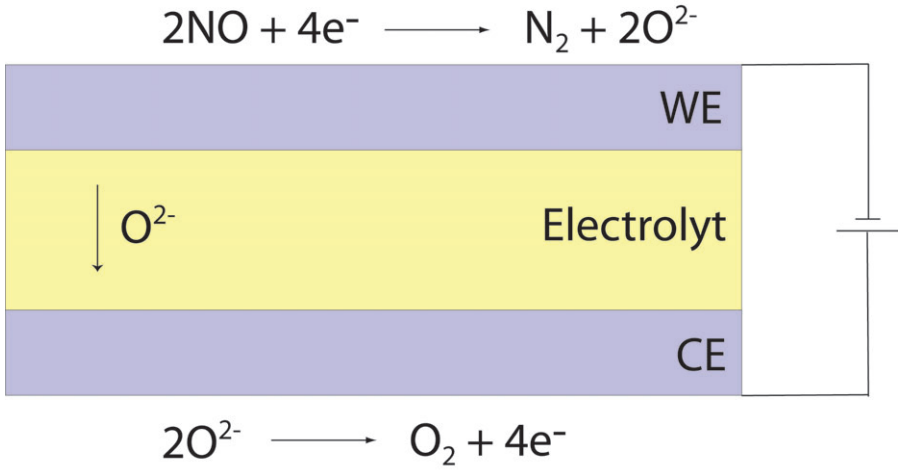

Figure 1.4: The concept behind electrochemical reduction of NO_x gases over an all solid state cell. NO_x gases are reduced at the working electrode (WE) and oxygen is formed at the counter electrode (CE). Oxygen ions are transported through the electrolyte.

in such a way that the valence electrons of the electrode material are placed at an energy level in between the antibonding orbitals of NO (or NO_2) and O_2, it will be possible to reduce the NO_x gases selectively.

Figure 1.5 shows the theoretical calculations on the molar fraction as function of the open circuit voltage[1] (OCV) at 400 °C using the Nernst equation 1.20:

$$E = \frac{-\Delta G^{\ominus}}{nF} + \frac{RT}{nF} \ln K, \tag{1.20}$$

where $\Delta G^{\ominus}$, is the standard potential, n is the number of transferred electrons, F is the Faraday constant, R is gas constant, T is the temperature and K is the molar reaction constant. An example of K for the reduction of NO to N_2 (equation 1.17) is shown in

[1]The OCV is in fact the same as the electromotive force, however, very often a small leak current is present in the system. Therefore, in 'fuel cell terminology', OCV is used to determine that leak current with respect to the electromotive force. OCV is therefore used in this thesis.

equation 1.21:

$$K = \frac{(1-\chi)^2}{\chi \cdot p_{O_2}/p^\theta}, \tag{1.21}$$

where χ is the molar fraction of the reaction and p_{O_2}/p^θ is the partial pressure of oxygen in air divided with the standard pressure. Figure 1.5 shows that the reduction of NO and NO_2 to N_2 lies at relative high potentials whereas the potentials of an almost complete reduction of O_2 lies at potentials around -0.1 V. A suitable electrode material must therefore be able to reduce NO (or NO_2) selectively without reducing O_2. Reactions involving N_2O are also shown, however, they are meant as a demonstration of how many processes there can occur in the potential range. The electrode also has to be a relative good electronic conductor and/or a good ion conductor in order to reduce the consumption of current over the cell.

Several reports on electrochemical reduction of NO has been published using metal

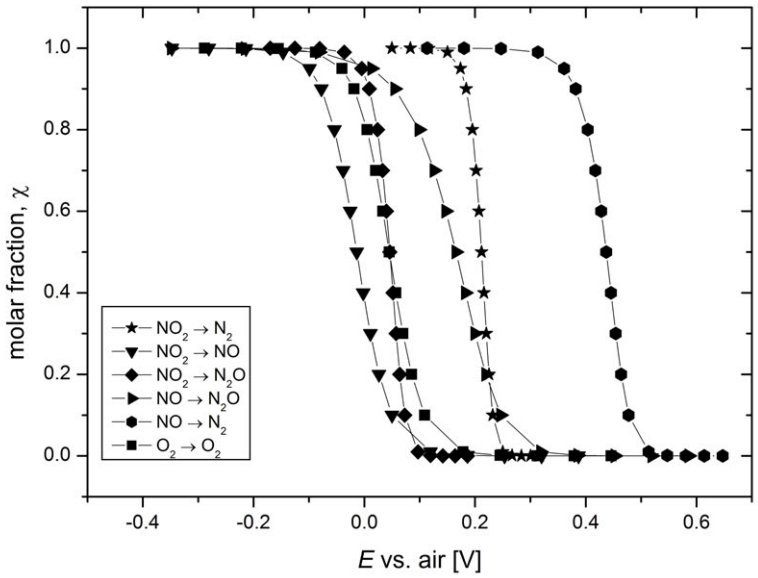

Figure 1.5: Theoretical calculations on the molar fraction as function of OCV at 400 °C. χ referees to the molar conversion of the reactants.

electrodes such as Pd, Pt, Au, Ag and Ir [49–55]. Many of them have shown some interesting results, however, in most cases experiments were not made in the presence of O_2 or, if they were, the activity of the electrode was lowered considerable. Apart from that most of the metals are relative expensive which has intensified the research for low cost ceramics to be used as electrode materials. A few of the experiments with metal electrodes are described below.

Reduction of nitric oxides was first reported by Pancharatnam *et al.* [49] in an all solid

state electrochemical cell which was based on a Sc stabilized zirconia electrolyte having a porous Pt or Au electrode. Experiments were carried out in the temperature range from 600−800 °C in NO and results showed that a reduction of NO could be obtained by applying a high over-potential of -2.2 V versus air, which resulted in a formation of F-centres (colour-centres) on the surface of the electrolyte. However, no experiments were made by adding O_2 to the NO gas. Hibino [52, 53] investigated the simultaneous reduction of NO and oxidation of CH_4 at 700 °C in a gas mixture containing 2−10 % O_2 using symmetrical cell with Pd-electrodes on an YSZ electrolyte. He proposed that NO was reduced to N_2 at the cathode, in competition with the reduction of O_2, and that CH_4 was oxidized to CO_2 at the anode.

NiO and RuO_2 has also been suggested as candidates for electrochemical removal of NO_x [51, 54, 55], however, RuO_2 is highly poisonous and forms volatile higher oxides such as RuO_3 and RuO_4. In the case of NiO, operation temperatures are too high compared with the temperature of the exhaust gas from a diesel engine. Different perovskites [56–59] and individual members of the Ruddleston-Popper phases [60] have also been reported as possible electrode materials, however, current densities are relative low and the activity in O_2 is high compared to the activity in NO. Neither was any gas analysis performed on the reaction products to verify if in fact NO was reduced to N_2. To our knowledge only few studies have been made on electrochemical reduction of NO_x gases over a spinel-type electrode. Simonsen *et al.* [61] reported an electrochemical reduction of NO over a $NiFe_2O_4$ electrode in the temperature range from $400 - 600$ °C. The electrode had a high cathodic activity (potential range -1.0 V − 0.5 V) compared to O_2, however, theoretically electrochemical calculations [15] show that $NiFe_2O_4$ is reduced to Ni + Fe_3O_4 at potentials lower than -0.86 V (600 °C). This might question whether the electrode in fact only contained one single phase. Hansen *et al.* [62] analyzed Co_3O_4 from 300−500 °C in 2 % NO, however, their data have not been normalized to current densities and estimated values of the current ratios are relative low.

In order to accommodate problems with excess oxygen in the exhaust, Hamamoto *et al.* [63] fabricated an solid state electrochemical cell with a multilayer electrode (cathode) on a CGO10 electrolyte (Gd-doped CeO_2, see section 2.2). Results showed that a 90 % conversion of NO could be achieved at 250 °C even in an atmosphere containing 20 % oxygen [64]. In short, the cathode consist of four layers starting with a catalytic layer of NiO-CGO10, with a porous Pt layer (current collector) screen-printed on top. A cover layer of CGO10 and a NO_x-adsorbent layer of $Pt/K_2O/Al_2O_3$ is situated on top of the Pt current collector and the catalytic layer. Applying a square-wave AC voltage (±4 V), NO_x were adsorped/desorped on the cathode and transported through the cover layer to

1.2. Removal of NO_x Gases

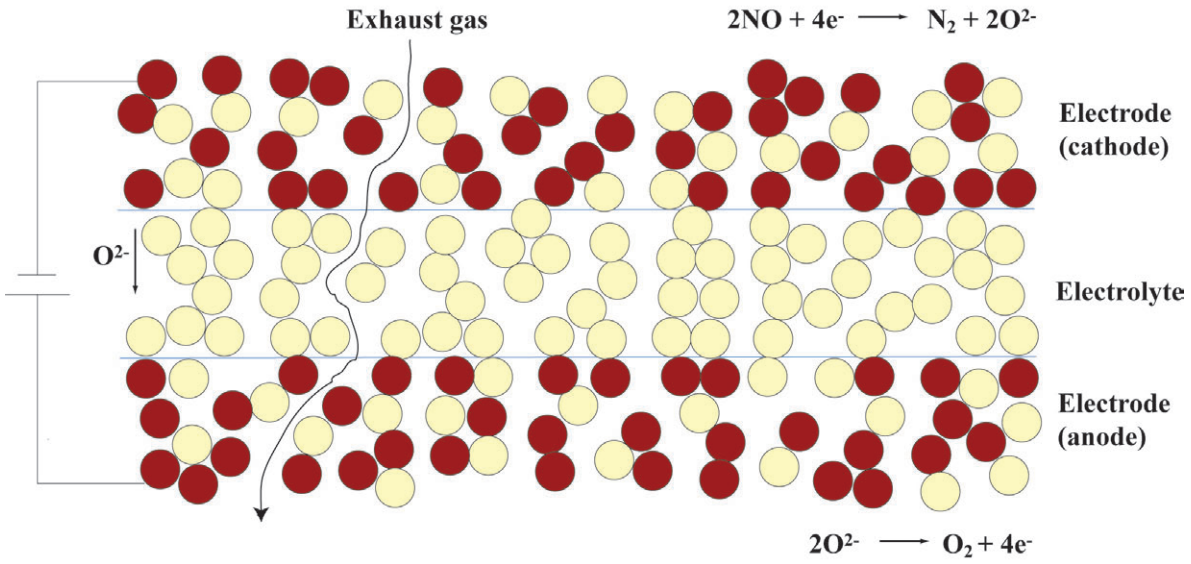

Figure 1.6: Concept of the porous cell for electrochemical reduction of NO_x gases. Yellow spheres represent an oxygen ion conduction material and red sphere represent an electron conduction material, which also serve as electro-catalyst for the reduction of NO. Blue lines represent the boundaries between the electrodes and the electrolyte.

the catalytic layer where the NO_x gases were decomposed.

We have proposed an alternative electrochemical way of removing the NO_x gases in the present of oxygen. The concept of the cell is to design it in such a way that the exhaust gas passes through a porous cell. This will of cause challenge not only the design of the cell concerning porosities, interfaces and other microstructural problems [65] but also, and most important, the choice of electrode material which has to be selective towards reduction of NO_x. Passing the exhaust gas through the cell would eliminate problems with the formation of a concentration gradient in the gas phase which could cause a problem with a cell design where the gas flow is applied over a planar cell. The gas conversion is assumed to take place in the vicinity of the electrolyte [66], therefore, a very thick electrode (for example 200 μm) would in principle show almost the same amount of activity as a thinner electrode. In order to have a large surface area of the electrode, a cell stack consisting of 5 porous symmetrical cells was proposed. The cells were stacked into a single 11-layer structure without any interconnects. CGO10 was used as electrolyte (20 μm thick) and a composite of $La_{1-x}Sr_xMnO_3$ (LSM) and CGO10 or LSM/CPO (30 μm thick) was used as electrode (CPO: Ceria Praseodymium Oxide). The number of cells was chosen in such a way that the stack would be strong enough to operate during testing. Adding more cells to the stack would increase the surface area of the electrode, however, it would also increase the pressure drop across the cell. The concept of the porous cell is illustrated on Figure 1.6. Figure 1.7 shows an early test 5-cell stack of LSM/CGO10 electrodes (dark gray layers) and CGO10 electrolytes (white layer).

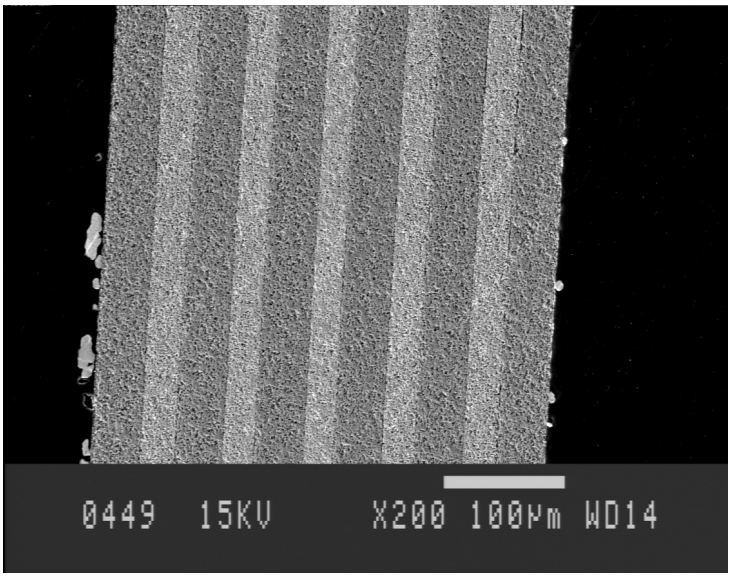

Figure 1.7: SEM picture of the 5-cell stack. The stack consists of LSM/CGO10 electrodes (gray layers) and CGO10 electrolytes (white layer). Remains of an Au current collector can be seen as large particles on each side of the cell stack. The total thickness of the cell stack is around 375 μm.

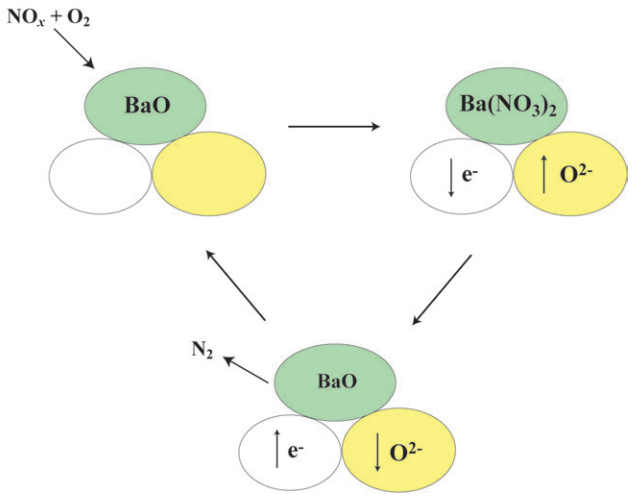

Figure 1.8: The concept of a storage catalyst combined with the electrochemical method. The figure illustrates a case with a two-phases composite electrode, one phase being ion oxide conducting and the other being electron conducting.

An alternative way of reducing NO_x gases is to combine the principles of a storage catalyst (see section 1.2.3) with the electrochemical method. If an alkali earth oxide, like BaO, is combined with the electrode material it should be possible to form $Ba(NO_3)_2$ in reaction with NO_x and O_2, during a period of anodically polarization. When the current is switched into a cathodically polarization, N_2 would be formed while oxygen ions are transported away from the Ba-containing compound through the electrolyte. The mechanisms of the electrochemical storage is illustrated in Figure 1.8.

Chapter 2

Materials

2.1 Spinels

Spinels are a very large class of compounds which are isotypic with the mineral spinel $MgAl_2O_4$. Spinel materials are widely used in the industry because of their usefulness as magnetic materials, semi-conductors, pigments, catalysts and refractories. Most of them are oxides but also sulphates, selenides and tellurides are know to have the spinel structure [67–69].

The spinel structure of oxides (AB_2O_4) is build up around O^{2-} ions which form a close cubic packing (CCP) sequence, with 16 tetrahedral (T) sites and 64 octahedral (O) sites per unit cell. However, only one eighth of the T sites and one half of O sites are occupied by cations. The CCP layers of oxygen are stacked parallel to {111}, resulting in alternating layers of O sites and T sites. The occupancy of the interstitial sites results in a large unit cell with 32 oxygen atoms which makes it difficult to illustrate the structure. Figure 2.1 shows the spinel structure in terms of the cation polyhedrals.

Several different cations can be introduced in the structure which leads to a variety of different charge combinations for example $SnMg_2O_4$, $LiCrTiO_4$ or Na_2WO_4 [70–72]. Spinels are traditionally divided into two different ideal types of structures: the *normal* spinel structure and the *inverse* spinel structure. In normal spinels, A ions are located only on T sites and B ions only on O sites. Inverse spinels have half the B ions located on T sites, while the rest of the B ions and the A ions occupies the O sites. The cation distribution is often quantified with the parameter γ, which corresponds to the fraction of A ions on the O sites. Spinel-type materials with a normal spinel structure will have $\gamma = 0$, whereas inverse spinel structures will have a γ-value of 1. In cases where there is more than two different cations in the structure, the terminology of normal versus inverse

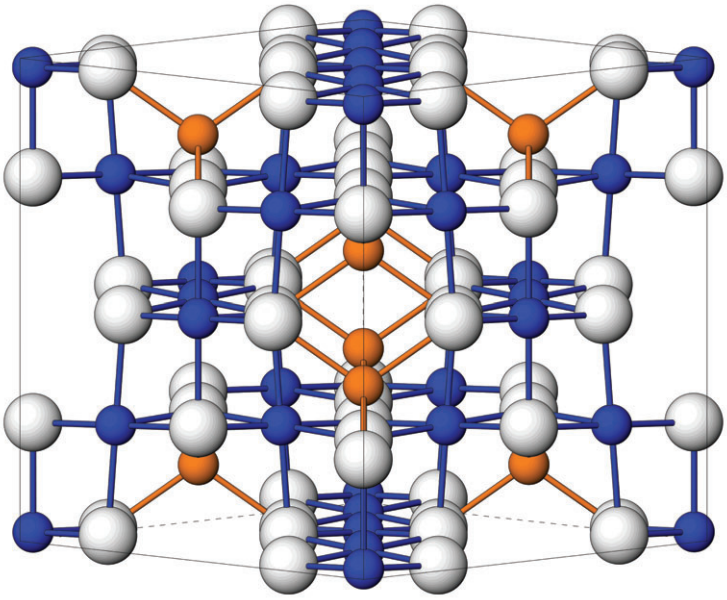

(a)

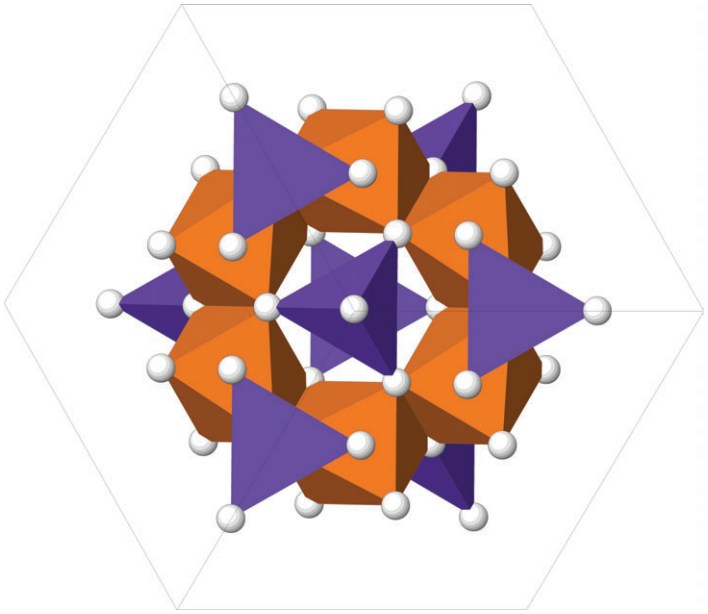

(b)

Figure 2.1: (**b**) The spinel structure viewed almost along the [110] axis in a slightly tilted angle. Blue and orange spheres represent the cations on octahedral sites and tetrahedral sites respectively. White spheres represent the oxygen atoms. (**b**) The spinel structure viewed along the [111] axis. Orange polyhedrons represent the octahedral coordinated sites whereas blue polyhedrons represent the tetrahedral coordinated sites.

spinels is more difficult to apply, however, if the valences of the atoms are arranged like that of the traditional spinels (2+, 3+ and 3+), the terminology can still be used. An example would be $NiCrFeO_4$: Fe^{3+} occupy the T sites whereas Cr^{3+} and Ni^{2+} occupies the O sites, which will make the spinel inverse. In cases with more than two different atoms, all having different valences (for example $LiCrTiO_4$) the terminology cannot be used.

The oxygen ion conductivity of spinels is very low with diffusion constants of about $\sim 10^{-10}$ cm^2s^{-1} [73–76]. Instead, spinels are semi-electron conductors ranging from 225 to $\sim 10^{-2}$ Scm^{-1} at elevated temperatures, but also spinels with a more insulating behaviour is known [77].

In this thesis, mainly ferrite spinels were synthesized, but also a few manganates, cobalt and chromium spinels were fabricated. The spinels are listed in section 4.1.

2.2 Electrolyte Materials

Two different electrolyte materials were used in this thesis. Both are solid state oxygen ion conductors, however, the main differences lies in their operation temperatures and their costs.

The most common electrolyte material is Y_2O_3-stabilized ZrO_2 (usually 8 percent yttria, abbreviated YSZ). ZrO_2 has a monoclinic crystal structure below 1200 °C, which is stabilized into a cubic structure above 2370 °C [78]. Incorporating Y_2O_3 into the structure, stabilizes the cubic form, which is much more suitable for oxygen ion conductivity compared to the monoclinic form. YSZ is especially used in high temperature solid oxide fuel cells (SOFC) because of their good stability in both oxidizing and reducing atmospheres. However, the oxygen ion conductivity decreases dramatically when going to temperatures below $600 - 700$ °C [79]. YSZ was used though in this thesis at much lower temperatures (down to 300 °C) and still it was possible to conduct oxygen ions.

Gd-doped CeO_2 (usually 10 percent gadolinia, abbreviated CGO10) is a more expensive electrolyte material, however, it is a much better oxygen ion conductor at low temperature [79]. CGO10 has a cubic fluorite structure with Ce and Gd situated on O sites. Each oxygen ion is tetrahedral coordinated by four Ce cations. A more detailed description of the crystal structure of CeO_2 and other cerium oxides can be found elsewhere [80, 81]. In this thesis, CGO10 was used not only as electrolyte material but also in the electrode, in combination with spinels. The latter was done in order to increase the oxygen ion conductivity and the number of three-phase-boundaries (TPB) in the electrode.

Chapter 3

Characterization of Materials

3.1 Non-electrochemical Analysis Methods

3.1.1 X-ray Powder Diffraction

X-ray diffraction (XRD) is a well known and frequently applied technique in solid state chemistry characterization. It is used to identify crystalline phases by means of their lattice parameters and crystal structure. In short, XRD is based on elastic scattering of X-ray photons by the electrons associated with the ions. Figure 3.1 illustrate how X-rays are diffracted by crystal planes. Structural information can be obtained using the Bragg equation 3.1,

$$n\lambda = 2d\sin\theta, \tag{3.1}$$

where n is an integer (1,2,3, ...) that determines the order of the reflection, λ is the wavelength of the X-ray, d is the distance between two lattice planes and θ is the angle between the incoming X-ray and the reflecting lattice plane. If the Bragg equation is not satisfied, the interference will not be constructive. Knowing the distance between two parallel atomic planes having a Miller indices of (hkl), the lattice parameters can be calculated. In the case of a cubic crystal structure (like the spinel-type structure), the lattice parameters, a, can be calculated using equation 3.2,

$$d_{hkl} = \frac{a}{\sqrt{h^2 + k^2 + l^2}}. \tag{3.2}$$

The scattering factor increases linearly with the number of electrons, which makes it difficult and sometime impossible to detect light elements or distinguish between elements

with almost the same number of electrons. This is especially a problem with X-ray powder diffraction when only a limited number of reflections are recorded in the diffractogram. If experiments are required to distinguish between elements with almost the same number of electrons or to detect light elements, neutron diffraction is often more useful.

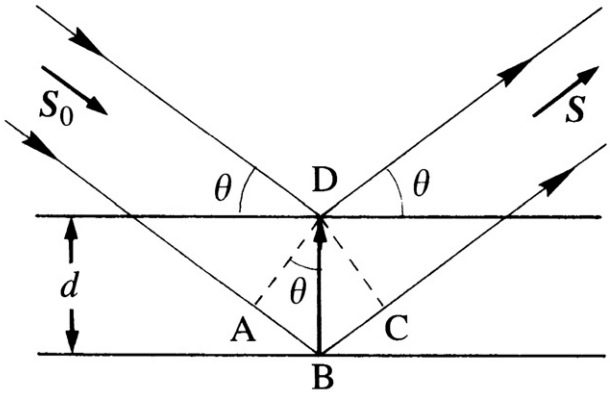

Figure 3.1: Principles of XRD. S_0 and S represent the incoming and diffracted beam respectively. d is the distance between the atomic planes.

3.1.2 Neutron Diffraction

Neutron diffraction is closely related to XRD, however, instead neutrons are used as the incoming beam hitting the sample. The technique is less common, compared to XRD, since it requires a nuclear power source in order to generate neutrons. The difference between XRD and neutron diffraction techniques lies in the scattering process. In XRD the photons are scattered by the electrons around the nucleus, whereas neutrons are scattered by the nucleus. The neutron scattering factor of elements varies for different atoms in an non-predicted way and there can be very large variations between isotopes of the same element [82]. It is, therefore, possible to detect light elements or distinguish between elements with almost the same number of electron.

An additional magnetic scattering of neutrons from paramagnetic atoms arises from the neutron spin interacting with the magnetic moment of an atom. Neutron diffraction is, therefore, often used to detect magnetic transitions in a crystal structure. However, magnetic neutron scattering was not observed in the recorded data of this thesis and therefore no further details will be given on this matter.

3.1.3 Scanning Electron Microscopy

A scanning electron microscope (SEM) is a powerful and highly used instrument to observe and characterize materials down to 1 nm [83]. In short, a SEM consist of a very fine probe of electrons which is focused onto the surface of a specimen and scanned across it. When the electrons hits the surface a number of phenomena occur with the emission of high energy backscattered electrons and secondary electrons being the most important ones in SEM. Backscattered electrons are electrons from the incident beam which have interacted with the atoms in the specimen and are reflected back again. Therefore, the intensity of backscattered electrons is much dependent on the average atomic number in the specimen at a given position. Secondary electrons, on the other hand, results from electrons emitted from the specimen due to a collision with the incident beam. In many materials the mean free path length of secondary electrons is typically of the order of 10 Å, which is much smaller compared with the mean free path length of backscattered electrons. This makes the resolution from secondary electrons much better compared to the backscattered electrons. The intensity is very sensitive to the angle between the incident beam and the surface of the specimen, which makes it possible to detect the surface topography of the specimen with a very high accuracy.

In this thesis a Low Vacuum (LV) JSM-5310LV SEM with an EDS (Energy Dispersive Spectroscopy) detector for element analysis was used to analyze the samples.

3.1.4 Dilatometry and Thermogravimetry (TG)

Thermal expansion compatibility is important in order to avoid formation of cracks during thermal cycling. Dilatometry is a technique to measure the thermal expansion coefficients of a material in different atmospheres. The expansion can be divided into three cases; 1) pure thermal expansion of the structure due to an increase of bond distances caused by the increase of thermal vibrations of the elements. 2) reordering of the cation (or anion) between lattice sites of different coordination geometry [84] and 3) chemical expansion of ions when their oxidation states are changed. The latter case is only very important when the structure is non-stoichiometrical [85, 86].

Thermogravimetry (TG) is a technique to measure the weight changes in a material as function of temperature. Weight changes are caused by desorption of H_2O, chemical reactions that involves evaporation of gases from the crystal structure or other kinds of thermal decomposition of the material. The TG technique is often used to determine the oxygen stoichiometry of a material in different atmospheres and temperatures. Any

changes in weight are usually measured isothermally while changing the atmosphere. Knowing the oxygen stoichiometry makes it often possible to determine the oxidation state of an element in the sample.

3.1.5 Conductivity Measurements

Electrical resistance or conductivity measurements are normally done with a two-point measurement technique. However, lead resistances and contact resistances then becomes significant factors especially when measuring very low values of ohms (mΩ or $\mu\Omega$). This problem is eliminated using a four-point DC technique where the current contacts are separated from the voltage contacts. DC current, I, is sent through the sample and the voltage drop, ΔU, is measured across the sample. Using Ohm's law ($\Delta U = I \cdot R$) the resistance, R, can now be calculated. Figure 3.2 illustrates the principles of the four-point DC technique. The specific resistance, ρ, can be calculated from Ohm's law by applying a geometrical factor, g_f,

$$\rho = \frac{g_\mathrm{f} U}{I}. \tag{3.3}$$

g_f is equal to the cross section area, A, of the sample divided by the distance, $l = U_2 - U_1$, between the voltage leads. In this thesis electron resistivity measurement were performed with a four-point DC technique using an in-house setup (see section 4.3.1).

3.1.6 X-ray Absorption Spectroscopy (XAS)

X-ray Absorption Spectroscopy (XAS) is a powerful technique to study the structure as well as the oxidation states of an element. XAS arises from excitation of electrons from s-states to higher unoccupied states and to the continuum. Typically, synchrotron radiation is used as energy source to excite the electrons.

In XAS, the main issue is the absorption coefficient, μ, which gives the probability that X-rays will be absorbed according to Beers Law, (see equation 3.4),

$$I = I_0 \exp(-\mu t). \tag{3.4}$$

I_0 is the X-ray intensity incident on a sample, t is the sample thickness, and I is the intensity transmitted through the sample. The X-ray intensity is proportional to the number of X-ray photons and at most X-ray energies, μ, is a smooth function of energy, with a value that depends on the sample density, ρ, the atomic number, Z, atomic mass,

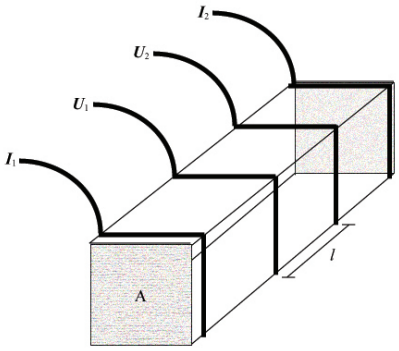

Figure 3.2: The principle of the four point conductivity measurements. Pt-paste is applied on each ends of the rod. A is the cross section area and l is the distance between the two probes.

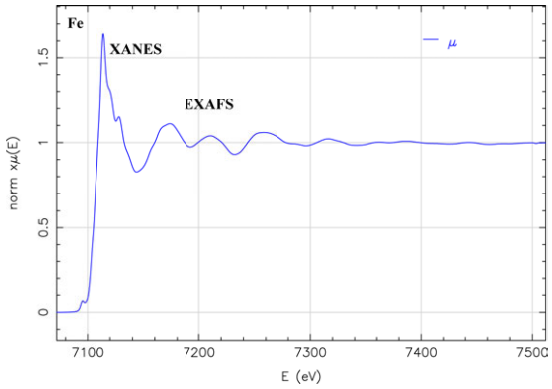

Figure 3.3: Example of the XANES and the EXAFS regions for $NiFe_2O_4$.

A, and the X-ray energy, E, roughly as,

$$\mu \approx \frac{\rho Z^4}{AE^3}. \tag{3.5}$$

The strong dependence of μ on both Z and E is a fundamental property of X-rays, and is the key to why X-ray absorption is a useful technique. Due to the Z^4 dependence, the absorption coefficient can be very different between elements and a good contrast between different materials can be achieved for nearly any sample thickness and concentrations by adjusting the X-ray energy.

XAS can be divided into regions: The X-ray Absorption Near Edge Structure (XANES) region and the Extended X-ray Absorption Fine Structure (EXAFS) region (see Figure 3.3). XANES is a method for analyzing the local coordination geometry and oxidation state of the adsorbing atom in a specific structure. The XANES region spans the energy region around the main absorption edge of the element of interest. The origin of the main edge[1] results from excitation of an $1s$ electron into an unoccupied $4p$-states [87]. The position of the K-edge depends of the oxidation state of the analyzed atom. The higher the valence, the more the main edge will move towards higher energies. The oxidation state can be determined by analyzing the position of the K-edge, by measuring two suitable reference materials, where the oxidation state of the element of interest is known, under the same conditions as the sample. The oxidation state of the element can then be found by a linear interpolation of the references on the sample data with the unknown oxidation state. However, this method is not very accurate and can only be applied if more than 5 % of the (transition) element changes oxidation state [88]. A

[1]Only the K-edge of selected transition elements is used in these measurements.

small pre-edge is often seen when reduced local symmetries are present. The pre-edges, in transition metals, rises from an excitation of an $1s$ electron into an unoccupied $3d$-state.

At higher energies with respect to the main edge we have the EXAFS region. One way of visualizing the EXAFS processes is to consider the excited photoelectron as an outwardly propagating spherical wave which is scattered from the surrounding atoms. The interference between the outgoing wave and the backscattered waves is the source of the oscillatory structure in EXAFS. The impact of these scattering paths on the EXAFS can be described according to the EXAFS equation,

$$\chi(k) = \sum_j \frac{N_j f_j(k) \exp(-2k^2\sigma_j^2)}{kR_j^2} \sin[2kR_j + \delta_j(k)], \tag{3.6}$$

where N is the number of neighbouring atoms in each coordination shell, R is the distance to these neighbouring atoms and σ is the mean-square-displacement in the neighbour distance. $f(k)$ and $\delta(k)$ denotes the scattering amplitude and phase-shift respectively as a function of the wave number, k, of the photo-electron. k is defined as

$$k = \sqrt{\frac{2m(E - E_0)}{\hbar}}, \tag{3.7}$$

where E_0 is the absorption edge energy and m is the electron mass. $\hbar$ is the Planck constant, h divided by 2π. Both $f(k)$ and $\delta(k)$ depend on the scattering properties of the atoms neighbouring and the excited atoms. As these depend on the Z of the neighbouring atom, EXAFS is sensitive to the atomic species of neighbouring atoms.

In this thesis EXAFS was preformed on $ZnFe_2O_4$ with the purpose of evaluating the Rietveld refinements on neutron diffraction data (see section 5.4.6). Data recorded in the XANES region at room temperature were only used to detect the position of the cations in the spinels relative to each other. $MgFe_2O_4$ and $NiFe_2O_4$ were also analyzed in 1 % NO in Ar, 1 % NO_2 in Ar and in a mixture of 0.5 % NO and 10 % O_2 in Ar. This was done in order to analyze the relative changes in oxidation state of the cations. Metal foils of the different transition elements of interest were used as reference material for the XANES data recorded at room temperature.

3.2 Electrochemical Analysis Methods

3.2.1 Cyclic Voltammetry (CV)

Cyclic voltammetry is a widely used technique to analyze the current response as function of an applied potential over an electrochemical cell. The method is particular powerful for initial studies of new systems because it is fast and relative easy to set up [89]. The potential is limited to a range in which the electrode material is stable. Moreover is the range set in such a way that possible electron reactions can occur (equation 3.8),

$$Red \rightarrow Ox + ne^{-}. \tag{3.8}$$

Red and Ox are the reduced and oxidized species respectively and n is the number of transferred electrons, e^{-}. An applied potential will therefore change the reaction from a steady state reaction to a non-steady state reaction. By using different sweep rates it is sometimes possible to determine diffusion constants if peaks appear in the voltammograms. The number of transferred electrons, reaction constants and the rate determining step of a certain electrochemical reaction can sometimes also be found by making a Tafel plot [90]. In this thesis, however, CV was mainly used to analyze the activities of the electrode materials relative to each other as well as to determine a diffusion constant of a single material.

3.2.2 Electrochemical Impedance Spectroscopy (EIS)

Electrochemical impedance spectroscopy (EIS) is a measure of the ability of a circuit to resist a flow of electrical current [91]. The most common and standard approach, is to measure the impedance by applying a single-frequency voltage to the interface and measuring the phase shift and amplitude of the resulting current using either analogue circuit or fast Fourier transform analysis of the response. At time $t = 0$ a small AC signal is applied to the system having the form of

$$E_t = E_0 \sin(\omega t), \tag{3.9}$$

where E_t is the potential at time t, E_0 is the amplitude of the applied signal and ω is the radial frequency given as $\omega = 2\pi\nu$, where ν is the frequency. The response signal, I_t, in

a linear system is given by,

$$I_t = I_0 \sin(\omega t + \phi), \tag{3.10}$$

where I_0 is the amplitude and ϕ is the phase shift. The impedance, Z, of the system is defined similar to the resistivity in Ohm's law which gives an impedance as shown in equation 3.11,

$$Z = \frac{E_t}{I_t} = \frac{E_0 \sin(\omega t)}{I_0 \sin(\omega t + \phi)} = Z_0 \frac{\sin(\omega t)}{\sin(\omega t + \phi)}. \tag{3.11}$$

Using Euler's relationship, the impedance can be represented as a complex function given by:

$$Z(\omega) = Z_0 \exp(j\phi) = Z_0(\cos\phi + j\sin\phi), \tag{3.12}$$

where $j = \sqrt{-1}$. For a system with different components connected in series the overall impedance is given by:

$$Z_{\text{tot}} = Z_1 + Z_2 + ... + Z_m, \tag{3.13}$$

while components connected in parallel give an overall impedance of:

$$\frac{1}{Z_{\text{tot}}} = \frac{1}{Z_1 + Z_2 + ... + Z_m}, \tag{3.14}$$

The impedance is often shown as a 'Nyquist Plot' with the real part of the impedance plotted on the x-axis and the negative imaginary part plotted on the y-axis. On a Nyquist plot, the impedance is represented as a vector of length $|Z|$ and with the phase angle between the vector and the x-axis. The impedance responses used in this study have the form:

Resistor:	Z	$=$	R
Capacitor:	Z	$=$	$\frac{1}{j\omega C}$
Constant Phase Element (CPE):	Z	$=$	$\frac{1}{Q(j\omega)^n}$

The CPE response can be viewed as non-ideally capacitors for which $n < 1$. When $n = 1$ the CPE has the form of a pure capacitor and $Q = C$ according to equation 3.2.2. However, in many cases of solid state electrochemistry, $n < 1$, which depicts the CPE response as a compressed half circle in the impedance plane. This is due to non-ideal microscopic differences in a material which results in a 'mean value' response to all the

different capacitors in the system [92]. Since the value of n affects the unit, it is difficult to compare with other CPE having a different n value. Therefore, CPE it often converted to near-equivalent capacitance (NEC) [93] as shown in equation 3.15,

$$C_{\mathrm{ne}} = \frac{(RQ)^{n^{-1}}}{R}. \tag{3.15}$$

The output signal is described by an equivalent circuit and in the impedance spectra obtained in this study, the electrical components are resistors (reaction resistances, R_m) or CPE. In order to compare the activity of point-electrodes, the current response must be normalized by dividing with the contact area between the electrolyte and the electrode. The contact area was determined by EIS using Newman's formula [94], equation 3.16,

$$r = \frac{1}{4\sigma R_{\mathrm{e}}}. \tag{3.16}$$

Newman's formula assumes that the contact area is circular with r being the radius of the contact area, σ being the specific conductivity of the electrolyte material and R_{e} being the electrolyte resistance. σ (YSZ-electrolyte) can be determined from equation 3.17 [95].

$$\sigma = \frac{1.51 \cdot 10^6}{T} \cdot \exp\left(\frac{-0.94[\mathrm{eV}]}{T k_{\mathrm{B}}}\right), \tag{3.17}$$

where T and k_{B} are the temperature (in Kelvin) and Boltzman's constant respectively. In this thesis, measurements were performed with a Gamry Femtostate having an AC potential as input signal. EIS were recorded from 177793(1) Hz to 0.050(1) Hz with 10 points/decade and with an amplitude of 24 mV (rms)[2] on cone-electrodes. EIS recorded on symmetrical cells and 3-electrode pellets were recorded from $300000(1) - 0.050(1)$ Hz with an applied amplitude ranging from $36 - 100$ mV (rms).

3.2.3 Chronoamperometry

Chronoamperometry is a technique where a potential gradient is applied over the cell. The potential is kept constant while the current response is recorded over time. This will show the activity of the electrode and possible gas conversions can then be detected. Chronoamperometry also give informations on the response time of the electrode. In this thesis, chronoamperometry was applied in two ways: 1) The potential was kept constant over a few hours while analyzing the composition of the exhaust gas over the cell. 2) A

[2]rms: root mean square.

square-wave potential was applied over the electrode, constantly shifting every 1 second between OCV and a given potential.

Chapter 4

Experimental

4.1 Material Synthesis

A variety of different spinel-type oxides were tried synthesized using various methods. This section describes the different methods of synthesis and list the successfully synthesized compounds in Table 4.2. Spinel-type oxides which failed to be synthesized as a single phase compound are not shown in this thesis.

4.1.1 Glycine-Nitrate Combustion Synthesis (GNCS)

The spinels oxides synthesized with the glycine-nitrate combustion synthesis (GNCS) [96] were done from aqueous metal-nitrates (see Table 4.1) which were mixed stoichiometrically in a glass beaker with glycine powder (glycine/nitrate=0.548). The beaker was then placed on a magnetic stirrer inside a fume cupboard until the glycine was dissolved in the mixture. The aqueous solution were then divided into a number of glass beakers, all containing 0.1 mol of spinel to insure a controlled combustion (see Figure 4.1a). The beakers were placed on hot-plates and heated at 110 °C until a thick viscous solution was obtained. The beakers were then, one by one, placed under a chimney with a fine grid mounted on top and the temperature was increased to 250 °C. This resulted in a controlled combustion leaving a fine powder which was collected from the beakers and from the inside of the chimney. The powder was ball milled over night and then placed in an alumina crucibles and calcined in air at 1000 °C for $6-10$ hours. Table 4.2 shows the calcination temperatures and calcination times of the spinels synthesized with the GNCS technique. After the calcination process, the powder was analyzed with XRD in order to establish the purity of the phases.

Table 4.1: Aqueous metal-nitrates and metal powders used in the material synthesis.

metal-nitrates	Purities [%]	metal powders	Purities [%]
$Mg(NO_3)_2 \cdot 2.6\ H_2O$	99	MgO	98
$Cr(NO_3)_3 \cdot 3.9\ H_2O$	99.999	Cr_2O_3	99.99
$Mn(NO_3)_3 \cdot 2.4\ H_2O$	99.999	MnO_2	99.6
$Fe(NO_3)_3 \cdot 3.9\ H_2O$	99.5	Fe_2O_3	99.9
$Co(NO_3)_2 \cdot 2.6\ H_2O$	99	-	-
$Ni(NO_3)_2 \cdot 2.6\ H_2O$	99.9	NiO	99
$Cu(NO_3)_2 \cdot 2.6\ H_2O$	99.9	-	-
$Zn(NO_3)_2 \cdot 2.6\ H_2O$	99.99	ZnO	99.99

4.1.2 Citric-Acid Synthesis (CAS)

The citric-acid synthesis (CAS) [97] was like the GNCS done from aqueous metal-nitrates which were stoichiometrical mixed in a large glass beaker. Citric acid was then added (citric acid/metal ions 1:1) and the aqueous solution were then divided into a number of glass beaker, all containing 0.1 mol of spinel to insure a controlled combustion. The beakers were then placed on hot-plates and heated slowly at 110 °C for $3-4$ hours. Then ethylene-glycol was added to each of the beakers while heading (ethylene glycol/citric acid 1:1.2). After approximate 30 minutes depending on the water content, the mixture started to foam and send out orange NO_x gases. The glass beakers were then left at the hot-plates at 120 °C for a few hours until the mixture had turned into at thick viscous solution of powder and unreacted gel. The beakers were then heated in air at 350 °C for 6 hours with a ramp rate of 50 °C/h and the solution was burned into a brittle pellet of ceramic powder filled with vesicles (see Figure 4.1b). A ceramic plate was placed as a lid on top of the beakers during heating in order to minimize a large amount of carbon particles to escape the beakers. The pellets were then crushed on a ball mill over night and then calcined at 1000 °C for 6 hours with a ramp rate of 100 °C/h. After the calcination process, the powder was analyzed with XRD in order to establish the purity of the phases.

4.1.3 Solid State Reactions (SSR)

Powders of metal oxides (see Table 4.1) were mixed stoichiometrical in an agate mortar together with ethanol. After the ethanol had evaporated the powder was uniaxial pressed at 1 ton for 30 seconds into a pellet. The powder was then placed in a furnace and heated to elevated temperatures for 30 hours. The powder was then crushed and the process was repeated until a single-phase powder of the right composition was obtained. Table 4.2 shows the calcination temperatures and the calcination times of the spinels synthesized with the SSR technique.

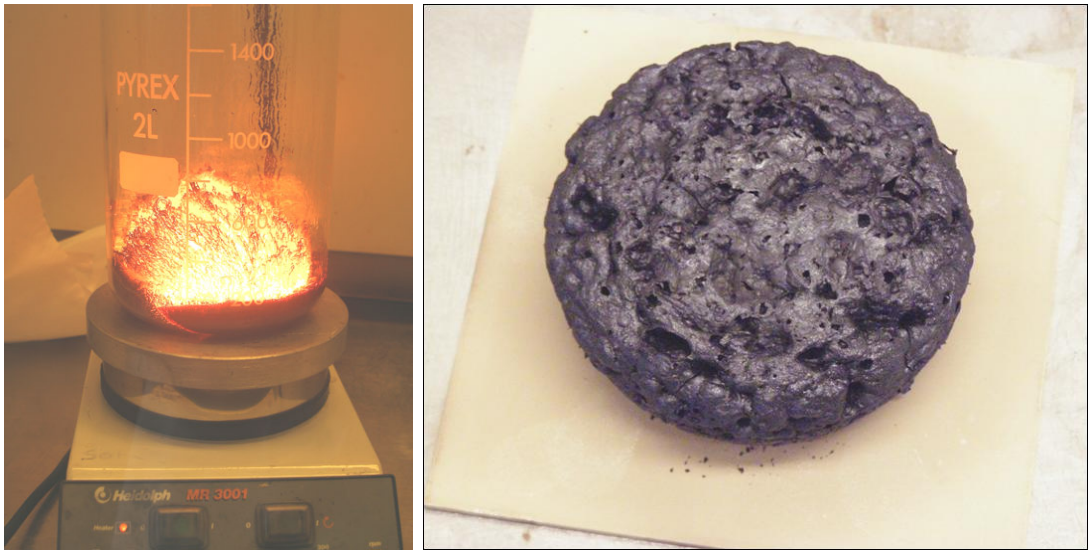

(a) (b)

Figure 4.1: (**a**) shows the controlled combustion process of the GNCS. (**b**) shows the brittle pellet of ceramic powder from the CAS after calcination of the sample at 350 °C. The diameter of the pellet is 10 cm.

Table 4.2: Synthesized spinel-type materials. A few compounds were calcined twice in order to obtain a single phase powder.

Compounds	Synthesis	Calcination		Sintering	Impurities
$NiFe_2O_4$	GNCS	1000 °C/6h		1050 °C/6h	
$Ni_{0.7}Mg_{0.3}Fe_2O_4$	GNCS	1000 °C/6h		1050 °C/6h	
$Ni_{0.5}Mg_{0.5}Fe_2O_4$	SSR	950 °C/60h		1200 °C/6h	$\sim$ 1 % NiO
$Ni_{0.4}Mg_{0.6}Fe_2O_4$	CAS	350 °C/5h,	1000 °C/6h	1050 °C/6h	
$MgFe_2O_4$	CAS	350 °C/5h,	1000 °C/6h	1050 °C/6h	
$NiCr_{0.5}Fe_{1.5}O_4$	GNCS	1000 °C/6h		1050 °C/6h	
$NiCrFeO_4$	GNCS	1000 °C/6h		1050 °C/6h	
$NiCr_{1.5}Fe_{0.5}O_4$	GNCS	1000 °C/6h		1050 °C/6h	
$NiCr_2O_4$	GNCS	1000 °C/6h		1050 °C/6h	$\sim$ 5 % NiO
$MgMn_{0.2}Fe_{1.8}O_4$	SSR	950 °C/30h,	1050 °C/60h	1100 °C/6h	
$MgMn_{0.4}Fe_{1.6}O_4$	SSR	950 °C/30h,	1050 °C/60h	1100 °C/6h	
$MgMn_{0.6}Fe_{1.4}O_4$	SSR	950 °C/30h,	1050 °C/60h	1100 °C/6h	
$MgMn_{0.8}Fe_{1.2}O_4$	SSR	950 °C/30h,	1050 °C/60h	1100 °C/6h	
$MgMnFeO_4$	SSR	950 °C/30h,	1050 °C/60h	1100 °C/6h	
$NiMn_2O_4$	CAS	1000 °C/6h		1050 °C/6h	
$MnCo_2O_4$	CAS	900 °C/8h		1050 °C/6h	
$ZnFe_2O_4$	SSR	950 °C/30h,	1000 °C/30h	1050 °C/6h	

4.2 Preparation of Samples and their Geometries

4.2.1 Cone-Shaped Electrodes

Different sample geometries were used in the characterization of the electrodes. Cone-shaped electrodes (point-electrodes) were basically used to screen the different electrode materials in order to find out which were electrochemical interesting. The cone-shaped electrodes were fabricated by pressing the powder uniaxially at 1 ton for 30 seconds followed by an isostatic pressing at 50 tons for 20 seconds. This was done in order to make the pellets more dense and to increase their mechanical strength. The samples were then sintered in air at 1000 °C for 6 hours. The pellets were then mechanically tooled into identical cone-shaped electrodes [57, 98] (see Figure 4.2).

The advantage of this geometry is to suppress the effect of microstructures such as porosity, grain size and grain shape. Recorded data would therefore reflect the true electro-catalytic properties of the material. However, using a cone-shaped electrode would not make it possible to measure any gas conversion because of the small contact area[1] compared to the flow rate. Instead, current ratios of I_{NO_x}/I_{O_2} were used as indicators of the apparent selectivity of the reduction of NO_x gases.

A general problem when working with cone-shaped electrodes is the ohmic drop across the electrode. If the conductivity of the electrode is very low compared to the ionic conductivity of the electrolyte, Newman's formula (equation 3.16) will give inaccurate contact areas. In our case the high frequency interception with the real axis in the impedance plot will be given by equation 4.1:

$$R_s = R_e + R_c, \tag{4.1}$$

where R_c is the ohmic resistivity of the cone-shaped electrode[2]. If $R_e \gg R_c$, R_e can be taken as equal to R_s which is then used in Newman's formula to calculate the contact areas. Knowing the specific conductivity of the electrode material, finite element calculations, using the software program COMSOL 3.4 Multiphysics [99], can be applied to calculate the resistance of the cone.

[1] Assuming that the electro-catalytic process takes place in the vicinity of the tip of the cone-electrode.
[2] R_c actually also contains contributions from the counter electrode and the wires.

4.2.2 Symmetrical Cells

Symmetrical cells consist of an electrolyte with identical electrode material on each side. They are used to analyze the electrode resistance in varies temperatures and atmospheres using electrochemical impedance spectroscopy. Symmetrical cells are well suited for electrode development because there is no ambiguity about the source of electrode properties in this case. It also makes it possible to analyze different electrodes in a separated manner. However, its use is limited to investigations with EIS close to the OCV as no reference electrode can be used. Working conditions of a final electrochemical cell is not operated at OCV, however, symmetrical cells are still a valuable test design, not only because they are easy to fabricate, but the experiment give a fast indication of the performance of the electrode. Any changes in fabrication methods and cell composition can therefore quickly be evaluated of how it affects the performance of the cell.

In this thesis, two different types of electrode materials were analyzed with the symmetrical cell design. The symmetrical cells were made using a 6×6 mm^2 and 160 μm thick YSZ-tape as electrolyte. A slurry of 50 vol% AFe_2O_4 (A = Mg or Zn), 50 vol% low surface area (LSA) CGO10 and a mixture of organic compounds (confidential recipy) were prepared and ball milled for 24 hours. The spinel materials were grained in a planetary mill until a mean particle size[3] of around 1 μm ($MgFe_2O_4$: 1.1 μm, $ZnFe_2O_4$: 1.0 μm) were obtained. The slurries were sprayed (one layers of 15 μm) on both sides of the electrolyte and sintered in air at 1000 °C for 6 hours using a ramp rate of 100 °C/h (see Figure 4.3). A current collector of 80 w% Au-paste and 20 w% carbon powder, mixed with a few drops of ethanol was brushed on top of the two electrodes. The cells were then heated to 800 °C in order to burn away the carbon, leaving a porous Au current collector (Figure 4.4). The mean in-plane resistivity (sheet resistivity) of the Au current collector was measured to 21 Ω at room temperature.

A few button-shaped symmetrical cells were also fabricated with the purpose of optimizing the performance of the $MgFe_2O_4$/CGO10 electrode. Two different composite porous electrodes were fabricated $MgFe_2O_4$/CGO10 with volume ratios of 65/35 and 75/25. Each slurry were tape casted into a 1000 μm thick tape and five circular discs of each tape were calcined in a gradient furnace from 900 °C−1150 °C with a temperature step of 50 °C. Symmetrical cells of each composite electrode were fabricated by laminating the electrodes on each side of a 20 μm thick (after calcination) CGO10 electrolyte. Unfortunately no further tests were made on the cells as results of the recorded data on the symmetrical cells which showed a poor electrochemical performance (see section 5.1.5).

[3]The particle size distribution was measured with a Bechman LS 13320 laser diffraction particle size analyser.

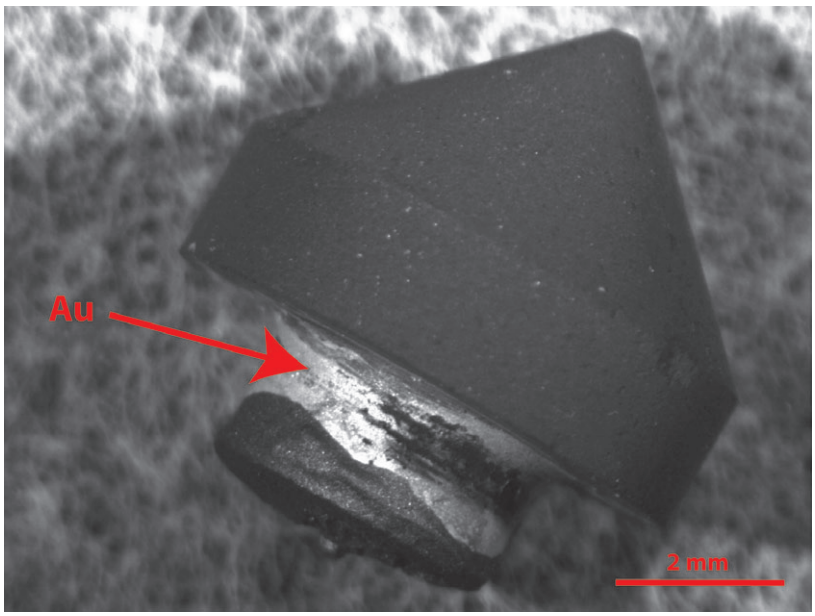

Figure 4.2: Picture of the cone-electrode with the Au current collector taken in an optical microscope.

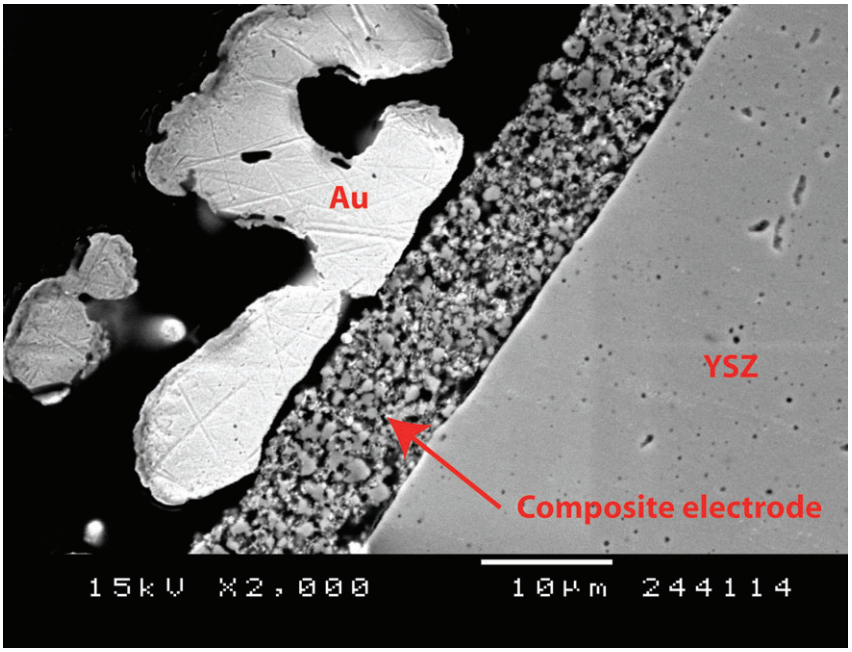

Figure 4.3: A SEM pictures of the cross section of a symmetrical cell. The composite electrode is sandwiched in between the YSZ electrolyte and the Au current collector.

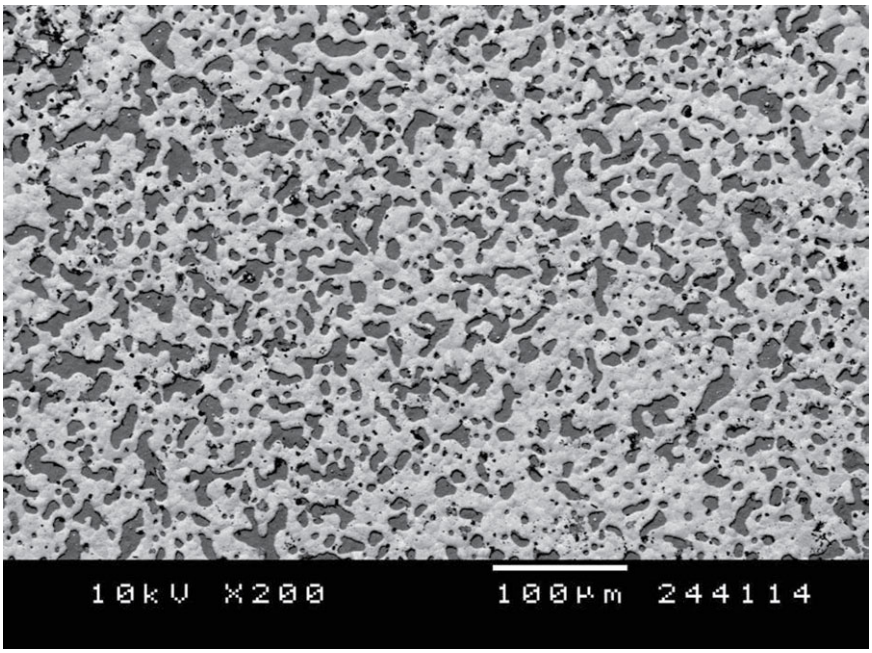

Figure 4.4: SEM pictures of the porous Au current collector after burning off the carbon. The current collector is situated top of an YSZ electrolyte.

4.2.3 CGO10 Electrolytes for 3-Electrode (3E) Pellets

Electrolyte pellets for the 3E-setup (see section 4.3.2) were only available in YSZ at the beginning of this thesis. Experiments were therefore performed on manufacture '3E electrolytes' of CGO10. This was done in order to lower the working temperature of the experiments as the oxygen ion conductivity is significant higher for CGO10 compared with YSZ at low temperatures (see section 2.2). High Surface Area (HSA) CGO10 (Rhodia) and Ultra High Surface Area (UHSA) were pressed uniaxially at 1 ton for 1 minute. The pellets were then placed in a rubber sleeve and air was evacuated using a vacuum pump. The sample inside the rubber sleeve was then pressed isostatically at 50 tons for 30 seconds. Results showed a dense but also a fragile pellet. A new experiment was then made by adding ethanol to the CGO10 and letting it evaporate before pressing the pellets. This made the CGO10 powder agglomerate and made it much easier to handle the sample loading of the pressing tool. However, it did not have any effects on the pressed pellet which continued to be fragile. Experimental tests were therefore preformed on adding a small amount of organic binder (1, 3 and 5 w%), ethanol, 1 w% glycerine and 1 w% starin acid to the HSA CGO10 ($97-93$ w%) and letting it ball mill over night. The slurry was then dried and crushed into powder and then pressed at the same conditions as in the case of the pure CGO10 powder. This removed most of the fragile behaviour but it was still impossible to cut them into the right shape before sintering as the materials that were cut away peeled of in small flakes. No apparent physical differences were observed

between pellets containing 3 or 5 w% organic binder, however, pellets containing only 1 w% organic binder seemed more fragile. Since it was not the goal of this thesis to optimize the electrolyte, it was decided to sinter the CGO10 pellets containing 5 w% organic binder using the temperature profile illustrated on Figure 4.5a. The pellets were then mechanically tooled with a diamond cutter into their final shape (see Figure 4.5b). This process was very time consuming and could therefore only be used for small scale

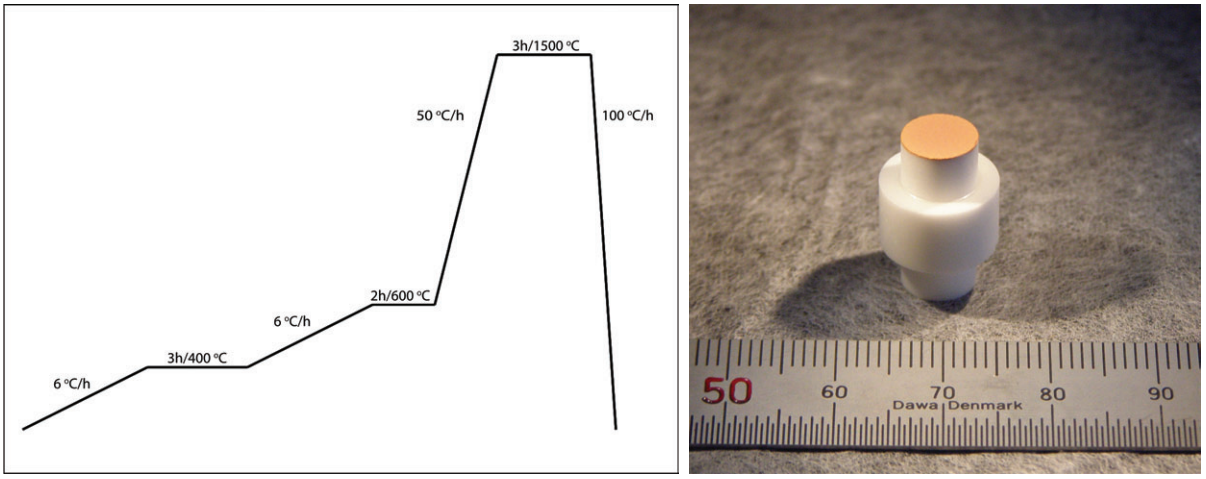

(a) (b)

Figure 4.5: (**a**) Temperature profile of the sintering of the 3E-pellets. The temperature is increased slowly in the beginning so that the organic compounds can have time to evaporate from the pellet interior without leaving cracks in the specimen. (**b**) A 3E YSZ pellet with a working electrode consisting of $ZNFe_2O_4$/CGO10 sprayed on top.

test productions. Measurements on the porosity and pore size distribution were made with a Micromeritics AutoPore IV Mercury Porosimeter and results showed a porosity of 0.4(2) % and a mean pore diameter of 0.7(1) μm. The overall process of manufacturing good dense CGO10 3E pellets may be optimized by pressing the pellets at lower pressures before cutting them, however, since it was not necessary to make a large production no further optimization was made.

4.2.4 3-Electrode (3E) Pellets

The slurries, described in section 4.2.2 were sprayed on top of the electrolytes of the 3E pellets (one layer of 10 μm) to serve as the working electrode (see Figure 4.5b). The 'half' cell was then calcined at 1000 °C for 6 hours using a ramp rate of 100 °C/h. The process was repeated with a second layer of electrode material because small pinhole was observed in the first electrode layer. After calcination of the second electrode layer no pinholes were observed in microscope. Pt-paste was then brushed on the 3E pellets to

act as counter electrode, and the current collector (80 w% Au-paste and 20 w% carbon powder) where then brushed on top of the working electrodes. The cells were then heated to 800 °C to burn away the carbon. Six 3E pellets of each slurry were fabricated; four with an YSZ electrolyte and two with a CGO10 electrolyte.

4.2.5 Preparation of Samples for XAS Analysis

In order to obtain good quality measurements, a thin homogeneous sample had to be used in the setup. However, in order to avoid a large drop in intensity of the signal, the material of interest had to be mixed with material having a low adsorption coefficient. An in-house made powder of alumina powder, mixed with ethanol and a 2 % aqueous PVE (Polyvinyl-Ethanol) solution was used as the backbone material. The three components were mixed until a smooth viscous paste was obtained. The paste was then dried at 80 °C for 1 hour until the paste had taken a pure solid form. The mixture was then grained into fine powder. 5 mg of spinel-type oxide powder was mixed with 30 mg of the alumina powder and the sample was prepared by dry-pressing the powder at 4 tons for 30 seconds into disc-shaped pellets with a thickness of $0.5 - 1$ mm and a diameter of 13 mm. The discs were mounted vertically in the sample chamber and measurements were performed on the samples.

4.3 Experimental Setups

4.3.1 Non-Electrochemical Setups

X-ray Diffraction

All samples, recorded with XRD in this thesis, were mounted on a sample holder and analyzed on a STOE theta-theta diffractometer with a Cu anode. No monochromator was installed on the diffractometer so both Kα_1 ($\lambda = 1.54051$ Å) and Kα_2 ($\lambda = 1.54433$ Å) radiation were present in the ration of 1:2. XRD was recorded with a step width of 0.05° in the 2θ range of $15° - 90°$ depending on the material. 10×8 mm^2 slits were used for the inclined beam and 10×3 mm^2 soller slits on the diffracted beam. The technique is schematically shown in Figure 4.6a.

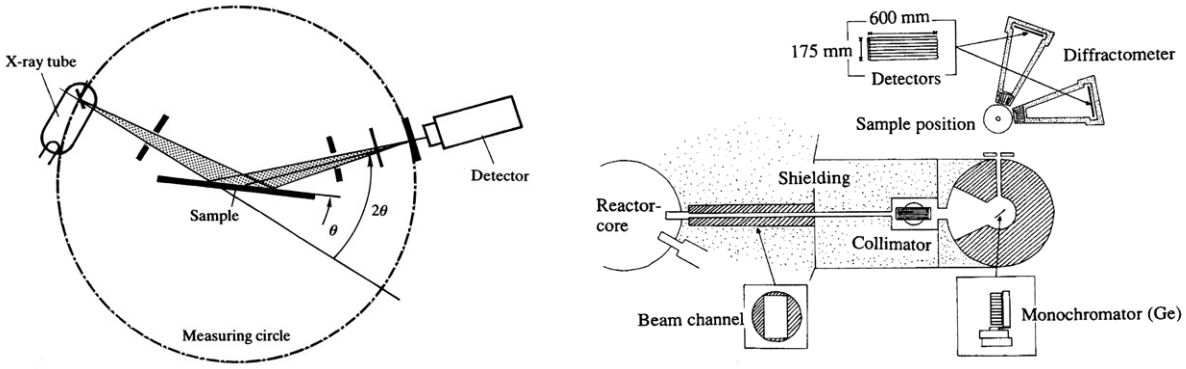

(a) (b)

Figure 4.6: (**a**) Illustration of the setup of the XRD [100]. (b) A schematic drawing of the powder universal spectrometer installed at the 2 MW JEEP II reactor at the Institute for Energy Technology in Kjeller, Norway [101].

Neutron Diffraction

High temperature *in situ* measurements were performed with a high-resolution powder neutron diffractometer, installed at a 2MW JEEP II reactor at the Institute for Energy Technology in Kjeller, Norway. The powder was placed in a quartz tube inside a furnace and measured in air with a 2θ-range of $10° - 130°$, a step width of $0.05°$ and a wavelength of 1.555 Å using a Ge(511) monochromator. Two detector banks, each covering $20°$ in 2θ and containing seven ^{3}He position sensitive detectors stacked on top of each other, were used to record the neutron diffraction pattern. A schematic drawing of the setup is shown on Figure 4.6b. A more detailed description of the diffractometer can be found elsewhere [101].

Dilatometry and Thermogravimetry (TG)

The linear thermal expansion was measured in air (flow rate: 50 ml/min) using a NETZSCH DIL 402C dilatometer with a sample load of 30.000 cN. The sample-rod was heated from room temperature up to 1000 °C and back at 2 °C/min. The sample remained at 1000 °C for 2 hours. Data were calibrated to an Al_2O_3 standard at identical conditions. In this thesis, TG was used to verify the thermal instability of $MgFe_2O_4$ at high temperatures and to improve the understanding the electrical conductivity and the dilatometry data recorded on the spinel. TG measurements were performed on a NETZSCH TG 439 thermo microbalance in air (flow rate: 50 ml/min). The measurement was run with the same temperature profile as used in the dilatometry measurements.

4.3. Experimental Setups

X-ray Absorption Spectroscopy

XAS measurements were conducted on beamline E4 at HASY LAB, DESY (Deutsches Electronen Synchrotron), Hamburg, Germany. The synchrotron radiation (4.5 GeV) was sent through a double Si(111) monochromator as illustrated on figure 4.8. Scan details of the energy steps for the XANES and the EXASF regions are shown in Table 4.3. Data recorded at 400 °C were carried out on an in-house setup [102] where the pellet was mounted vertically inside a horizontally positioned quartz tube placed in a tube furnace. A gas inlet and a gas outlet was mounted in each end of the quartz tube (see Figure 4.7). A Kapton® window was mounted at each end of the quarts tube to allow radiation to pass. Data were recorded 3 hours after changing the atmosphere in order to stabilize an equilibrium inside the tube.

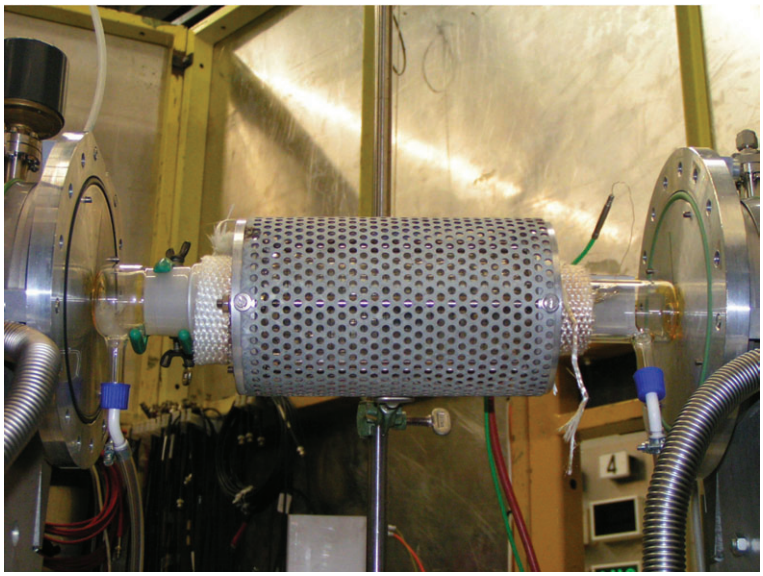

Figure 4.7: Setup of the furnace for EXASF analysis. The sample is placed horizontally inside the tube furnace.

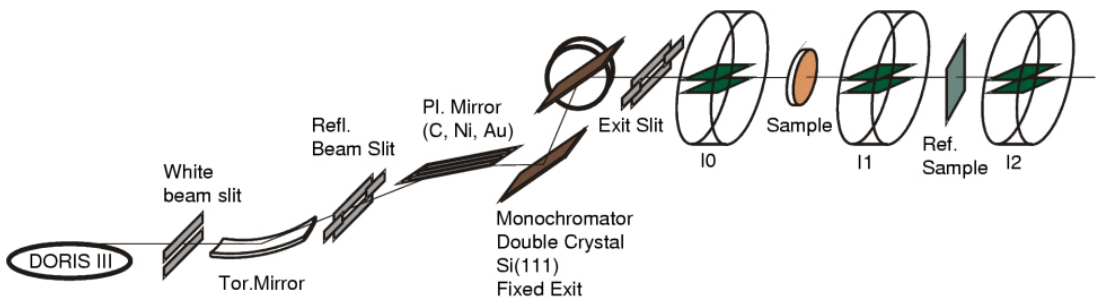

Figure 4.8: Schematic of the beamline E4 at HasyLab, DESY, Hamburg, Germany - used for the XAS experiments carried out during this study [103].

Conductivity Measurements

Two Pt leads were applied to each end of the elongated sample (see section 3.1.5). Pt paste was then brushed on at each end of the sample to insure a good contact and to make the field lines inside the sample as homogeneous as possible. The sample was placed in an alumina tube with two Pt potential probes, separated with a fixed distance (6.55 mm), positioned so that they would press against the sample. A push-rod was applied to the sample to insure a good contact with the two Pt potential probes. The alumina tube was then placed in a tube furnace. Data were collected with an in-house data acquisition software, ELCHEMEA. In our measurement, the samples had the dimensions of $4 \times 4 \times 16$ mm^3 with a cross section area of 0.16 cm^2. The resistivities of the samples was measured every 5 minutes from room temperature to 1000 °C and back again with a ramp rate of 2 °C/min and a two-hours dwell at every 50 °C interval. The resistivities were corrected for the porosity using the Bruggeman asymmetric model [104]. The porosities were measured by the Archimedes principle or with a Micromeritics AutoPore IV Mercury Porosimeter.

4.3.2 Electrochemical Setups

Cone-Electrode Setup

The electrochemical technique of using a cone-shaped electrodes (see section 4.2.1) was initially developed by Fabry *et al.* [105]. The base of the cone-electrode was painted with Au-paste in order to insure a good electrical contact. The cone-electrode, acting as the working electrode was arranged with the tip placed downwards on a polished one-end closed YSZ-tube electrolyte containing air as reference gas. The area of the YSZ-tube in contact with the cone-electrode was polished with 1 μm diamond-paper in order to minimize any microstructural effects which could change the true electro-catalytic properties of the material. The thickness of the electrolyte was approximately

Table 4.3: Scan details for the XANES and the XASF measurements. The count times for each step were 1 s. The energies are starts of intervals, with sizes of the energy steps between data points in each interval given as ΔE.

Cr, eV	Fe, eV	Ni, eV	Zn, eV	ΔE
5826	6949	8170	9496	5.0
5945	7068	8289	9611	0.5
5975	7098	8319	9645	0.2
6025	7148	8369	9695	0.5
6085	7208	8429	9755	1.0
7026	8149	9370	10696	-

2 mm. Inside the polished end of the tube, Ag-paste was applied and the hole tube was fired at 600 °C to get a good electrical contact. The Ag-electrode was then used as the counter/reference electrode. The much smaller contact area of the cone-electrode (point-electrode) compared to the counter electrode, suppresses a polarization of the counter electrode as it at the same time, and constantly, is exposed to a reference gas. A reference electrode can therefore be placed together with the counter electrode (a pseudo-three-electrode setup). Figure 4.9 illustrates the principles of the setup. A working gas was applied at the cone-electrode with a flow of 20 ml/min controlled with a Brook Instrument 0154 mass flow controller. The working gas was confined by a sealed alumina tube with Pt painted on the outside to act as a Faraday cage. The hole setup was placed vertically in a tube furnace inside a fume cupboard.

Symmetrical Cell Setup

The symmetrical cell setup is a two electrode setup in an one atmosphere chamber. The symmetrical cells were placed on a rig which could contain up to four cells. Each symmetrical cell was connected to four Au leads that ran through four-holed alumina tubes to the junction box. The four Au leads were arranged in two pairs in contact with the sample. Each pair was placed on both side of the cell. As the setup was used to measure the electrochemical impedance of the cell, a small AC signal was applied through the one pair of leads whereas the impedance was recorded at the other pair of leads. The rig was placed vertically inside a gas-tight alumina tube sitting in a furnace. The alumina tube was painted with Pt on the outside to act as a Faraday cage. A working gas was applied with a flow of 20 ml/min controlled with a Brook Instrument 0154 mass flow controller. Measurements were performed at one electrode at the time, after which the leads had to be changed manually in order to record the impedance spectra from the other cells.

3-Electrode Setup

The 3E setup was developed in 1998 at Risø National Laboratory [106]. A 3E pellet was mounted vertically between two alumina tubes. Two Au ring-shaped discs with a low temperature glass tape (confidential recipy) placed on each side of the two Au rings were used to seal the alumina tubes and 3E pellet together at a 1000 °C. 2 kg of weight was applied on top of the alumina tubes in order to insure a tight sealing. A Pt probe was placed so it touched the surface of the working electrode. A reference electrode of Pt was placed inside the 3E pellet together with a Pt-Rh(10%) wire which acted as thermocouple.

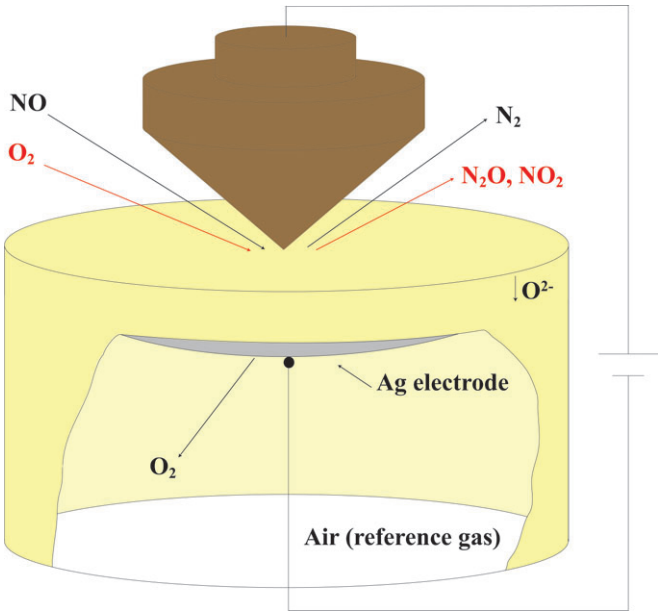

Figure 4.9: Principles of the cone-setup. The cone-electrode is placed with the tip downwards on an YSZ tube. Inside the tube is the Ag counter/reference electrode.

The counter electrode was in contact with the Au sealing and current could therefore be extracted by placing leads on the Au sealing outside the alumina tube. Working gases were applied by mass flow controllers from Brooks Instruments. A quartz tube was placed outside the alumina tubes and a inert purge gas (Ar) was applied inside the quartz tube in order to avoid possible atmospheric air to disturb the measurements. Figure 4.10 illustrates the 3E-setup.

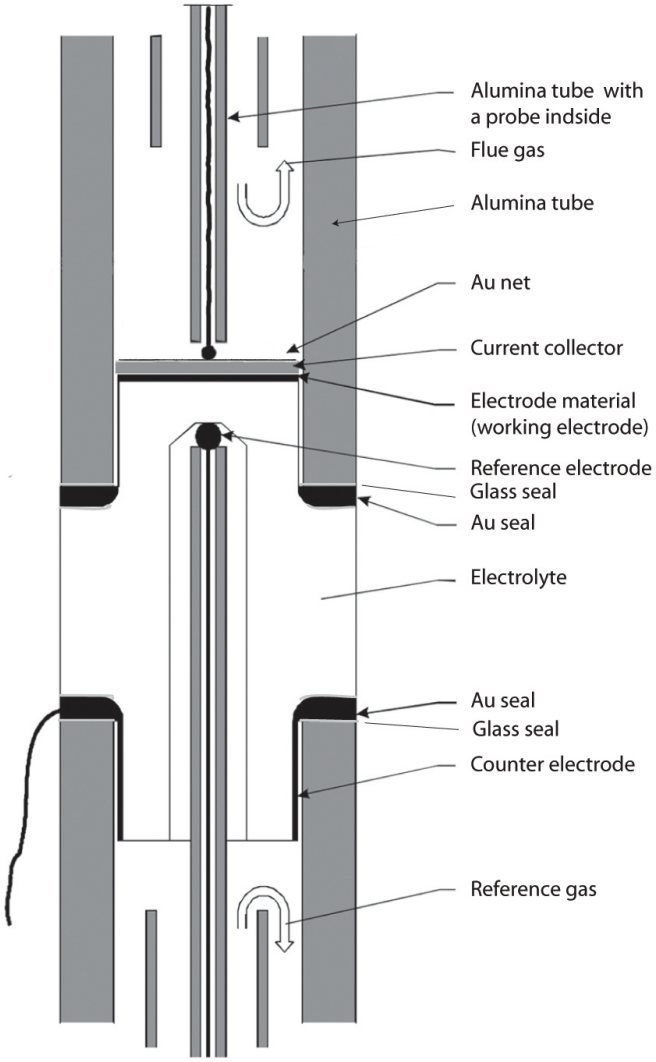

Figure 4.10: Principles of the 3E-setup. Different kind of sealing materials were tested and the best one found was a combination of thin Au plates and low temperature glass tape (recipe confidential).

Chapter 5

Results and Discussions

5.1 The $Ni_{1-x}Mg_xFe_2O_4$ Series

Earlier reports by Simonsen *et al.* [61] on $NiFe_2O_4$ electrodes showed high cathodic activities in NO compared to O_2. Therefore, the first part of the project was concentrated on characterizing the $NiFe_2O_4$ material. Alkali earth oxides are good candidates as NO_x sorbents [107] and the main purpose were therefore to investigate the effect of substituting Mg into the structure of $NiFe_2O_4$. A series of $Ni_{1-x}Mg_xFe_2O_4$ compounds were synthesized as described in section 4.1.1 and the compounds were characterized by XRD, dilatometry, CV, EIS as well as with conductivity measurements. Thermogravimetry was also performed on $MgFe_2O_4$. Results from this section are published in Journal of Solid State Electrochemistry [84].

5.1.1 Structural Properties

XRD, recorded at room temperature, showed an increase in unit cell parameters with increasing Mg content (Figure 5.1). $NiFe_2O_4$ has an inverse spinel-type structure [108] with Ni^{2+} located primarily on the octahedral (O) sites and Fe^{3+} located on both the tetrahedral (T) sites and the O sites. The ionic radius of Ni^{2+} on a T or an O site is 0.55 Å and 0.69 Å respectively, whereas Fe^{3+} has an ionic radius of 0.63 Å (tetrahedral sites) or 0.65 Å(octahedral sites) [109]. When Mg^{2+}, having an ionic radius of 0.57 Å (T sites) or 0.72 Å (O sites) is introduced in the structure in favour of Ni^{2+}, it will enter the T site and thereby force Fe^{3+} to move into an O site. That should in principle not increase the volume of the unit cell. However, although the increase in unit cell is very small, and in the range of $0 \leq x \leq 0.6$, some of the Mg^{2+} must be located on the O sites or one

would otherwise see no expansion of the unit cell. This is due to the fact that Mg^{2+} is 11 % bigger than Fe^{3+} on an O site. The relative large unit cell expansion of $MgFe_2O_4$ is a result of the structure now favouring a pseudo-inverse spinel-type structure [110] with Mg^{2+} located mainly on O sites and Fe^{3+} on T and O sites. The solid solution of $NiFe_2O_4$ and $MgFe_2O_4$ covers, therefore, the change from an inverse spinel-type structure towards a more normal spinel-type structure and back to a pseudo-inverse spinel-type structure.

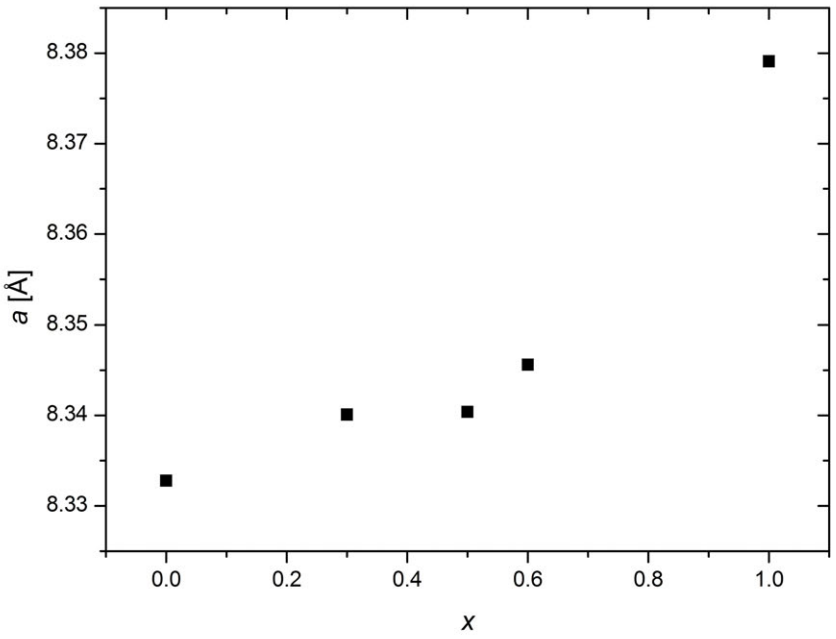

Figure 5.1: Unit cell parameters, a, at different spinel compositions. A small increase in a is observed from $0.0 \leq x \leq 0.6$ whereas the unit cell is significantly higher at $x = 1.0$. Error bars are at the same magnitude as the dimension of the points.

5.1.2 Dilatometry and Thermogravimetry

Earlier reports show that spinels are bad oxygen ion conductors (see section 2.1). A composite electrode of spinel and, for instance, CGO10 are therefore needed in order to have a proper current running.

Measurements with dilatometry showed, with an exception of $MgFe_2O_4$, a single discontinuity of the relative linear expansion (see Figure 5.2a) This was observed both during the heating and cooling stage and is related to the Curie temperature, T_c [111]. The thermal expansion coefficient, α, defined as $\alpha = \frac{1}{L}\frac{\delta L}{\delta T}$ did not change much before or after T_c although it reached a slightly lower value after T_c (see Table 5.1). In general, T_c measured

during cool down is located at a slightly lower temperature compared to the heating stage (see Table 5.1). T_c also decreases with increasing Mg content of the Ni containing spinels. Figure 5.2b show the dilatometry measurements of $MgFe_2O_4$. The relative linear expansion reveals two discontinuities at 327 °C and 800 °C, both appearing during the heating and the cooling stage. α shows a sharp peak at 327 °C as in the case of the Ni-containing materials whereas the peak at 800 °C is much more broad (starts appearing at 620 °C (heating) or 570 °C (cooling)). The first discontinuity is related to the magnetic ordering of the Fe electrons, although there seem to be some disagreements on the type of magnetic ordering [112–114]. The T_c-peak was not observed by Carter [115] and Weil [116] who concluded that the magnetic exchange interaction energy is independent of the $Fe-O-Fe$ spacing. Our results, however, show that this is not the case. In $MgFe_2O_4$, T_c is highly sensible to the cation distribution [112], which again is very sensible to the thermal history of the spinel. The reason for the different results is most likely to be found in differences in sample preparation (more Fe^{3+} on O sites will increase the number of super-exchange interactions and make the Curie point more pronounced) or the number of collected data points. Carter narrowed his data set down to ~ 20 data points which makes it difficult to detect a relative narrow peak if present.

The second discontinuity, starting at 620 °C, is more difficult to explain but seems to be related to some sort of structural expansion superimposed onto the thermal expansion. Carter also detected the same kind of upward curvature of the expansion of $MgFe_2O_4$ but was not able to explain the phenomena. One origin of the structural expansion would be a change of stoichiometry (loss of oxygen). This would result in a structural expansion as also reported for different oxides [85, 86, 117]. However, our TG measurements show no sign of oxygen loss at that particular temperature. Another explanation would be to relate the upward curvature of the expansion to the order-disorder transition between cations on T and O sites. As discussed in section 5.1.1 it is the ionic radius of the cations that is responsible for the change of the lattice parameters. In most cases the compounds are not in equilibrium at low temperatures where the ordering of the cations are controlled by the kinetics [118]. At high temperatures the spinels are in equilibrium with respect

Table 5.1: Curie temperatures, T_c, and expansion coefficients, α. The α-value marked with, *, is measured at 500 °C.

compound	T_c (heating)	T_c (cooling)	$\alpha_{400\ ^\circ C}$	$\alpha_{800\ ^\circ C}$
$NiFe_2O_4$	584 °C	581 °C	$1.13 \cdot 10^{-5}$	$8.08 \cdot 10^{-6}$
$Ni_{0.7}Mg_{0.3}Fe_2O_4$	516 °C	510 °C	$1.30 \cdot 10^{-5}$	$1.26 \cdot 10^{-5}$
$Ni_{0.5}Mg_{0.5}Fe_2O_4$	510 °C	499 °C	$1.20 \cdot 10^{-5}$	$1.10 \cdot 10^{-5}$
$Ni_{0.4}Mg_{0.6}Fe_2O_4$	468 °C	466 °C	$1.16 \cdot 10^{-5}$	$7.75 \cdot 10^{-6}$
$MgFe_2O_4$	327 °C	325 °C	$^*6.17 \cdot 10^{-4}$	$1.41 \cdot 10^{-5}$

to the cation order-disorder, reflecting the thermodynamic drive towards high temperature disorder. The increase of the relative linear expansion at 620 °C results from the starting value of the ordering parameter being lower than the equilibrium value. When the interaction between kinetics and thermodynamic allows it, Mg^{2+} will start to jump to an O site and thereby force the unit cell to expand faster than the thermal vibrations allow. At around 800 °C the cation order-disorder has reached an equilibrium leading the thermal expansion to take over the main process and thereby decreasing the relative linear expansion. Earlier reports [112, 119] show that the ordering of the cations at equilibrium temperatures starts somewhere between 400 °C and 650 °C, which is in good agreement with our results. The structural expansion takes place over a range of $\sim$ 180 °C, which is also similar to what is reported by Harrison *et al.* [112]. Antao *et al.* [120] measured the cation ordering in $MgFe_2O_4$ using *in situ* high temperature synchrotron X-ray powder diffraction. They found that when heating the sample the cations start to jump between lattice sites at 581 °C (more Mg^{2+} on O sites) and during cooling the cations jump back to their original position until a the blocking temperature is reached at 543 °C. This explains not only the change of conductivity in the same temperature range but also the behaviour of the linear expansion in our experiments.

A small uptake of oxygen at 985 °C was detected with TG. Thermodynamic calculations (FactSage 5.5 [15]), show that $MgFe_2O_4$ will decompose to MgO and a more Fe-rich spinel at 980 °C. $MgFe_2O_4$ have been found to be slightly over-stoichiometric with respect to the metal ions [121] which explains the small uptake of oxygen following reaction 5.1:

$$\delta O_2 + MgFe_2O_{4-\delta} \rightarrow \delta MgO + Mg_{1-\delta}Fe_2O_4. \tag{5.1}$$

The phase change was not observed in the dilatometry measurements because of slow kinetics [122], however, it is likely that a small amount of the material have decomposed during the experiment. The expansion coefficient of the spinels ($\alpha = 10 \cdot 10^{-6} - 15 \cdot 10^{-6}$ $°C^{-1}$) are very similar to the expansion coefficient of CGO10 ($\alpha = 11.9 \cdot 10^{-6}$ $°C^{-1}$ [123]) so a composite electrode of our spinels and CGO10 seems possible.

5.1.3 Conductivity Measurements

Figure 5.3 shows the specific conductivity of the spinels as a function of temperature. A large hysteresis is only observed for $Ni_{0.7}Mg_{0.3}Fe_2O_4$. At high temperatures (above $\sim$ 700 °C) the conductivity increases as more Mg is substituted with Ni (maximum at $x = 0.5$). At higher Mg content the conductivity decreases again as also described in earlier

5.1. The $Ni_{1-x}Mg_xFe_2O_4$ Series

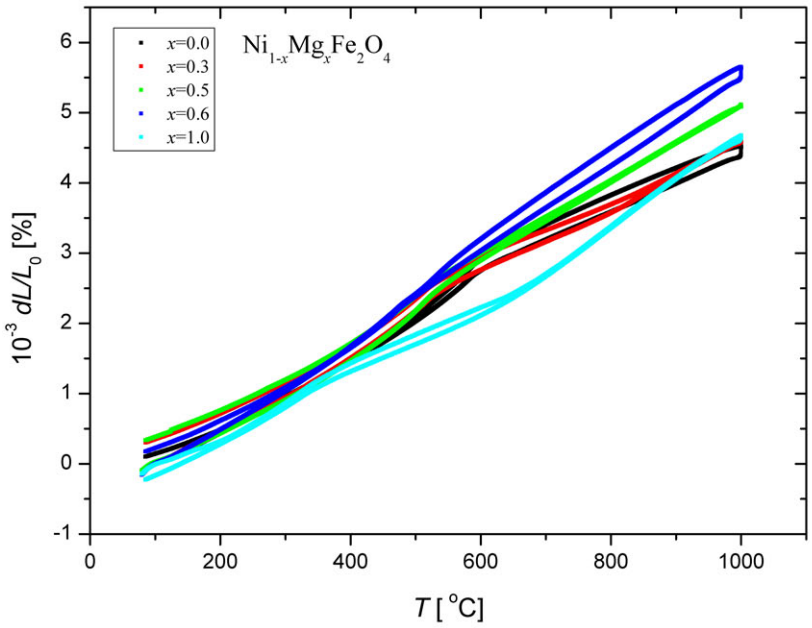

(a)

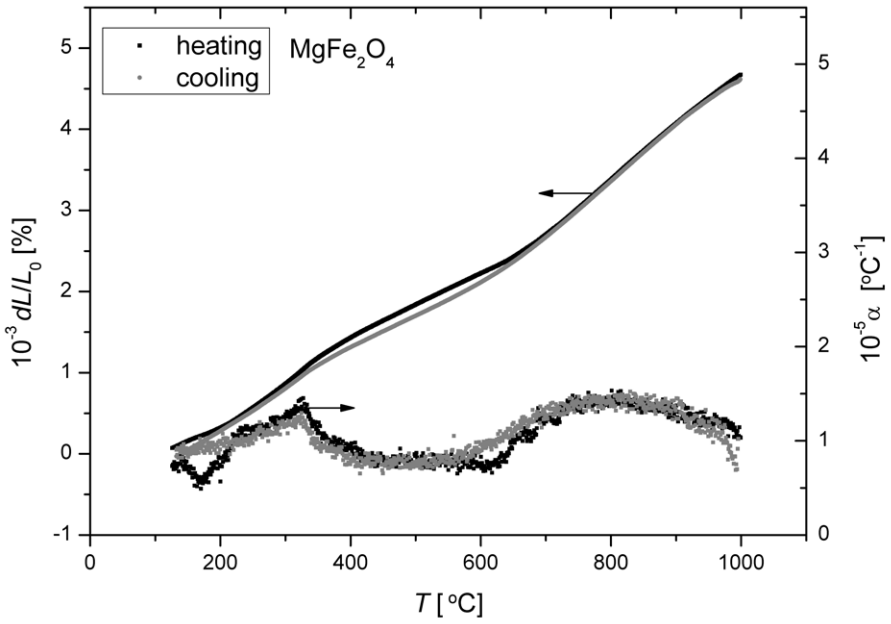

(b)

Figure 5.2: (**a**) Linear expansion of the different spinels measured in the temperature range of 80 °C to 1000 °C. The Curie point is detectable for all of the spinels. (**b**) Linear expansion and expansion coefficients of $MgFe_2O_4$. The peak at $\sim$ 325 °C is the Curie temperature, T_c and the broad peak at 800 °C is due to cation ordering.

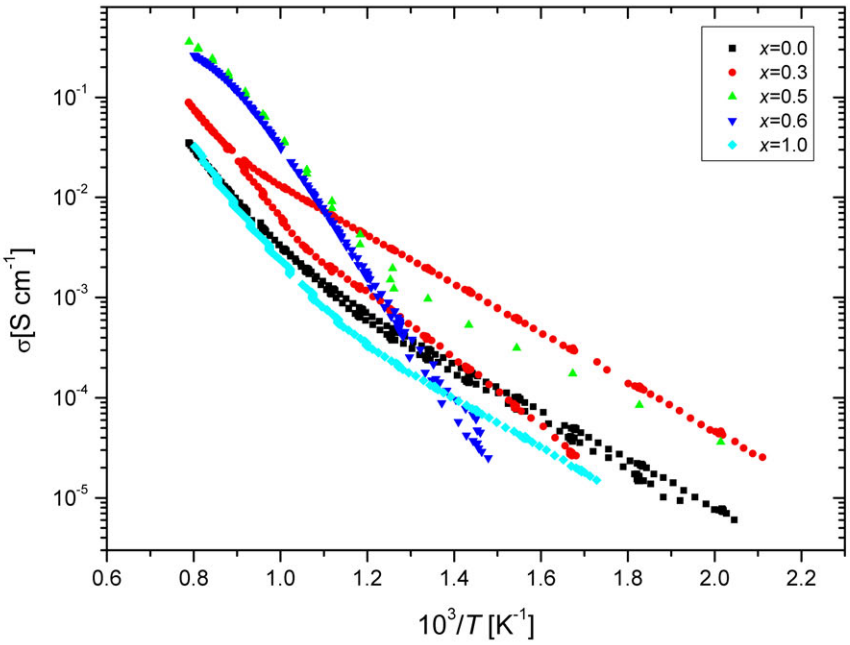

Figure 5.3: Four-point DC conductivity measurements of the spinels measured from room temperature to 1000 °C in air.

reports [124, 125]. However, they found a maximum conductivity for $Ni_{0.4}Mg_{0.6}Fe_2O_4$. The conductivity is mainly attributed to the cation − anion − cation super-exchange interactions, where the transport property rises from hopping of localized *d*-electrons between cations on O sites [126,127]. Mg^{2+} will, as discussed in section 5.1.1, enter the T sites resulting in a migration of Fe^{3+} ions into the O sites. The increase in concentration of Fe^{3+} on the O sites will increase the hopping rate of the electrons. Increasing the Mg^{2+} content will eventually force the Mg^{2+} ions to occupy the octahedral sites leaving the Fe^{3+} ions to migrate back onto the T sites. This will lower the concentration of Fe^{3+} ions on the O sites and therefore also the hopping rate of the electrons. The data were fitted with an Arrhenius equation 5.2,

$$\sigma = \sigma_0 \exp \frac{-E_a}{k_B T}, \tag{5.2}$$

where σ is the specific conductivity and E_a is the activation energy.

The conductivities of $NiFe_2O_4$ and $MgFe_2O_4$ behave in a similar way. Both show a slightly curved behaviour starting at 607 °C ($NiFe_2O_4$) and 574 °C ($MgFe_2O_4$). $NiFe_2O_4$ has a Curie point in the range of 585 °C−590 °C [111,128] which could explain some of the changes in conductivity. However, the change in conductivity of $NiFe_2O_4$ and $MgFe_2O_4$

is more likely to be a result of a reordering of the cations (see section 5.2.3). Activation energies (Table 5.2) are very similar for $NiFe_2O_4$ and $MgFe_2O_4$. At lower temperatures activation energies are in the range of 0.408(6) eV − 0.493(5) eV with $MgFe_2O_4$ having the highest activation energies. Similar activation energies have also been reported in literature [108, 129]. At high temperatures activation energies decrease to 0.956(2) eV − 1.234(8) eV. The conductivity of $Ni_{1-x}Mg_xFe_2O_4$, ($x = 0.5, 0.6$) shows a more different behaviour. The conductivity increases quite rapidly from 500 °C to 800 °C compared to the other samples.

During heating $Ni_{0.7}Mg_{0.3}Fe_2O_4$ follows the same trend as both $NiFe_2O_4$ and $MgFe_2O_4$, but the conductivity during cooling is significantly higher. The large hysteresis observed for $Ni_{0.7}Mg_{0.3}Fe_2O_4$ is a result of the changes in the cation distribution. When the sample is cooled below the critical temperature (blocking temperature) a relative large amount of Mg^{2+} is trapped in the T sites. This will leave the Fe^{3+} and the Ni^{2+} on the O sites and thereby increase the conductivity relative to the heating stage.

Table 5.2: Activation energies, E_a, calculated from the conductivity measurements. H and C represent the heating and the cooling stage. T is the temperature. Estimated standard deviations in parentheses.

compound	E_a, high T, H	E_a, high T, C	E_a, low T, H	E_a, low T, C
$NiFe_2O_4$	0.956(2) eV	1.034(2) eV	0.486(2) eV	0.477(2) eV
$Ni_{0.7}Mg_{0.3}Fe_2O_4$	1.964(5) eV	1.085(2) eV	0.481(2) eV	0.482(1) eV
$Ni_{0.5}Mg_{0.5}Fe_2O_4$	1.126(4) eV	1.032(6) eV	-	0.413(2) eV
$Ni_{0.4}Mg_{0.6}Fe_2O_4$	0.661(2) eV	0.686(3) eV	-	-
$MgFe_2O_4$	1.234(8) eV	1.098(6) eV	0.408(6) eV	0.493(5) eV

5.1.4 Electrochemical Properties on Cone-Electrodes

Cyclic voltammetry (CV) and electrochemical impedance spectroscopy (EIS) were recorded in a pseudo-three-electrode setup as described in section 4.3.2. CV and EIS were recorded at 400 °C, 500 °C and 600 °C in 10 % O_2 in Ar or 1 % NO in Ar (Air Liquide) with a flow rate of 20 ml/min. Additional measurements were performed on the $MgFe_2O_4$-electrode in 1 % NO_2 in Ar and gas mixtures of 0.5 % NO + 5 % O_2, 0.5 % NO + 10 % O_2 and 0.5 % NO_2 + 10 % O_2. Measurements containing NO_2 gas (Air Liquide) were performed only at 300 °C and 400 °C as the molecule is unstable at higher temperatures and will decompose [15]. A 1 hour equilibrium time was used to record the OCV before recording the voltammograms in the potentional range of -0.6 V − 0.5 V with a sweep rate of 1.0 and 10 mVs^{-1}. In order to compare the electrodes directly, the current in the voltammograms were converted to current densities by dividing with the contact area.

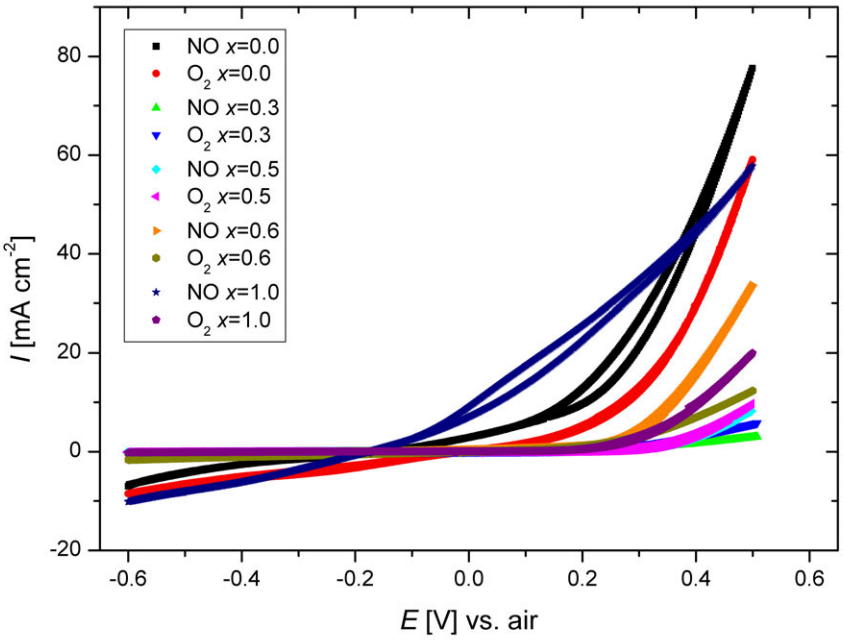

Figure 5.4: Cyclic voltammograms on the different spinels at 400 °C. Data were recorded in 1 % NO and in 10 % O_2 with air as reference gas (sweep rate: 1mV/s).

No corrections were made for the IR drop since calculations showed that the corrections were less than 1 % at all temperatures. Figure 5.4 shows the voltammogram recorded at 400 °C. Similar voltammograms were also recorded at 500 °C and 600 °C, however, they look very similar to those recorded at 400 °C and they are therefore not shown for all of the spinels. Part of the voltammograms recorded on $NiFe_2O_4$ and $MgFe_2O_4$ are shown in Figure 5.5 since they show a more interesting behaviour than that of the rest of the spinels. $NiFe_2O_4$ has the highest cathodic activity in NO and O_2 at 500 °C and 600 °C. However, at 400 °C $MgFe_2O_4$ shows higher activity in NO than $NiFe_2O_4$ does. The activity in O_2 differs significantly between the two electrode materials with $NiFe_2O_4$ showing the highest activity. Figure 5.6a shows the current densities in NO and O_2 as a function of the Mg^{2+} content. As more Mg^{2+} is substituted into the $NiFe_2O_4$ compound the activity in NO and O_2 decreases significant until a minimum is reached at the $Ni_{0.5}Mg_{0.5}Fe_2O_4$ electrode. The activity on $Ni_{0.4}Mg_{0.6}Fe_2O_4$ increases slightly again but on the $MgFe_2O_4$ electrode the picture looks more blurry. Figure 5.6b shows the current ratios of NO with respect to O_2. Ni-containing electrode materials all show current ratios in the range of $0.4 - 2.4$ but without any systematic trends. It was not possible for us to reproduce the measurements from Simonsen *et al.* [61] who got some very interesting results on $NiFe_2O_4$ (potential range -1.0 V $-$ 0.5 V). However, theoretically electrochemical calculations [15]

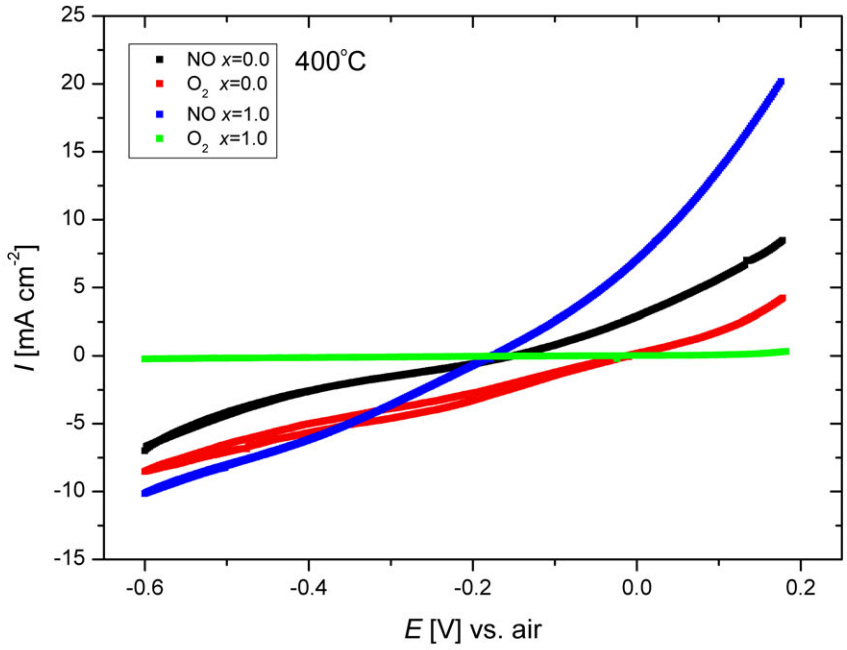

(a)

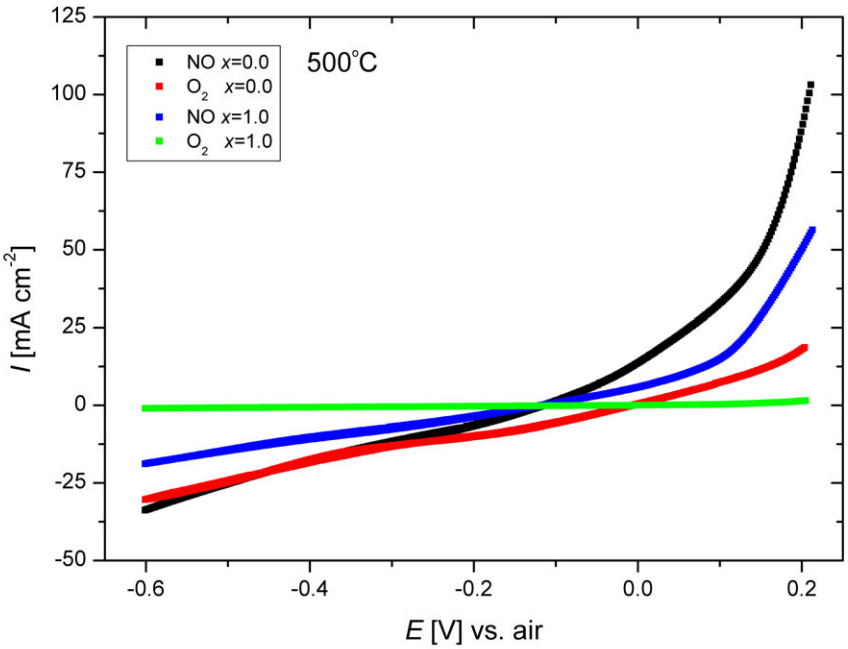

(b)

Figure 5.5: Cyclic voltammograms on $NiFe_2O_4$ and $NiFe_2O_4$. **(a)** and **(b)** show a part of the voltammograms (-0.6 V – 0.2 V) at 400 °C and 500 °C respectively. The voltammograms were recorded in 1 % NO and in 10 % O_2 with air as reference gas (sweep rate: 1mV/s).

show that $NiFe_2O_4$ is reduced to Ni + Fe_3O_4 at potentials lower than -0.86 V (600 °C). In our measurements we did not go below -0.6 V at any temperatures which might explain why our measurements did not match theirs. A comparison of our results with Hansen *et al.* [62] is more difficult. Their data have not been normalized to current densities and the NO concentration used is twice as high as in our measurements. However, estimated values of the current ratios are much smaller ($(I_{NO}/I_{O_2} \leq 1)$ than we find, which makes our materials more interesting.

The activities of the spinels seem to be correlated to the distribution of Fe^{3+} on different lattice sites. The more Fe^{3+} is located on the T sites, the more active is the spinel. $NiFe_2O_4$ has the highest content of Fe^{3+} on T sites among the spinels and it also has the highest activity. As more Mg^{2+} is incorporated into the lattice, the more Fe^{3+} will be located on O sites causing an increase in conductivity (in air) and a decrease in activity. When the Mg^{2+} content reaches a critical value ($x = 0.5$), the structure now favours Mg^{2+} to move to octahedral sites and Fe^{3+} to move to T sites. This causes a decrease in conductivity and an increase in activity. If Ni^{2+} had the dominant effect on the activity we would expect a decrease in activity with increasing Ni^{2+} content, but we will be left to explain the high activity on $MgFe_2O_4$. If Mg^{2+} on the other hand had the dominant effect on the activity we would expect an increase in activity with increasing Mg^{2+} content.

In general, $MgFe_2O_4$ shows higher activity in NO than in O_2 at all temperatures with a maximum current ratio at 400 °C. Additional measurements in 1 % NO_2 and different gas mixtures (0.5 % NO_2 + 5 % O_2, 0.5 % NO_2 + 10 % O_2, 0.5 % NO + 10 % O_2) were therefore performed on the $MgFe_2O_4$ electrode material in the temperature range of 300 °C − 600 °C. Figure 5.7a and 5.7b show the voltammogram at 400 °C and 300 °C. Measurements at 300 °C show that activity in NO at -0.6 V is higher than in O_2. The activity in NO_2 and 0.5 % NO + 5 % O_2 is higher than in both NO and O_2. The much higher activity in 0.5 % NO + 5 % O_2 is presumable influenced by the fact that a small concentration of NO_2 is formed in the gas mixture. The presence of 5 % O_2 together with NO does not seem to block the active sites otherwise the activity would have been somewhat lower. A higher oxygen partial pressure seems to inhibit the reduction of NO quite substantial.

Figure 5.8a shows the current ratios with respect to O_2 at -0.6 V as function of temperature. In the case of NO and NO + O_2 the current ratios peak at 400 °C with a maximum of 44 and 168 respectively. Measurements in NO_2 and NO_2 + O_2 at 300 °C and 400 °C show a maximum current ratio of 136 and 55 respectively. No measurements were made at lower temperatures because of the relative low electronic conductivity of $MgFe_2O_4$. The ratios of the current densities peak at 400 °C and then fall off almost

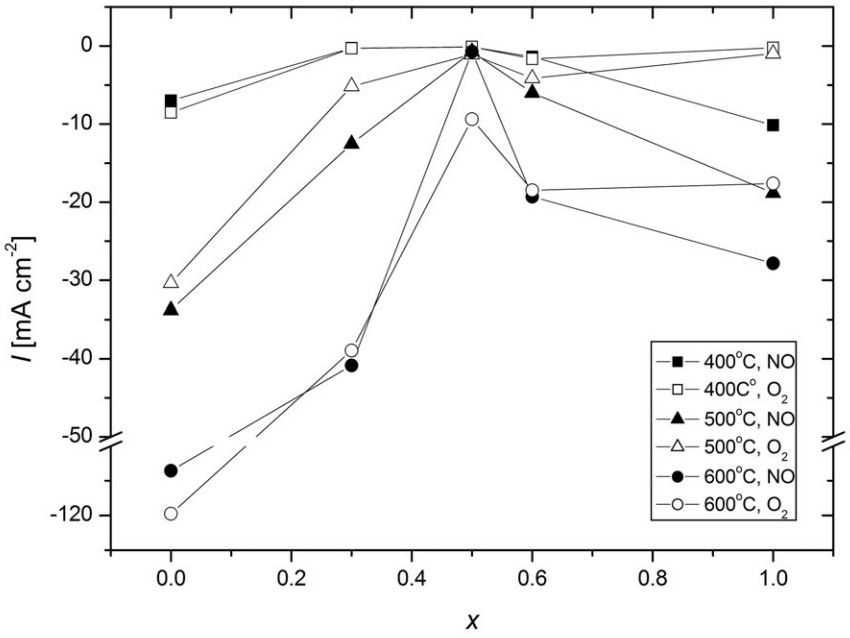

(a)

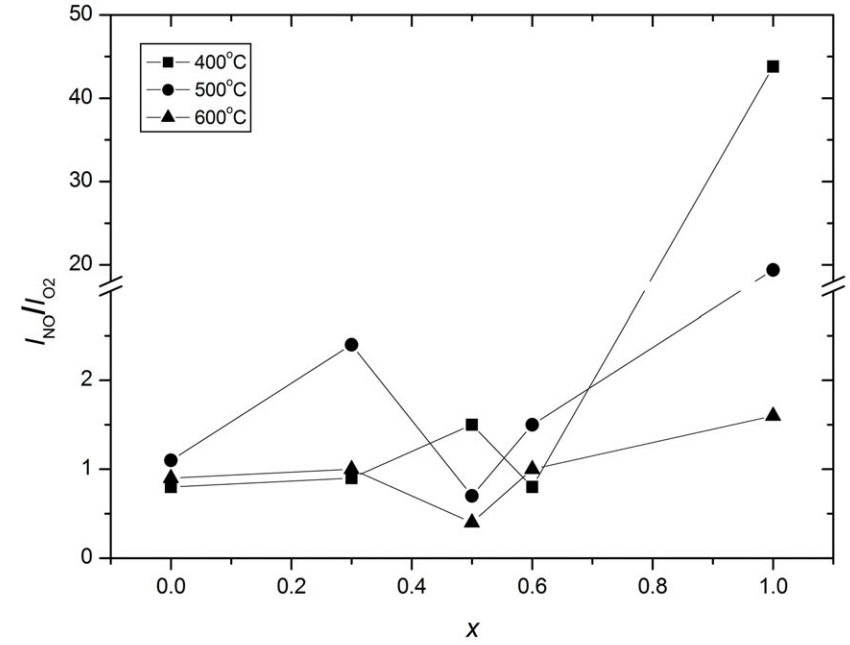

(b)

Figure 5.6: (**a**) Current densities at -0.6 V in NO and O_2. (**b**) Current ratios between NO and O_2 for the different spinels ($Ni_{1-x}Mg_xFe_2O_4$). $MgFe_2O_4$ shows significantly higher current ratios at 400 °C and 500 °C compared to the other spinels. x refer to the Mg content.

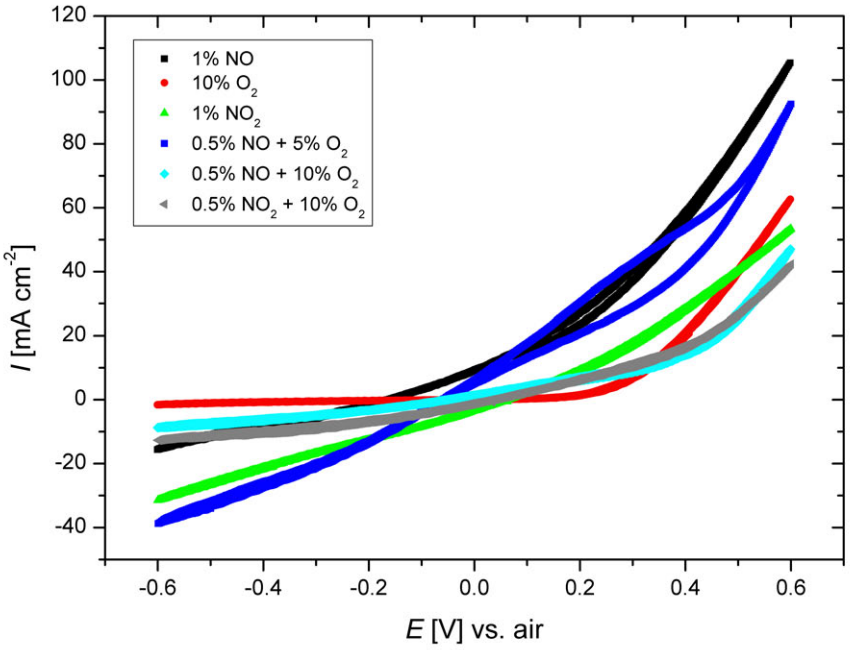

(a)

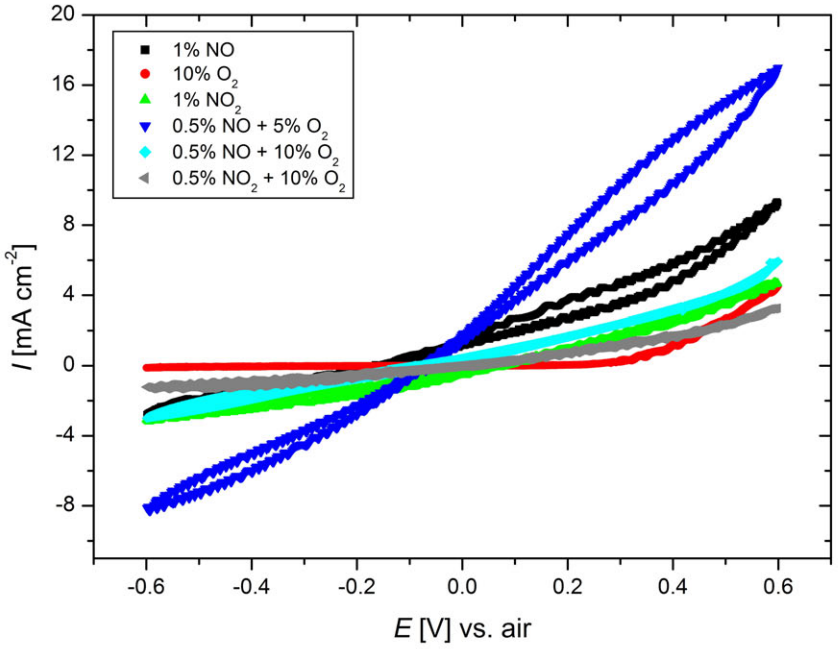

(b)

Figure 5.7: Cyclic voltammograms on $MgFe_2O_4$ in different gas mixtures at 400 °C and 300 °C. Air was used as reference gas and data were collected with a sweep rate of 1 mV/s. The electronic noise at 300 °C is notable.

symmetrically around the peak. Measurements in $O_2 + NO_2$ and in NO_2 were only made at two different temperatures so we can therefore not verify a similar same kind of current densities peak at 400 °C. No voltammograms were recorded above 400 °C because of the thermal decomposition of NO_2 at higher temperatures [15]. Recorded data from a portable flue gas analyzer (TESTO 350-S) on a different cell setup show that ~ 20 % of the NO_2 have reacted into NO and O_2 at 400 °C, which has to be considered when the data are evaluated.

The recorded OCV of the different gas mixtures are shown in Figure 5.8b. The OCV of NO has much lower potentials compared to the thermodynamic calculations (Figure 1.5) and it changes only very little as a function of temperature. This implies that a relative large over-potential is needed in order to reduce NO on a $MgFe_2O_4$ electrode. The concentration gradient of O_2 over the electrolyte could increase the local oxygen partial pressure at the point electrode, which opens up for reactions 1.19 and 5.3 to occur. This, and reaction kinetics will explain the lowering of the OCV.

$$O^{2-} + NO \rightarrow NO_2 + 2e^-. \tag{5.3}$$

The OCV of O_2 shows that the potentials at 500 °C and 600 °C are around -0.02 V which is close to the standard potential calculated with FactSage 5.5. At 300 °C and 400 °C OCV could not be measured with a trustworthy accuracy. This is essentially a consequence of the shape of the CV curve which has a wide region where the current is close to zero. This makes it difficult to measure the OCV since small fluctuations will have a great influence on recorded value. The presence of O_2 together with NO causes OCV to coincide with the OCV of O_2 suggesting that NO does not react at these potentials. The OCV of NO_2 and NO_2 + O_2 fall fairly close to each other with NO_2 + O_2 at slightly lower potentials. The presence of O_2 and possible NO should decrease the OCV of NO_2 + O_2 according the measurements. However, OCV of NO_2 + O_2 still lies fairly close to the OCV of NO_2 suggesting a reaction involving NO_2 to be the dominant one.

Figure 5.9 shows the Tafel plots of $MgFe_2O_4$ and $NiFe_2O_4$ recorded in NO. The Volmer-Butler equation 5.4 was used to calculate the number of transferred electrons in the cathodic and anodic region. The Volmer-Butler equation is defined as,

$$i_F = i_0 \left(\exp\left[(1-\alpha) n\eta \frac{F}{RT}\right] - \exp\left[-\alpha n\eta \frac{F}{RT}\right] \right), \tag{5.4}$$

where i_F and i_0 is the Faradaic current and the exchange current respectively, α is the charge transfer coefficient, n is the number of transferred electrons (see equation 3.8), η is the over-potential (in this case takes as the applied potential), F is the Faraday

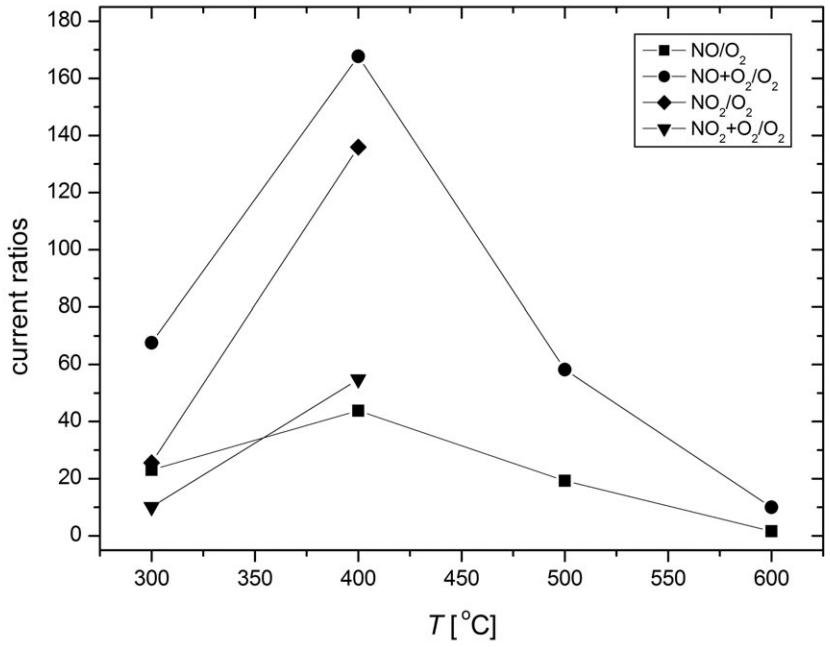

(a)

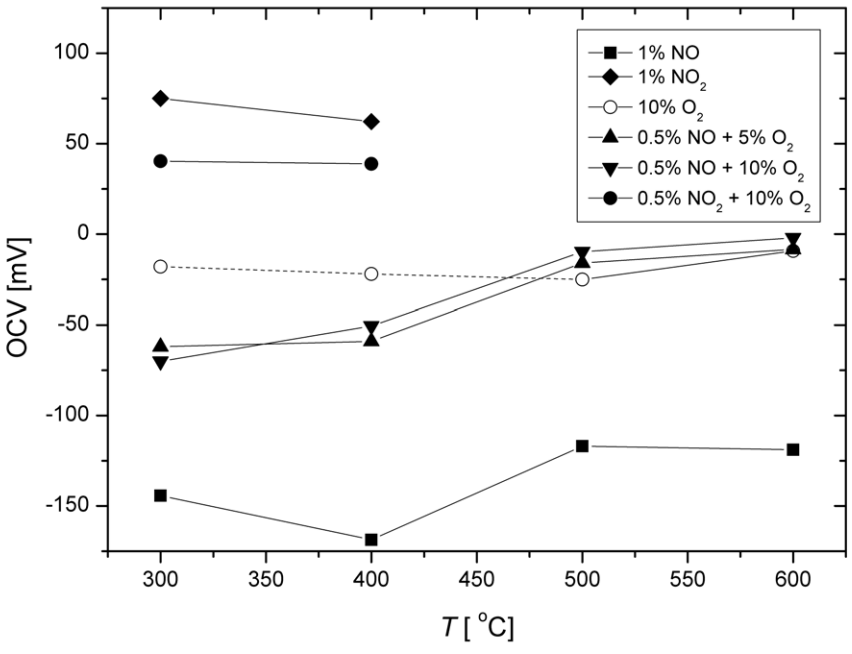

(b)

Figure 5.8: (**a**) Current ratios for the $MgFe_2O_4$ electrode measured as a function of temperature at -0.6 V. (**b**) OCV of $MgFe_2O_4$ in different gas mixtures as a function of temperatures. The dotted line of 10 % O_2 from 300 °C − 400 °C show the theoretical values of the standard potential.

constant, R is the gas constant and T is the temperature. Taking $\alpha = 0.5$, gave values of 0.261(1) ($MgFe_2O_4$) and 0.66(1) ($NiFe_2O_4$) at 400 °C in the cathodic region. The number of transfered electrons were therefore much lower than the expected with values of 2 assuming that NO was reduced to N_2 (equation 1.17). The reason for the low values of n reflect that we have a mixed potential due to a variety of different processes taking place in the cell simultaneously. The anodic region of the $MgFe_2O_4$ electrode showed a calculated n-value of 0.326(1) which reflects the same problems found in the cathodic region. The anodic region of the $NiFe_2O_4$ looks a bit different with a small 'bump' on the graph. This suggest that at least two processes are taking in the anodic region, however, it was not possible to separate them and to calculate any of their n-values. Tafel plots were also made on the data recorded in the other gases, however, they show similar results and will therefore not be shown here.

5.1.5 Symmetrical Cells

On the basis of the data recorded on cone-electrodes of the $Ni_{1-x}Mg_xFe_2O_4$ series, $MgFe_2O_4$ was chosen as the most promising cathode material for electrochemical reduction of NO_x. Symmetrical cells were therefore manufactured with a composite electrode consisting of $MgFe_2O_4$ and CGO10 as described in section 4.2.2. Data were recorded on two symmetrical cells in 1% NO and in air at 300 °C, 400 °C and 500 °C and in 1% NO_2 at 300 °C, 350 °C and 400 °C. Experiments were also tried at lower temperatures (250 °C), however, the impedances were much to high.

All impedance spectra were fitted with Equivalent Circuit for Windows version 1.2beta using equivalent circuits as shown in Figure 5.10. R_m are the reaction resistances[1] and Q_m and n_m are values of the constant phase elements (CPE). Other types of models involving diffusion impedance and Gerischer impedance were also tested but with no great success. Measurements recorded at 300 °C and 350 °C with an amplitude of 36 mV (rms) show a relative high level of noise in the frequency range of $\sim$ 3 kHz to $\sim$ 750 Hz. This was not caused by the Gamery Femtostate. Applying the larger amplitude (100 mV (rms)) minimized the problem at high frequency, however, a distinct decrease of impedance in the low frequency region was observed. Figure 5.11 show an example of the recorded data on the $MgFe_2O_4$/CGO10-electrode at 400 °C in air. The decrease in impedance seems to be a result of an activation of the electrodes changing the cell response from linear (or pseudo-linear) to a non-linear response. This was seen as well at the Lissajous figures at

[1]The electrode resistance obtained from the impedance plot must be divided by two, since it is caused by the two electrodes in series.

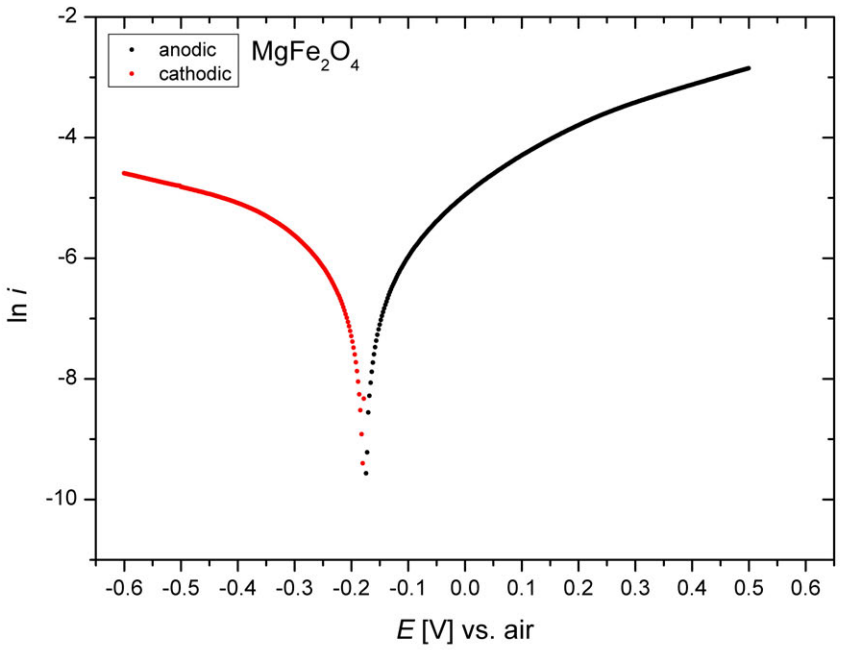

(a)

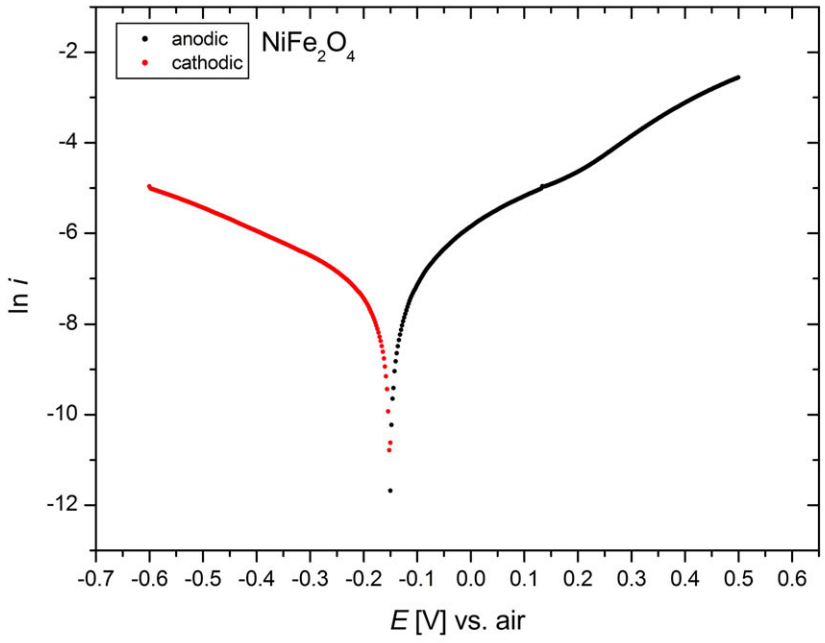

(b)

Figure 5.9: Tafel plots of $MgFe_2O_4$ and $NiFe_2O_4$ recorded at 400 °C in 1% NO.

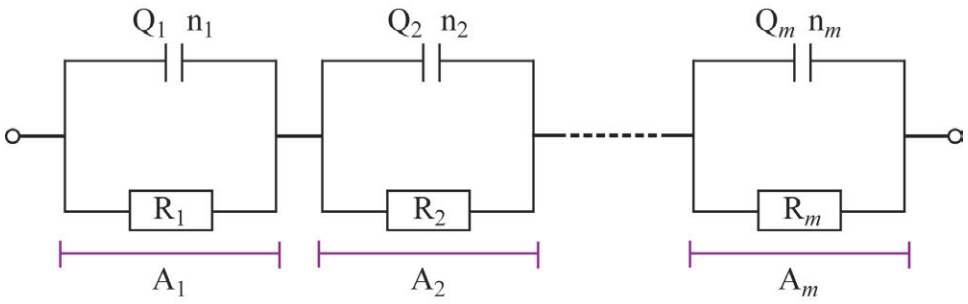

Figure 5.10: Equivalent circuit used to fit the impedance data. R_m are the reaction resistances and Q_m and n_m are values of the constant phase elements. Each semi-circle in the Nyquist plot is described by a R_m in parallel with a CPE (a RQ-circuit). A_m represents the different arcs in the Nyquist plot.

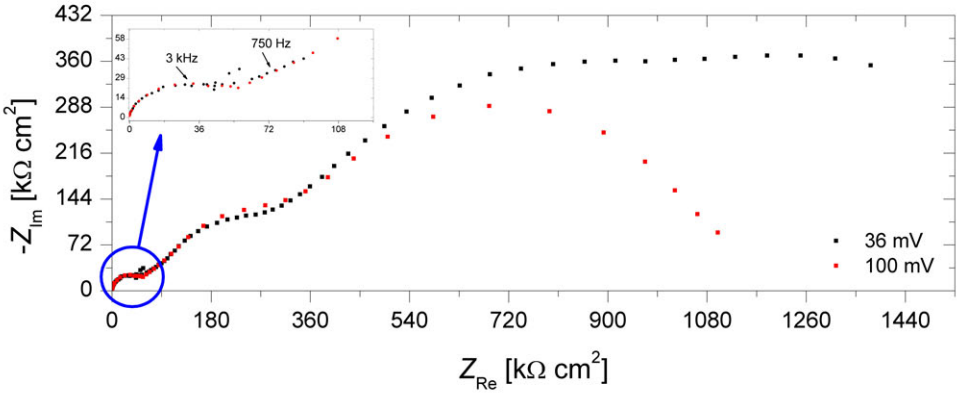

Figure 5.11: Nyquist plot of the $MgFe_2O_4$/CGO10 electrode, recorded at 400 °C in air with different amplitudes. The 'noisy frequency region' is shown in the upper left corner of the main impedance spectra. For some spectra this region looks even worse than seen on this graph.

500 °C which had a more "banana-shaped" form. However, at lower temperatures this was more difficult to observe. By plotting similar spectra, recorded at different amplitudes, the apparent activation of the electrode could be detected. In order to accommodate the activation at low frequencies and the high level of 'noise' at high frequencies, impedance spectra recorded with a 100 mV amplitude were used to fit the high frequency range, when necessary, and the results were then used to fit the impedance spectra recorded with a 36 mV amplitude. The origin of the 'noisy frequency range' is not yet understood, but adding a negative *RQ*-circuit to the fit, placed in the 'noisy frequency range', did improve the fit considerably. However, the physical meaning of the negative *RQ*-circuit is not known and a better understanding of the impedance spectra must be accomplished with further tests.

Figure 5.12 and 5.13 show a typical impedance spectra of the symmetrical cells recorded in different atmospheres. In general, the impedance is very high in air compared to the NO_x gases. At 300 °C the total impedance arranges like $Z_{NO_2} < Z_{NO} < Z_{air}$

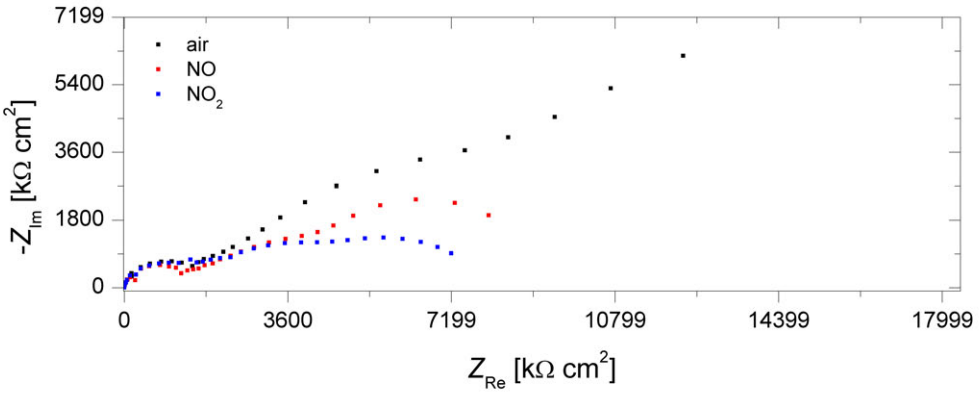

Figure 5.12: Nyquist plot of the $MgFe_2O_4$/CGO10 electrode, recorded at 300 °C.

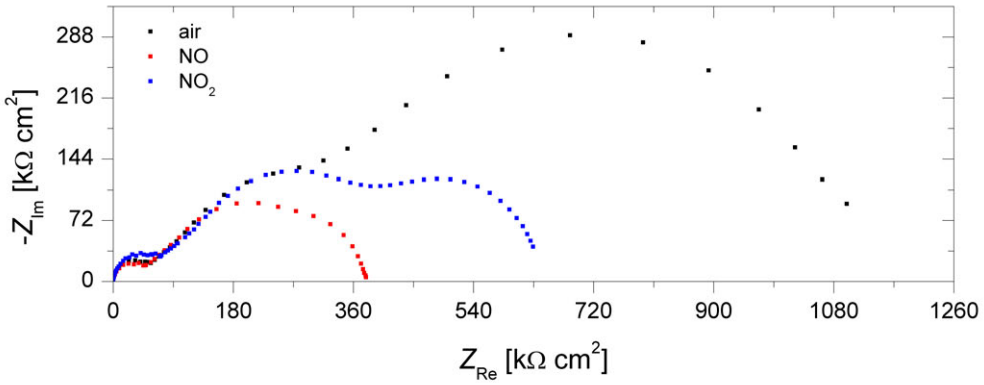

Figure 5.13: Nyquist plot of the $MgFe_2O_4$/CGO10 electrode, recorded at 400 °C.

whereas at 400 °C the total resistivities were listed $Z_{NO} < Z_{NO_2} < Z_{air}$. This may arise from the fact that a small fraction of the NO_2 have decomposed into NO and O_2 at this temperature [15]. As the impedance reflects the slope of a voltammogram (at OCV), we expect that the presence of O_2 would increase the impedance. The voltammogram recorded on the 3E pellet in 10 % O_2 (see section 5.1.6 has a very 'flat' shape which, in combination with the current response of (pure) NO_2, would decrease the slope of the total current response in NO_2 at 400 °C.

The R_m's were all plotted in order to calculate the activation energy, E_a, of the reactions using the Arrhenius equation 5.5,

$$lnR = lnR_0 + \frac{E_a}{Tk_B}. \tag{5.5}$$

Figures 5.14a and 5.14b show two examples of the Arrhenius plot from different atmospheres. Table 5.3a list the recorded activation energies. The high frequency arc (A_1) seems independent of the atmosphere and comparing the E_a with the reported data on YSZ [130, 131] shows that A_1 originates from the electrolyte. The CPE in parallel with A_1 have exponents in the range of $0.9 \leq n_1 \leq 1.0$, which indicates that it is close to a pure capacitor. $n_1 = 1$ was tried fixed for all measurements, however, it did not give a satisfying fit in the high frequency region.

Calculations of the near-equivalent capacitances, C_{ne}, (see section 3.2.2) for the A_1

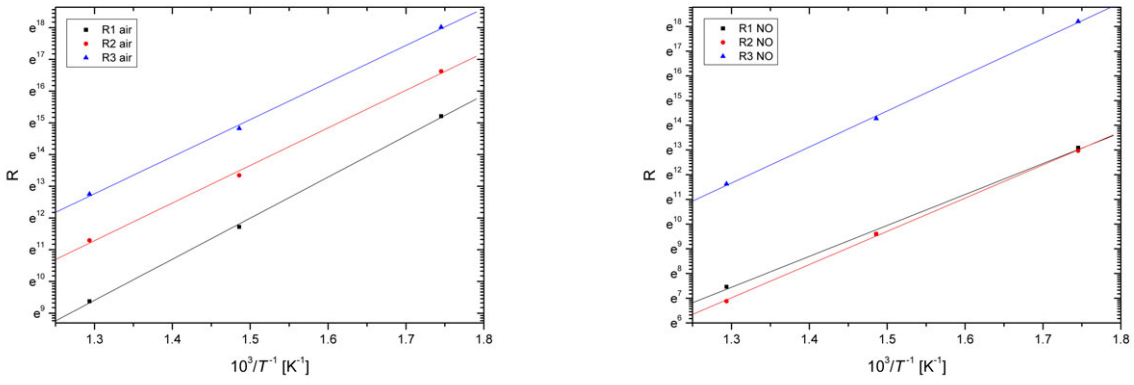

(a) (b)

Figure 5.14: Arrhenius plots on the $MgFe_2O_4$/CGO10-electrode, calculated from different atmospheres.

arc are shown in Table 5.3b. Some of the spectra recorded at 350 °C was not possible to fit properly and therefore some of the capacitances are missing.

Assuming an ideal capacitive behaviour of the high frequency response, the capacitance can be calculated using the relationship between the capacitance and the geometry of the

cell. The geometrical capacitance, C_{g}, can be calculated from equation 5.6.

$$C_{\mathrm{g}} = \frac{\epsilon_0 \epsilon_r \mathcal{A}}{d}, \tag{5.6}$$

where ϵ_0 is the permittivity of free space, ϵ_r is the relative electrical permittivity of the non-conduction media, $\mathcal{A}$ is the surface area of one of the plates and d is the distance between the two plates. Taking the YSZ-electrolyte (160 μm thick) as the non-conduction media having a relative electrical permittivity of 30 [132, 133], gives a geometrical capacitance, $C_{\mathrm{g}} \sim 60$ pF. The stray capacitances, C_{s}, measured on symmetrical cells on a similar setup were measured to around 25 pF by Høgh [134] which gives a total expected capacitance of 85 pF. This is around a factor of 2 smaller than the ones calculated from the recorded data. This phenomenon must be due to problems with the refinement process, where contributions from semi-circles at lower frequencies seem to disturb the fitting and make it impossible to get a correct value. Refinements of the data were also tried fixing the capacitance of the first arc to the calculated values. However, this did not improved the fit. The corresponding E_{a} still implies that the high frequency semi-circle originates from the impedance of the electrolyte. Activation energies of the second and third arc, A_2 and A_3, does not seem to follow a general trend and since no series of measurements were made with different partial pressures of NO_x gases and flow rates it is impossible to present a sufficient explanation.

In general, processes occurring in composite electrodes includes electron transport

Table 5.3: (**a**) Activation energies of the symmetrical cells. (**b**) Mean values of the NEC of the first semi-circle on the $MgFe_2O_4$/CGO10-electrode. Uncertainties are given in parentheses.

(a)

-	NO [eV]	NO_2 [eV]	air [eV]
A_1	1.05(5)	1.09(1)	1.08(3)
A_2	1.06(3)	1.26(3)	1.06(7)
A_3	1.21(3)	1.24(6)	1.03(4)

(b)

temp	NO [pF]	NO_2 [pF]	air [pF]
500 °C	170(20)	-	170(15)
400 °C	172(5)	173(3)	174(6)
350 °C	-	163(7)	-
300 °C	170	162	170(15)

from the electronic current collector, electrochemical reaction at the TPB, gas diffusion in the pores and ion transport from TPB to the electrolyte [92]. It is, however, not possible to match any of the semi-circles, recorded at lower frequencies than A_1, directly to one of these processes. A comparison of the recorded data from the symmetrical cells with the cone-electrodes must be done with care as the electrodes are not completely identical. Some general observations can, however, be explained quantitatively by the

CV measurements on the point electrode. The activities of the cone-electrodes suggest that the total impedance would be $Z_{NO_2} < Z_{NO} < Z_{O_2}$. This was also observed on the symmetrical cells at 300 °C but not at 400 °C. This could be related to a thermal decomposition of NO_2 to NO and O_2, which would change the oxygen partial pressure in the recorded atmosphere. At 300 °C NO_2 would be more stable and oxygen partial pressures would differ significantly from the experimental conditions at 400 °C and 300 °C.

5.1.6 Gas Conversion over 3E Pellets

A 3E pellet (see section 4.2.4) with a CGO10 electrolyte was placed in the 3E setup as described in section 4.3.2. Measurements were performed at 636 °C, 513 °C and 400 °C and in 1000 ppm NO + 10 % O_2. CV and EIS were recorded on the sample. The pellet was polarized at ±0.6 V for ∼ 3 hours and NO_x gases were analyzed with a Thermo Scientific Chemiluminescence analyzer (Model 42i). In order to detect a gas conversion, a small flow rate of 10 ml/min was applied, however, as the chemiluminescence required a minimum flow of 25 ml/min, the gas from the setup was diluted with air just before entering the chemiluminescence analyzer. The gas composition was analyzed before and after reaching the sample without polarizing the cell (OCV gas conversion). A square-wave potential was also applied over the cell, switching between OCV and -0.6 V every 1 second, however, no gas conversion was detected. Unfortunately a mass spectrometer was not available during these measurement and minor leaks were therefore difficult to detect. However, our earlier tests on sealing the 3E pellet showed that applying an Au sealing in combination with a low temperature glass tape made a tight sealing. After the measurements ended, an over-pressure was applied inside the alumina tubes and the sealing was leak tested. No leaks were found. In order to investigate the catalytic properties of the material, a 'blank 3E pellet' with a porous Au-electrode on an YSZ-electrolyte was inserted in the 3E setup and the gas composition was recorded before reaching the sample and after leaving the sample (see Figure 5.15). The results reveal a more complex reaction scheme in order to explain the recorded data. At 600 °C, NO is the main species present in the gas phase. A small amount of NO_2 is formed, properly most of it in the outlet pipe before entering the chemiluminescence analyzer. Calculations show that it takes ∼ 45 seconds for the gas to leave the electrode and reach the chemiluminescence analyzer which should be enough time to form a relative large amount of NO_2 [135, 136]. Apart from NO and NO_2 some N_2O and/or N_2 must also be formed either catalytically or thermally through the overall

reactions 5.7 and 5.8,

$$2\mathrm{NO} \rightarrow \mathrm{N_2O} + \frac{1}{2}\mathrm{O_2} \tag{5.7}$$

$$2\mathrm{NO} \rightarrow \mathrm{N_2} + \mathrm{O_2}. \tag{5.8}$$

At 500 °C the formation of NO_2 accelerates. This causes a decrease in the NO content, however, not enough to explain the entire increase in NO_2. Therefore, the formation of N_2O and/or N_2 must also decrease in order the make the total NO_x level increase. Decreasing the temperature to 400 °C or 300 °C increase the formation of NO_2 as expected, however, a small increase in the NO content is also observed. This must reflect that the formation of N_2O and/or N_2 has slowed down faster than the increase in NO_2 formation. At 35 °C the formation of N_2O and/or N_2 has decreased even further whereas the formation of NO_2 has increased to such a level that the total NO content decreases. The reaction mechanisms described here are speculative, however, they do explain the graphs and some of the basic trends observed over the other 3E pellets measured in this thesis. The total NO_x concentration over the $MgFe_2O_4$/CGO10-electrode is $10 - 15$ ppm higher than the recorded data over the blank pellet and since a catalytic activity over the plank pellet is not plausible[2], the higher concentration of NO_x over the $MgFe_2O_4$/CGO10-electrode is most likely due to a small leak in the Au sealing of the blank pellet.

Figures 5.15 show the recorded gas conversion over the $MgFe_2O_4$/CGO10 electrode. The total NO_x concentration recorded over the spinel electrode increases as the temperature is lowered, which was also observed in the case of the blank pellet. Also the NO and NO_2 content follows the basic trend observed over the blank pellet. During polarization, the total amount of NO_x is very stable. However, recorded data on the NO concentrations shows that the total amount of NO increased or decreased during polarization depending on weather it is done cathodically or anodically. When the cell is polarized cathodically we see an increase of the NO concentration but at the same time a decrease in the NO_2 concentration which matches exactly the increment of the NO concentration. Same picture is observed when the cell is polarized anodically, but now the increase in NO_2 is

[2]Even though nano size Au particles have been reported as catalytic active [137] it is not believed that Au can have a measurable catalytic effect at these temperatures. In-house measurement on Au electrodes in a NO atmosphere is also suggest that Au is not active towards NO reduction [138]. Pt wires were used to contact the working electrode but even though Pt is known to have a catalytic effect for a direct conversion of NO to N_2, it is also known in literature that in the presence of oxygen the catalytic activity is reduced significantly (see section 1.2.2). The size of the Pt wire i also very small which will make any contribution to the gas conversion insignificant. The only materials left as candidates are the alumina tubes, the stainless steel wires, where the gas flows, and the YSZ/CGO10 electrolytes. To our knowledge no catalytic activities in NO + O_2 have been reported for these materials, others than YSZ when polarized cathodically at -1.3 V versus air [50].

balanced by the decrease in the NO content. The overall reaction over the electrode is therefore,

$$NO + O^{2-} \leftrightarrow NO_2 + 2e^-. \tag{5.9}$$

Table 5.4 shows recorded gas conversion as well as the current efficiencies, η. The latter can be defined as the ratio between I_{NO}/I_{pol},

$$\eta = I_{NO}/I_{pol}, \tag{5.10}$$

where I_{pol} is the recorded polarization current and I_{NO} is current due to the NO conversion. I_{NO} is defined as:

$$I_{NO} = \Delta NO nF, \tag{5.11}$$

where ΔNO is the amount of converted NO, n is the number of transferred electrons and F is the Faraday constant. The highest gas conversion was recorded at 513 °C when polarized cathodically. Even though the gas conversion is only around 4 % (see Table 5.4), η is very high and to our knowledge no reports on such a high current efficiency has been published. However, both gas conversion and η drops down to practically zero at 400 °C as well as it was not even possible to detect a gas conversion at 600 °C. Current ratios recorded on the cone-electrode showed a similar 'peak', although it was observed at 400 °C, which might be related to the presence/absence of CGO10.

Figure 5.16−5.18 show the voltammograms recorded on the $MgFe_2O_4$/CGO10-electrode at different temperatures and atmospheres. At 400 °C, the activity is relative low and does not change much between the different gas compositions. At 500 °C, the cathodic activity in O_2 is about twice as high as in NO, whereas the activity in NO + O_2 falls in between that of NO and O_2. It is difficult to compare the results on the 3E pellets with the ones recorded on the cone-electrode because of the difference in the gas composition as well as in electrode composition. However, both cells were recorded in 10 % O_2 and the current density only changed from approximate $-3.5 \cdot 10^{-2}$ mA/cm^2 to $-4.5 \cdot 10^{-2}$ mA/cm^2. The activity in O_2 is therefore much unchanged when changing the electrode from a spinel point-electrode to a spinel/CGO10 composite electrode on a 3E pellet. Same pattern is also observed at 500 °C. The cathodic activity in NO + O_2 is also difficult to compare with the cone-electrode as the NO concentration was 5 times higher than in the case of the 3E pellet. Keeping that in mind, we see a quite significant decrease in cathodic activity (-0.6 V) from around -10 mA/cm^2 (cone-electrode) to approximate $-4.5 \cdot 10^{-2}$ mA/cm^2 (3E pellet). The activity in NO is lowered by a factor of ~ 220 which is surprisingly low. The origin of that is not known but apparently the CGO10 plays a crucial role in the decomposition of NO.

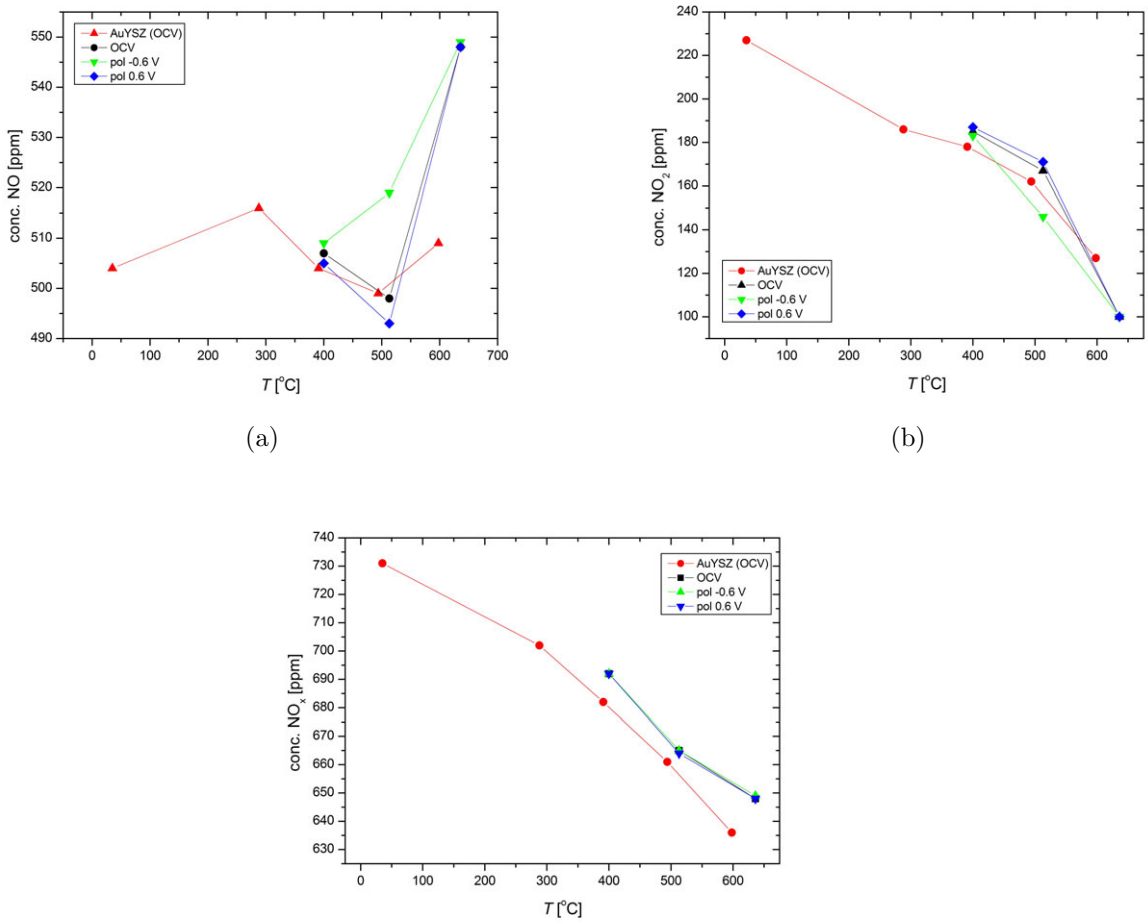

Figure 5.15: Gas conversion over the $MgFe_2O_4$/CGO10 electrode recorded over a 3E pellet.

Table 5.4: Gas conversion, GC, and current efficiencies, η, recorded over the $MgFe_2O_4$/CGO 3E pellet. Estimated standard deviations are given in parentheses.

	GC		η	
temp	-0.6 V	0.6 V	-0.6 V	0.6 V
636 °C	0	0	-	-
513 °C	4.2(4) %	1.0(2) %	24(4) %	6(3) %
400 °C	0.4(4) %	0.4(4) %	2(3) %	3(2) %

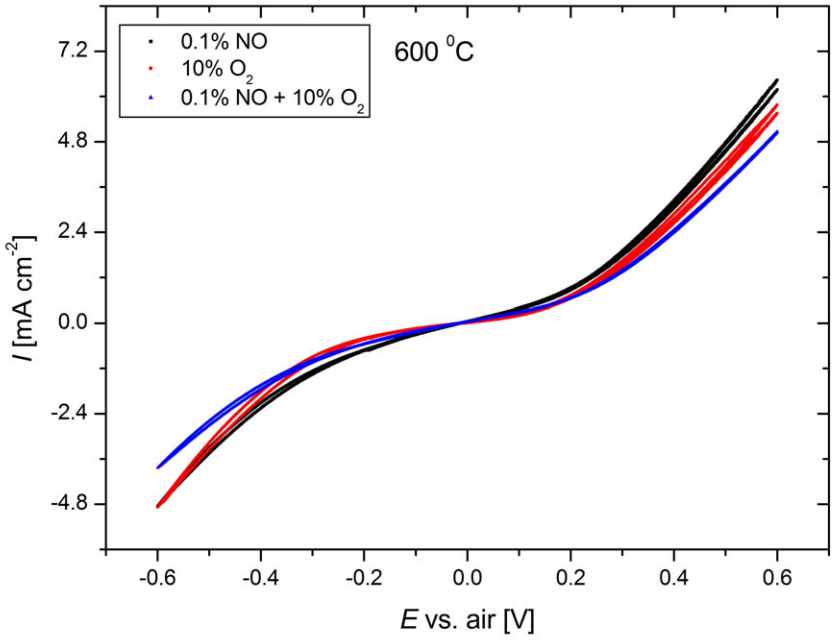

Figure 5.16: CV on the $MgFe_2O_4$/CGO10-electrode at 636 °C.

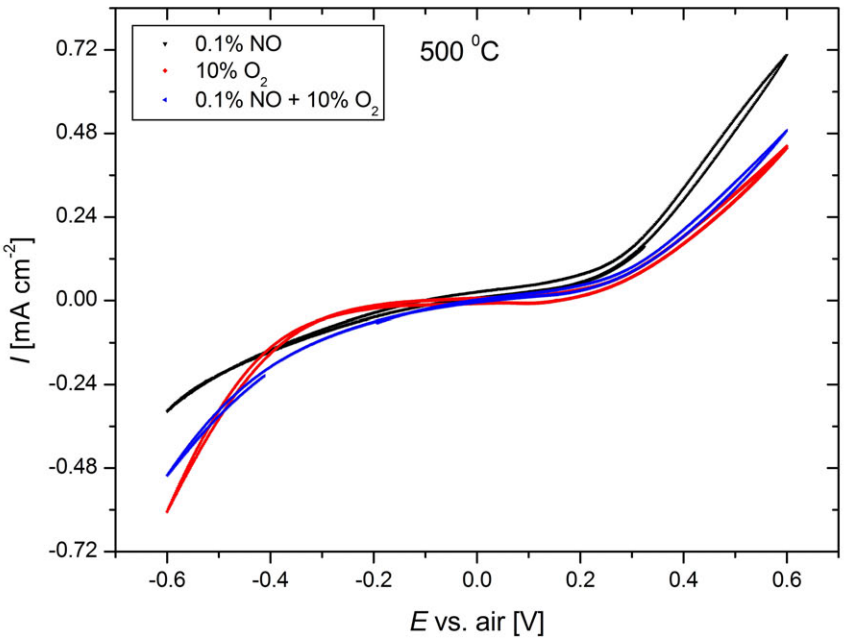

Figure 5.17: CV on the $MgFe_2O_4$/CGO10-electrode at 513 °C.

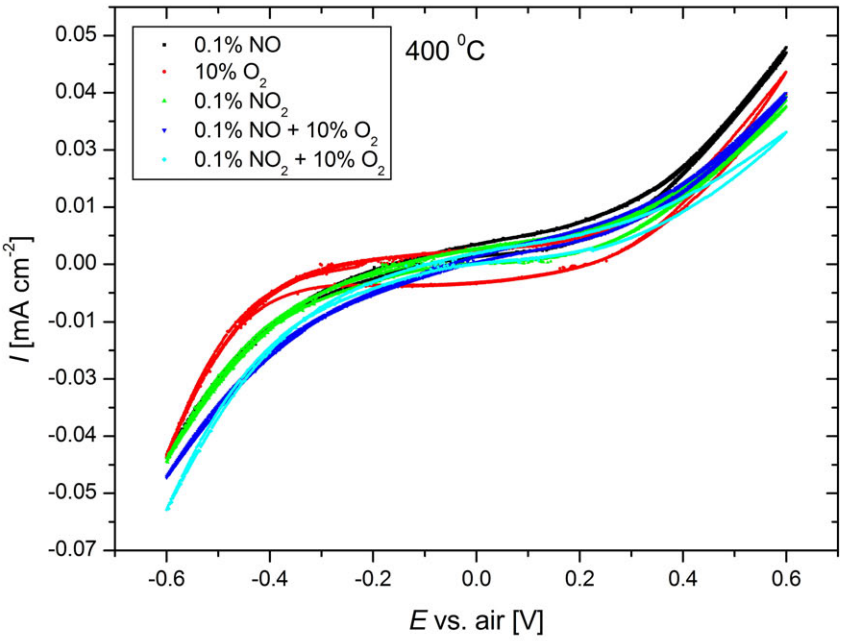

Figure 5.18: CV on the $MgFe_2O_4$/CGO10-electrode at 400 °C.

5.2 The $NiCr_xFe_{2-x}O_4$ Series

$NiCr_2O_4$ has been suggested as a possible sensor material [110, 139, 140] to detect NO_x gases in presence of O_2. It has shown high selectivity towards detection of NO_x and no cross selectivity with respect to CO_2. Therefore, due to the relative high activity of $NiFe_2O_4$ in NO and O_2 [84], a series of $NiCr_xFe_{2-x}O_4$ ($x = 0.0, 0.5, 1.0, 1.5, 2.0$) were synthesized with the main purpose of studying the electrochemical reduction of NO_x and O_2. Other characterization methods like XRD, resistivity measurements and dilatometry were also performed on the materials. Results from this section are published in Journal of Solid State Electrochemistry [141].

5.2.1 Structural Properties

Almost all materials were single phase cubic spinel-type oxides. However, two small impurity phases of tetragonal $NiCr_2O_4$ (approx. 5 %) and NiO (approx. 5 %) was detected together with the cubic $NiCr_2O_4$. $NiFe_2O_4$ has an inverse spinel-type structure with Ni^{2+} located primarily on the octahedral (O) sites and Fe^{3+} located on both the tetrahedral (T) and the O sites. The ionic radius of Ni^{2+} on a T or an O site is 0.55 Å and 0.69 Å respectively, whereas Fe^{3+} has an ionic radius of 0.63 Å (T coordinations) or 0.65 Å (O coordinations) [109]. When Cr^{3+}, having an ionic radius of 0.62 Å (O coordinations) is introduced in the structure in favour of Fe^{3+}, it will enter the O site [142, 143], keeping the structure inverse as long as $x \leq 1$. When $x > 1$, Ni is forced to leave the O sites and move to a T site, which causes a shrinkage of the unit cell because of the different ionic radii of Fe and Ni. Replacing more Fe with Cr, the structure will now change towards a normal spinel structure [144]. XRD, measured at room temperature, shows an decrease in unit cell parameters with increasing Cr content (Figure 5.19). A relative large change of the unit cell parameter is observed when half of the Fe has been replaced by Cr. We would have expected a larger unit cell in the case of $NiCrFeO_4$, however, one explanation would be that a relative large amount of the Ni^{2+} is located on the T sites where its ionic radius is smaller relative to Fe^{3+}.

5.2.2 Conductivity Measurements

Figure 5.20 shows the specific conductivity of the spinels as a function of temperature. Data were corrected for the porosity using Bruggeman's formula [104]. The porosity of the samples were measured with a Micromeritics AutoPore IV Mercury Porosimeter. Below

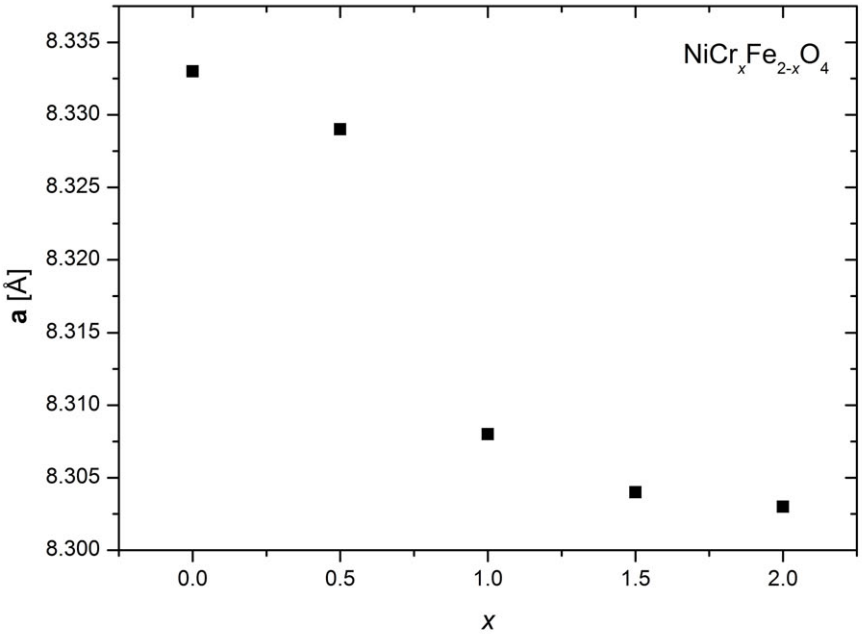

Figure 5.19: Unit cell parameters, a, measured at different spinel compositions. A small decrease in a is observed. Error bars are at the same magnitude as the dimension of the points.

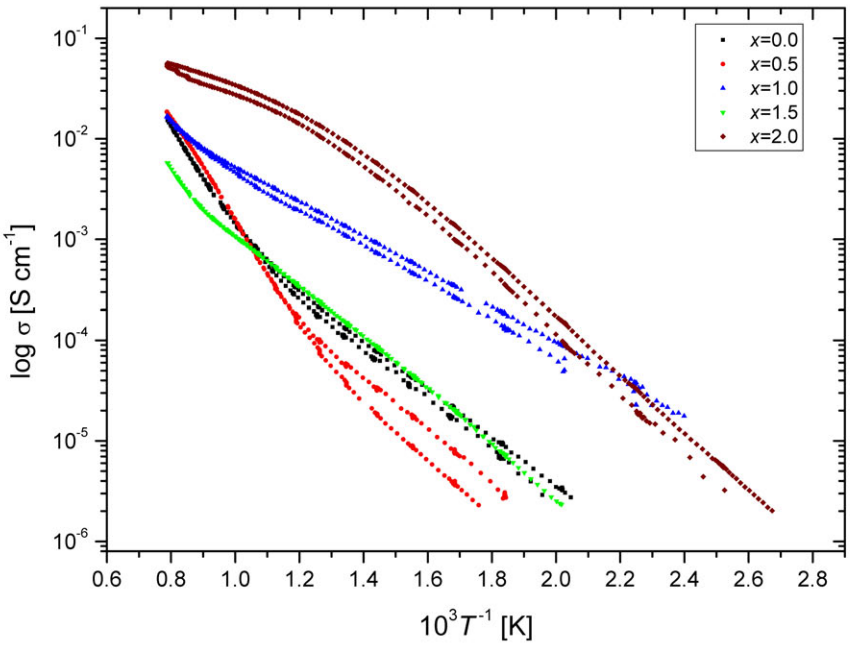

Figure 5.20: Four-point DC conductivity measurements of the spinels measured from room temperature to 1000 °C in air. x refers to the Cr content.

~ 650 °C, the conductivity decreases slightly when Cr^{3+} is introduced in the lattice. The conductivity then increases as more Cr^{3+} is incorporated into the lattice with $NiCr_2O_4$ having the highest conductivity. The conductivity of $NiFe_2O_4$ is mainly attributed to the cation − anion − cation indirect interactions between O sites, where the transport property rises from hopping of localized *d*-electrons between cations [126, 127]. When Cr^{3+} is introduced into the structure it tends to shield this interaction mechanism and thereby decrease the conductivity. However, as more Cr^{3+} is introduced into the structure the unit cell decreases and so does the $Cr^{3+} - Cr^{3+}$ distance. This will strengthen the direct interaction between the Cr^{3+} ions and eventually be the dominating interaction mechanism in the spinel [145]. This interaction will cause an increase in the conductivity at high temperatures as also observed in Figure 5.20.

5.2.3 Dilatometry

Measurements with dilatometry show a gradual decrease in the relative linear expansion (see Figure 5.21a) as more Cr is incorporated into the structure. The thermal expansion coefficients, α, for the different compounds are shown on Table 5.5. For most of the samples, the Curie temperature, T_c, can be detected as a relative narrow and asymmetrical peak in the graph of thermal expansion coefficients [146]. T_c decreases with increasing Cr content (see Table 5.1) which was also reported by Rais *et al.* [147].

For most of the spinels the relative linear expansion reveals an almost reversible dis-

Table 5.5: Electrode porosities, Curie temperatures, T_c and expansion coefficients, α. The expansion coefficients are mean values calculated from 600−800 °C. Curie temperatures were read of the graphs and therefore on statistical errors are given.

compound	porosities	T_c	α
$NiFe_2O_4$	12.5 %	584 °C	$8.0(2) \cdot 10^{-6}$ °C^{-1}
$NiCr_{0.5}Fe_{1.5}O_4$	5.8 %	423 °C	$4.6(1) \cdot 10^{-6}$ °C^{-1}
$NiCrFeO_4$	13.7 %	284 °C	$2.3(1) \cdot 10^{-6}$ °C^{-1}
$NiCr_{1.5}Fe_{0.5}O_4$	8.4 %	∼130 °C	$4.1(1) \cdot 10^{-6}$ °C^{-1}
$NiCr_2O_4$	3.6 %	-	$5.6(3) \cdot 10^{-7}$ °C^{-1}

continuity (see Figure 5.21b) at around 700 − 900 °C, all appearing during the heating and the cooling stage. This suggests a redistribution of cations between the T sites and O sites. In most cases the compounds are not in equilibrium at low temperatures whereas the ordering of the cations is controlled by the kinetics [118]. At high temperatures the spinels are in equilibrium with respect to the cation order-disorder, reflecting the thermodynamic drive towards high temperature disorder. When the cation rearrangement has reached equilibrium, the thermal expansion takes over the main process, which causes

a decrease of the relative linear expansion. Similar observations have been reported on other ferric-spinels [84].

In order to measure any gas conversion, the number of TPB must be increased. A composite electrode of spinel and (CGO10) is therefore needed. Results show that the thermal expansion coefficient of the spinels is in general smaller than the thermal expansion coefficient of CGO10 ($\alpha = 11.9 \cdot 10^{-6}$ °C^{-1} [123]). A mixed electrode manufactured with one of our spinels and CGO10 would therefore be a disadvantage because of the large difference in expansion coefficients. A small particle size and a high porosity could maybe reduce tensions in the microstructure but experiments must be made in order to verify this.

5.2.4 Electrochemical Properties on Cone-Electrodes

CV and EIS were recorded in the temperature range from 300 °C to 600 °C with a 100 °C step. Data were recorded in 10 % O_2 in Ar, 1 % NO in Ar or in 1 % NO_2 in Ar (Air Liquide) with a flow rate of 20 ml/min. Measurements containing NO_2 gas were performed only at 300 °C and at 400 °C. A 1 hour equilibrium time was used to record the OCV before recording the voltammograms in the potential range of -0.6 V $-$ 0.6 V with different sweep rates (1.0, 10, 100, 200, 400 and 600 mVs^{-1}). EIS were recorded from 177793(1) Hz to 0.050(1) Hz with 10 points/decade and an amplitude of 24 mV (rms). In order to compare the electrodes directly, the current recorded in the voltammograms (typically in the order of $10^{-8} - 10^{-7}$ A at 500 °C, -0.6 V) were converted into current densities by dividing with the contact area. Results show that the area correction is less than 5 % at all temperatures and therefore no correction of R_s is needed (see section 4.2.1). Also, no corrections were made for the IR drop since calculations showed that the corrections were less than 0.2 % at all temperatures.

Part of the voltammograms recorded at 300 °C, 400 °C and 500 °C in 1 % NO are shown on Figure 5.22. The highest activity is recorded for $NiFe_2O_4$ but when Cr^{3+} is introduced into the structure, a gradual decrease of the activity is detected. A small increase in activity is seen when all Fe^{3+} have been substituted by Cr^{3+} and it suggests that Fe^{3+} is more electro-catalytic active than Cr^{3+} in NO.

Figure 5.23 shows three voltammograms recorded on $NiCr_2O_4$ in 1 % NO_2 at 400 °C. At high sweep rates the voltammograms appears as straight lines in the potential range and only at 1 or 10 mVs^{-1} a small curvature is observed at maximum and minimum applied potential. Voltammograms recorded at 300 °C are similar to the ones recorded at 400 °C although the I/E-curves are linear at all sweep rates. The linearity seems to be caused

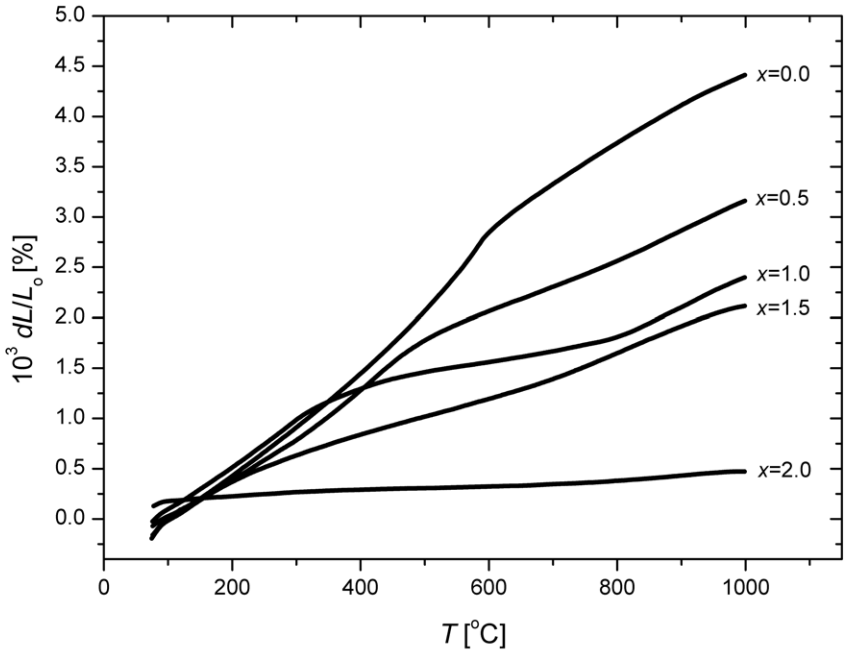

(a)

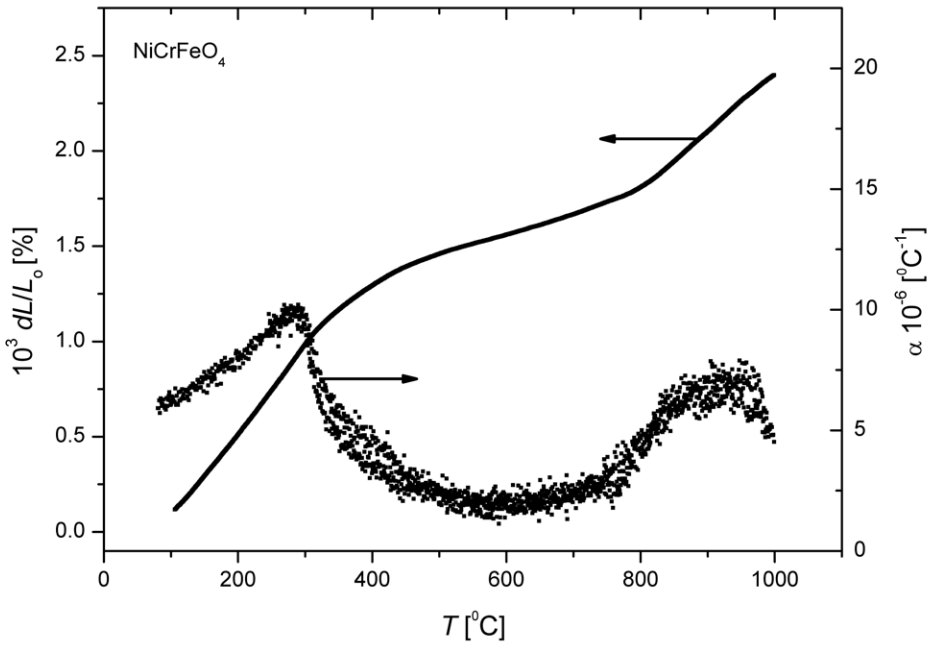

(b)

Figure 5.21: (**a**) Linear expansion of the different spinels measured in the temperature range of 80 °C to 1000 °C. x refers to the Cr content.(**b**) Linear expansion and the expansion coefficient recorded on the $NiCrFeO_4$ electrode. The Curie temperature can easily be detected at $\sim$ 284 °C.

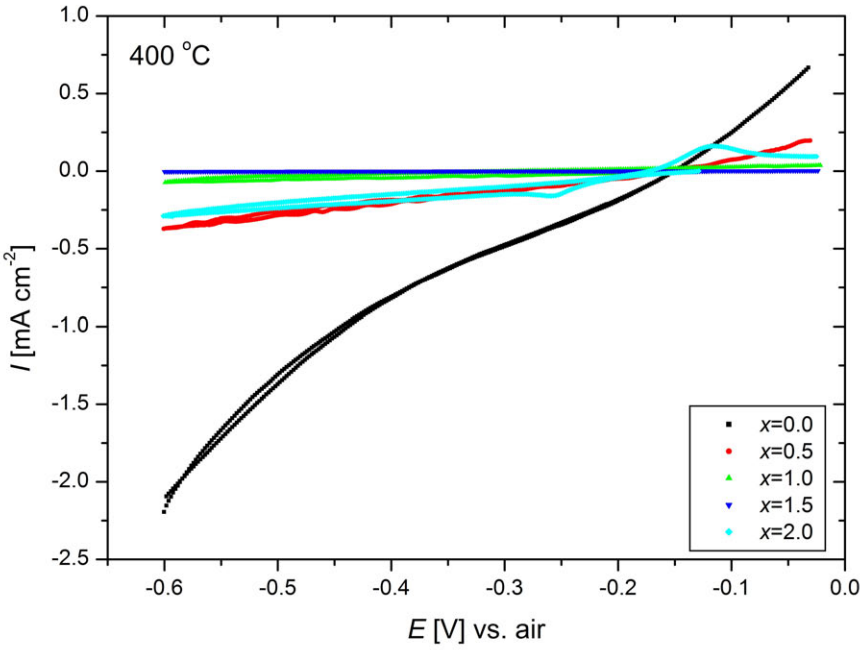

(a)

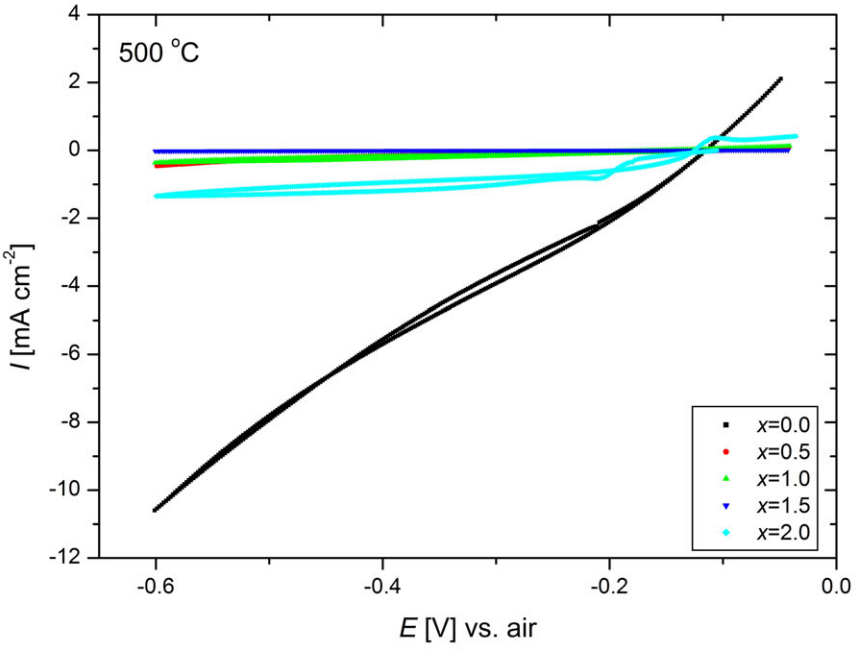

(b)

Figure 5.22: Cyclic voltammograms on $NiCr_xFe_{2-x}O_4$. (**a**) and (**b**) show a part of the voltammograms (-0.6 V − 0 V) recorded at 400 °C and 500 °C respectively. The voltammograms were recorded in 1 % NO with air as reference gas (sweep rate: 1 mVs^{-1}).

by limitations of the ionic conductivity in the electrolyte. It is not clear why the activity of the $NiCr_{1.5}Fe_{0.5}O_4$ electrode is much lower than the other materials. Measurements were repeated several times but with the same result.

Analyzing the current densities of the spinels show that the activities in O_2 and NO (see Figure 5.24) changes only little (not including $NiFe_2O_4$), however, current densities in NO_2 seems to vary in a non-systematic way at 300 °C as function of the Cr content. At 400 °C current densities in NO_2 seems more stable through the series until no more Fe is left in the structure. Then, the current density on the $NiCr_2O_4$ electrode changes significantly. Same picture is seen in NO and O_2, however, this time it is the second end member of the series, $NiFe_2O_4$, that shows the largest activities, whereas the Cr-containing spinels show lower activities. The cathodic activity in O_2 is in general quite

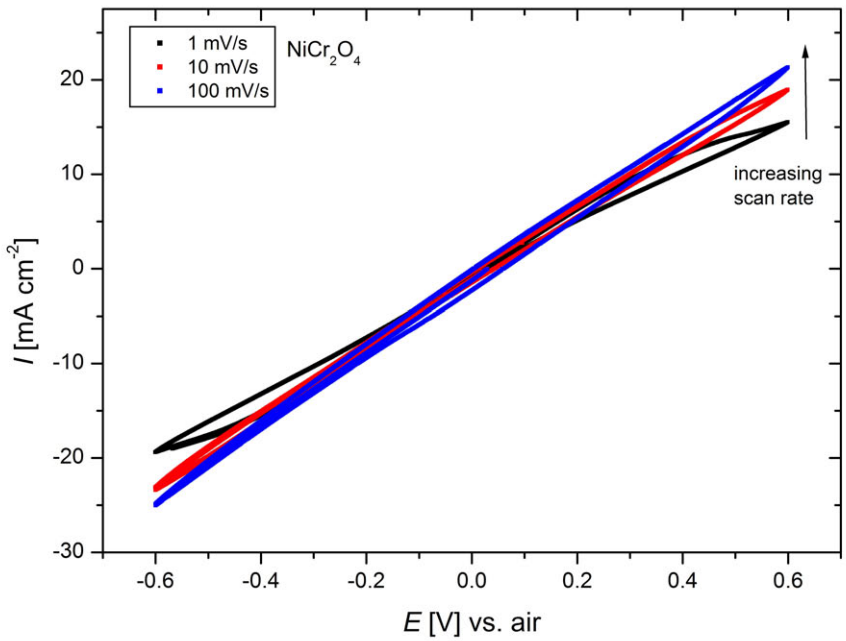

Figure 5.23: Cyclic voltammetry on $NiCr_2O_4$ at 400 °C. Data were recorded in 1 % NO_2. Only voltammograms recorded with sweep rates of 1 mVs^{-1}, 10 mVs^{-1} and 100 mVs^{-1} are shown.

low at all temperatures which is an advantage since it will minimize the extra consumption of current caused by the reduction of O_2 in the exhaust gas from a diesel engine (see section 1.2.4). The porosities of the electrodes were in general low and relatively similar in values. They were, therefore, not taken further in to account.

Because of the small contact area and the relative high flow rate, no direct gas conversion could be measured. Therefore, in order to evaluate the compounds as possible electrode materials, current ratios between NO_x and O_2 were used as a relative tool to

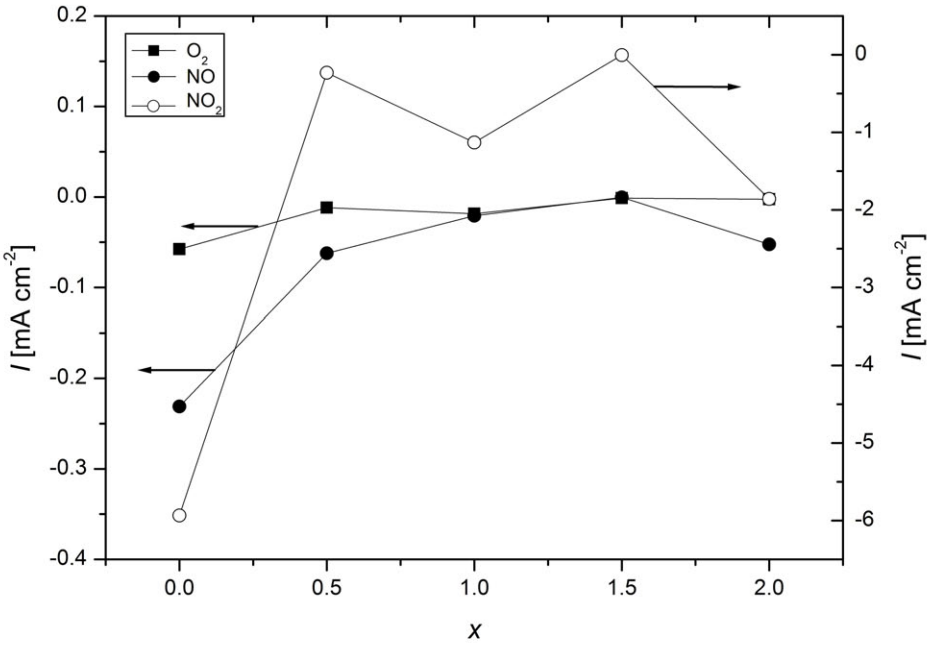

(a)

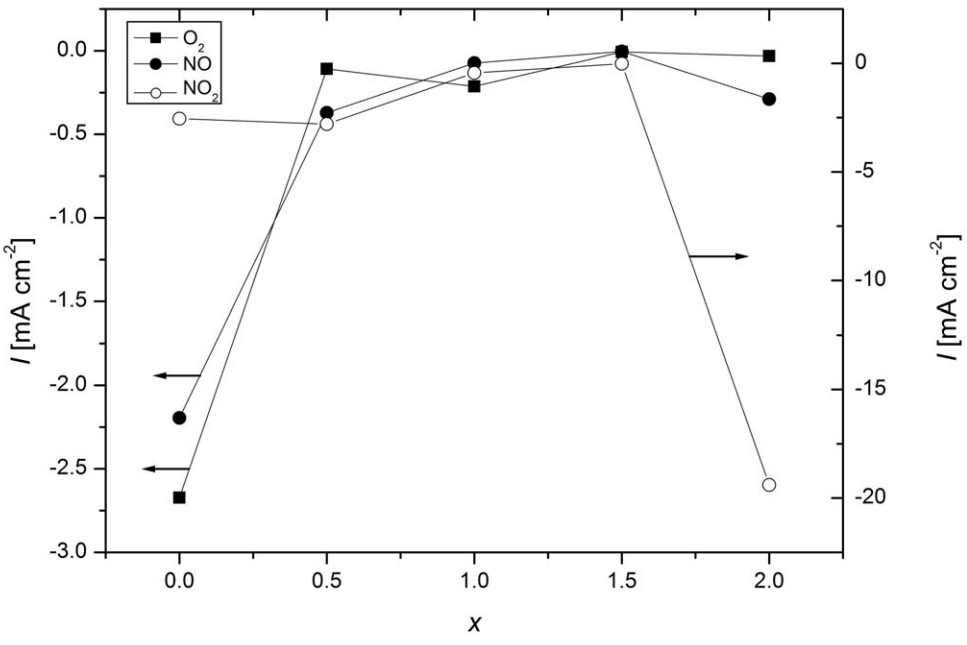

(b)

Figure 5.24: Current densities recorded on $NiCr_xFe_{2-x}O_4$ at **(a)** 300 °C **(b)** 400 °C with an applied potential of -0.6 V. x refer to the Cr content.

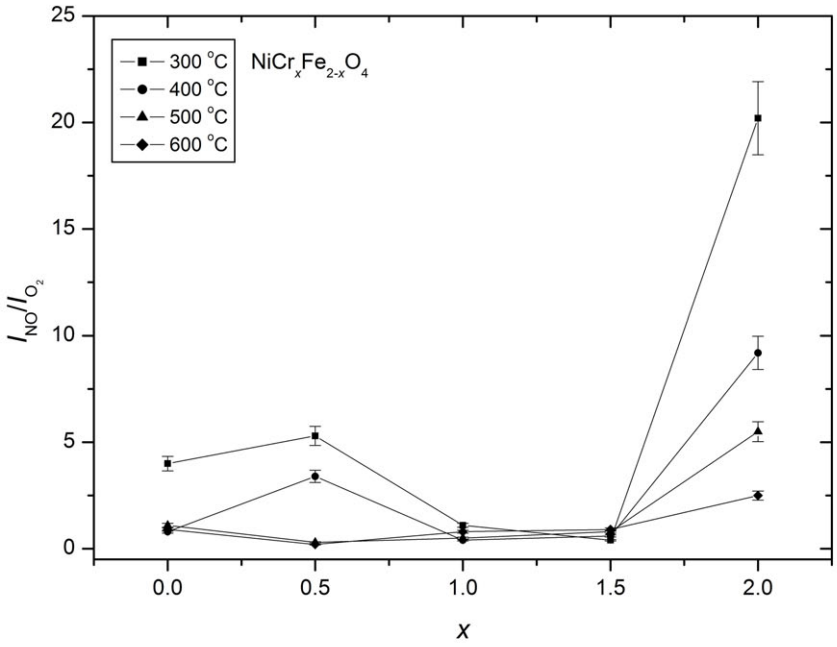

(a)

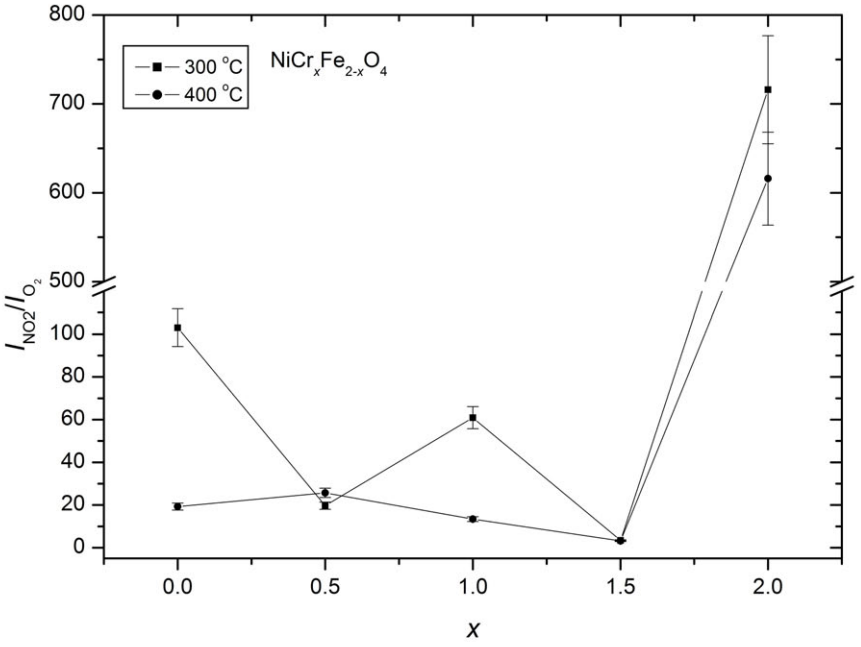

(b)

Figure 5.25: Current ratios between (**a**) NO and (**b**) NO_2 with respect to O_2 for the $NiCr_xFe_{2-x}O_4$-electrodes. $NiCr_2O_4$ shows higher current ratios compared to the other spinels. x refer to the Cr content.

give information of which spinels should be tested further.

Figure 5.25a shows the ratio of the current densities with respect to O_2 (I_{NO}/I_{O_2}). $NiCr_2O_4$ has the highest ratio which decreases with increasing temperature. $NiFe_2O_4$ and $NiCr_{0.5}Fe_{1.5}O_4$ also show relatively high current ratios, however, only at 300 °C and in the case of $NiCr_{0.5}Fe_{1.5}O_4$ also at 400 °C. The much lower current ratio of $NiFe_2O_4$ at 400 °C seems to be the result of the relatively high activity in O_2 at temperatures above 300 °C (see Figure 5.24).

Figure 5.25b shows the current ratios, I_{NO_2}/I_{O_2}, of NO_2 with respect to O_2 at -0.6 V. All electrode materials, except of $NiCr_{1.5}Fe_{0.5}O_4$, show much higher activity in NO_2 compared to NO and O_2. $NiCr_2O_4$ shows significantly higher current ratios from 600−700, which appears to be a result of the relatively low activity in O_2.

5.2.5 Peaks in Voltammograms

Peaks were detected on the voltammograms recorded in the NO atmosphere using the $NiCr_2O_4$-electrode (see Table 5.6). Peaks were not detected in O_2 and NO_2, however, the 10 times higher activity in NO_2 as compared to NO might explain why no peaks are detected on the $NiCr_2O_4$ electrode. Figure 5.26 shows the cyclic voltammograms recorded on $NiCr_2O_4$ at 500 °C with increasing sweep rates. Voltammograms recorded at 400 °C and 600 °C look similar to the one recorded at 500 °C and are therefore not presented. Voltammograms recorded at 300 °C are smeared out when sweep rates exceed 10 mVs^{-1}. This is caused by limitations of the electronic conductivity in the electrode and the ionic conductivity in the electrolyte.

Two oxidation (and reduction) peaks positioned very close to each other are observed at high sweep rates ($200 - 600\ mVs^{-1}$) at 500 °C and 600 °C (see Figure 5.27). The smaller oxidation peak is most detectable after the second cycle. The larger reduction/oxidation peaks shift approximate 20 mV towards lower potentials after the second cycle. The peaks does not reflect a complete reversible reaction because $|I_{red}/I_{ox}| \neq 1$. The origin of the peaks is not understood completely, however, speculations can be made: Since no peaks were observed in O_2 or in NO_2, an obvious conclusion would be to assign at least one set of peaks to the reduction/oxidation of NO as shown in equations 5.12 and 5.13,

$$4e^- + 2NO \rightarrow N_2 + 2O^{2-}, \tag{5.12}$$

$$2O^{2-} + 2NO \rightarrow 2NO_2 + 4e^-. \tag{5.13}$$

We would not expect the reverse reaction of equation 5.12 because of the high elec-

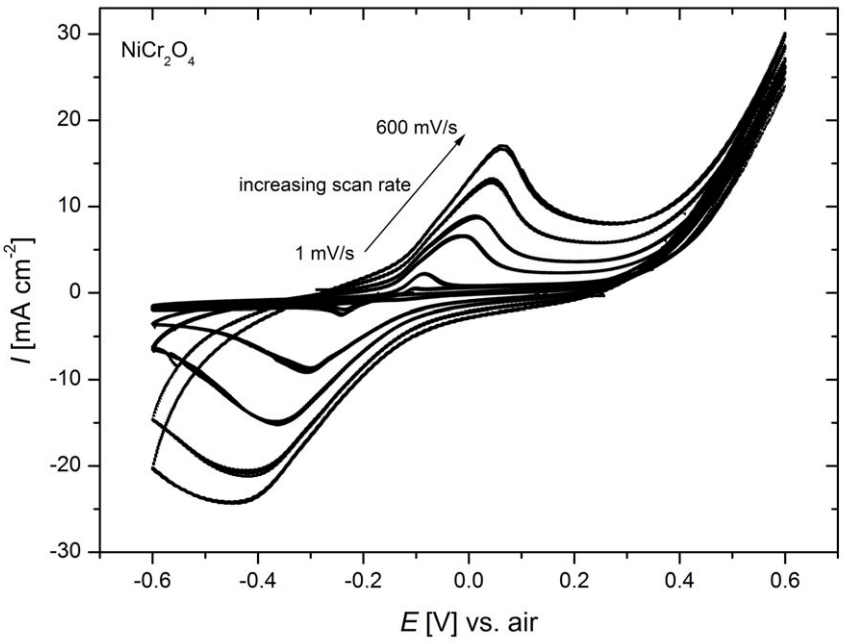

Figure 5.26: Cyclic voltammetry on $NiCr_2O_4$ at 500 °C. Data were recorded in 1 % NO using different sweep rates.

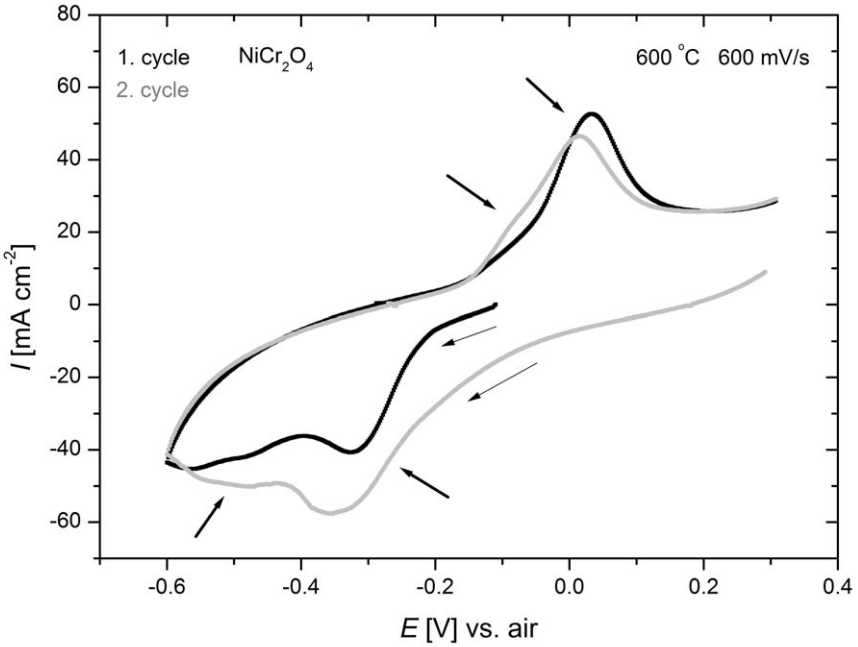

Figure 5.27: Part of the cyclic voltammogram recorded at 600 °C on $NiCr_2O_4$ (sweep rate: 600 mVs^{-1}). Bold arrows show the reduction/oxidation peaks whereas the thin peaks show the direction of the scan.

trochemical stability of N_2. In order to verify that the peaks are related to the reduction/oxidation of NO, the peak heights of the larger oxidation peak were plotted versus the square root of the sweep rate (see Figure 5.28). A linear trend line is observed at 400 °C, 500 °C and 600 °C, however, at high sweep rates at 600 °C a deviation from the linear trend is observed. This is caused by the interference with the peak at slightly lower potential. The apparent diffusion constant of the reaction can be calculated using equation 5.14 [148],

$$\frac{i_\mathrm{p}}{A} = 0.4463F\sqrt{\frac{F}{RT}}c^*\sqrt{\nu}\sqrt{D_\mathrm{a}}, \tag{5.14}$$

where i_p is the peak height, A is the contact area, F is the Faraday constant, c^* is the initial concentration of the active species, ν is the sweep rate and D_a is the apparent diffusion constant. D_a was calculated to 2.3 $\cdot 10^{-13}$ $\mathrm{m^2 s^{-1}}$ at 500 °C in the atmosphere containing 1% NO. The diffusion constant of a perfect gas (kinetic theory of a perfect gas [149]) is equal to

$$D = \frac{1}{3}\lambda\bar{c}, \tag{5.15}$$

where λ is the mean free path, given as:

$$\lambda = \frac{k_\mathrm{B}T}{\sqrt{2}\sigma p}, \tag{5.16}$$

and $\bar{c}$ is the mean speed, given as:

$$\bar{c} = \sqrt{\frac{8RT}{\pi M}}. \tag{5.17}$$

σ is the collision cross-section, p is the pressure, R is the gas constant and M is molar mass. Calculations show that for a perfect gas (1 % NO) $D = 4.1 \cdot 10^{-4}$ $\mathrm{m^2 s^{-1}}$ (500 °C) which is much larger than the measured value. This suggests that the origin of the peak or peaks might be coupled to a bulk diffusion.

Table 5.6: Positions of oxidation (Ox) and reduction (Re) peaks for the $NiCr_2O_4$-electrode. The position of the reduction peak could not be determined for all sweep rates at 400 °C. All positions were read of the graphs and therefore no statistical errors are given.

sweep rate	400 °C		500 °C		600 °C	
-	Ox	Re	Ox	Re	Ox	Re
1 $\mathrm{mVs^{-1}}$	-111 mV	-261 mV	-102 mV	-212 mV	-80 mV	-194 mV
10 $\mathrm{mVs^{-1}}$	-55 mV	-306 mV	-85 mV	-242 mV	-68 mV	-224 mV
100 $\mathrm{mVs^{-1}}$	34 mV	-	-15 mV	-304 mV	-37 mV	-264 mV
200 $\mathrm{mVs^{-1}}$	64 mV	-	15 mV	-324 mV	-18 mV	-284 mV
400 $\mathrm{mVs^{-1}}$	91 mV	-	42 mV	-422 mV	3 mV	-318 mV
600 $\mathrm{mVs^{-1}}$	114 mV	-	65 mV	-455 mV	18 mV	-361 mV

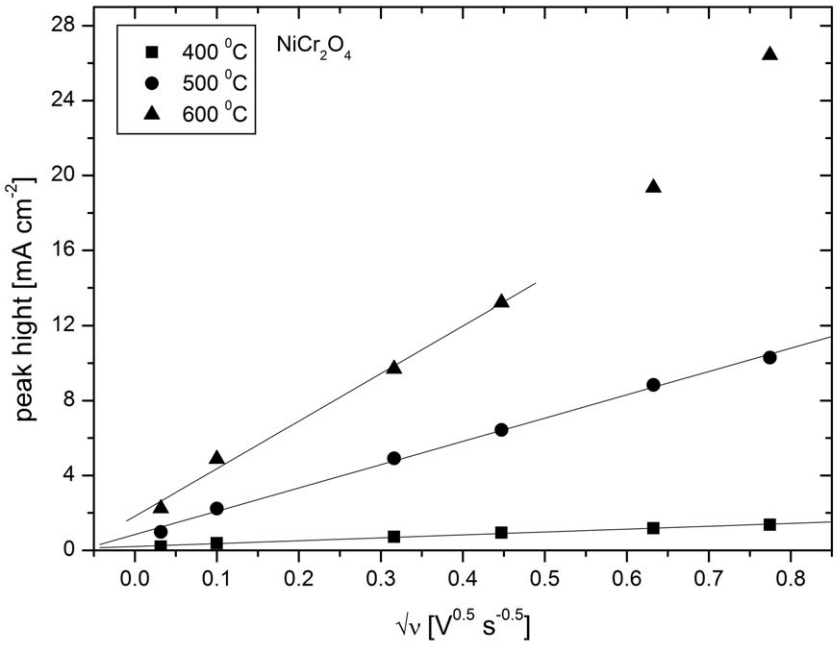

Figure 5.28: Peak height plotted versus the square root of the sweep rate. A linear trend can be detected at 400 °C and 500 °C, however, at 600 °C the linearity is disturbed at high sweep rates.

Within the potential range, two electrochemical reaction can occur as shown in equations 5.18 and 5.19:

$$\frac{1}{2}O_2 + NiCr_2O_4 \rightarrow NiO + 2CrO_2 \qquad E = -0.14 \text{ V}, \tag{5.18}$$

$$\frac{3}{2}O_2 + NiCr_2O_4 \rightarrow NiO + 2CrO_3 \qquad E = -0.28 \text{ V}. \tag{5.19}$$

The equilibrium potentials are calculated at 500 °C using FactSage 5.5 [15]. The position of the reduction and oxidation peaks at 400 °C and 500 °C (1 mVs^{-1}) matches quite well with the equilibrium potential of equation 5.18, however, the position of the peaks at 600 °C does not coincide well with the equilibrium potential of equation 5.18. The oxidation peak seems to be shifted and approximately 50 mV towards higher potentials than expected. Formation of CrO_3 seems, however, not to be present due to the position of the peaks. Considering the charge transfer and assuming a perfect cone shows that the reaction 5.18 proceeded approximate 19 μm up in the cone electrode (500 °C, 1 mVs^{-1}). If the oxidation/reduction of Cr is in fact the explanation of the peaks, we are still left with the questions of why no peaks are observed in O_2 or NO_2? Why no voltammograms of the other Cr-containing spinels appear to show peaks in any of the gases? What causes the second reduction/oxidation peak. Finally, why do we start by seeing a reduction peak

when no CrO_2 could be detected by XRD before starting the experiment?

Since no peaks were detected in the O_2 containing atmosphere for $NiCr_2O_4$, it suggests that the origin of the peaks are not due to the formation of Cr-oxides but must be found in the formation of other unknown nitrogen-containing species on the surface. Similar observations were reported by Simonsen *et al.* [61] and peak formations were also attributed to the formation of nitrogen-containing species on the surface. Earlier reports show that Cr species evaporates relatively easy at elevated temperatures [150, 151] and it is possible that some of the Cr in the outer most atomic layers of the particles has evaporated during sintering. This would lead to a depletion of Cr at the surface of the materials and would explain the absence of peaks in the Fe-containing materials since it has been more of less shielded from contact with any of the reaction gases. The second set of peaks is very difficult to ascribe a certain process but it may be due to reduction/oxidation processes of the NO gas. Therefore, the missing peaks in O_2 on the $NiCr_2O_4$ electrode suggests the formation of other (unknown) stable or metastable nitrogen-containing species on the surface of the electrode. However, it cannot be $Ni(NO_3)_2$ or $Cr(NO_3)_3$ since they will decompose above 300 °C [152, 153]. The position of the peaks fits on the other hand quite well with the oxidation of Cr and it can not be ruled out that it contributes to the peak formation.

5.3 The $MgMn_xFe_{2-x}O_4$ Series

$MgFe_2O_4$ is a promising electrode material in NO and NO_2 sensors [84] and it has also received some interest as a possible humidity sensor material [154]. However, $MgFe_2O_4$ is a pore electronic conductors which will limit the current passing through the cell. The purpose of this work was therefore to investigate the effects of substituting Mn into the $MgFe_2O_4$ structure on the consequence of Fe and determined the conductivity with respect to the electro-catalytic activity. Therefore, a series of $MgMn_xFe_{2-x}O_4$ ($x = 0.0, 0.2, 0.4, 0.6, 0.8, 1.0$) were synthesized and the results of this section are submitted to Journal of Applied Electrochemistry [155].

5.3.1 Structural Properties

All samples were analyzed as single phase cubic spinel-type oxides. Plotting the unit cell parameter, a, as function of the Mn content shows that a only changes a little when Fe is substituted on the consequence of Mn (see Figure 5.29). Mg^{2+} ions have a strong preference to occupy the octahedral (O) sites and partially occupy tetrahedral (T) sites [156]. Fe^{3+} on the other hand occupies both T and O sites with no preference, since its ionic radii are very similar [109]. Mn^{3+} tends to occupy O sites instead of T sites [157]. However, the ionic radius of Mn^{3+} is slightly bigger than Fe^{3+} [158], which will explain the small increase of the unit cell as more Mn is incorporated into the structure. Earlier reports [159] show similar increase in unit cell, but they state that the Mn content could not exceed $x = 0.4$ in order to synthesize a single phase powder. However, magnetic measurements on [160] $MgMn_xFe_{2-x}O_4$, $x \geq 1$, show that the material could be synthesized as a single phase with a solid state reaction.

5.3.2 Dilatometry and Resistivity Measurements

Figure 5.30a shows the dilatometry measurements of the samples. It shows, with the exception of $MgFe_2O_4$, a gradual decrease of the linear thermal expansion as more Mn is incorporated into the structure. The graphs (not shown for all materials) of the expansion coefficient show for all samples a peak positioned around 150 °C − 325 °C. The shape and position of the peaks agrees with the expected Curie temperature, T_c [112, 113, 146, 160]. Figure 5.30b shows an example of the thermal expansion and expansion coefficient in the case of $MgMn_{0.2}Fe_{1.8}O_4$. Table 5.7 shows the decreasing Curie temperatures and the mean expansion coefficient in the temperature range of 600 °C − 800 °C. As discussed in section

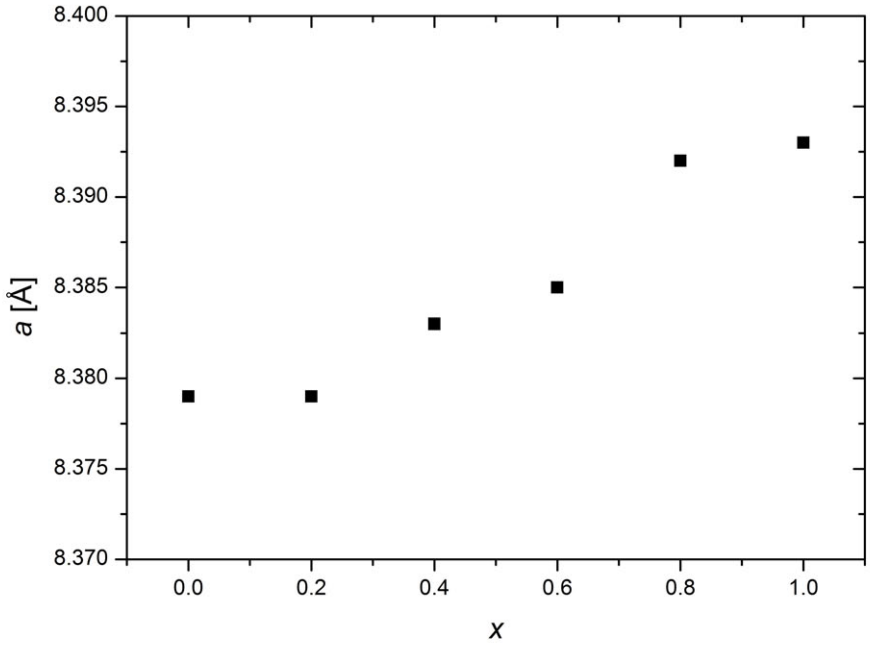

Figure 5.29: Unit cell parameters, a, measured at different spinel compositions. A small increase in a is observed. x refers to the Mn content. Error bars are at the same magnitude as the dimension of the points.

2.1, spinels are in general bad oxygen ion conductors. Therefore, an oxygen ion material, such as CGO10, must be mixed with the spinel material when more advanced cells needs to be produced. Results show that the thermal expansion coefficient of the spinels is in general smaller than the thermal expansion coefficient of CGO10, however, it should be possible to manufacture a suitable microstructure based on similar expansion coefficients in solid oxide fuel cells [123, 161]. Experiments, however, must be made to verify this.

Figure 5.31 shows the Bruggeman-corrected specific conductivities. The porosity of the samples was measured with a Micromeritics AutoPore IV Mercury Porosimeter.

Table 5.7: Electrode porosities, Curie temperatures, T_c, expansion coefficients, α and activation energies, E_a. The expansion coefficients are mean values calculated from 600−800 °C. The T_c were read of the graphs and therefore on statistical errors are given. E_a of $MgFe_2O_4$ was not calculated due the interference of the hysteresis.

compound	porosities	T_c	α	E_a
$MgFe_2O_4$	27.18 %	322 °C	$1.25(1) \cdot 10^{-5}$ °C^{-1}	-
$MgMn_{0.2}Fe_{1.8}O_4$	29.92 %	304 °C	$1.40(1) \cdot 10^{-5}$ °C^{-1}	0.7596(2) eV
$MgMn_{0.4}Fe_{1.6}O_4$	33.16 %	251 °C	$1.27(1) \cdot 10^{-5}$ °C^{-1}	0.6360(9) eV
$MgMn_{0.6}Fe_{1.4}O_4$	33.78 %	163 °C	$1.195(5) \cdot 10^{-5}$ °C^{-1}	0.4384(5) eV
$MgMn_{0.8}Fe_{1.2}O_4$	37.92 %	141 °C	$1.05(1) \cdot 10^{-5}$ °C^{-1}	0.4310(7) eV
$MgMnFeO_4$	32.04 %	138 °C	$1.010(9) \cdot 10^{-5}$ °C^{-1}	0.3972(2) eV

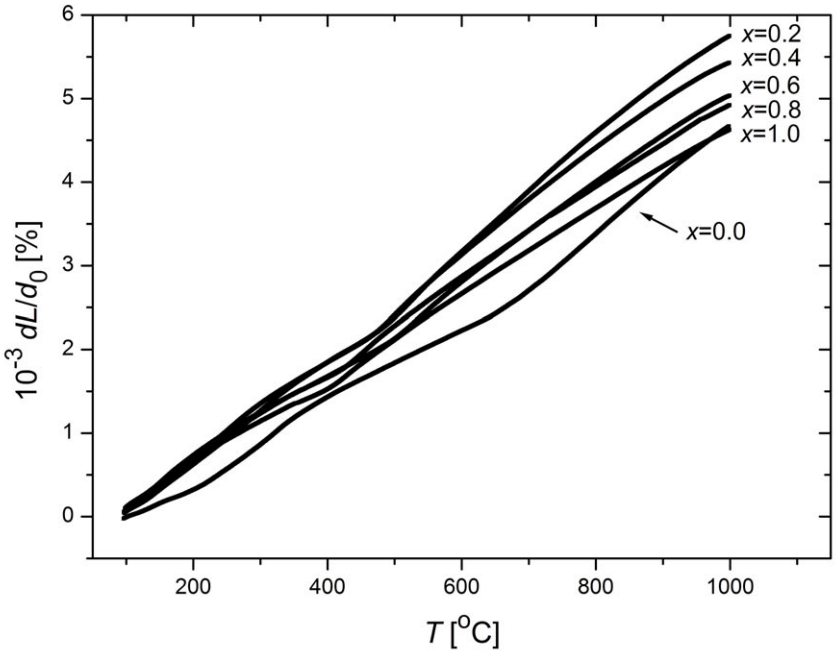

(a)

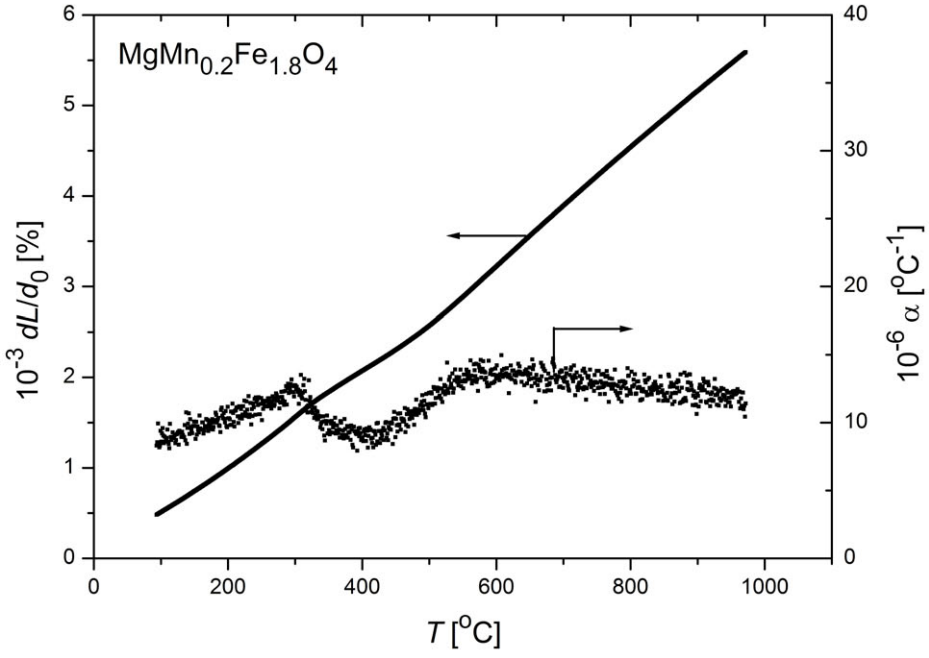

(b)

Figure 5.30: (**a**) Linear expansion of the different electrode materials measured in the temperature range of 80 °C to 1000 °C. x refers to the Mn content. (**b**) Linear expansion and the expansion coefficient recorded on the $MgMn_{0.2}Fe_{1.8}O_4$ electrode. The Curie temperature can easily be detected at $\sim$ 304 °C.

Results show that the conductivity increases when Fe is substituted with Mn. A large hysteresis were also observed for the $MgFe_2O_4$-spinel which is a result of cation reordering (see section 5.2.3). The conductivity is mainly caused by exchange interactions between O-sites ($O-O^{2-}-O$) with hopping of localized *d*-electrons between cations [126, 127]. Substituting Mn into the structure will increase the conductivity as Mn can exist in more than one valence state (2+, 3+ and 4+) with Mn^{2+} primarily occupying the T-sites and Mn^{3+} and Mn^{4+} occupying the O sites [157]. It is, however, believed that the oxidation state on Mn found in the samples is primarily 3+. The data were fitted with a small polaron [162] Arrhenius equation and it shows that the activation energies (see Table 5.7) decreases as more Mn is substituted into the structure. A significant change in the activation energies were found when $x > 0.4$. It suggests that at this composition enough Mn is present to form a 'network' through the structure so that the exchange interaction can make the electrons move much easier through the structure.

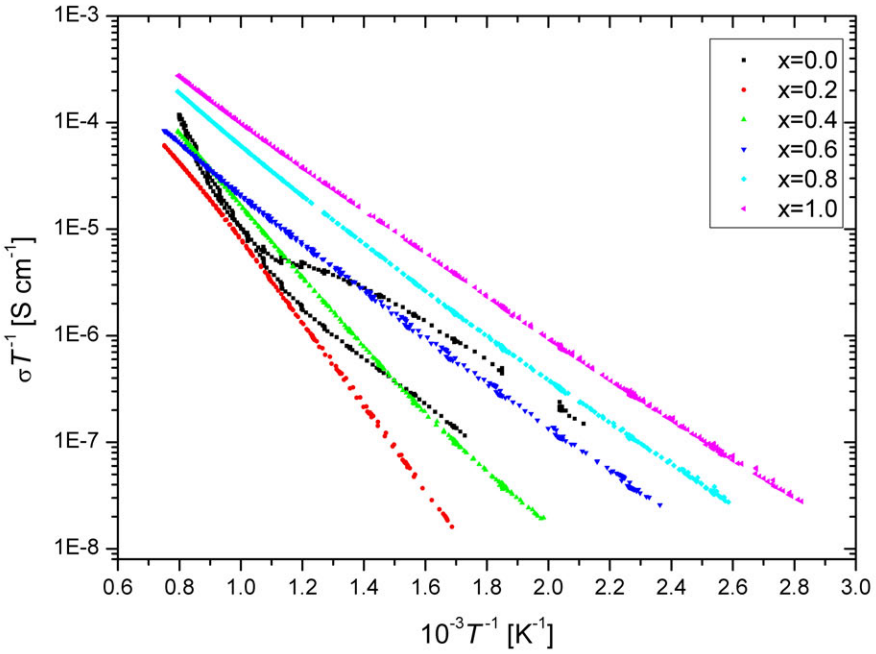

Figure 5.31: Four-point DC conductivity measurements of the spinels measured from room temperature to 1000 °C in air. x refers to the Mn content.

5.3.3 Electrochemical Properties on Cone-Electrodes

Data were recorded in 10 % O_2 in Ar, 1 % NO in Ar (Air Liquide) at 300 °C, 400 °C, 500 °C and 600 °C and in 1 % NO_2 in Ar (Air Liquide) at 300 °C and 400 °C. A flow

rate of 20 ml/min was applied during all measurements. A 1 hour equilibrium time was used to record the OC) before recording the voltammograms in the potential range of -0.6 V − 0.6 V with different sweep rates (1.0 and 10 mVs^{-1}). In order to compare the different electrode materials directly, the recorded current was converted into current densities by dividing with the contact area between the electrode and the electrolyte. The IR drop was less than 5 % in cases and no corrections were therefore made.

The activity in 10 % O_2 is for all materials very low ($\ll$ 1 mA cm^{-2}, -0.6 V) and within the uncertainties of the recorded data and contact areas (10 %). It was, therefore, not possible to determine a general trend with respect to activities and the Mn content.

The cathodic activities recorded in 1 % NO at 400 °C, 500 °C and 600 °C are generally low and the differences between the Mn-containing materials are small. Only $MgMn_{0.4}Fe_{1.6}O_4$ has a slightly higher cathodic activity (-0.6 V) at 400 °C and 500 °C than the other Mn-containing samples. At all temperatures, the cathodic activity on $MgFe_2O_4$ was significantly higher. Figure 5.32 show an example of the voltammograms recorded at 400 °C and 500 °C. It is not known why $MgMn_{0.4}Fe_{1.6}O_4$ has higher activities but porosity measurements show no distinct differences compared to the other electrodes.

Data recorded in 1 % NO_2 show a higher activity of the electrodes as compared to the recorded data in NO and O_2. Earlier reports show similar trend on ferrite spinel-type electrodes [84, 141] and perovskites [57]. However, the cathodic activities of the Mn-containing electrodes are significantly lower compared to those of $MgFe_2O_4$ as also observed in NO. The activity of $MgMn_{0.2}Fe_{1.8}O_4$ is slightly higher than that of the other electrodes at 400 °C, whereas $MgMn_{0.8}Fe_{1.2}O_4$ shows higher activity at 300 °C.

Figure 5.34 shows the current ratios of I_{NO}/I_{O_2} and I_{NO_2}/I_{O_2}. At 400 °C, current ratios of I_{NO_2}/I_{O_2} show ratios of $25 - 30$, with the exception of $MgMn_{0.4}Fe_{1.6}O_4$ which has a much higher current ratio of ~ 65. Measurements were repeated but with the same result and therefore it were not possible to explain the one-point jump on the graph. At 300 °C, current ratios increase with $MgFe_2O_4$ having the highest value of ~ 135. It then drops to $40 - 50$ for the Mn-containing electrodes.

Current ratios of I_{NO}/I_{O_2} show in general much lower values compared to I_{NO_2}/I_{O_2}. At 600 °C current ratios are low and in the range of 1 to 3. At 500 °C, the highest current ratio is observed for $MgFe_2O_4$; however, the curves show a small broad peak at $0.4 \leq x \leq 0.6$. Still ratios only range from 1 to 5 for the Mn-containing electrodes. At 400 °C we see a large peak at $0.2 \leq x \leq 0.8$ with a maximum current ratio of ~ 46. We were not able to explain the sudden drop at $x = 0.2$, and again porosity measurements did not help answer it. We therefore believe that the porosity of the electrode materials have very little effect on the recorded data from a cone-setup.

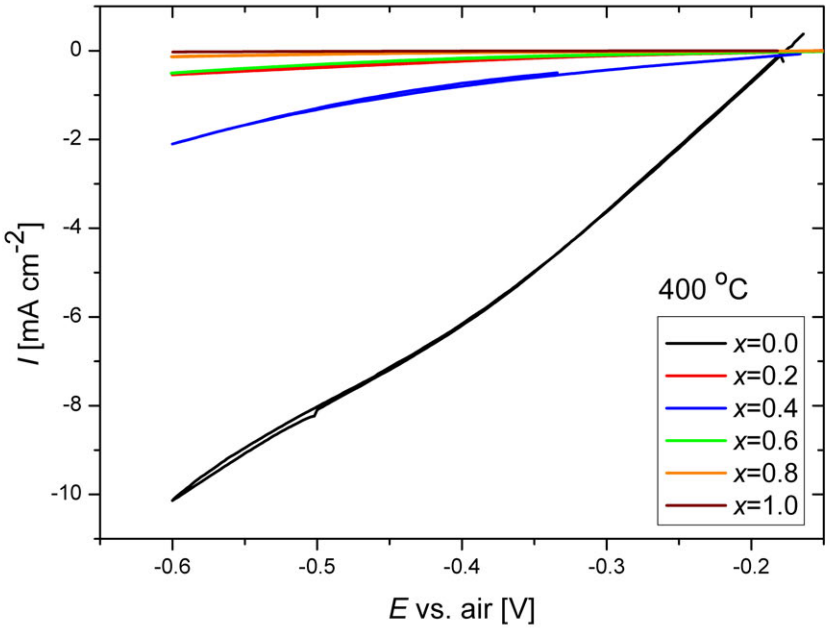

(a)

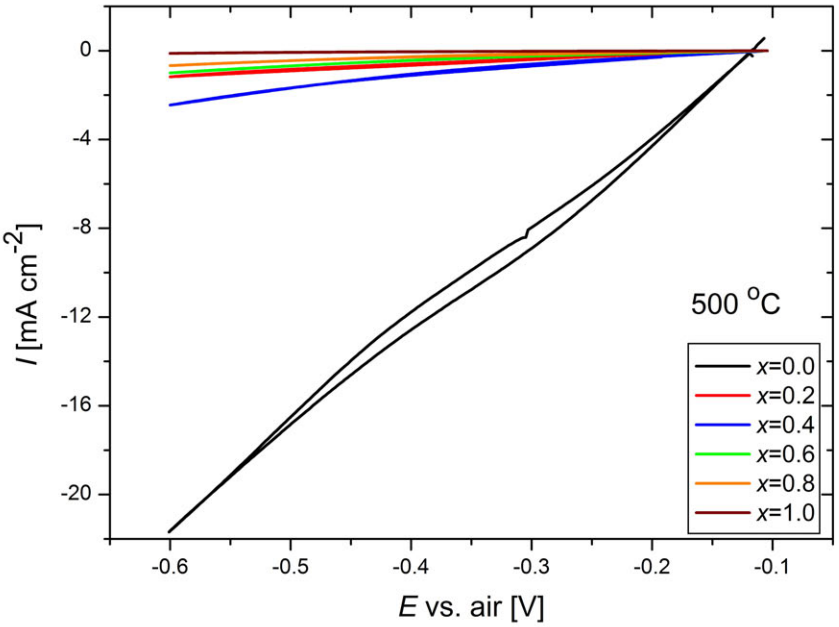

(b)

Figure 5.32: Cyclic voltammograms on $MgMn_xFe_{2-x}O_4$. (**a**) and (**b**) show a part of the voltammograms recorded at 400 °C and 500 °C respectively. The voltammograms were recorded in 1 % NO with air as reference gas (sweep rate: 1 mVs^{-1}). Voltammograms recorded at 10 mVs^{-1} looked similar and are therefore not shown.

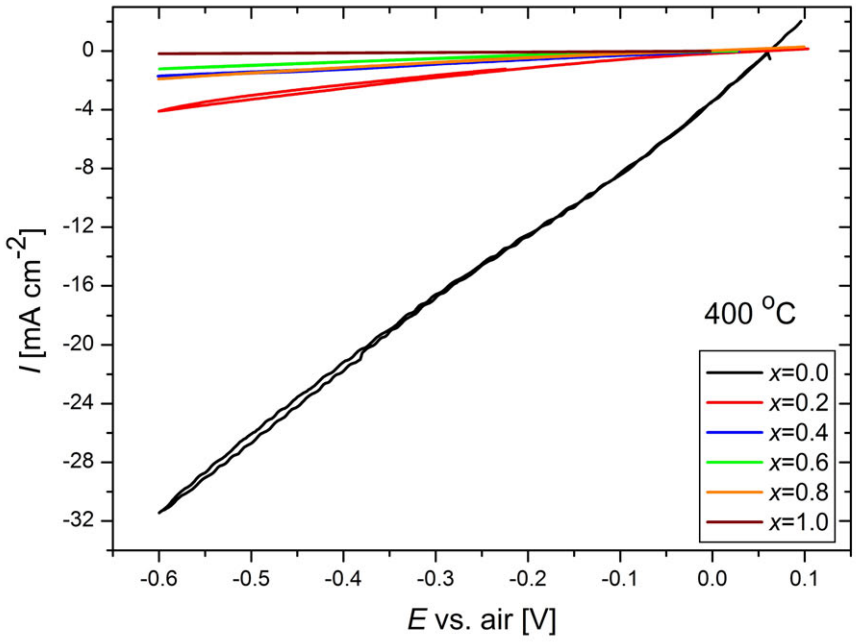

Figure 5.33: Part of the cyclic voltammograms recorded at 400 °C in 1 % NO_2 with a sweep rate of 1 mVs^{-1}. Voltammograms recorded at 10 mVs^{-1} looked similar.

Tafel plots were also made for the different electrode materials. However, they look much the same as reported for the $Ni_{1-x}Mg_xFe_2O_4$ series (see section 5.1.4). A relative high electronic conductivity form a 'bump' in the anodic part of a Tafel plot (see Figure 5.35) as also observed in the case of $NiFe_2O_4$. The origin of that is not yet known.

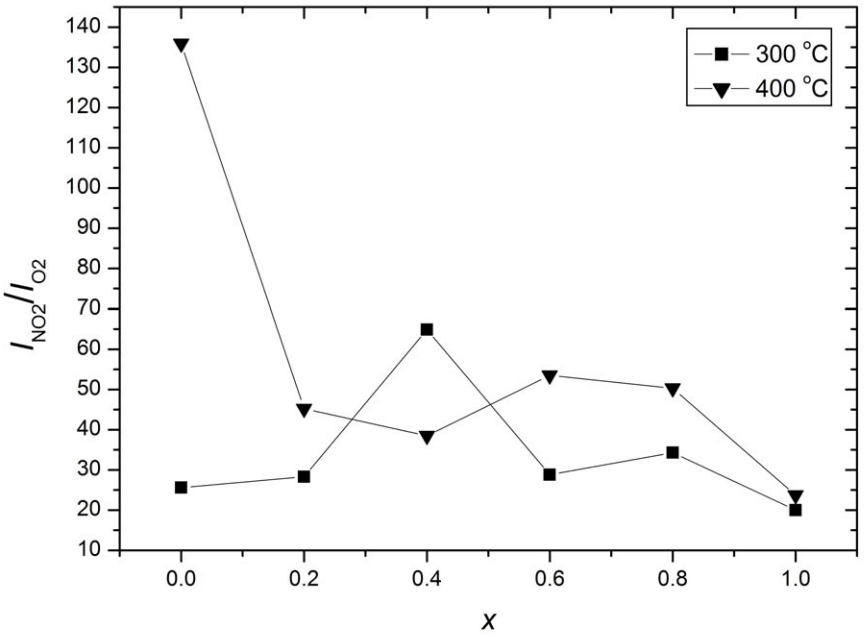

(a)

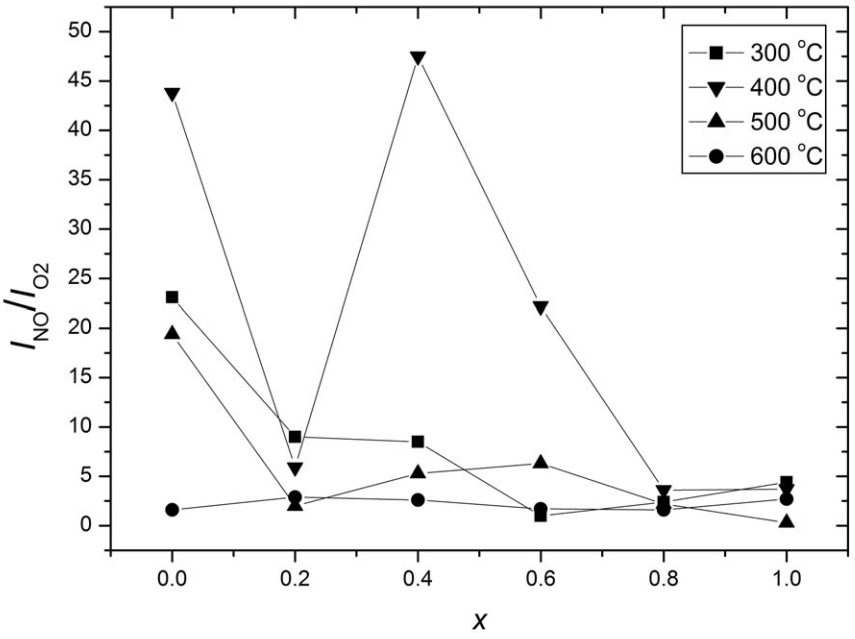

(b)

Figure 5.34: Current ratios of **(a)** I_{NO_2}/I_{O_2} and **(b)** I_{NO}/I_{O_2} recorded on $MgMn_xFe_{2-x}O_4$ with an applied potential of -0.6 V. x refer to the Mn content.

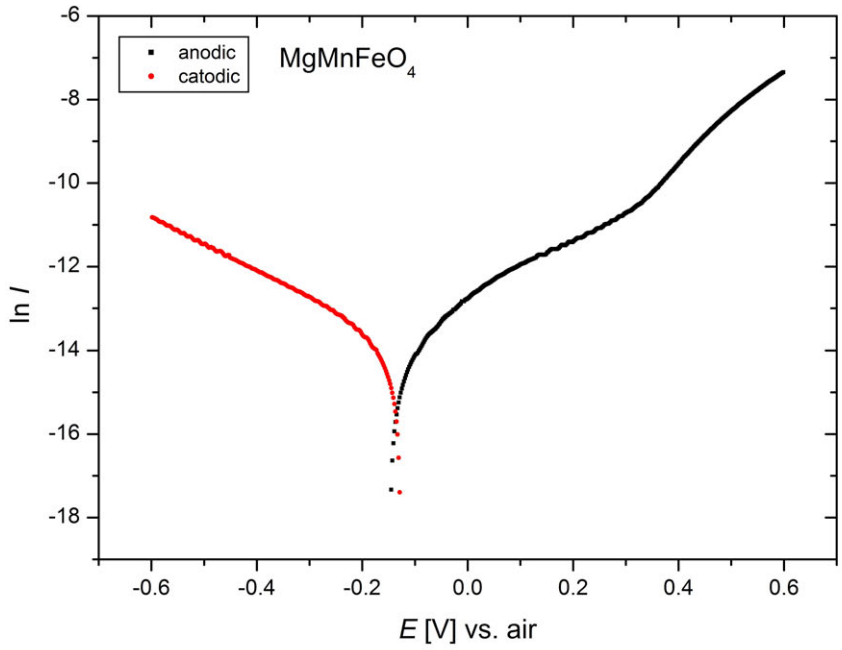

Figure 5.35: Tafel plot of $MgMnFeO_4$ and at 500 °C in 1% NO.

5.4 $ZnFe_2O_4$

This section contains the results obtained from $ZnFe_2O_4$. Measurements were made with CV, EIS on cone-electrodes, symmetrical cells and 3E-pellets. Measurements were also performed on Ba-doped $ZnFe_2O_4$ 3E-pellets. Additionally measurements were made concerning the electronic conductivity, the linear thermal expansion and cation distribution. The latter was performed with *in situ* high temperature neutron diffraction. Results concerning the electronic conductivity, the linear thermal expansion and cation distribution are published in Journal of Solid State Chemistry [163].

5.4.1 Introduction

$ZnFe_2O_4$ has an almost normal spinel structure with Zn^{2+} located on T sites and Fe^{3+} located on O sites. $ZnFe_2O_4$ is a promising electrode material in NO and NO_2 sensors [164, 165] and the material has also received much interest as a possible sensor material for organic compounds such as ethanol, acetone and propanol [166, 167]. Other reports also indicates that $ZnFe_2O_4$ is active toward Cl_2 gas-sensing [160].

5.4.2 Conductivity and Dilatometry Measurement

Figure 5.36b shows an Arrhenius plot of the specific conductivity of $ZnFe_2O_4$. Data have been corrected for the closed porosity (1.7 %) using Bruggemans formula [104]. The closed porosity was determined with the Archimedes principle. $ZnFe_2O_4$ behaved as a semi-conductor already at room temperature, but after running the sample with the temperature profile described in section 4.3.1, the semi-conducting behaviour disappeared below the detection limit of the setup at around 120 °C. The graph shows a semi-conducting behaviour with a linear increase in conductivity but with a distinct change of slope at 630 °C. The data were fitted with an small polaron [162] Arrhenius-type equation 5.20,

$$\sigma = \sigma_0 T^{-1} \exp \frac{-E_a}{k_B T}, \tag{5.20}$$

where σ is the specific conductivity and k_B and T are the Boltzmann constant and the temperature respectively. The activation energies in the lower and upper temperature range were calculated to $E_a = 0.248(1)$ eV and $E_a = 0.126(4)$ eV respectively.

Figure 5.37 shows the relative linear expansion of $ZnFe_2O_4$ as function of temperature.

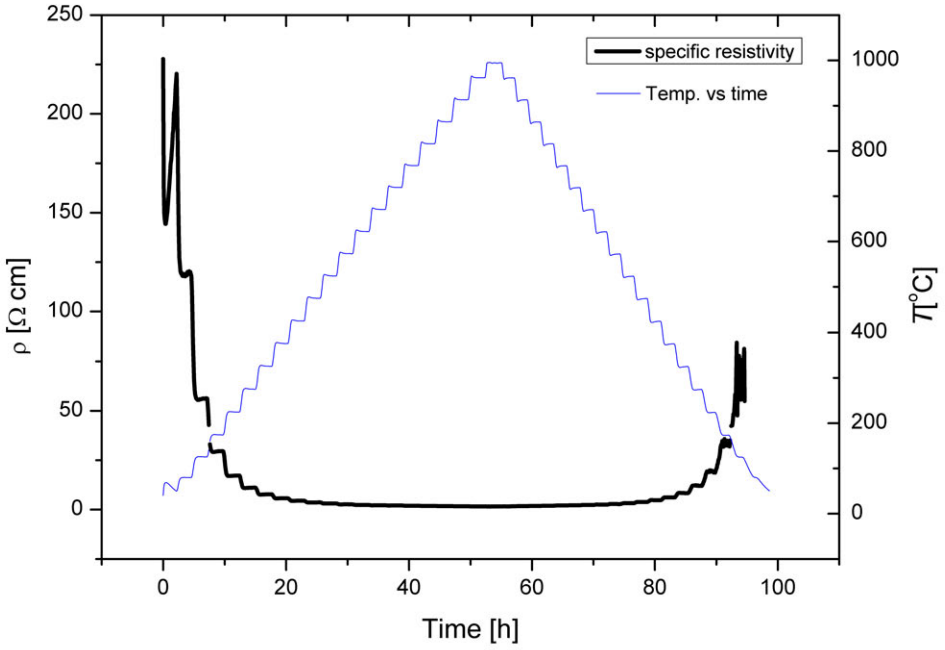

(a)

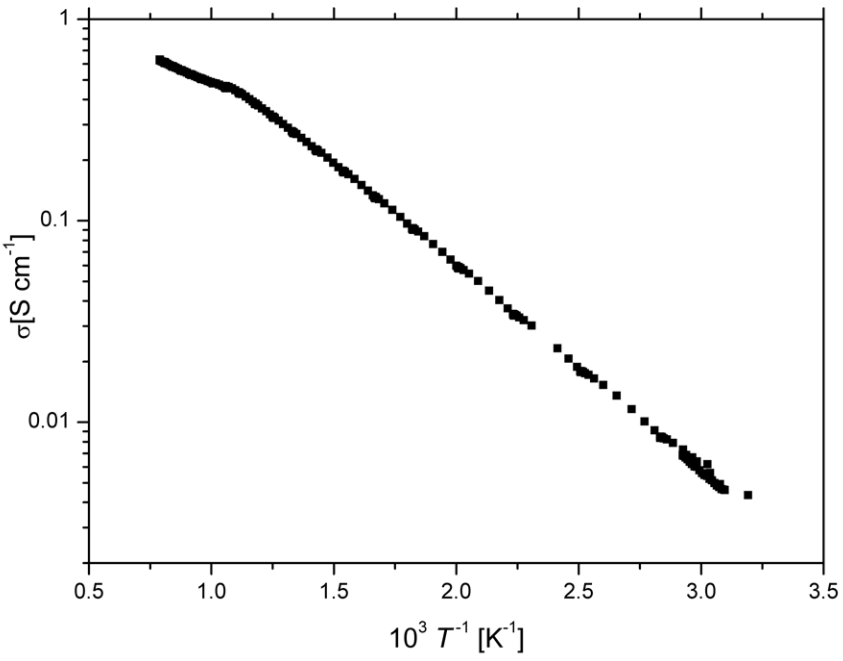

(b)

Figure 5.36: **(a)** The specific resistivity as a function of time and temperature. **(b)** The specific conductivity as a function of temperature shows that $ZnFe_2O_4$ is a relative good semi-conductor all ready at room temperature. At temperature above 630 °C the slope of the graph decreases.

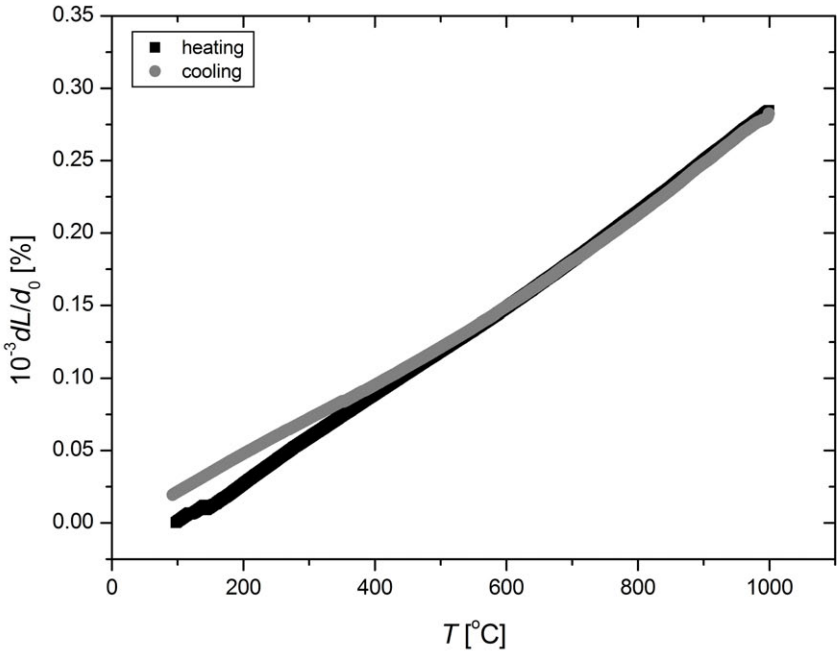

Figure 5.37: The linear thermal expansion measured in air from room temperature to 1000 °C.

The curve is slightly bended towards a larger relative expansion coefficient, α, at high temperatures ($\sim$ 550 °C) and with only a small hysteresis shown below 330 °C. α changes from $\alpha = 5.7 \cdot 10^{-7}$ °C^{-1} at 430 °C to $6.3 \cdot 10^{-7}$ °C^{-1} at 630 °C.

It cannot be ruled out completely that a small amount of ZnO evaporates at high temperatures, leaving some of the Fe^{3+} to be chemically reduced to Fe^{2+}. The effective ion radius of Fe^{3+} and Fe^{2+} in a T coordination are practically the same (0.63 Å) whereas the effective ion radius of Fe^{3+} (0.65 Å) and Fe^{2+} (0.78 Å) on an O site differs by 20 %. If any Fe^{2+} ions are found in the structure, they will mainly be located at O sites [168] and therefore they will certainly contribute to the expansion of the octahedrons. Measurements of the relative linear thermal expansion also show a slightly positive deviation at 550 °C but that seems to be related to the cation disorder and not the oxidation state of iron. Similar observations was observed by Brabers [169] on stoichometrically synthesized $ZnFe_2O_4$. However, he also observed that a small surplus of Fe^{2+} incorporated into the structure will make the relative thermal expansion decrease at $\sim$ 600 °C. Therefore it is assumed that the concentration of Fe^{2+} in our sample is small since the starting material was mixed stoichometrically and calcined at 900 °C where no substantial ZnO evaporation exist and because we do not see a negative deviation from the main trend of the relative thermal expansion.

Zn has closed atomic shells and will therefore not contribute directly to the conductiv-

ity. Only Fe can contribute to the conductivity. Anderson [170] pointed out that if the cation − anion − cation angle is 90° the domination interaction is a cation-cation interaction whereas if the angle is 180° or as low as 120° the cation − anion − cation exchange interaction is assumed to be the dominant one. The cation − anion − cation angle between T and O sites is ∼ 122° (Table 5.12) and therefore this interaction could have an influence on the conductivity whereas the cation − anion − cation angle on T sites (109.47°) is too low to cause a cation − anion − cation distinct interaction. It has been shown for $ZnFe_2O_4$ that Fe on a T site and its twelve nearest Fe ions on O sites form a cluster in which each of the Fe ions on the O sites interact through an oxygen ion with a Fe ion on a T site [171–173]. However, those experiments were preformed mainly at low temperatures. In the measured temperature range, the conductivity of $ZnFe_2O_4$ is mainly attributed to the Fe − O − Fe super-exchange interactions between octahedral sites, [126,127,168] where the transport property rises from hopping of localized *d*-electrons between cations on O sites. In an ideal spinel structure cations on O sites are distributed in such a way that we have a cation − anion − □ − anion − cation, with □ representing an empty site. Structural defects are therefore the main key in creating the cation − anion − cation interaction in $ZnFe_2O_4$. At 630 °C the conductivity decreases slightly and seems to be related to a direct cation − cation interaction between Fe atoms on O sites (maximum bond length ∼ 3 Å). The activation energy, 0.126(4) eV, is very similar to the one found by Hosseinpour *et al.* [174] in $ZnFe_2O_4$ containing 0.5 % Fe^{2+} on O sites. This, however, does not support the observations of the thermal expansion as discussed earlier in this section. Similar high temperature cation − cation interaction between O sites has also been reported in Cu- and Ga-doped $ZnFe_2O_4$ [126, 127, 168], although it was attributed the Cu − Cu interaction. However, these materials were only measured at a maximum temperature of 427 °C which is far below our transition temperature.

5.4.3 Electrochemical Properties on Cone-Electrodes

CV and EIS were recorded on cone-electrodes placed in a pseudo-three-electrode setup (see section 4.3.2). Data were recorded at 400 °C, 500 °C and 600 °C in 10 % O_2 in Ar or 1 % NO in Ar (Air Liquide) with a flow rate of 20 ml/min. Additional measurements were performed in 1 % NO_2 in Ar at 300 °C and 400 °C. An 1 hour equilibrium time was used to record the OCV before recording the voltammograms in the potentional range of -0.6 V to V 0.5 V (or 0.6 V) with a sweep rate of 1.0 and 10 mVs^{-1}. The voltammograms were converted into current densities by dividing with the contact area which was found by using equation 3.16. No corrections were made for the IR drop since calculations showed

that the corrections were less than 1 % at all temperatures.

Data recorded at 400 °C, 500 °C and 600 °C look very similar with insignificant cathodic activities in both NO and O_2. Figure 5.38b and 5.38a show the voltammograms recorded at 400 °C and 600 °C. The cathodic activities in NO_2 are significant higher compared to NO and O_2. Similar behaviour was found for most of the spinels analyzed in this thesis, however, current ratios (see Figure 5.39) are very high and only exceeded by the $NiCr_2O_4$-electrode. Comparing the anodic activities with the spinels described in earlier sections, recorded at similar conditions, shows that the anodic activities are much higher. An interesting phenomenon is observed in the anodic region. At 600 °C the highest activity is recorded in NO. This is the most common behaviour and results from the difference in concentration gradients between NO and O_2. At 500 °C the voltammograms (not shown) of NO and O_2 falls on top of each other, however, at 400 °C the graphs have 'interchanged' compared with the ones recorded at 600 °C. Now the activity in O_2 is higher than in NO. Speculations can be made on the origin of that but it seems that NO is inhibiting the formation of O_2 (and NO_2) by blocking the active sites. Alternatively is the activation energy of NO_2 formation simply higher than the activation energy of O_2 [138]. To our knowledge, no similar observations have been reported on electrode materials working in NO_x gases and O_2.

An analysis of the OCV were not made as most of the CV curves contain a wide region with the current close to zero. A small error in form of a vertical displacement would therefore have a large effect on the OCV. Tafel plots were also made (not shown here), however, they look very similar to the ones recorded in $NiFe_2O_4$, but with the 'bump' in the anodic region more distinct. The calculated number of transferred electrons is similar to the results of the $NiFe_2O_4$ and therefore no distinct conclusion can be made.

5.4.4 Symmetrical Cells

The activities recorded on the cone-electrode in NO_2 were very high and therefore a few symmetrical cell were fabricated similar to those described in section 5.1.5, but having a $ZnFe_2O_4$/CGO10 electrode instead of a $MgFe_2O_4$/CGO10 electrode. EIS was recorded on two cells at the same conditions as the $MgFe_2O_4$/CGO10 electrode. The Equivalent circuit used to fit the impedance data were also identical to the one used in section 5.1.5.

Figure 5.40 shows the Nyquist plot of the symmetrical cell recorded at 400 °C. The high frequency arc, A_1, coincide in all three cases regardless of the atmosphere. This arc is, as in the case of the $MgFe_2O_4$/CGO10 symmetrical cell, related to the YSZ-electrolyte and Table 5.8a and Table 5.8b list the calculated activation energies as well as the NEC. Some

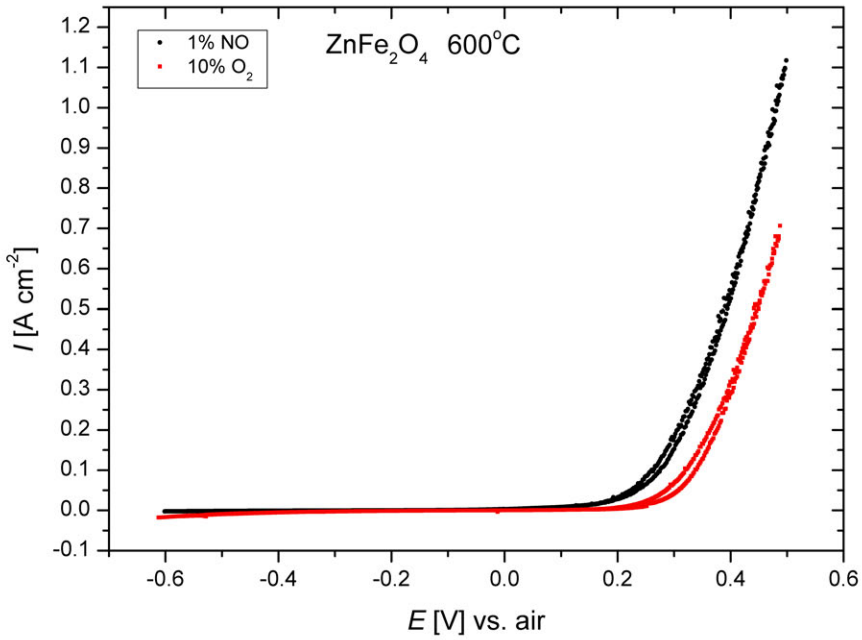

(a)

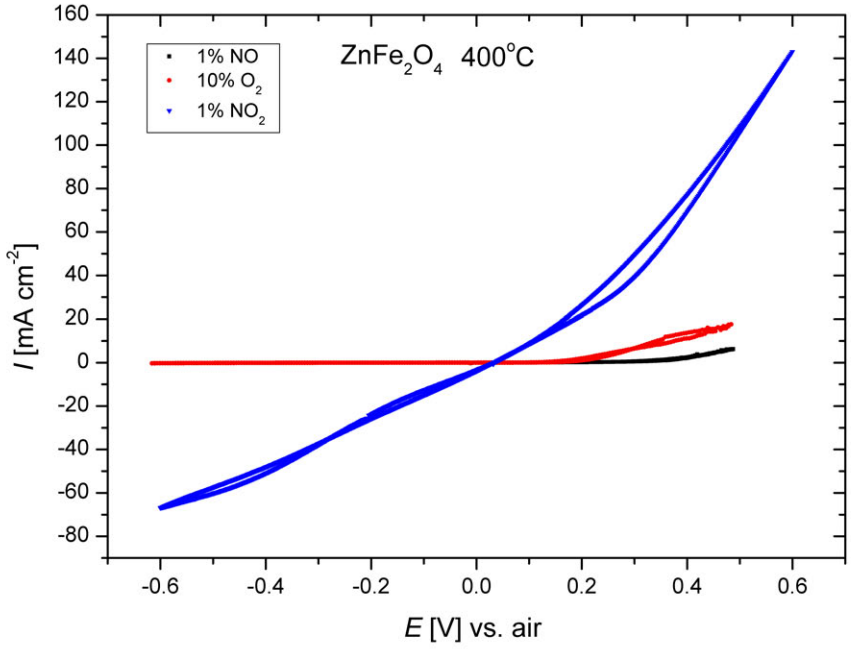

(b)

Figure 5.38: CV on $ZnFe_2O_4$ at 600 °C and 400 °C. The voltammograms were recorded with a scan rate of 1 mVs^{-1}. The anodic activity is relative high in the measured temperature range.

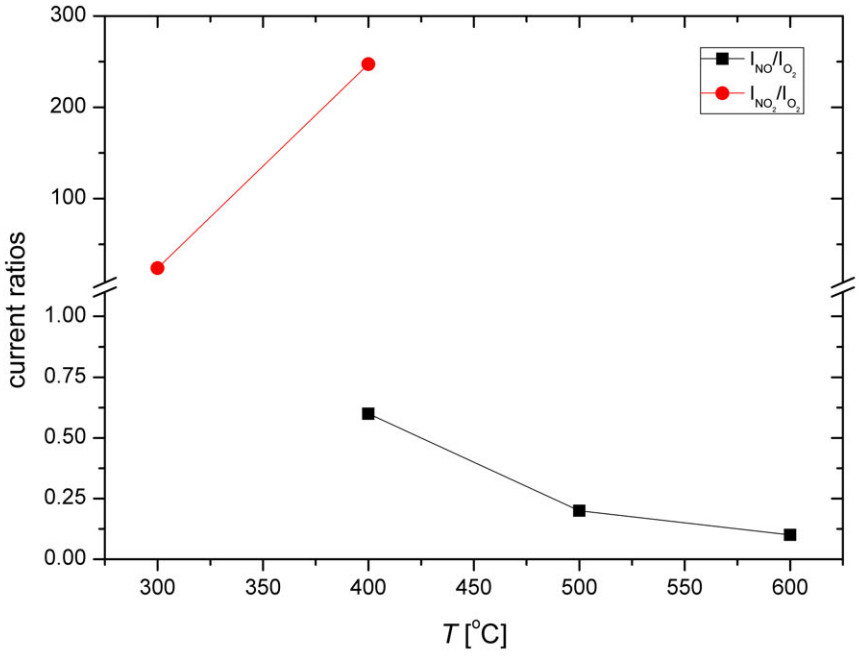

Figure 5.39: Current ratios at -0.6 V in $ZnFe_2O_4$ as function of temperature.

of the spectra recorded at 300 °C and 350 °C were not possible to fit properly and therefore some of the capacitances and resistances are missing. Activation energies are very similar to the ones found for the $MgFe_2O_4$/CGO10 electrode (see Table 5.3) for A_1, however, E_a of arcs at lower frequencies, (A_2 and A_3), are generally 10 % lower than the one found for the $MgFe_2O_4$/CGO10 electrode. Unfortunately it was not possible to make a proper fit to the spectra recorded in NO_2 at 350 °C and 300 °C. Therefore, no activation energies were calculated in NO_2. The uncertainties on the NEC of the first arc are very high and around 1.5 times higher than the ones recorded on the $MgFe_2O_4$/CGO10 electrode and about 4 times larger than the theoretical value calculated in section 5.1.5. As in the case of the $MgFe_2O_4$/CGO10 electrode there is no obvious explanation of the relative high values other than the fitting procedure (or model) failed to separate the contributions from the different arcs in a proper way. It is, however, important to notice that the NEC values are fairly constant which suggests a systematic error which might be related to the choice of model. On the other hand, the model was the only one that clearly gave a good fit. Adding a number of more *RQ*-circuits to the model would have made the fit even better of obvious reasons, however, as it was not possible to relate all the different parts of the spectra to a physical process, the most simple model should be chosen. The total impedance showed that $Z_{NO_2} < Z_{NO} < Z_{air}$ which is similar to the results of the cone-electrode (even though the cone-electrodes were measured in 10 % O_2 and not air).

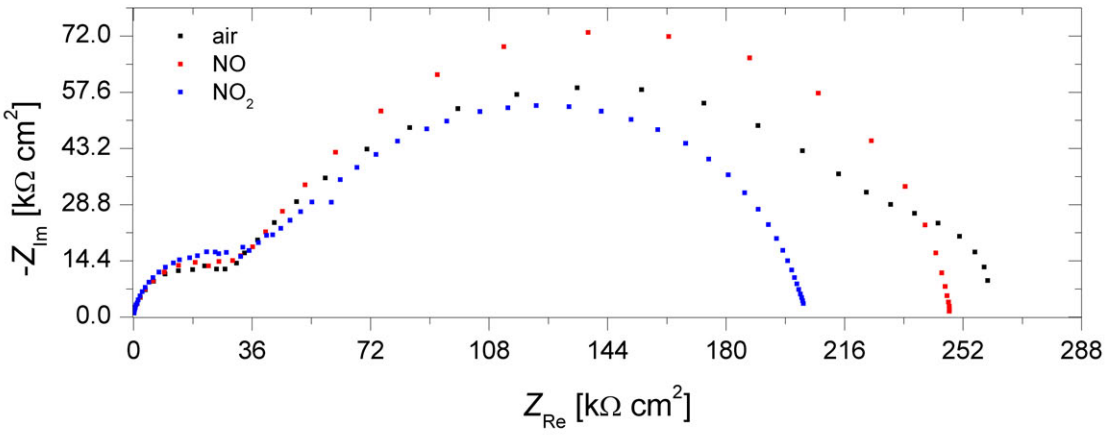

Figure 5.40: Nyquist plot of the $ZnFe_2O_4$/CGO10 electrode, recorded at 400 °C in air with different amplitudes.

The qualitative order of the total impedance basically reflects that the presence of CGO10 does not change the general trends of the system found on cone-electrodes. Results also show that the resistivity of the cell is very high which may be a challenge with respect to gas conversion and current efficiencies on larger cells.

Table 5.8: (**a**) Activation energies of the symmetrical cells. (**b**) Mean values of the NEC of the first semi-circle on the $ZnFe_2O_4$/CGO10-electrode. Uncertainties are given in parentheses.

(a)

-	NO [eV]	NO_2 [eV]	air [eV]
A_1	1.04(1)	-	1.05(4)
A_2	0.94(8)	-	0.96(9)
A_3	0.91(7)	-	0.97(6)

(b)

temp	NO [pF]	NO_2 [pF]	air [pF]
500 °C	280(50)	-	300(20)
400 °C	280(30)	280(50)	300(80)
350 °C	-	-	-
300 °C	310(20)	-	270(30)

5.4.5 Gas Conversion over 3E Pellets

Measurements were performed over a 3E pellet (see section 4.2.4) having an YSZ electrolyte. Data were recorded at 600 °C, 500 °C, 400 °C and 350 °C in 1000 ppm NO, 1000 ppm NO + 10 % O_2 and 10 % O_2. CV was recorded in the potential range from -0.6 V to 0.6 V. EIS was recorded at OCV. The pellet was polarized at ±0.6 V for ∼ 3 hours and NO_x gases were analyzed with a Thermo Scientific Chemiluminescence analyzer (Model 42i). A flow rate of 10 ml/min was applied, however, as the chemiluminescence required a minimum flow of 25 ml/min, the gas from the setup was diluted with air just before

entering the chemiluminescence analyzer. The gas composition was analyzed before and after reaching the sample without polarizing the cell (OCV gas conversion). A square-wave potential was also applied over the cell, however, no gas conversion was detected with this technique. No mass spectrometer was available during these measurement and minor leaks were therefore difficult to detect. However, the 3E pellet was sealed similarly to the one described in section 5.1.6. A blank pellet[3] was used as a reference regarding the gas conversion (see section 5.1.6).

Figure 5.41 shows the CV recorded at 600 °C and 400 °C. Results show that the activities in O_2 and NO are very similar in the entire potential range. The cathodic activities recorded in NO + O_2 are a bit higher but not distinct. Comparing the voltammograms recorded on the 3E pellets with the ones recorded on cone-electrodes are not straight forward as the electrode material and NO concentrations were not identical in the two cases. However, both cells were recorded in 10 % O_2 and the difference in current densities are very distinct. At 600 °C the current density at -0.6 V changed from approximate -16.8 mA/cm^2 (cone-electrodes) to -1.03 mA/cm^2 (3E pellets) which correspond to a 95 % drop in activity. Same pattern is also observed at the other temperatures (90 % activity drop at 400 °C). The cathodic activity in NO is more difficult to compare as the NO concentration over the cone-electrodes were 10 times higher than in the case of the 3E pellet. The cathodic activity (-0.6 V, 600 °C) decreases from -2.5 mA/cm^2 (cone-electrode) to approximate -0.4 mA/cm^2 (3E pellet), which correspond to a lowering of the activity in NO by a factor of $\sim$ 6 (83 %). Similar results were found at 400 °C with a drop in activity of 84 %. However, keeping in mind that the NO concentration of the working gas over the 3E pellet was 10 times lower than in the case of the cone-electrode, the results are actually quite uplifting with respect to the selectivity towards NO reduction, as the relative decrease in activities is much higher in O_2 than in NO.

Gas conversion was measured in the NO + O_2 mixture and the results are shown on Figure 5.42. Figure 5.42c shows the total NO_x concentration recorded on the spinel electrode increases as the temperature is lowered. This was also observed in the case of the blank 3E pellet (see section 5.1.6 for a more detailed analysis of the blank 3E pellet).

When the cell is polarized cathodically the NO concentration increases but at the same time the NO_2 concentration decreases equally. The total NO_x concentration does not change during the polarization. The same picture was observed when the cell was polarized anodically, however, now with an increase of the NO_2 content, balanced out by an equal decrease in NO concentrations. Again no changes of the total NO_x concentration was observed. The overall reaction over the electrode is therefore similar to equation 5.9

[3] Au on an YSZ electrolyte.

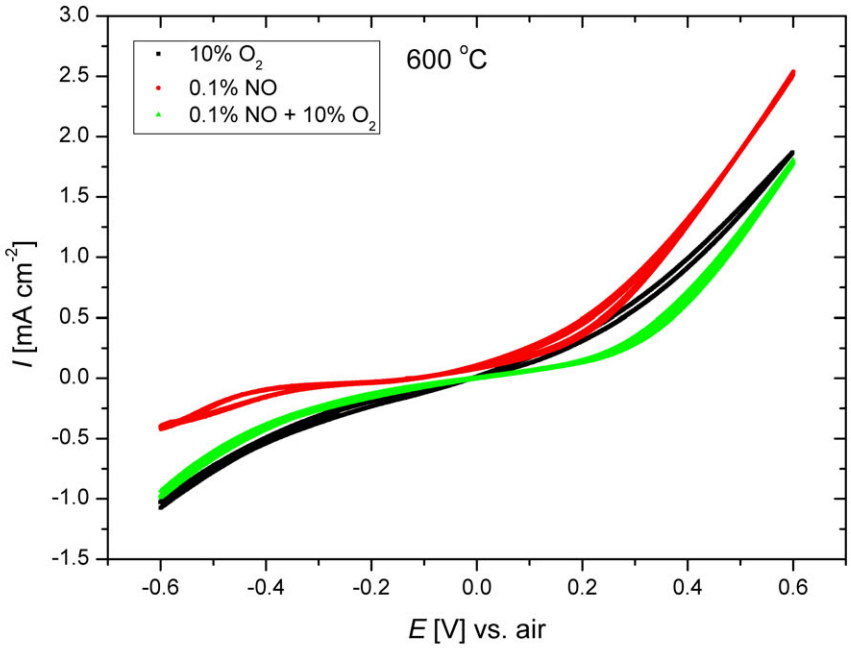

(a)

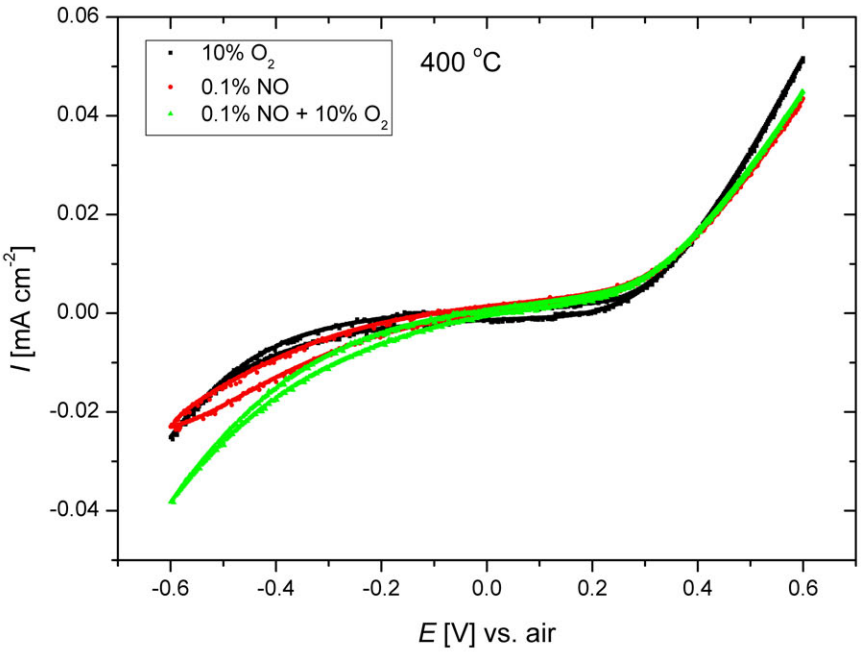

(b)

Figure 5.41: CV on $ZnFe_2O_4$/CGO10 3E pellet at 600 °C and 400 °C. The voltammograms were recorded with a scan rate of 1 mVs^{-1}. The anodic activity is relative high in the measured temperature range.

where NO is converted to NO_2 and visa versa, as also observed in section 5.1.6. Table 5.9 shows the recorded gas conversions as well as the current efficiencies, η. The latter was calculated using equation 5.10 and 5.11. No gas conversion is detected at 350 °C (Ba-free electrode) as well as at 400 °C when it was polarized anodically. The maximum gas conversion is found at 500 °C where also η has the highest values. Even though the gas conversion is very small, η, calculated from cathodic polarization, are generally high. This might indicate that a limited amount of O_2 is reduced during polarization and most of the Faradaic current is used to reduce NO_2. To our knowledge no electrochemical reduction of NO_2 to NO with similar high η have been reported.

There appears to be a catalytic activity over the cell at OCV. At 600 °C the total NO_x concentration is identical to the NO_x concentration recorded over the blank 3E pellet. However, it covers the fact that the total NO concentration is about 20 ppm higher whereas the total NO_2 concentration is about 20 ppm lower than the plank 3E pellet. At lower temperatures an overall decrease in the NO_x relative to the blank 3E pellet is detected. At the same time the NO concentration drops and follows the graph of the blank 3E pellet (see Figure 5.42a). The total NO_2 stays constant on the other hand below the NO_2 level recorded on the blank pellet. Since N_2O is not thermally stable at temperature above $\sim$ 500 °C [175] the following mechanisms are proposed: At 600 °C N_2O or N_2 is formed over the $ZnFe_2O_4$/CGO10 pellet. At lower temperatures the NO concentration drops to a level very close to what is recorded over the blank pellet, whereas the recorded NO_2 level is lower than the blank pellet. This indicates that the NO_2 is converted into N_2O over the pellet. Alternatively is NO converted into N_2 or N_2O and at the same time NO_2 is converted into NO. As no mass spectrometer was available during the measurements it is in principle not possible to determine which of the to catalytic routes are correct. Table 5.9 shows the catalytic gas conversions at the different temperatures.

Due to the relative high electronic conductivity as well as the ability of the electrode to reduce NO_2, $ZnFe_2O_4$/CGO10 was tried mixed with BaO in order to investigate weather the compounds could be used as electrode material in an electrochemical storage catalyst as described in section 1.2.4. First, a few grams of $ZnFe_2O_4$-powder were mixed with an aqueous solution of $Ba(NO_3)_2$ and calcined at 600 °C. XRD showed that no chemical reaction between the spinel and the Ba-compound had occurred and the two phases of BaO and $ZnFe_2O_4$ were easily detected in the diffractograms. A 3E pellet (YSZ-electrolyte) with a $ZnFe_2O_4$/CGO electrode on top was therefore infiltrated with a few drops of the aqueous solution of $Ba(NO_3)_2$ (corresponding to $\sim$ 6 w% BaO assuming no other Ba-compounds were present such as $BaCO_3$) and evacuated in order to distribute the Ba-compounds in the electrode. The pellet was applied with an Au current collector

5.4. $ZnFe_2O_4$

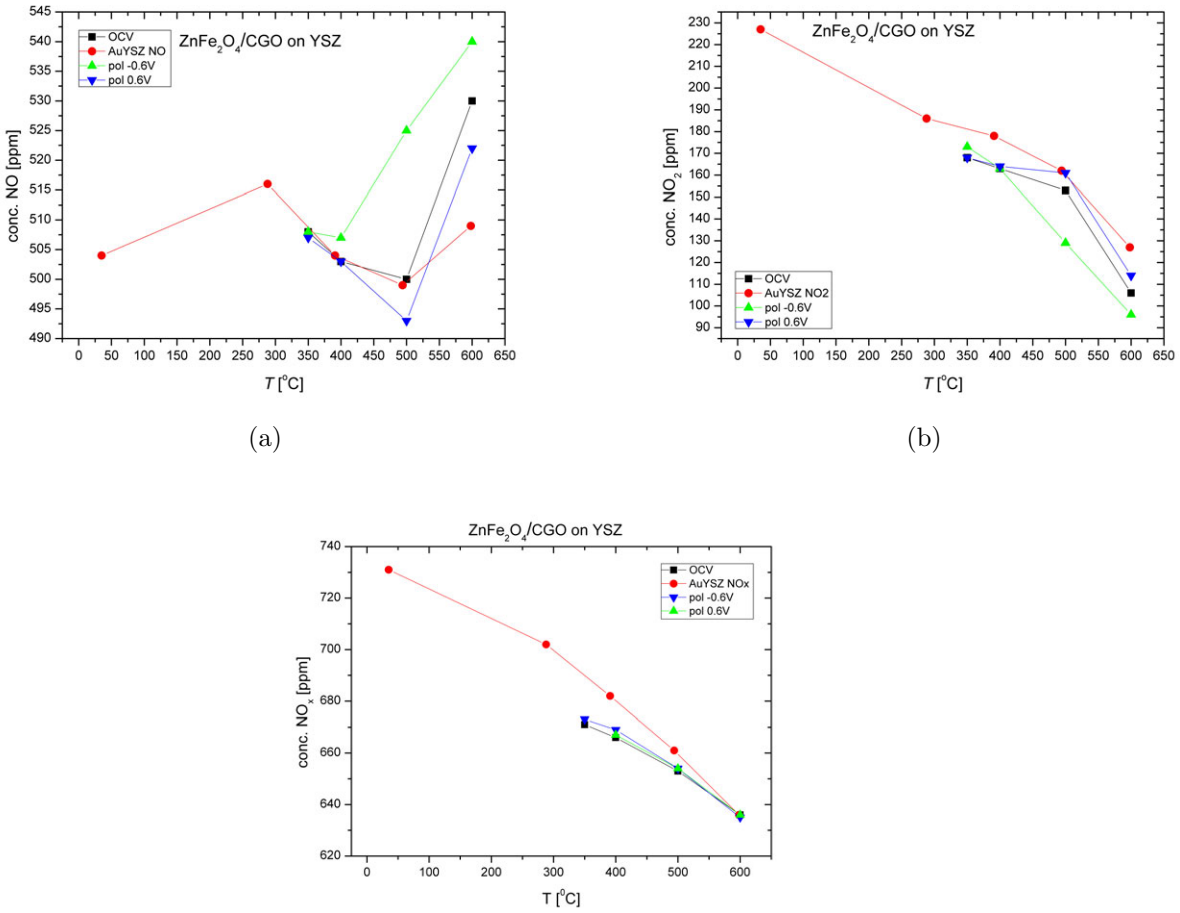

Figure 5.42: Gas conversion over the $ZnFe_2O_4$/CGO10 3E pellet. The graphs show the changes in concentrations of **a**) NO, (**b**) NO_2 and (**c**) NO_x during polarizations. The plank pellet (AuYSZ) is shown as reference.

Table 5.9: Gas conversion, GC, current efficiencies, η, and catalytic gas conversion (CGC) recorded over the $ZnFe_2O_4$/CGO10 3E pellet. A, -, represent zero gas conversion and the temperature marked with, *, referrers to the recorded data on the Ba-doped 3E pellet. Estimated uncertainties are given in parentheses.

	GC		η		
temp	-0.6 V	0.6 V	-0.6 V	0.6 V	CGC
600 °C	1.9(4) %	1.5(4) %	5(1) %	1.1(4) %	-
500 °C	5.0(4) %	1.4(4) %	39(4) %	9(3) %	1.1(3) %
400 °C	0.8(4) %	-	30(20) %	-	2.3(2) %
350 °C	-	-	-	-	2.9(3) %
*350 °C	-	2.7(4) %	-	32(7) %	-

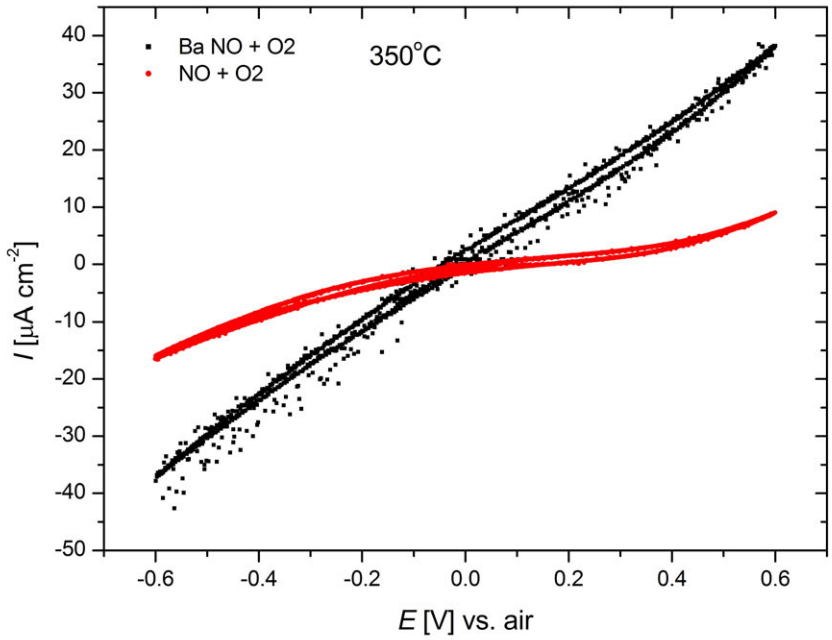

Figure 5.43: CV on the two $ZnFe_2O_4$ 3E pellets at 350°C. Data were recorded in 1000 ppm NO + 10 % O_2 with a scan rate of 1 mVs^{-1}. The noisy appearance of the Ba-doped $ZnFe_2O_4$/CGO10 3E pellet arises from remains of unburned carbon from the current collector.

like the other 3E pellets and then heated to 600 °C for 2 hours. The pellet was mounted in the setup using high temperature Cu-silicone (Mega Copper, VersaChem®) as sealing material. The new sealing material was used since we wanted to stay below 400 °C in order to avoid any possible reactions between the Ba-compound and the electrode material at 1000 °C which was the sealing temperature used otherwise (see section 4.3.2). Data were only recorded at 350 °C (the maximum temperature of the Cu-silicone). CV was recorded in 1000 ppm NO + 10 % O_2 with a scan rate of 1 mVs^{-1} (see Figure 5.43). Unfortunately there appeared a significant amount of electronic noise on the voltammogram, which later was recognized as being a result of unburned carbon from the current collector, which was not removed completely during the heating process. The activity over the Ba-doped 3E pellet is higher than in the case of the pure $ZnFe_2O_4$/CGO10 3E pellet, however, it is not possible to decide weather the carbon affected the activity in a positive direction or the BaO alone causes an increase in the activity. Beside that, the electrolytes were also different. We would therefore also expect the Ba-doped $ZnFe_2O_4$/CGO10 3E CGO10-pellet to have a higher activity than the one with the YSZ electrolyte.

The gas conversion was measured similarly to the other pellets using a square-wave potential or applying a constant potential. The latter did not have any measurable effect

on the conversion of the gas and only with the square-wave potential technique (switching between OCV and 0.6 V every 1 second) a small gas conversion (0.8(4) %) was measured when polarizing anodically (see Table 5.9). Again, the gas conversion is attributed to the conversion of NO to NO_2, but, η is relative high although the uncertainty is high. More experiments should be made on optimizing the BaO content as well as the square-wave potential in order to clarify whether the electrode material could be used in a future electrochemical storage catalyst.

5.4.6 Cation Distribution as Function Temperature

In order to understand the conductivity measurements, *in situ* high temperature neutron diffraction was performed on the $ZnFe_2O_4$-powder with the purpose to determine the cation distribution as function of temperature. Measurements were performed with a high-resolution powder neutron diffractometer at the Institute for Energy Technology in Kjeller, Norway as described in section 4.3.1.

Figure 5.44 shows the neutron diffraction patters of the spinel measured from room

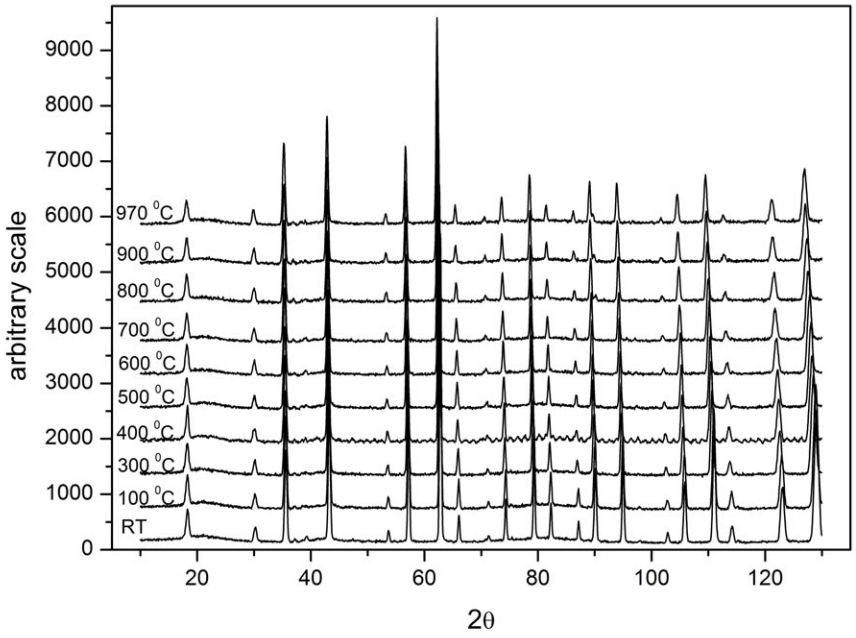

Figure 5.44: HTND profiles of $ZnFe_2O_4$ at measured temperatures.

temperature (RT) to 970 °C. 21 - 22 peaks were used in the refinement depending on the temperature. Rietveld refinements were carried out using the program Jana2000 [176].

The neutron scattering lengths and the X-ray form factors were taken from the Jana2000 library. Pseudo-Voigt profile functions were used, and the background was modelled with a 10 terms Legendre polynomials. All diffraction patterns were refined with the space group $Fd\bar{3}m$ (no. 227, origin choice 1) [177] but diffraction patterns measured at temperatures above 600 °C were also refined with the space group $I4_1/amd$ (no. 141), which is reported for different spinel-type materials [178]. Refinements, however, gave no satisfying results. Site occupancies of Zn and Fe were coupled not only between elements on the same lattice site but also between the T sites and the O sites. Cations on same lattice sites where assigned the same isotropic displacement parameter, U_{iso}. No impurity phases were detected as also found by XRD. Table 5.10 shows an example of the refined structural parameters for $ZnFe_2O_4$ at 600 °C and Fig. 5.45 shows the corresponding fitted neutron diffraction pattern. Refined parameters at different temperatures are shown in Table 5.11.

Figure 5.46 shows the increase of the unit cell as a function of temperature. From

Table 5.10: Refined structural parameters of $ZnFe_2O_4$ at 600 °C. Occupancies are given by the multiplicity of the site symmetry divided by the multiplicity of general sites.

atom	site	occupancy	x	y	z	U_{iso} [Å^2]
Zn1	8a	0.0357(2)	0	0	0	0.0354(6)
Fe1	8a	0.0059(2)	0	0	0	0.0354(6)
Zn2	16d	0.0119(4)	0.625	0.625	0.625	0.0204(4)
Fe2	16d	0.0715(2)	0.625	0.625	0.625	0.0204(4)
O	32e	0.16667	0.3851(2)	0.3851(2)	0.3851(2)	0.0300(6)

RT to 600 °C, **a** increases linear with a rate of $7.3(4) \cdot 10^{-5}$ Å °C^{-1}. At 600 °C the rate increases to $1.01(3) \cdot 10^{-4}$ Å °C^{-1} which is 38 % faster than in the low temperature range.

Refinements show that the tetrahedrons are undistorted (not shown in Table 5.12) within experimental errors and the change of bond distances does not seem to follow a trend through the measured temperature range. The octahedrons are on the other hand slightly distorted with increasing bond distances as a function of temperature. However, the bond distances on the O sites do not follow a linear trend in the whole temperature range. A sudden increase is observed at 600 °C as can be seen in Figure 5.47a. The bond length at 100 °C and 400 °C is slightly higher than would be expected. Same phenomenon can also be detected in the increment of the volume (Figure 5.47b).

Figure 5.48a and 5.48b show the occupancy of Zn and Fe on the T sites and the O sites as a function of temperature. In the temperature range from RT to 400 °C the site occupancies are unchanged with 91% ($\gamma = 0.09$) of the Zn at the tetrahedral lattice site. At 500 °C there is a sudden change in occupancies towards a higher cation order-

5.4. $ZnFe_2O_4$

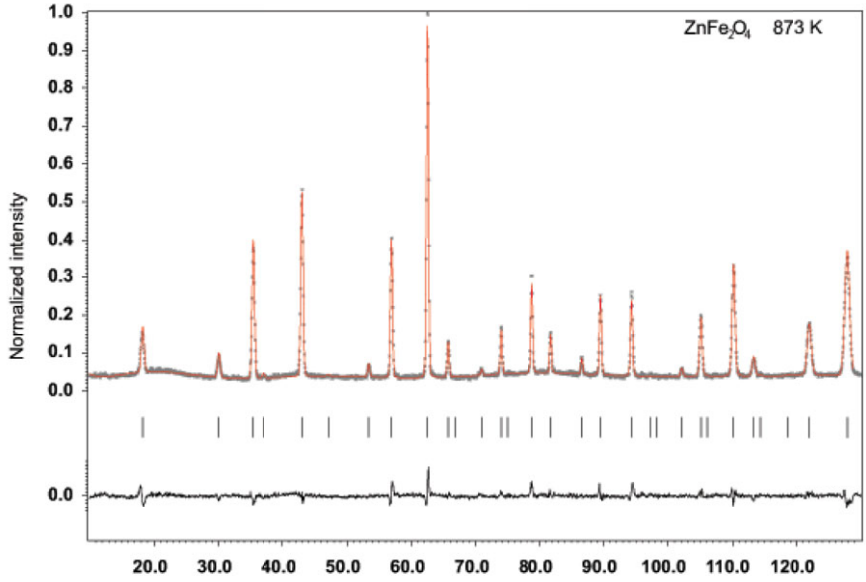

Figure 5.45: Observed (gray) and calculated (red) intensities from Rietveld refinements of $ZnFe_2O_4$ at 600 °C. The difference curve and the position of the Bragg reflections are shown in the lower part of the diffractogram.

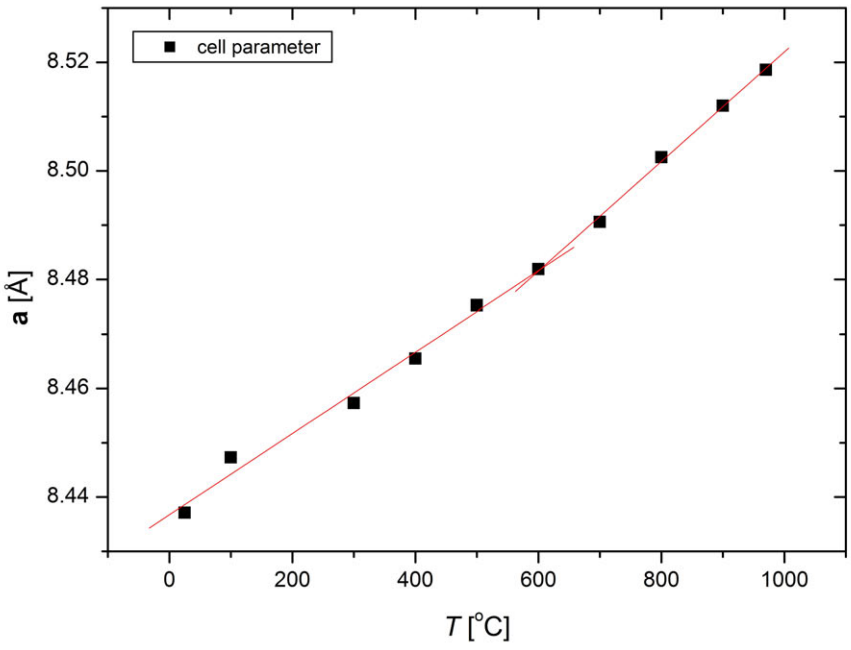

Figure 5.46: Two clear linear trend can be detected. The rate of which the unit cell expands accelerates at ∼600 °C. Error bars on the unit cell is shown by the radius of the points.

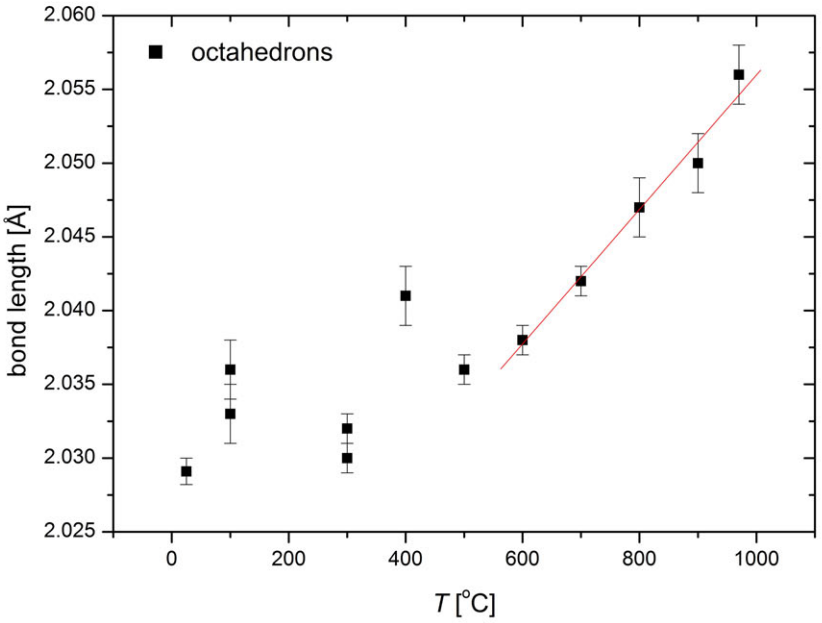

(a)

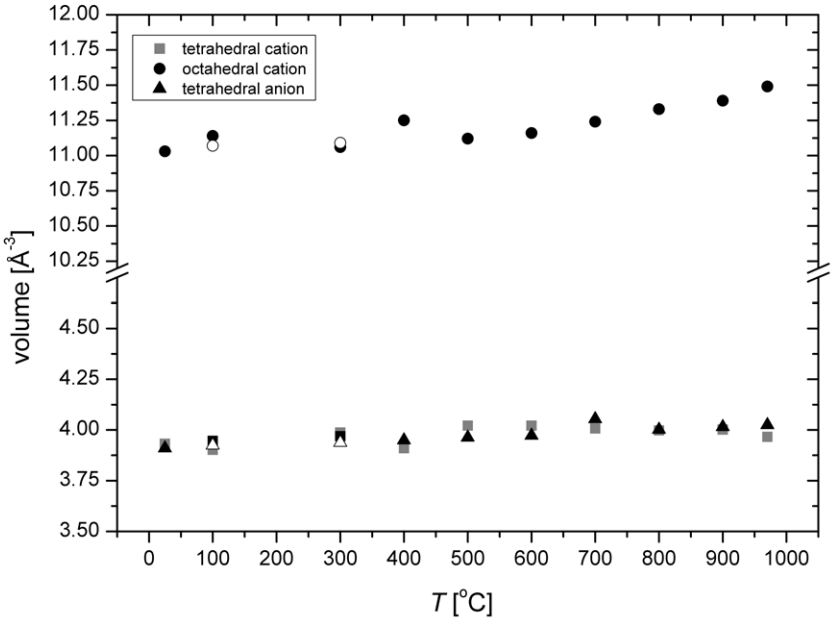

(b)

Figure 5.47: **(a)** Bond length of the octahedrons as function of temperature measured with HTND. **(b)** The volume of the polyhedrals as function of temperature. △ and ○ represent the measurements made during the cooling stage. Error bars on the unit cell parameter and the volumes are shown by the radius of the points.

5.4. $ZnFe_2O_4$

Table 5.11: R-values, 'goodness of fit', gof, unit cell parameters, **a**, the position of oxygen, O_x, and isotropic displacement parameters, U_{iso} (Å^2), from the Rietveld refinements of the HTND patterns. Values in square brackets referees to the coordination number of the cations. Temperatures marked with, *, referrers to the diffraction patterns measured during cool down. No correlation coefficients where lager than $\rho_{ij} = 0.72$. Estimated standard deviations in parentheses.

temp.	R_p	wR_p	gof	**a** (Å)	O_x	U_{iso}, [4]	U_{iso}, [6]	U_{iso}, O_x
25 °C	6.02	7.63	1.50	8.4371(4)	0.3849(1)	0.0164(7)	0.0124(4)	0.0175(5)
100 °C	6.88	9.08	1.94	8.4473(6)	0.3844(2)	0.0163(7)	0.0139(8)	0.0196(9)
300 °C	7.00	9.17	1.88	8.4573(6)	0.3852(1)	0.025(3)	0.0185(6)	0.0234(8)
400 °C	7.05	9.18	1.96	8.4655(6)	0.3842(2)	0.026(1)	0.0231(6)	0.0303(9)
500 °C	6.96	9.11	1.47	8.4753(3)	0.3853(2)	0.029(2)	0.0214(5)	0.0291(7)
600 °C	6.01	7.66	1.25	8.4819(4)	0.3852(1)	0.0354(9)	0.0204(4)	0.0300(7)
700 °C	5.89	7.38	1.20	8.4906(4)	0.3849(1)	0.0370(9)	0.0225(4)	0.0322(7)
800 °C	6.25	7.97	1.31	8.5025(4)	0.3846(2)	0.0394(9)	0.0251(5)	0.0345(7)
900 °C	6.02	7.70	1.25	8.5120(4)	0.3845(2)	0.0401(9)	0.0267(5)	0.0378(8)
970 °C	5.98	7.70	1.40	8.5186(4)	0.3840(2)	0.0414(9)	0.0272(5)	0.0415(8)
*100 °C	6.52	8.27	1.34	8.4473(4)	0.3849(1)	0.0197(7)	0.0138(4)	0.0198(6)
*300 °C	6.46	8.20	1.34	8.4573(4)	0.3850(2)	0.028(8)	0.0170(4)	0.0265(6)

ing ($\gamma = 0.03$), but from 500 °C − 970 °C the site occupancies changes almost linearly and at 970 °C only 77 % ($\gamma = 0.23$) of the Zn are still located at the tetrahedral site. After cooling down the sample a new diffraction pattern was recorded at 300 °C and 100 °C. Results show that the site occupancies are almost identical to those found while heating up the sample. The sudden change in occupancies at 500 °C was tried refined by constraining the occupancies so they followed the main trend of the graph, however, it was not possible to obtain reasonable isotropic displacement parameters of any of the atoms and R-values and goodness of fit did not improved significantly. A few correlation coefficients also increased, $\rho_{ij} > 0.8$.

The increase in unit cell parameters (Figure 5.46) consists of two linear trends. The first trend from room temperature to ∼ 600 °C is related to a simple thermal expansion due to the increase of lattice vibrations. However, the sudden increase of the unit cell parameter at ∼ 600 °C seems to be related to the increasing disorder of the cations. When the Zn ions jump from a T lattice sites to a O site, the volume of the octahedron will increase due to larger effective ion radius of Zn^{2+} ([4]: 0.60 Å, [6]: 0.74 Å) compared to Fe^{3+} ([4]: 0.63 Å, [6]: 0.65 Å) [109]. This also explains why the increase of the bond length at the O site coincides with the increase of the unit cell parameter. The T site does not seem to follow the same trend as the octahedrons, which can also be explained by the similarity of the ion radii of Zn^{2+} and Fe^{3+}. The octahedrons become less distorted at high temperatures, since the thermal energy makes the lattice expand. Refinements also indicated a decrease in atomic displacements of the oxygen position but the uncertainties are too high to give a clear image.

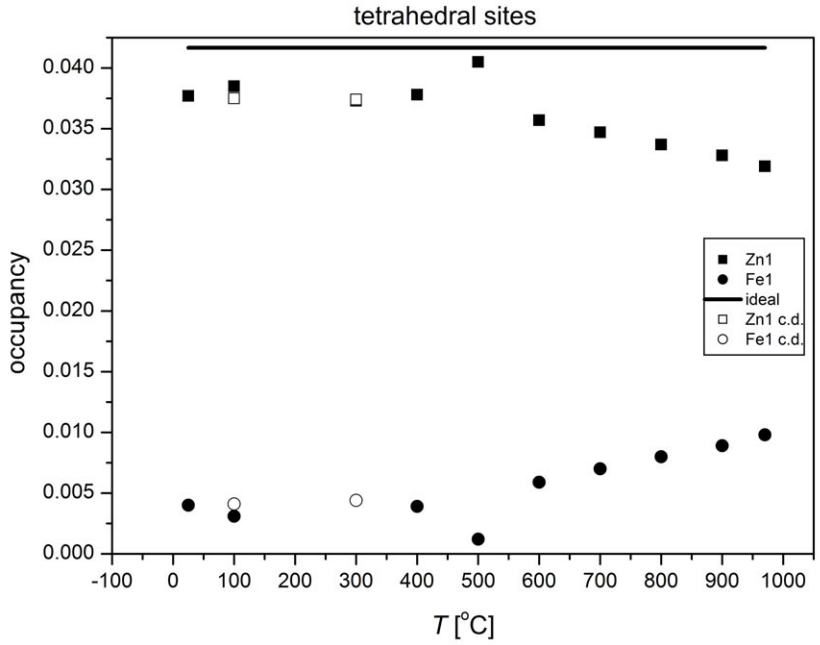

(a)

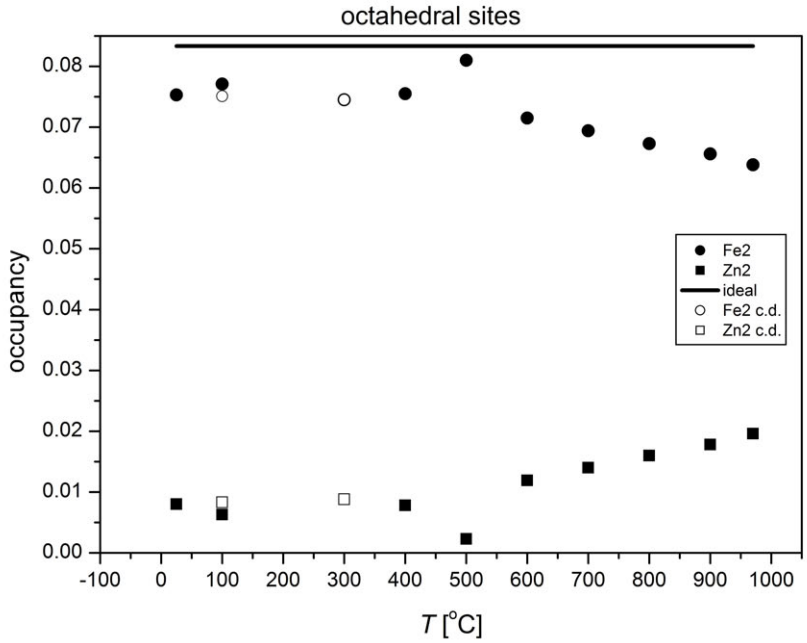

(b)

Figure 5.48: Occupancies on **(a)** the tetrahedral and **(b)** the octahedral site in $ZnFe_2O_4$ as a function of temperature. ■ and ● represents Zn and Fe respectively. □ and ○ represent the measurements made during the cooling stage. The upper horizontal line shows the ideal occupancy. Error bars are shown by the radius of the points.

Refinements of the occupancies show that the cations start to jump between lattice sites at 500 °C. The sudden increase of ordering observed at 500 °C reflects both the kinetics and the thermodynamics of the system [118]. At low temperatures the sample is not in equilibrium and the kinetics control the cation order-disorder. At high temperatures the spinel is in equilibrium with respect to the cation order-disorder, reflecting the thermodynamic drive towards high temperature disorder. The increase in order at 500 °C results from the starting value being lower than equilibrium and as soon as the temperature is high enough, the occupancies begin to converge towards the order-disorder equilibrium. The cations starts to jump between lattice sites at a lower temperature compared to the sudden increase in octahedrals. This shows that the crystal structure (and with the help of the thermal lattice vibrations) can incorporate a certain amount of cation disorder without a distinct change of the unit cell volume. The refinements of the HTND patterns also show that the cations switches back into there original lattice position when the sample is cooled down. However, the unsymmetrical behaviour of the resistivity on Figure 5.36a indicates that the occupancies are not completely identical to the ones before heating the specimen. Otherwise the specific conductivity would be the same before and after heating the sample. The difference between the occupancies and the resistivity measurements is, however, most likely due to the fact that the samples used for the different measurements were exposed to different kind of temperature profiles during the 'cool down'.

Table 5.12: Bond lengths and bond angles from the Rietveld refinement of the HTND patterns. [4] and [6] represent the cation − oxygen bond length of cations located on tetrahedral or octahedral coordinated lattice sites. ∠[4] and ∠[6] represent the oxygen − cation − oxygen bond angles whereas ∠[4][6] represent the cation − oxygen − cation bond angles between two different coordinated cations. Bond angles show that the octahedrons are slightly disturbed whereas the tetrahedrons are undisturbed within experimental errors. Temperatures marked with, *, referrers to the diffraction patterns measured during cool down. Estimated standard deviations in parentheses.

temp.	[4][Å]	[6][Å]	$\angle[6]_1$	$\angle[6]_2$	∠[6][4]
25 °C	1.972(1)	2.027(3)	94.82(4)°	85.18(4)°	121.92(4)°
100 °C	1.966(2)	2.036(2)	94.54(6)°	85.46(6)°	121.11(7)°
300 °C	1.982(1)	2.032(1)	94.99(4)°	85.01(4)°	121.80(6)°
400 °C	1.968(2)	2.041(2)	94.48(7)°	85.52(7)°	122.16(9)°
500 °C	1.986(2)	2.036(1)	95.00(4)°	85.00(4)°	121.80(7)°
600 °C	1.986(1)	2.038(1)	94.95(5)°	85.05(5)°	121.84(6)°
700 °C	1.984(2)	2.042(2)	94.81(3)°	85.19(3)°	121.93(4)°
800 °C	1.982(2)	2.047(2)	94.66(7)°	85.34(7)°	122.03(8)°
900 °C	1.983(2)	2.050(2)	94.61(7)°	85.39(7)°	122.07(8)°
970 °C	1.977(2)	2.056(2)	94.35(7)°	85.65(7)°	122.24(8)°
*100 °C	1.972(1)	2.030(1)	94.82(4)°	85.18(4)°	121.92(5)°
*300 °C	1.978(2)	2.033(3)	94.87(6)°	85.13(6)°	121.81(6)°

5.5 Cobalt and Manganate Spinels

This section contains the results and discussions of the experiments made on $MnCo_2O_4$ and $NiMn_2O_4$. Experiments were preformed on cone-electrodes in different gases and temperatures. Dilatometry measurements and results of conductivity measurements are also discussed, however, they were only carried out on $NiMn_2O_4$. At the end of this section results on Ba-doped $NiMn_2O_4$ are discussed.

5.5.1 $MnCo_2O_4$

$MnCo_2O_4$ has an inverse spinel structure with Mn situated on O sites and Co positioned on both O sites and T sites [179]. The material has been shown some interest regarding interconnect applications in SOFC [180] as well as a possible optoelectrochemical hydrogen-phosphate ion sensor [181]. To our knowledge no results have been published on electrochemical reduction of NO over a $MnCo_2O_4$-electrode.

CV and EIS were recorded at 300 °C, 400 °C and 500 °C in 1 % NO, 1 % NO_2, 1 % N_2O, 0.5 % NO + 10 % O_2 and 10 % O_2. The cone-electrodes were also recorded in 1 % NO_2 at 300 °C and 400 °C. The potential range was set from 0.6 V to -0.6 V like in the case of the other cone-electrodes discussed in previous sections. At 500 °C, results show a very poor cathodic activity and only the activity in NO + O_2 seemed a bit higher. This is supposedly due to small amount of NO_2 forming. The anodic activities are much higher, however, there is not much difference between the different gases. At 400 °C (see Figure 5.49b), the cathodic activities in NO_2 and NO + O_2 are higher than the activities recorded in the other atmospheres. Again the anodic activity in NO is small compared to the other gases. Activities in O_2 and N_2O are very small. The level of electronic noise is quite significantly at 300 °C (see Figure 5.49a), however, the cathodic activities in NO_2, NO + O_2 and to some extend NO are higher than in O_2 and N_2O which seem much unaffected by a decrease in temperature. Anodic activities look similar but again the activity in NO is small compared to the other gases.

As discussed in section 4.2.1, current ratios can be used to quantify the apparent selectivity. Figure 5.50 shows the current densities and current ratios on the point-electrode recorded at -0.6 V. Current densities decreases rapidly with temperature but are comparable to the spinels of the $Ni_{1-x}Mg_xFe_2O_4$ series. Current ratios of NO with respect to O_2 are almost constant in the measured temperature region and ranges from $2-5$. This is similar to what has been reported on most of the members of the $Ni_{1-x}Mg_xFe_2O_4$ series (see section 5.1.4), the $NiCr_xFe_{2-x}O_4$ series (see section 5.2.4) as well as the $MgMn_xFe_{2-x}O_4$

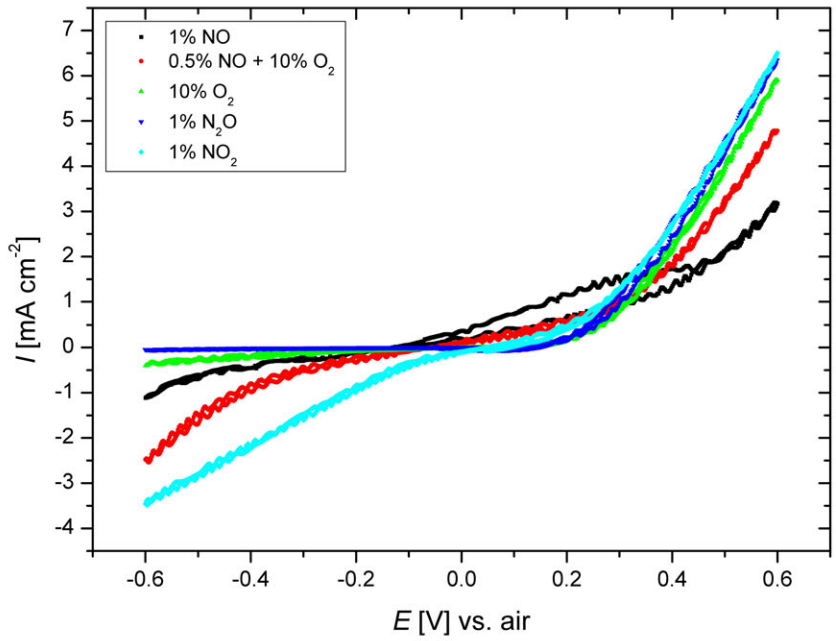

(a)

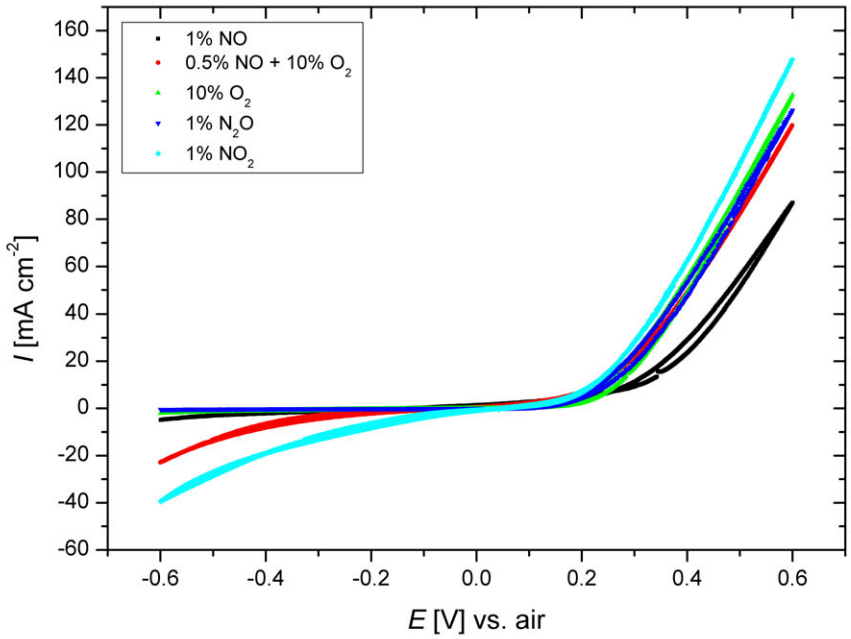

(b)

Figure 5.49: CV on $MnCo_2O_4$ recorded at 300 °C and 400 °C.

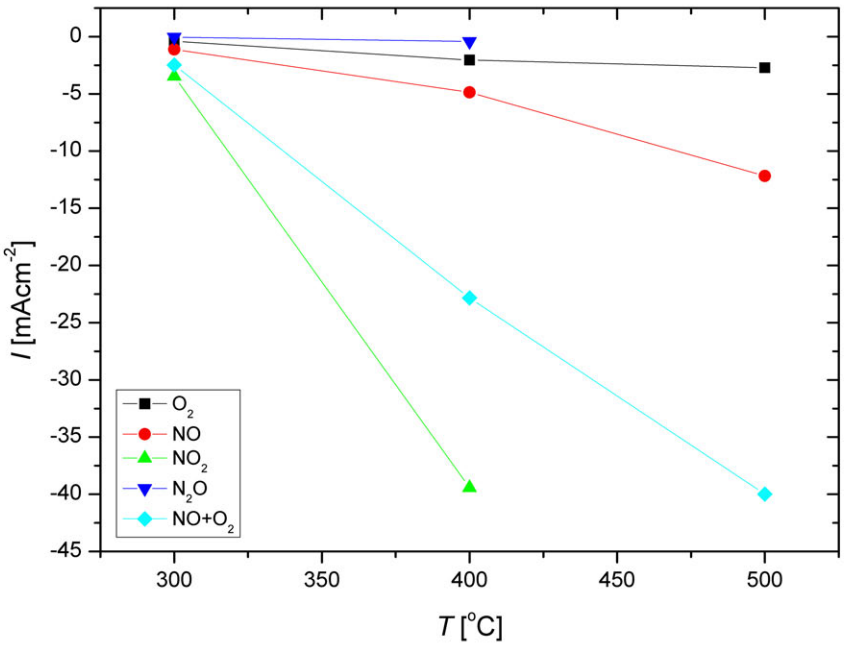

(a)

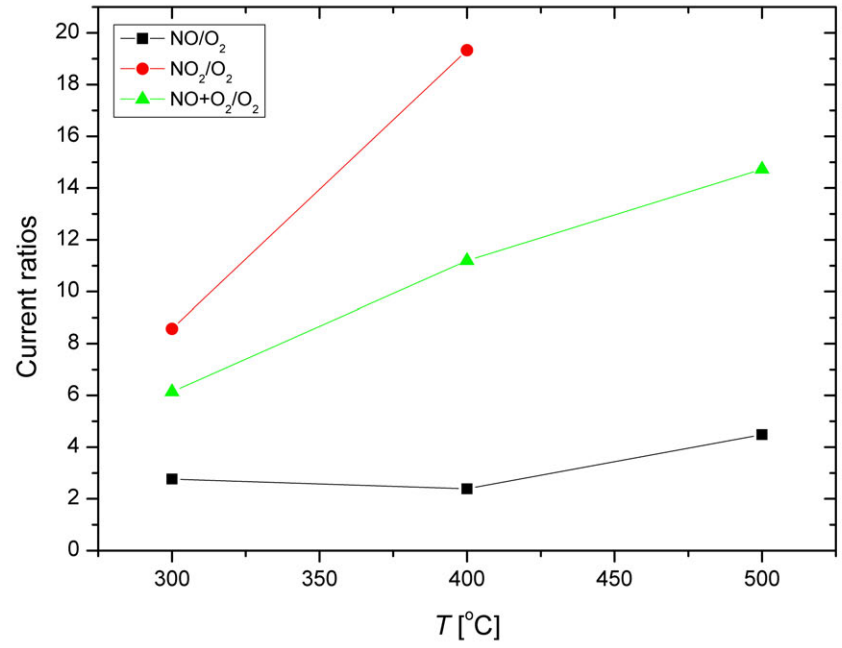

(b)

Figure 5.50: Current densities and current ratios on $MnCo_2O_4$.

series (see section 5.3.3). Similar ratios were also reported by Simonsen [182] on different perovskites and members of the Ruddelston-Popper series. Current ratios of NO_2 and $NO + O_2$ with respect to O_2 are higher than in the case of NO, but they decrease rapidly as the temperature is lowered.

5.5.2 $NiMn_2O_4$

$NiMn_2O_4$ has an inverse spinel structure with Ni situated mainly on O sites and Mn distributed among T sites and O sites, but with the cation distribution very sensitive to the thermal history [157]. The oxidation state of Mn is mainly 3+, but 2+ and 4+ can also be found in the structure. Earlier reports show that an oxygen excess or loss can occur in $NiMn_2O_4$ depending on the sintering history [183,184]. $NiMn_2O_4$ fractionate into NiO and a more Mn-rich spinel at 907 °C [185], following the reaction 5.21 proposed by Csete de Györgyfalva *et al.* [185],

$$\begin{aligned}&\left[Ni^{2+}_{1-2\lambda}Mn^{2+}_{2\lambda}\right]^{T}\left[Ni^{2+}_{2\lambda}Mn^{3+}_{3-4\lambda}Mn^{4+}_{2\lambda}O_4\right]^{O} \rightarrow yNiO \\ &+\frac{3-y}{3}\left[Ni^{2+}_{x-2\lambda}Mn^{2+}_{2\lambda+(1-x)}\right]^{T}\left[Ni^{2+}_{2\lambda}Mn^{3+}_{3-4\lambda-(1-x)}Mn^{4+}_{2\lambda}O_4\right]^{O}+\frac{y}{6}O_2. \qquad (5.21)\end{aligned}$$

T and O represent the tetrahedral and octahedral sites, $x = (3 - 3y)/3 - y)$, y is the amount of NiO generated and λ is the degree of inversion, defined as the fraction of O-site cations found on the T site. The process is partly reversible [185].

Figure 5.51b shows the specific conductivity of $NiMn_2O_4$ with the thermal decomposition of the spinel observed on the graph at $\sim$ 890 °C. At lower temperatures the activation energy is calculated to be 0.3700(7) eV, however, a distinct change of activation energy (0.527(3) eV) is found in the temperature range from 420 °C to 890 °C. Similar activation energies ($\sim$ 0.39 eV) were reported by Schmidt *et al.* [183] for the low temperature region. The conduction mechanism is based on an exchange interaction upon thermal activated electrons hopping between Mn^{3+} and Mn^{4+} on the O sites [183]. Gillot *et al.* [157] reported that a reordering of the cations begin at around 450 °C, following reaction 5.22,

$$Ni^{2+}_{T} + 2Mn^{3+}_{O} \leftrightarrow Ni^{2+}_{O} + Mn^{4+}_{O} + Mn^{2+}_{T}. \qquad (5.22)$$

This might explain the change in activation energy observed at 420 °C.

The thermal expansion changes linearly with temperature, until it reaches $\sim$ 890 °C where the decomposition starts (see Figure 5.51a). Around 525 °C a small increase of the expansion coefficient was observed. This was not related to a magnetic transition as T_c

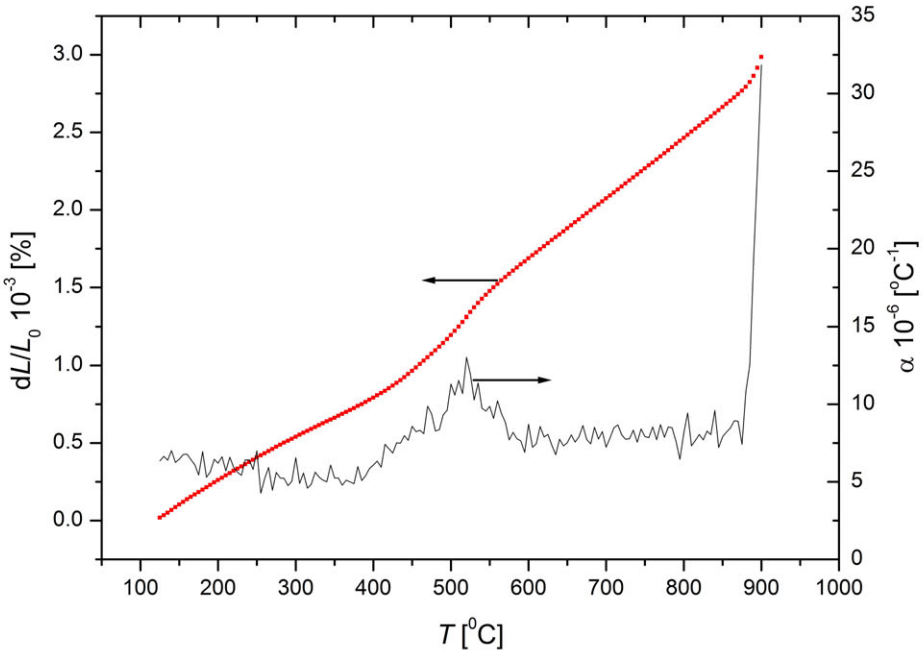

(a)

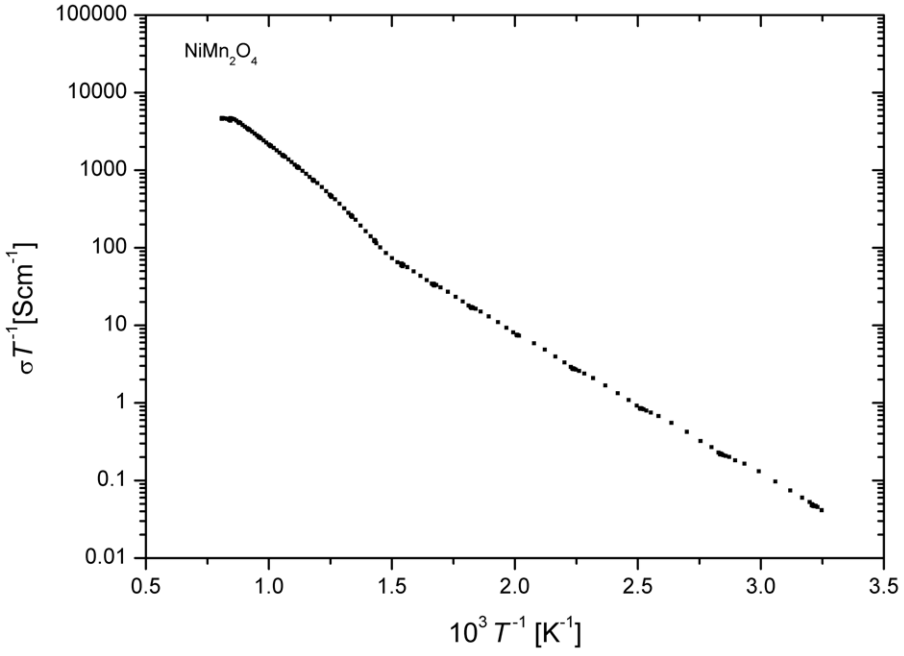

(b)

Figure 5.51: (**a**) Dilatometry measurements and (**b**) conductivity measurements on the $NiMn_2O_4$-electrode.

is found at much lower temperatures (approximate -120 °C) [183]. The small increase in the thermal expansion might result from a change in cation distribution or alternatively in a loss of excess air assuming non-stoichiometrical $NiMn_2O_4$.

CV and EIS were recorded on cone-electrodes at 400 °C, 500 °C and 600 °C in 1 % NO and 10 % O_2. The electrodes were also recorded in 1 % NO_2 at 300 °C and 400 °C. The potential range was set from 0.5 V to -0.5 V. As in the cases of $ZnFe_2O_4$ and $MnCo_2O_4$ voltammograms reveal a very poor cathodic activity in NO and O_2. The anodic activities are much higher with not much difference between the different gases other than at 600 °C where current density in O_2 (0.48 Acm^{-2}, 0.5 V) is notable higher compared to NO (0.34 Acm^{-2}, 0.5 V). Results also show that it is easier to oxidize NO than to have an oxygen evolution at high temperature (600 °C). A 400 °C (see Figure 5.52b) the anodic activity in O_2 is higher than in NO as also observed for the $ZnFe_2O_2$-electrode. The explanation is similar to the one in section 5.4.3.

At 400 °C, (see Figure 5.52b) the cathodic activity in NO_2 is significant higher compared to the activities recorded in the other atmospheres. A small peak is observed at 300 °C (see Figure 5.52a) in NO_2 but since the voltammograms supposedly reflect a mixed potential it is difficult to identify the reaction responsible for the peak formation. However, it either reflects an oxidation of NO_2 or alternatively a formation of nitrates on the surface of the electrode as suggested by Simonsen *et al.* [61].

Figure 5.53 shows the current ratios, recorded at -0.5 V. As expected from the voltammograms, the apparent selectivity towards NO reduction is very low, however, current ratios of NO_2 with respect to O_2 show high values in the range of 18 to 37 depending on the temperature.

Ba-doped $NiMn_2O_4$

Due to the relative high electronic conductivity and the promising apparent selectivity towards reduction of NO_2, $NiMn_2O_4$ was mixed with BaO in order to investigate weather the compounds could be used as electrode material in an electrochemical storage catalyst (see section 1.2.4). First, a pellet of $NiMn_2O_4$-powder mixed with 15 w% $BaCO_3$ was fabricated. After calcination (900 °C/6 hours), the pellet was analyzed with XRD and results showed that the mixture had reacted and formed an additional phase of a perovskite-type structure. Apart from that, the pellet also contained large amounts of vesicles as a result of the formation of CO_2 during decomposition of $BaCO_3$. The synthesis process was not repeated using BaO because the powder also contained 'impurities' of $BaCO_3$ formed from the reaction with air. Instead, tests were made on mixing the $NiMn_2O_4$-powder with

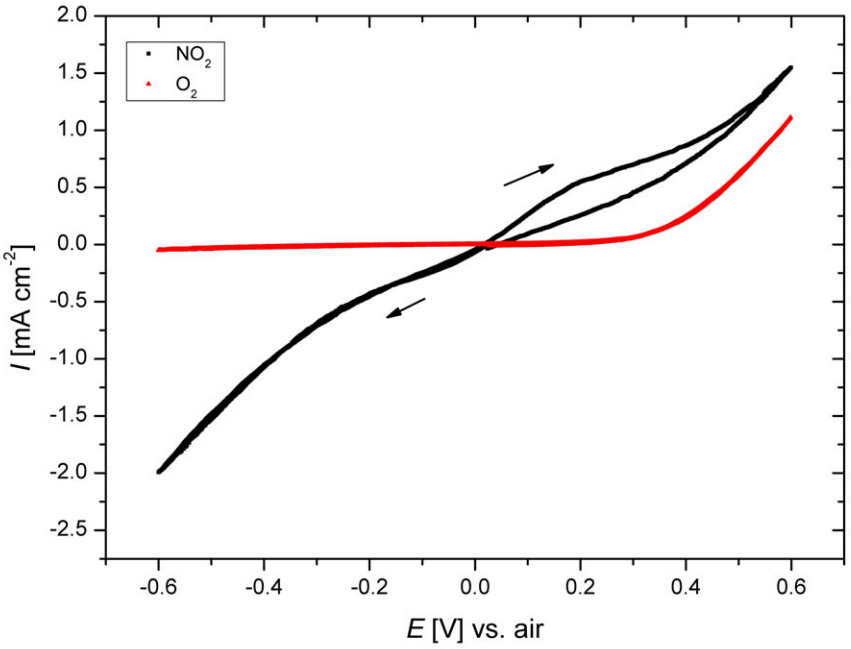

(a)

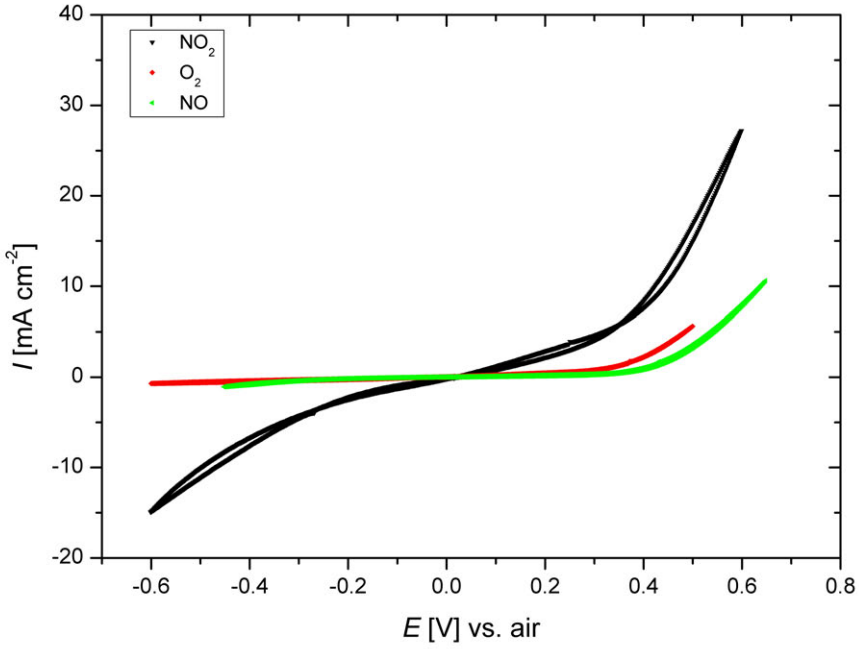

(b)

Figure 5.52: CV on $NiMn_2O_4$ at 300 °C and 400 °C. The voltammograms were recorded with a scan rate of 1 mVs^{-1}. The arrows show the direction of the scan.

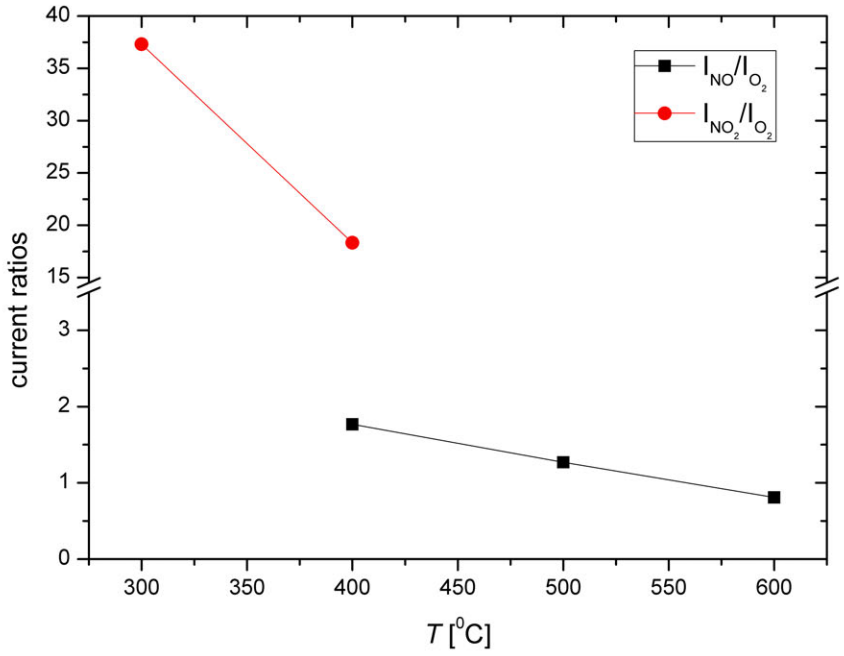

Figure 5.53: Current ratios of the $NiMn_2O_4$-electrode.

an aqueous solution of $Ba(NO_3)_2$ and calcined it at much lower temperatures (600 °C). Unfortunately the spinel reacted again with the Ba-compound and therefore no further measurements were performed on Ba-doped $NiMn_2O_4$.

Chapter 6

XAS

In order to improve the understanding of the fundamental properties of the materials, XAS was performed on a few selected spinels. Unfortunately no standards were recorded at the same conditions as the spinels and therefore only quantitative information on the oxidation states in the spinels can be given from the XANES data. Results of the EXAFS refinement on $ZnFe_2O_4$ is shown in the last section. The amount of new information regarding the structural properties are in fact limited, however, the results of the EXAFS refinement serve as a comparison and a validation of the results obtained with neutron diffraction.

6.1 XANES

In spinel-type oxides cations can occupy two different lattice sites (see section 2.1). Since the energy levels are not identical when an atom is located in a tetrahedral or an octahedral coordinated site, the cation distribution will effect the K-edge as well as the pre-edge.

The energies of all spectra were calibrated using the spectra of the reference metal foils, taking the first inflection points in the reference absorptions as edge energies. Background absorptions were found by fitting linear functions to the measured data in energy ranges up to approximately - 40 eV relative to the observed absorption edges. These functions were subtracted from the data. For the XANES measurements, the edge steps of the absorptions were normalized to unity using quadratic functions, fitted to the data in the range of 175250 eV above the absorption edges.

Figure 6.1 shows the normalized spectra of Fe for four spinels: $MgFe_2O_4$, $NiFe_2O_4$, $ZnFe_2O_4$ and $NiCrFeO_4$. The K-edges are located at very similar positions, which indicate that the oxidation states of Fe are the same in all of the spinels. A sharp increase of the

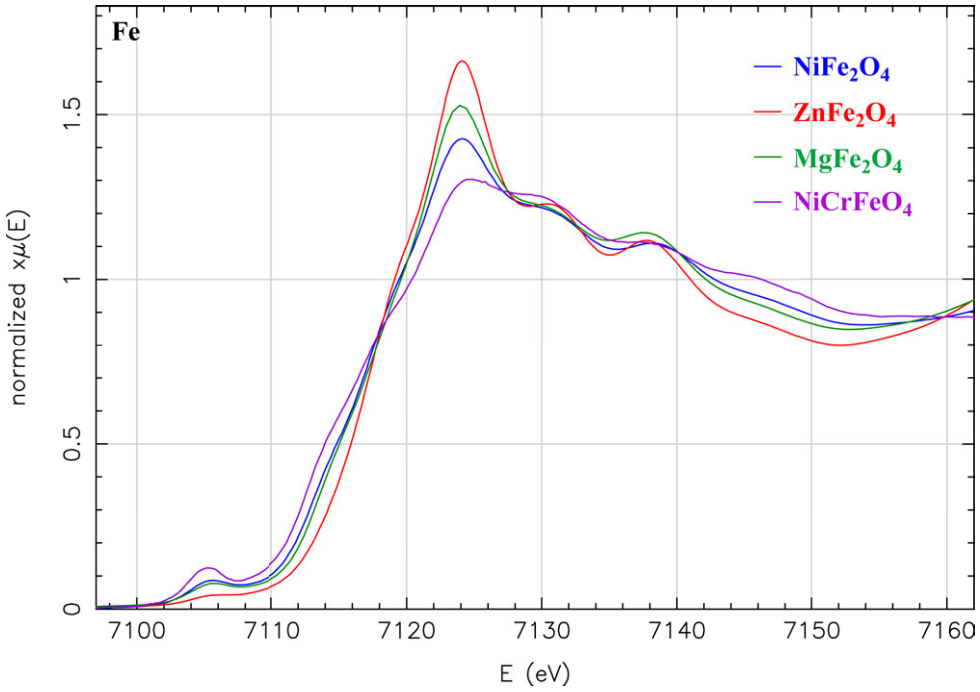

Figure 6.1: XANES Fe-spectra on $MgFe_2O_4$, $NiFe_2O_4$, $ZnFe_2O_4$ and $NiCrFeO_4$, recorded at room temperature.

K-edge is observed in the case of $ZnFe_2O_4$ but it is much less pronounced in the case of $NiCrFeO_4$. The height of the normalized K-edges is arranges so that $ZnFe_2O_4 > MgFe_2O_4 > NiFe_2O_4 > NiCrFeO_4$, however, the reverse order is observed for the pre-edge with the relative peak heights arranged so that $NiCrFeO_4 > NiFe_2O_4 > MgFe_2O_4 > ZnFe_2O_4$. Pre-edges were observed in all spectra except of $ZnFe_2O_4$ as also reported by Safontseva *et al.* [186]. Earlier reports (see section 5.4.6) show that $ZnFe_2O_4$ is a normal spinel with Fe located only on O sties. Therefore we do not expect to see any pre-edge in the XANES spectra. $MgFe_2O_4$ is a partly-inverse spinel whereas $NiFe_2O_4$ is considered more inverse compared to $MgFe_2O_4$ (see section 5.1.1). This is also reflected by the height of the K-edges where $MgFe_2O_4$ is higher than $NiFe_2O_4$. $NiCrFeO_4$ on the other hand is the most inverse of the analyzed spinels and it has the lowest K-edge but the highest pre-edge. The arrangements of the peaks show that the more Fe is placed on O sites, the higher the peak of the K-edge and the lower the pre-edge peak. Same kind of attenuation was also observed by Haas *et al.* [187] on the Fe K-edge of the crystal structure of $La_{1-x}Sr_xFeO_{3-\delta}$. However, he suggested that less well-defined energy levels would cause a decrease in the K-edge and an increase of the pre-edge. That might also hold for the measured spinels in this thesis, however, the coincidence with the cation distribution is worth noticing.

Figure 6.2a shows the normalized spectra of Ni for three spinels: $NiFe_2O_4$, $NiCr_2O_4$ and $NiCrFeO_4$. A small pre-edge is observed in the case of $NiCr_2O_4$ which agrees with the fact that it is a normal spinel with Ni located predominantly on T sites. This is

6.1. XANES

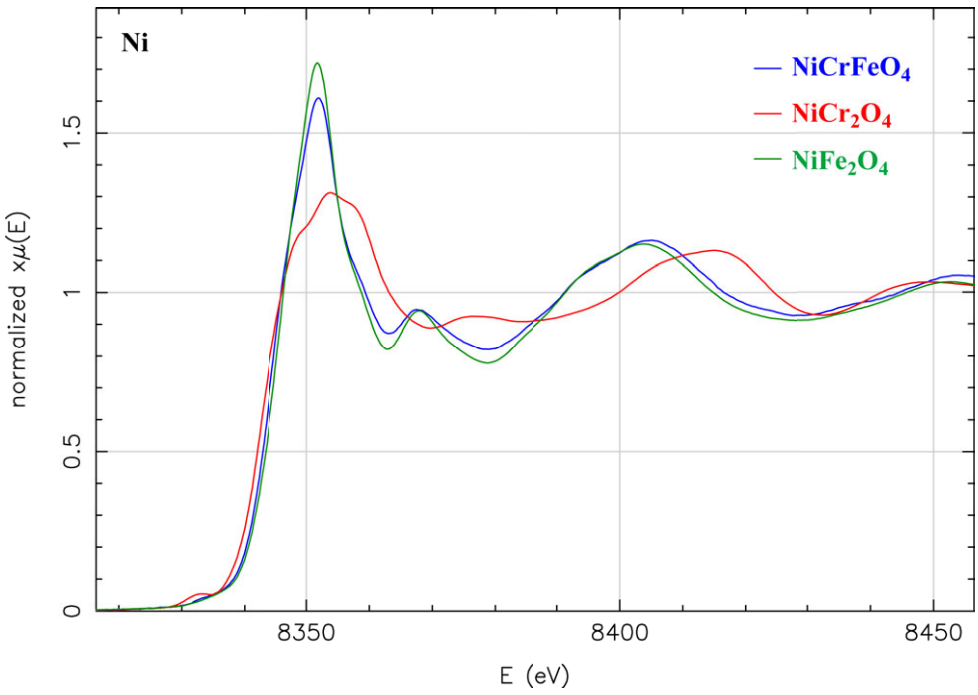

(a)

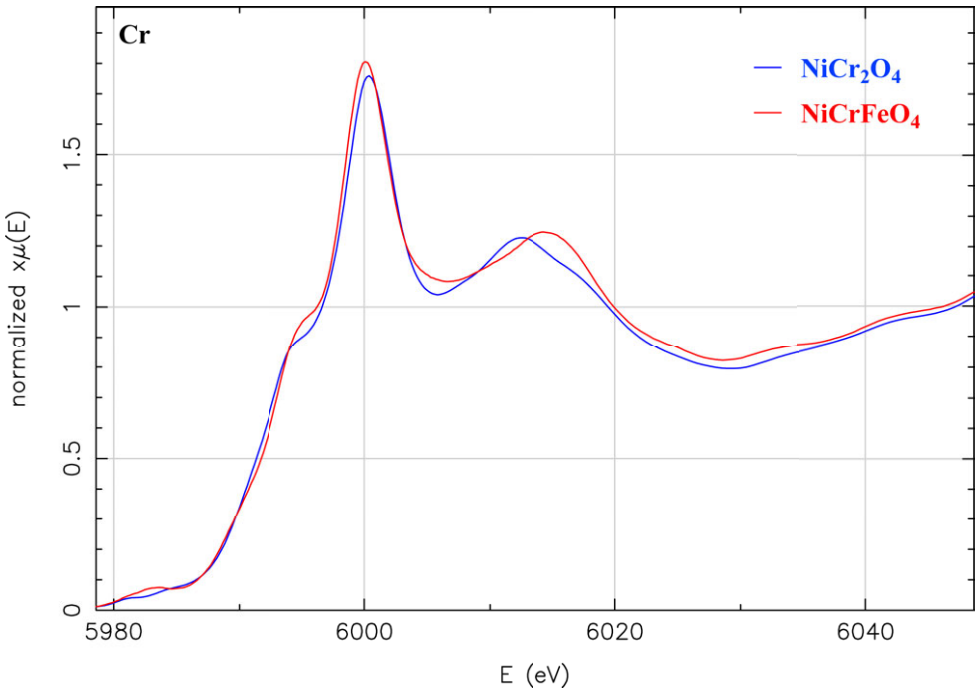

(b)

Figure 6.2: (**a**) Normalized XANES Ni spectra on $NiFe_2O_4$, $NiCr_2O_4$ and $NiCrFeO_4$. (**b**) Normalized XANES spectra on the Cr spectrum on $NiCr_2O_4$ and $NiCrFeO_4$.

also confirmed by the peak height of the K-edge which is the lowest of the three spinels. Indications of a very small pre-edge is observed in the case of $NiCrFeO_4$, however, it is of such low intensity that the amount of Ni present on T sites must be close to the detection limit of the recorded data. Again, we see that the peaks heights follow the same trend as observed in the Fe spectra; the more Ni, placed on O sites, the higher the K-edge and the lower the pre-edge peak. The normalized spectra of Cr are shown in Figure 6.2b. The spectra seem a bit different from the ones recorded on Fe and Ni, with a 'secondary' peak on the left side of the K-edge. This is due to a change in ground state when the $1s$ electron is removed and the system is permitted to relax [87]. A very small pre-edge is observed on $NiCrFeO_4$ which indicates that a small fraction of the Cr is placed on the T sites.

6.1.1 High Temperature Measurements on $NiFe_2O_4$

Figure 6.3 show the normalized Fe- and Ni-spectra of $NiFe_2O_4$ recorded in 1 % NO, 1 % NO_2 and 0.5 % NO + 10 % O_2. Results again show practically no difference between the oxidation states of Fe. However, the spectra recorded on Ni reveals a shift (0.8 eV) of the K-edge towards a higher oxidation states of Ni in sequence of NO_2 > NO + O_2 > NO. Apparently NO_2 is reduced on the Ni^{2+} ions which is then oxidized to Ni^{3+}. This is of cause speculative but the results agrees with the electrochemical measurements on cone-electrodes where a very high activity was observed in NO_2 (see section 5.1.4). On the basis of the results of the XANES measurements future cell tests upon gas conversion should be performed on $NiFe_2O_4$ similar to those measured on $MgFe_2O_4$ (see section 5.1.6) and $ZnFe_2O_4$ (see section 5.4.5).

Similar high temperature measurements in different gas atmospheres were also tested on $MgFe_2O_4$. However, as soon as NO and especially NO_2 was applied over the sample, the intensity of the signal dropped very fast and it was not possible to conduct any measurements. This indicates that NO_x gases are very strongly adsorbed on $MgFe_2O_4$ which may also explain the low degree of gas conversion, observed in section 5.1.6. Changing the polarization potential or to apply a different square-wave potential would be an obvious procedure to follow in future. More tests should be made to learn as much as possible on the catalytic and electrocatalytic mechanisms of the material.

6.1. XANES

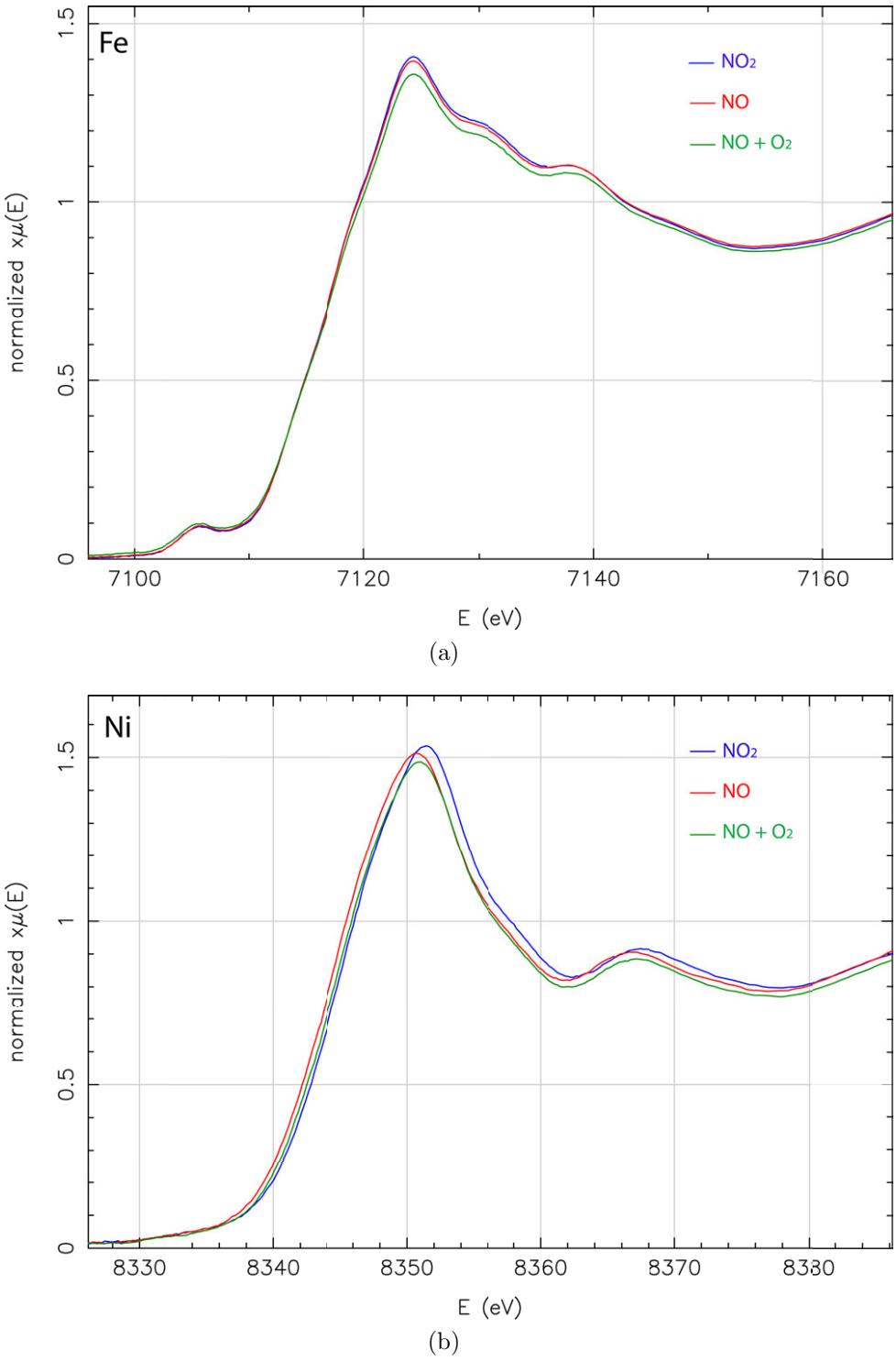

Figure 6.3: XANES on $NiFe_2O_4$ recorded at 400 °C in 1 % NO, 1 % NO_2 and 0.5 % NO + 10 % O_2. (**a**) shows the normalized Fe spectrum and (**b**) shows the normalized Ni spectrum. A shift in K-edges is observed in the Ni spectrum.

6.2 EXAFS

The evaluation of the EXAFS data were performed by calculating the spectrum of a model structure *ab initio* (a 'theoretical standard'). The theoretical standard was calculated using the Ifeffit program, using data for a cubic spinel structure generated by the Atoms program. The theoretical standard was then imported into the Artemis program as a set of separate 'scattering paths' around the absorbing atom. Each such scattering path represents a unique way for the photoelectron to scatter from the absorbing atom, between neighbouring atoms, and back to the absorbing atom. The theoretical standard was then modified by varying the absorption energies E_0, the path lengths, dR, the mean-square displacements of the different coordination shells, σ^2, and the cation distributions in the materials. These parameters were subsequently optimized by performing a least-square fit to the data. Another standard EXAFS parameter, S_2^0, the amplitude reduction factor for each element, was set to a constant value of 0.9. The value was based on an average of a large number of optimizations on the reference foils and different spinel, made by Ph.D. student Jonas Östby [188]. Using constant amplitude reduction factors may have caused some errors in the fits, but because of the complexities of the models, the amount of data was not considered enough to optimize the S_2^0 parameters further. The k-range was chosen as large as possible for each spectrum without changing the R-factor of the reduced χ^2 considerably. The model structure obtained from the Ifeffit program was based on an ideal spinel type-structure. However, in spinel-type structures, the oxygen parameter, u, is often very different from the ideal structure. A large variation in bond length (cation–anion) is also allowed through the u parameter, which makes it more difficult to handle. Therefore a new model, developed by Jonas Östby [189], was used in the refinements. The model divides the structure into several sub-lattices each having their own lattice parameter and u parameter. When the cation distribution was considered different from the two ideal spinel-type cases (normal spinel or inverse spinel), several modelled sub-lattices were superimposed on each other. The stoichiometry was assumed perfect regarding the oxygen content as well a the ratio between cations. Each type of cation was only allowed one bond distance to its nearest anion neighbour per sub-lattice. A more detailed description of the model can be found elsewhere [189].

To evaluate the quality of refinements, the EXAFS agreement factor, also known as the R-factor is commonly used, along with a reduced chi-squared factor. The R-factor is a simple measure of the fractional difference between the data (d) and the refinement (r);

$$R = \frac{\sum_j (\chi_j^{\mathrm{r}} - \chi_j^{\mathrm{d}})^2}{\sum_j (\chi_j^{\mathrm{d}})^2}, \tag{6.1}$$

where χ is defined in equation 3.6.

6.2.1 EXAFS on $ZnFe_2O_4$

Figure 6.4 show the spectra obtained on Zn and Fe in $ZnFe_2O_4$. Both spectra was refined simultaneously in order to obtain the most reliable result. Table 6.1 summarizes the refined parameters as well as the agreement factors and fitted k-range. Results show that a better fit could be obtained on the Zn spectrum as compared with the Fe spectrum. Especially are the refined σ^2 parameters much higher than expected[1]. This indicates the presence of an Fe impurity phase, such as hematite, $\alpha - Fe_2O_3$, or magnetite, Fe_3O_4. This was not observed with XRD or neutron diffraction, however, Fe_3O_4 has a spinel-type structure and therefore the diffraction peaks will be superimposed on the diffraction peaks from $ZnFe_2O_4$, as the unit cell parameters of the two spinels are very similar [190]. The presence of about 1 % Fe_3O_4 will therefore be practically invisible in XRD or neutron diffraction. In EXAFS measurements, Fe_3O_4 will have a minor effect on the spectra, however, this is not the case of $\alpha - Fe_2O_3$, which has a hexagonal crystal structure (space group $R\bar{3}c$ [191]. Even the presence of a small content of $\alpha - Fe_2O_3$ will disturb the Fe spectrum of $ZnFe_2O_4$. It was not possible to include an extra phase in the model for the EXAFS refinements, so the presence of $\alpha - Fe_2O_3$ remains speculatively.

The inversion parameter (see section 2.1) was calculated to $\gamma = 0.02$ which is a bit lower than found by neutron diffraction at room temperature. The length of the unit cell, a, and the oxygen coordinate, u, agree fairly well with the results of neutron diffraction ($a = 8.4371(4)$ Å and $u = 0.3849(4)$, for further information see section 5.4.6) although no uncertainties were given by the EXAFS model. Bond lengths cause a much bigger problem. Especially the ^{O}Fe–O distance, which seems to be higher than reported in literature and found by neutron diffraction (see Table 5.12). The reason of that might be related to the quality of the recorded data; either because of impurity phases (as already mentioned) or by the signal to noise level of the recorded data. Calvin *et al.* [192] did similar measurements on manganese zinc ferrite spinels, however, he performed several scans at each edge and then an average was made. At better set of data is maybe required or a new model must be constructed in order to verify whether EXAFS can be used to determine the structural parameters as well as the cation distribution in spinels.

[1]Expected values of σ^2 should be in the range of 0.002–0.004 [Å^2], however, we observe values up to 0.007 Å^2.

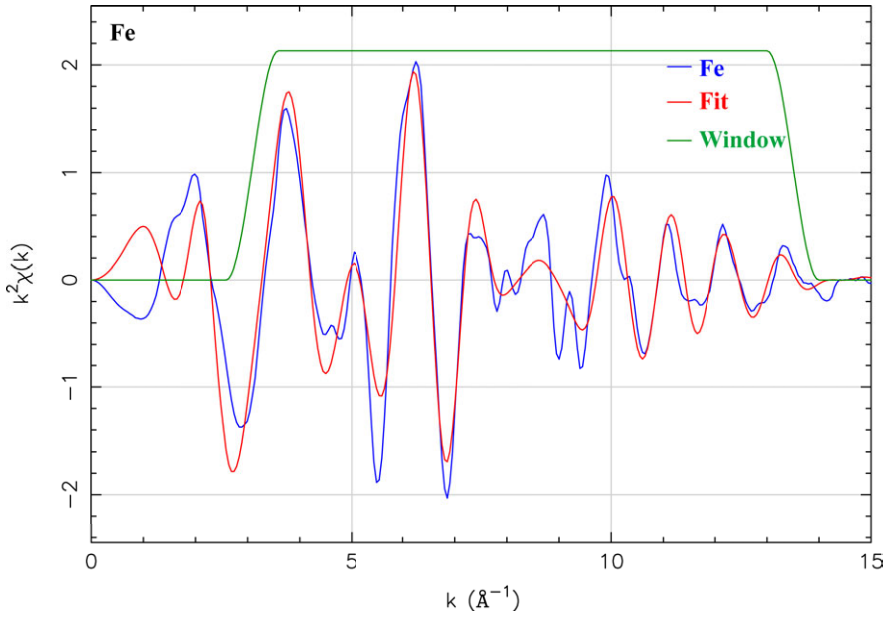

(a)

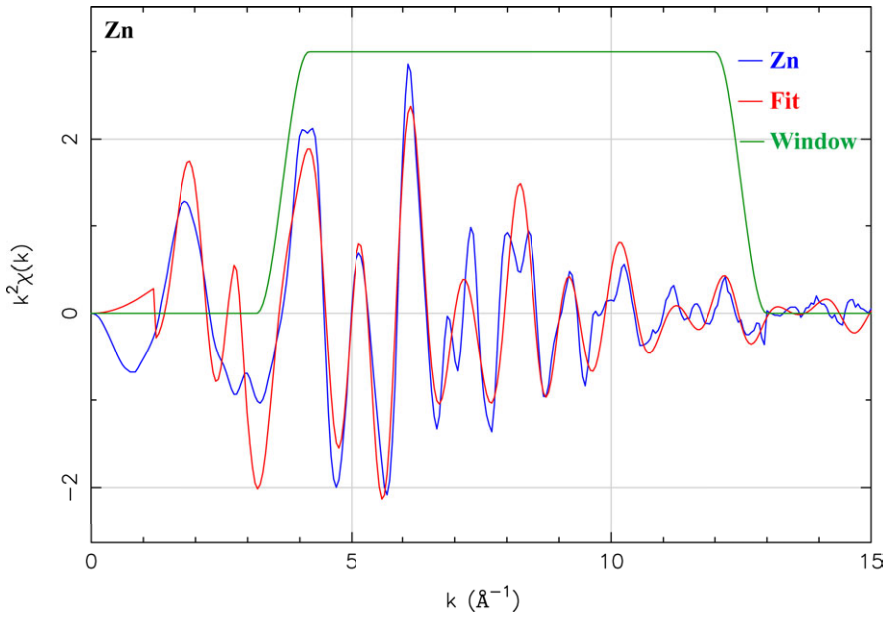

(b)

Figure 6.4: Refined EXAFS Fe and Zn spectra on $ZnFe_2O_4$. (**a**) The refinements on the Fe spectrum is not as good as the Zn spectrum (**b**).

Table 6.1: Refined EXAFS parameters from $ZnFe_2O_4$. No uncertainties were given by the model on the unit cell parameter, a, and the fractional oxygen coordinate, u. T and O represent the tetrahedral and octahedral sites. A strong correlation was found between ΔE_0 and the Fe–O bond length equal to 0.84. All other correlations were below 0.54.

R-factor	0.027	Zn, ΔE_0 [eV]	7.5(8)
Reduced χ^2	470	Fe, ΔE_0 [eV]	-5.8(7)
Independent points	39	σ^2, Zn-O, [Å^2]	0.004(1)
Number of variables	8	σ^2, Fe-O, [Å^2]	0.0071(8)
a, [Å]	8.426	σ^2, Zn-Zn, [Å^2]	0.006(1)
u	0.388	σ^2, Fe-Fe, [Å^2]	0.0056(5)
k-range Zn, [Å]	3.7-12.5	σ^2, Zn-Fe, [Å^2]	0.006(1)
k-range Fe, [Å]	3.1-13.5	σ^2, Fe-Zn, [Å^2]	0.0056(5)
$^{\mathrm{T}}\mathrm{Zn}-\mathrm{O}$, [Å]	2.019(9)	-	-
$^{\mathrm{O}}\mathrm{Fe}-\mathrm{O}$, [Å]	2.016(6)	-	-

Chapter 7

Conclusion and Outlook

7.1 Conclusion

The main object of this Ph.D. project was to investigate new electrode materials, based on the spinel-type structure, to be used in a solid state cell for electrochemical reduction of NO_x gases.

7.1.1 The $Ni_{1-x}Mg_xFe_2O_4$ Series

The electrochemical studies on cone-electrodes show that the two end members of the $NiFe_2O_4$−$MgFe_2O_4$ series have a relative high activity in NO in the measured temperature range. However, the activity in O_2 differs significantly from the two end members, with the $NiFe_2O_4$ electrode showing the largest activity. Recorded measurements on the $MgFe_2O_4$ electrode show that the current ratios of NO/O_2, $(NO+O_2)/O_2$, NO_2/O_2, and $(NO_2 + O_2)/O_2$ are much higher compared to the other spinels, with the exception of NO/O_2 at 600 °C. As more Fe^{3+} is incorporated on the O site, the higher the conductivity but the lower the activity in NO and O_2. Recordings of OCV suggest that the reduction of NO is inhibited by the presence of O_2, whereas the reduction of NO_2 seems to dominate in the presence of O_2. Four-point DC resistivity measurements show that $Ni_{0.5}Mg_{0.5}Fe_2O_4$ and $Ni_{0.4}Mg_{0.6}Fe_2O_4$ have the highest conductivity at elevated temperatures, whereas the spinels with low Mg content ($Ni_{0.7}Mg_{0.3}Fe_2O_4$ and $NiFe_2O_4$) have the highest conductivity at lower temperatures. An order-disorder of the cations could also be detected from the conductivity measurements in most of the samples. Measurement on thermal expansion show that the temperature of the magnetic order is detectable in all samples, but an additional wide peak is also detected in $MgFe_2O_4$ at 800 °C, which seems to be related to

a cation reordering. Thermal expansion coefficients are comparable with CGO10, which is important since a composite electrode of spinel and CGO10 is needed in order to construct a usable electrode.

EIS recorded on a $MgFe_2O_4$/CGO10 symmetrical cells show that the resistivity is very high. This might cause a challenge for the fabrication of larger cells for more advanced testing regarding gas conversion of diesel exhaust. Measurements show that it was possible to detect a small gas conversion over the $MgFe_2O_4$/CGO10 3E pellet. However, the gas conversion only involved electrochemical reduction of NO_2 to NO or oxidation of NO to NO_2. Therefore, an overall conclusion would be that $MgFe_2O_4$ is not suitable as the dominant compound in an electrode material. The material may be used to infiltrate cells having a more strong backbone structure regarding electron conductivity and gas conversion.

7.1.2 The $NiCr_xFe_{2-x}O_4$ Series

Substitution of Fe^{3+} with Cr^{3+} in the spinel-type oxides; $NiCr_xFe_{2-x}O_4$ show a decrease of unit cell parameters and an increase of the conductivity. Dilatometry measurements show a decrease in the linear expansion in the measured temperature range and, in most samples, the Curie temperature and cation redistribution could also be detected. CV and EIS were recorded on the spinels in 1 % NO, 1 % NO_2, and 10 % O_2 and results show that the cathodic activity of $NiFe_2O_4$ is relatively high in all gases compared to the other spinels. The cathodic activities of $NiCr_2O_4$ in NO and NO_2 are, although lower than for $NiFe_2O_4$, also relatively high. Most important, is that the activity in O_2 is very low, which makes it a good candidate for a possible electrode material in an electrochemical cell for the reduction of NO_x gases. Formation of peaks in the voltammograms on the $NiCr_2O_4$ electrode suggests the formation of nitrogen-containing species on the surface or, alternatively, oxidation of Cr in the electrode.

7.1.3 The $MgMn_xFe_{2-x}O_4$ Series

$MgMn_xFe_{2-x}O_4$, $x = 0.0, 0.2, 0.4, 0.6, 0.8, 1.0$ was successfully synthesized using solid state reactions. Dilatometry measurements showed a decreasing linear thermal expansion for the Mn-containing materials. Conductivity measurements show an increase in the electric conductivity when more Mn is incorporated into the structure. CV measurements in 1 % NO, 1 % NO_2 and 10 % O_2 show a decreasing activity when Mn is incorporated into the structure; however, current ratios are still relatively high compared to those of $MgFe_2O_4$.

7.1.4 $ZnFe_2O_4$

$ZnFe_2O_4$ was synthesized using a solid state reaction. Resistivity measurements reveal a semi-conducting behaviour of $ZnFe_2O_4$ from room temperature to 630 °C, which mainly arises from a Fe-O-Fe exchange interaction between O sites. Above 630 °C, $ZnFe_2O_4$ shows a more metallic behaviour which is attributed to the Fe-Fe interaction on O sites.

CV and EIS was recorded in 1 % NO, 1 % NO_2 and 10 % O_2. Results show that the cathodic activity in NO and O_2 is very poor, whereas the activity in NO_2 is much higher. It seems that a relatively higher electron conductivity, results in a high cathodic activity in NO_2 but with low cathodic activity in NO and O_2.

Data recorded on symmetrical cells of $ZnFe_2O_4$/CGO10 show that the resistance is relative high, however, lower than in the case of the $MgFe_2O_4$/CGO10 symmetrical cell which again will be a challenge for fabrication of larger cells.

Measurements regarding gas conversion over a $ZnFe_2O_4$/CGO10 3E pellet show, as in the case of the $MgFe_2O_4$/CGO10 electrode, that it was not possible to reduce the NO_x gases to N_2. Instead, electrochemical gas conversion of NO_2 to NO and the corresponding reverse reaction was obtained with a relative high current efficiency. BaO was found to improve the ability to oxidize NO to NO_2 electrochemically, however, no gas conversion during cathodic polarization could be detected. Therefore, $ZnFe_2O_4$ is not suitable as the dominant electrode material in a solid state cell. $ZnFe_2O_4$ might be used, as in the case of the $MgFe_2O_4$/CGO10 electrode, as an infiltration material in a cell having a more strong backbone structure regarding electron conductivity and gas conversion.

HTND was preformed on powder from RT to 970 °C and refinements show that $ZnFe_2O_4$ has a almost normal spinel structure with $\gamma = 0.09$ below 400 °C. Cations start to redistribute among tetrahedral and octahedral sites at temperatures above $\sim$ 400 °C, but they switch back to their original position when the sample is cooled down gain. The expansion of the unit cell parameter and octahedrons increases rapidly at $\sim$ 400 °C which seems to be related to the larger Zn^{2+} ion substituting the smaller Fe^{3+} on the octahedral sites.

7.1.5 Cobalt and Manganate Spinels

Results from CV measurements show that $MnCo_2O_4$ has a general low cathodic activity in NO, NO_2 and O_2 with an apparent selectivity in the lower range compared to the other measured spinels. No tests regarding gas conversion were made on the material, however, the compound is presumable a bad choice as an electrode material for electrochemical

reduction of NO_x gases over a solid state cell.

$NiMn_2O_4$ has a relative high electronic conductivity and an expansion coefficient very similar to CGO10. Data recorded with CV in 1 % NO, 1 % NO_2 and 10 % O_2 show a very poor cathodic activity in NO and O_2 whereas the activity in NO_2 is much higher. $NiMn_2O_4$ shows some resemblance with $ZnFe_2O_4$ in the sense that a relatively higher electron conductivity, results in a high cathodic activity in NO_2 but at the same time, a low cathodic activity in NO and O_2. $NiMn_2O_4$ would not be suitable as an electrode material in an electrochemical storage catalyst containing Ba compounds.

7.1.6 XAS

Results from XANES measurements show that it is possible to analyze spinels quantitatively regarding oxidation states and their relative cation distribution. High temperature measurements, at 400 °C show that Ni is oxidized in a NO_2 bearing atmosphere, however, due to the lack of measurements on samples with a known Ni^{3+}/Ni^{2+}-ratio, it was not possible to calculate how much Ni that have been oxidized.

Results from the EXAFS measurements on $ZnFe_2O_4$ show that a small impurity Fe-phase presumable was present in the specimen. The technique can be used to find reasonable cell parameters however, bond lengths differs from what is reported in literature. We must therefore conclude that neutron diffraction is a better technique to measure the structural properties of spinels.

7.2 Outlook

The main project to pursue in the future is to infiltrate cell stacks of porous cell (see section 1.2.4). This will decide weather spinels can be used as part of the electrode for electrochemical reduction of NO. A single test was made on a porous 5-cell stack with alternation layers of [LSM50/CPO10]−CGO10−[LSM50/CPO10]−... (LSM: $La_{0.5}Sr_{0.5}MnO_3$, CPO10: $Ce_{0.9}Pr_{0.1}O_2$), infiltrated with $MgFe_2O_4$. A small gas conversion could be detected, however, since only an inadequate test sequence was made no conclusions can be drawn. However, Figure 7.1 show the voltammograms recorded in 1000 ppm NO + 10 % O_2 and in 10 % O_2 at different temperature and it shows the formation of peaks which must be considered as reduction/oxidation peaks regarding NO_x species.

Another future aspect of electrochemical flue gas purification would be to fabricate porous cells where carbon particulates can be trapped and oxidized at the anode to CO_2

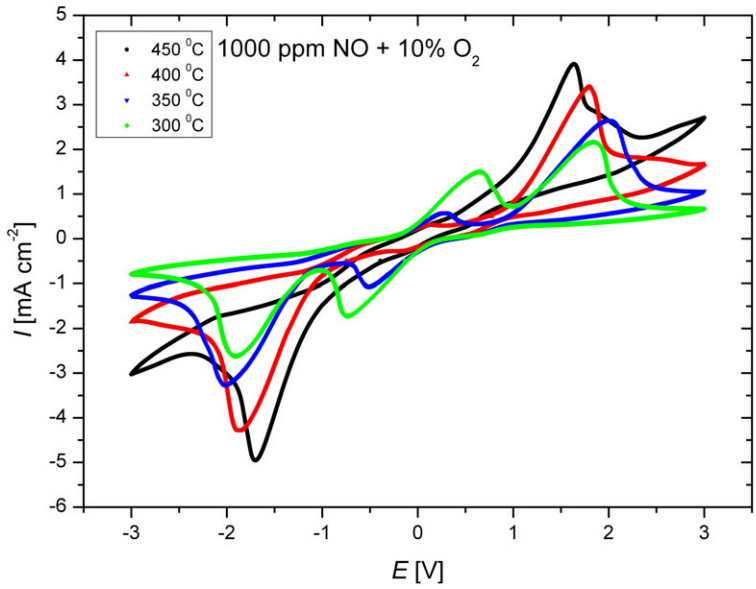

(a)

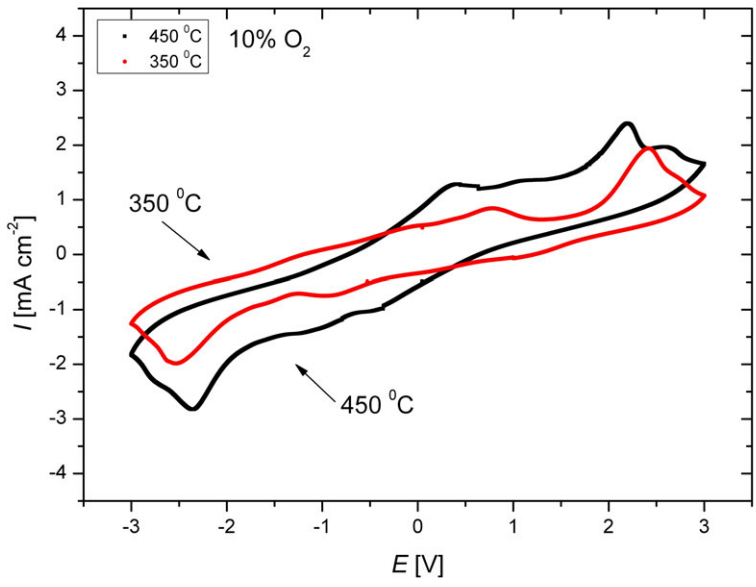

(b)

Figure 7.1: CV on a porous 5-cell stack with alternating layers of LSM50/CPO10 and CGO10. The voltammograms were recorded with a scan rate of 10 mVs^{-1}. Reduction/oxidation peaks can clearly be found in (**a**) those recorded in an NO_x containing atmosphere. (**b**) In 10 % O_2 peaks are either missing or reduced considerably.

as schematically shown on Figure 7.2. For this purpose, $ZnFe_2O_4$ or $NiMn_2O_4$ could be considered candidates as part of an electrode material due to their relative high anodic activities.

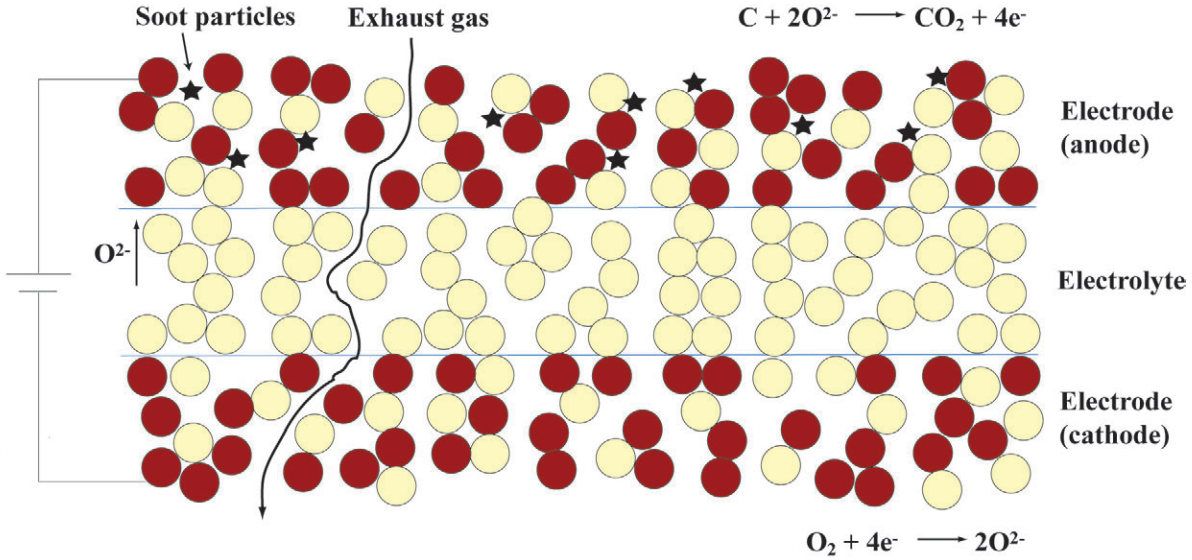

Figure 7.2: Concept of the porous cell for electrochemical reduction of carbon particulates. Yellow spheres represent an oxygen ion conduction material and red sphere represent an electronic conduction material, which also serve as electro-catalyst for the reduction of NO. Blue lines represent the boundaries between the electrode and the electrolyte.

Bibliography

[1] Klingstedt F, Arve K, Eränen K, and Murzin DY. Toward improved catalytic low-temperature NO_x removal in diesel-powered vehicles. *American Chemical Society*, 39:273–282, 2006.

[2] Friedrich R. Sources of pollutants. In Vovelle C, editor, *Pollutants from Combustion. Formation and Impact on Atmospheric Chemistry. Series* C*: Mathematical and Physical Sciences*, volume 547. Kluwer Academic Publishers, 2000.

[3] Gupta SK, Gupta RC, Chhabra SK, Eskiocak S, Gupta AB, and Gupta R. Health issues related to n pollution in water and air. *Indian Agriculture, Environment and Health*, 94:1469–1477, 2008.

[4] Fritz A and Pitchon V. The current state of research on automotive lean NO_x catalysis. *Applied Catalysis B: Environmental*, 13:125, 1997.

[5] Seinfeld JH and Pandis SN. *ATMOSPHERIC CHEMISTRY AND PHYSICS, From Air Pollution to Climate Change*, volume 2. edition. Wiley, USA, 2006.

[6] www.esa.int/esaCP/SEM340NKPZDindex3.html.

[7] Fenger J and Tjall JC. *Luftforurening*. Polyteknisk Forlag, Lyngby, DK, 1994.

[8] Zeldovich JB. *Oxidation of nitrogen in combustion and explosion*, volume 51. Academie des Science de l'URSS - Comptes Rendus, 1946.

[9] Bowman CT. *Gas-Phase Reaction Mechanisms for Nitrogen Oxide Formation and Removal in Combustion, Pollutants from Combustion. Formation and Impact on Atmospheric Chemistry. Series C: Mathematical and Physical Sciences*, volume 547. Kluwer Academic Publishers, Vovelle C (ed), 2000.

[10] Koltsakis GC and Stamatelos AM. Catalytic automotive exhaust aftertreatment. *Progress in Energy and Combustion Science*, 23:1–39, 1997.

[11] Allansson R, Blakeman PG, Cooper BJ, Hess H, Silcock PJ, and Walker AP. Optimising the low temperature performance and regeneration efficiency of the continuously regenerating diesel particulate filter ($CR-DPF$) system. *Society of the Automotive Engineers of Japan*, 01-0428:1–8, 2002.

[12] Webster DE. 25 years of catalytic automotive pollution control: a collaborative effort. *Topics in Catalysis*, 16/17:33–38, 2001.

[13] www.dieselnet.com/standards/eu/hd.php.

[14] www.dieselnet.com/standards/eu/ld.php.

[15] www.factsage.com, factsage version 5.5, thermfact inc., 2007.

[16] Glick HS, Klein JJ, and Squire W. Single-pulse shock tube studies of the kinetics of the reaction $N_2 + O_2 \rightleftarrows 2NO$ between $2000 - 3000$ K. *Journal of Chemical Physics*, 27:850–857, 1957.

[17] Amirnazmi A, Benson JE, and Boudart M. Oxygen inhibition in the decomposition of NO on metal oxides and platinum. *Journal of Catalysis*, 30:55–65, 1973.

[18] Falsig H, Bligaard T, Rass-Hansen J, Kustov AL, Christensen CH, and Nørskov JK. Trends in catalytic no decomposition over transition metal surfaces. *Topics in Catalysis*, 45:117–120, 2007.

[19] Centi G, Perathoner S, Shioya Y, and Anpo M. Role of the nature of copper sites in the activity of copper-based catalysts for NO conversion. *Research on Chemical Intermediates*, 17:125–135, 1992.

[20] Shelef M. On the mechanism of nitric oxide decomposition. *Catalysis Letters*, 15:305–310, 1992.

[21] Giamello E, Murphy D, Magnacca G, Morterra C, Shioya Y, Nomura T, and Anpo M. The interaction of NO with copper ions in ZSM5: An EPR and IR investigation. *Journal of Catalysis*, 136:510–520, 1992.

[22] Bell AT. Experimental and theoretical studies of NO decomposition and reduction over metal-exchanged $ZSM-5$. *Catalysis Today*, 38:151–156, 1997.

[23] Held W, Koenig A, Richter T, and Puppe L. Catalytic NO_x reduction in net oxidizing exhaust gas. *Society of the Automotive Engineers of Japan*, 900496:13–20, 1990.

[24] Iwamoto M, Yahiro H, Shundo S, Yu u Y, and Mizuno N. Selective reduction of no by lower hydrocarbons in the presence of O_2 and SO_2 over copper ion-exchanged zeolites. *Shokubai*, 32:430–433, 1990.

[25] Winter ERS. The catalytic decomposition of nitric oxide by metallic oxides. *Journal of Catalysis*, 22:158–171, 1971.

[26] Tersoka Y. Catalytic activity of perovskite-type oxides for the direct decomposition of nitrigen monoxide. *Chemistry Letters*, 1:1–4, 1990.

[27] Iwakuni H, Shinmyou Y, Matsumoto H, and Ishihara T. Direct decomposition of NO into N_2 and O_2 on $SrFe_{0.7}Mg_{0.3}O_3$ perovskite oxide. *Bulletin of the Chemical Society of Japan*, 80:2039–2046, 2007.

[28] Iwakuni H, Shinmyou Y, Yano H, Matsumoto H, and Ishihara T. Direct decomposition of NO into N_2 and O_2 on $BaMnO_3$ perovskite oxide. *Applied Catalysis B: Environmental*, 74:299–306, 2007.

[29] Zhu J, Xiao D, Li J, Yang X, and Wu Y. Kinetics and mechanism of NO decomposition over $La_{0.4}Sr_{0.6}Mn_{0.8}Ni_{0.2}O_3$ perovskite-type oxide. *Journal of Molecular Catalysis A: Chemical*, 236:182–186, 2005.

[30] Yentekakis IV, Tellou V, Botzolaki G, and Rapakousious IA. A comparative study of the $C_3H_6 + NO + O_2$, $C_3H_6 + O_2$ and $NO + O_2$ reactions in excess oxygen over na-modified $pt/\gamma - al_2o_3$ catalysts. *Applied Catalysis B: Environmental*, 56:229–239, 2005.

[31] Satokawa S. Enhancing the $NO/C_3H_8/O_2$ reaction by using H_2 over Ag/Al_2O_3 catalysts under lean-exhaust conditions. *Chemical Letters*, 3:294–295, 2000.

[32] Shangguan WF, Teraoka Y, and Kagawa S. Promotion effect of the potassium on the catalytic property of $CuFe_2O_4$ for the simultaneous removal of NO_x and diesel soot particulates. *Applied Catalysis B: Environmental*, 16:149–154, 1998.

[33] Shangguan WF, Teraoka Y, and Kagawa S. Kinetics of soot-O_2, soot-NO and soot-$O_2 - NO$ reactions over spinel-type $CuFe_2O_4$ catalyst. *Applied Catalysis B: Environmental*, 12:237–247, 1997.

[34] Shangguan WF, Teraoka Y, and Kagawa S. Simultaneous catalytic removal of NO, and diesel soot particulates over ternary AB_2O_4 spinel-type oxides. *Applied Catalysis B: Environmental*, 8:217–227, 1996.

[35] Fino D, Russo N, Saracco G, and Specchia V. Catalytic removal of NO_x and diesel soot over nanostructured spinel-type oxides. *Journal of Catalysis*, 242:38–47, 2006.

[36] Lin H, Huang Z, and Shangguan W. Characteristics of oxidation of diesel particulate matter over a spinel type $Cu_{0.95}K_{0.05}Fe_2O_4$ catalyst. *Chemical Engineering and Technology*, 31:1433–1437, 2008.

[37] Drouet C, Alphonse P, and Rousset A. New spinel materials for catalytic $NO - CO$ reaction: nonstoichiometric nickel-copper manganites. *Applied Catalysis B: Environmental*, 32:35–43, 2001.

[38] Kogelschatz U. Dielectric-barrier discharges: Their history, discharge physics, and industrial applications. *Plasma Chemistry and Plasma Processing*, 23:1–45, 2003.

[39] Higashi M, Uchida S, Suzuki N, and Fujii K. Soot elimination and NO, and SO, reduction in diesel-engine exhaust by a combination of discharge plasma and oil dynamics. *IEEE Transactions on Plasma Science*, 20:1–12, 1992.

[40] Penetrante BM, Brusasco RM, Merritt BT, and Vogtlin GE. Environmental applications of the low-temperature plasmas. *Pure and Applied Chemistry*, 71:1829–1835, 1999.

[41] Penetrante BM, Brusasco RM, Merritt BT, Pitz WJ, Vogtlin GE, Kung MC, Kung HH, Wan CZ, and Voss KE. Plasma-assisted catalytic reduction of NO_x. *Society of the Automotive Engineers of Japan*, 90:57–66, 1998.

[42] www.eere.energy.gov/vehiclesandfuels/pdfs/deer_2002/session8/2002_deer_johnson.pdf.

[43] www.dieselnet.com/news/1999/12jm.php.

[44] Grzybek T. Layered clays as SCR deNOx catalysts. *Catalysis Today*, 119:125–132, 2007.

[45] Serwicka EM. Clays as catalysts for the removal of nitrogen oxides. *Polish Journal of Chemistry*, 75:307–328, 2001.

[46] Rohr F, Peter SD, Lox E, Kogel M, Sassi A, Juste L, Rigaudeau C, Belot G, Gelin P, and Primet M. On the mechanism of sulphur poisoning and regeneration of a commercial gasoline NO_x-storage catalyst. *Applied Catalysis B: Environmental*, 56:201–212, 2005.

[47] www.dieselnet.com/standards/eu/fuel.php.

[48] www.wikipidia.org/wiki/ultra-low_sulfur_diesel.

[49] Pancharatnam S, Huggins RA, and Mason DM. Catalytic decomposition of nitric oxide on zirconia by electrolytic removal of oxygen. *Journal of The Electrochemical Society*, 122:869–875, 1975.

[50] Gür TM and Huggins RA. Decomposition of nitric oxide on zirconia in a solid-state electrochemical cell. *Journal of The Electrochemical Society*, 126:1067–1074, 1979.

[51] Iwayama K and Wang X. Selective decomposition of nitrogen monoxide to nitrogen in the presence of oxygen on RuO_2/Ag(cathode)/yttria-stabilized zirconia/Pd(anode). *Applied Catalysis B: Environmental*, 19:137–142, 1998.

[52] Hibino T. Electrochemical removal of both NO and CH_4 under lean-burn conditions. *Journal of Applied Electrochemistry*, 25:203–207, 1995.

[53] Hibino T, Ushiki K, and Kuwahara Y. Medium-temperature electrolysis of NO and CH_4 under lean-burn conditions using yttria-stabilized zirconia as a solid state electrolyte. *Journal of the Chemical Society, Faraday Transactions*, 91:1955–1959, 1995.

[54] Hamamoto K, Fujishiro Y, and Awano M. Intermediate temperature electrochemical reactor for NO_x decomposition. *Journal of the Electrochemical Society*, 153:D167–D170, 2006.

[55] Hamamoto K, Fujishiro Y, and Awano M. Reduction and reoxidation reaction of catalytic layers in electrochemical cells for NO_x decomposition. *Journal of The Electrochemical Society*, 154:F172–F175, 2007.

[56] Simonsen VLE, Johnsen MM, and Hansen KK. Influence of BaO in perovskite electrodes for the electrochemical reduction of NO_x. *Topics in catalysis*, 45:131–135, 2007.

[57] Hansen KK. Electrochemical reduction of NO_2 studied by the use of cone-shaped electrodes. *Electrochemical Communications*, 9:2721–2724, 2007.

[58] Kammer Hansen K, Skou EM, and Christensen H. Perovskites as cathodes for nitric oxide reduction. *Journal of The Electrochemical Society*, 147:2007–2012, 2000.

[59] Kammer K and Skou EM. LSFM perovskites as cathodes for the electrochemical reduction of NO. *Solid State Ionics*, 176:915–920, 2005.

[60] Simonsen VLE, Nørskov L, and Hansen KK. Electrochemical reduction of NO and O_2 on $La_{2-x}Sr_xCuO_4$-based electrodes. *Journal of Solid State Electrochemistry*, 12:1573–1577, 2008.

[61] Simonsen VLE, Find D, Lilliedal M, Petersen R, and Kammer K. Spinels as cathodes for electrochemical reduction of O_2 and NO. *Topics in Catalysis*, 45:143–148, 2007.

[62] Hansen KK, Christensen H, and Skou EM. Electrochemical reduction of NO and O_2 on oxide based electrodes. *Ionics*, 6:340–345, 2000.

[63] Hamamoto K, Fujishiro Y, and Awano M. Low-temperature NO_x decomposition using an electrochemical reactor. *Journal of the Electrochemical Society*, 8:E109–E111, 2008.

[64] www.aist.go.jp/aiste/latestresearch/2008/20080526/20080526.html.

[65] Zeming H, Andersen KB, Keel L, Nygaard FB, Menon M, and Hansen KK. Processing and characterization of porous electrochemical cells for flue gas purification. *Ionics*, DOI 10.1007/s11581-008-0286-0, 2009.

[66] Adler SB, Lane JA, and Steele BCH. Electrode kinetics of porous mixed-conducting oxygen electrodes. *Journal of the Electrochemical Society*, 143:3554–3564, 1996.

[67] Knop O, Reid KIG, Sutarno R, and Nakagawa Y. Chalkogenides of the transition elements. vi. X-ray, neutron, and magnetic investigation of the spinels Co_3O_4, $NiCo_2O_4$, Co_3S_4, and $NiCo_2S_4$. *Canadian Journal of Chemistry*, 46:3463–3476, 1968.

[68] Duda H, Jendrzejewska I, Groń T, Mazur S, Zajdel P, and Kita A. Influence of vacancies on the electrical properties of the $ZnCr_{2-x}Ni_xSe_4$ spinels. *Journal of Physics and Chemistry of Solids*, 68:80–86, 2007.

[69] Suzuyama T, Awaka J, Yamamotoa H, Ebisu S, Ito M, Suzuki T, Nakama T, Yagasaki K, and Nagata S. Ferromagnetic-phase transition in the spinel-type $CuCr_2Te_4$. *Journal of Solid State Chemistry*, 179:140–144, 2006.

[70] Al-Shahrani AA. Sintering behavior and thermal property of Mg_2SnO_4. *Journal of Materials Science: Materials in Electronics*, 16:193–196, 2005.

[71] Arillo MA, Lopez ML, Fernandez MT, Veiga ML, and Pico C. Preparation and magnetic properties of $LiCr_{1-x}Al_xTiO_4$ ($0 \leq x \leq 0.4$). *Journal of Solid State Chemistry*, 125:211–215, 1996.

[72] Busey RH and Keller Jr OL. Structure of the aqueous pertechnetate ion by raman and infrared spectroscopy. raman and infrared spectra of crystalline $KTcO_4$, $KReO_4$, Na_2MoO_4, Na_2WO_4, $Na_2MoO_4 \cdot 2H_2O$, and $Na_2WO_4 \cdot 2H_2O$. *The Journal of Chemical Physics*, 41:215–225, 1964.

[73] O'Bryan HM and Dimarcello FV. Oxygen diffusion in nickel ferrous ferrite. *Journal of the American Ceramic Society*, 53:413–416, 1970.

[74] Dieckmann R. Point defects and transport properties of binary and ternary oxides. *Solid State Ionics*, 12:1–22, 1984.

[75] Sakai N, Horita T, Xiong YP, Yamaji K, Kishimoto H, Brito ME, Yokokawa H, and Maruyama T. Structure and transport property of manganese-chromium-iron oxide as a main compound in oxide scales of alloy interconnects for SOFCs. *Solid State Ionics*, 176:681–686, 2005.

[76] Millot F and Niu Y. Diffusion of O^{18} in Fe_3O_4: An experimental approach to study the behavior of minority defects in oxides. *Journal of Physics and Chemistry of Solids*, 58:63–72, 1997.

[77] Petric A and Ling H. Electrical conductivity and thermal expansion of spinels at elevated temperatures. *Journal of the American Ceramic Society*, 90:1515–1520, 2007.

[78] Jurgen RK. *Automotive Electronics Handbook*, chapter 6. McGraw-Hill Professional, 2 edition, 1999.

[79] Kharton VV, Marques FMB, and Atkinson A. Transport properties of solid oxide electrolyte ceramics: a brief review. *Solid State Ionics*, 174:135149, 2004.

[80] Wallenberg R, Winthers R, Bevan DJM, Thompson JG, Barlow, and Hyde BG. The fluorite-related solid solutions of $CeO_2, -Y_2O_3$ i: A re-examination by electron microscopy and diffraction. *Journal of the Less-Common Metals*, 156:1–16, 1989.

[81] Wallenberg R, Winthers R, Bevan DJM, Thompson JG, Barlow, and Hyde BG. The fluorite-related solid solutions of $CeO_2, -Y_2O_3$ ii: A modulated structure approach. *Journal of the Less-Common Metals*, 156:17–27, 1989.

[82] Koester L, Rauch H, and Seymann E. Neutron scattering lengths: A survey of experimental data and methods. *Applied Catalysis B: Environmental*, 49:65120, 1991.

[83] Goldstein JI, Newbury DE, Echlin P, Joy DC, Lyman CE, Lifshin E, Sawyer L, and Michael JR. *Scanning Electron Microscopy and X-ray Microanalysis*. Springer, 3 edition, 2003.

[84] Bræstrup F and Hansen KK. The $NiFe_2O_4 - MgFe_2O_4$ series as electrode materials for electrochemical reduction of NO_x. *Journal of Solid State Electrochemistry*, DOI 10.1007/s10008-008-0653-9, 2009.

[85] Søgaard M, Hendriksen PV, and Mogensen M. Oxygen nonstoichiometry and transport properties of strontium substituted lanthanum ferrite. *Journal of Solid State Chemistry*, 180:1489–1503, 2007.

[86] Fagg DP, Kharton VV, Shaula A, Marozau IP, and Frade JR. Mixed conductivity, thermal expansion, and oxygen permeability of $Ce(Pr, Zr)O_{2-\delta}$. *Solid State Ionics*, 176:1723–1730, 2005.

[87] Grunes LA. Study of the edges of $3d$ transition metals in pure and oxide form by X-ray spectroscopy. *Physical Review B*, 27:2111–2131, 1983.

[88] Bare SR, Yang N, Kelly CD, and Mickelson GE. Design and operation of a high pressure reaction cell for in situ X-ray absorption spectroscopy. *Catalysis Today*, 126:18–26, 2007.

[89] Pletcher D. *A first course in electrode processes*. Alresford press Ltd, England, 1 edition, 1991.

[90] Tafel J. The polarisation of cathodic hydrogen development. *Zeitschrift fur Physikalische Chemie*, 50:641–712, 1905.

[91] Application note: Basic of Electrochemical Impedance Spectroscopy. www.gamry.com/app_notes/eis_primer/eis_primer_2007.pdf.

[92] Barsoukov E and JR Macdonald. *Impedance Spectroscopy, Theory, Experiment, and Applications*. John Wiley & Sons, Inc., 2 edition, 2005.

[93] Macdonald JR. Note on the parameterization of the constant-phase admittance element. *Solid State Ionics*, 13:147–149, 1984.

[94] Newman J. Resistance for flow of current to a disk. *Journal of the Electrochemical Society*, 113:501–502, 1966.

[95] Barfod R Wang WG, Larsen PH, Kammer K, Bentzen JJ, Hendriksen PV, Mogensen M, Editors: Singhal SC, and Dokiya M. *Improvement of* LSM *Cathode for High Power Density* SOFC*s*, volume 7. The Electrochemical Society Inc, Pennington, USA, 2003.

[96] Chick LA, Pederson LR, Maupin GD, Bates JL, Thomas LE, and Exarhos GJ. Glycine-nitrate combustion synthesis of oxide ceramic powder. *Materials Letters*, 10:6–12, 1990.

[97] Koteswara Rao K, Banu T, Vithal M, Swamy GYSK, and Ravi Kumar K. Preparation and characterization of bulk and nano particles of $La_2Zr_2O_7$ and $Nd_2Zr_2O_7$ by sol-gel method. *Materials Letters*, 54:205–210, 2002.

[98] Hansen KK and Vels Hansen K. A-site deficient $(La_{0.6}Sr_{0.4})_{1-s}Fe_{0.8}Co_{0.2}O_{3-\delta}$ perovskites as SOFC cathodes. *Solid State Ionics*, 178:1379–1384, 2007.

[99] www.comsol.com, comsol version 3.4 (2007).

[100] Smart L and Moore E. *Solid State Chemistry, an introduction.* Nelson Thomes Ltd, UK, 2 edition, 2001.

[101] Hauback BC, Fjellvag H, Steinsvoll O, Johansson K, Buste OT, and Jorgensen J. The high resolution powder neutron diffraction PUS at the JEEP II reactor at Kjeller in Norway. *The Journal of Neutron Research*, 8:215–232, 2000.

[102] Hagen A, Schueler K, and Roessner F. The performance of ti-MCM-41 in aqueous media and after mechanical treatment studied by in situ XANES, UV/Vis and test reactions. *Microporous and Mesoporous Materials*, 51:23–33, 2002.

[103] www.hasylab.desy.de/facilities/dorisiii/beamlines/e4exafsii/beamlinelayout/indexeng.html.

[104] Bruggeman DAG. Calculation of various physical constants of heterogeneous substances. i. dielectric constant and conductivity of mixtures of isotropic substances. *Annalen der Physik*, 24:636–664, 1935.

[105] Fabry P, Kleitz M, and Deportes C. Sur l'utilisation d'une electrode ponctuelle dans les cellules oxyde electrolyte solide. *Journal of Solid State Chemistry*, 5:1–10, 1972.

[106] Winkler J, Hendriksen PV, Bonanos N, and Mogensen M. Geometric requirements of solid electrolyte cells with a reference electrode. *Journal of The Electrochemical Society*, 145:1184–1192, 1998.

[107] Miletic M, Gland JL, Hass KC, and Schneider WF. First-principles characterization of NO_x adsorption on MgO. *Journal of Physical Chemistry B*, 107:157–163, 2003.

[108] Ponpandian N, Balaya P, and Narayanasamy A. Electrical conductivity and dielectric behaviour of nanocrystalline $NiFe_2O_4$ spinel. *Journal of Physics: Condensed Matter*, 14:3221–3237, 2002.

[109] C. Klein, C. S. Hurlbut, and J. D. Dana. *Manual of Mineralogy*, volume 21. John Wiley & Sons Inc, 1998.

[110] West DL, Montgomery FC, and Armstrong TR. Electrically biased NO_x sensing elements with coplanar electrodes. *Journal of The Electrochemical Society*, 152:H74–H79, 2005.

[111] Ziemniak SE, Anovitz LM, Castelli RA, and Porter WD. Magnetic contribution to heat capacity and entropy of nickel ferrite ($NiFe_2O_4$). *Journal of Physics and Chemistry of Solids*, 68:1021, 2007.

[112] Harrison RJ and Putnis A. Determination of the mechanism of cation ordering in magnesioferrite ($MgFe_2O_4$) from the time- and temperature-dependence of magnetic susceptibility. *Physics and Chemistry of Minerals*, 26:322–332, 1999.

[113] Turkin AI and Drebushchak VA. Synthesis and calorimetric investigation of stoichiometric Fe-spinels: $MgFe_2O_4$. *Journal of Crystal growth*, 265:165–167, 2004.

[114] Modi KB, Joshi HH, and Kulkarni RG. Magnetic and electrical properties of Al^{3+}-substituted $MgFe_2O_4$. *Journal of Materials Science*, 31:1311–1317, 1996.

[115] Carter RE. Thermal expansion of $MgFe_2O_4$, FeO, and $MgO \cdot 2FeO$. *Journal of the University of Chemical Technology and Metallurgy*, 43:53–58, 2008.

[116] Weil L. Anomalie de longueur des ferrites. *Le Journal de Physique et Le Radium*, 12:260–261, 1951.

[117] Søgaard M. *Undersøgelse af transport-egenskaber og oxygenstøkiometri i* $(La_{0,6}Sr_{0,4})_{0,99}Co_{1-y}Fe_yO_{3-\delta}$. PhD thesis, Kemisk Institut, Syddansk Universitet & Forskningscenter Risø, Roskilde, 2002.

[118] Redfern SAT. Neutron powder diffraction of minerals at high pressures and temperatures: some recent technical developments and scientific applications. *European Journal of Mineralogy*, 14:251–261, 2002.

[119] Levy D, Diella V, Dapiaggi M, Sani A, Gemmi M, and Pavese A. Equation of state, structural behaviour and phase diagram of synthetic $MgFe_2O_4$, as a function of pressure and temperature. *Physics and Chemistry of Minerals*, 31:122–129, 2004.

[120] Antao SM, Hassan I, and Parise JB. Cation ordering in magnesioferrite, $MgFe_2O_4$, to 982 °C using in situ synchrotron X-ray powder diffraction. *American Mineralogist*, 90:219–228, 2005.

[121] Bevan DJM, Shelton JP, and Anderson JS. Properties of some simple oxides and spinels at high temperatures. *Journal of the Chemical Society*, NOV:1729–1741, 1948.

[122] Brabers VAM and Klerk J. Kinetics of the cation redistribution in magnesium ferrites. *Journal de Physique*, 38:207–209, 1977.

[123] Corbel G, Mestiri S, and Lacorre P. Physicochemical compatibility of CGO fluorite, LSM and LSCF perovskite electrode materials with $La_2Mo_2O_9$ fast oxide-ion conductor. *Solid State Sciences*, 7:1216–1224, 2005.

[124] Berchmans LJ, Selvan RK, Kumar PNS, and Augustin CO. Structural and electrical properties of $Ni_{1-x}Mg_xFe_2O_4$ synthesized by citrate gel process. *Journal of Magnetism and Magnetic Materials*, 279:103–110, 2004.

[125] Berchmans LJ, Selvan RK, and Augustin CO. Evaluation of Mg^{2+}-substituted $NiFe_2O_4$ as a green anode material. *Materials Letters*, 58:1928 1933, 2004.

[126] Ata-Allah SS, Fayek MK, and Yehia M. Mössbauer and DC electrical resistivity study of Zn substituted tetragonal $CuFe_{2-y}Ga_yO_4$ compound. *Journal of Magnetism and Magnetic Materials*, 279:411–420, 2004.

[127] Ata-Allah SS, Sayedamed FM, Kaiser M, and Hashhash AM. Crystallographic and low frequency conductivity studies of the spinel systems $CuFe_2O_4$ and $Cu_{1-x}Zn_xGa_{0.1}Fe_{1.9}O_4$; $(0.0 \leq x \leq 0.5)$. *Journal of Materials Science*, 40:2923–2930, 2005.

[128] Bozorth RM. *Ferromagnetism*, chapter 14. D. Van Nostrand Company Inc., New York, 5 edition, 1951.

[129] Rezlescu N, Doroftei C, Rezlescu E, and Popa PD. The influence of Sn^{4+} and/or Mo^{6+} ions on the structure, electrical and gas sensing properties of Mg-ferrite. *Physics of the Solid State*, 203:306–316, 2006.

[130] Ciacchi FT, Crane KM, and Badwal SPS. Evaluation of commercial zirconia powders for solid oxide fuel cells. *Solid State Ionics*, 73:49–61, 1994.

[131] Fonseca FC and Muccillo R. Impedance spectroscopy analysis of percolation in (yttria-stabilized zirconia)-yttria ceramic composites. *Solid State Ionics*, 166:157–165, 2004.

[132] Hendriks MGHM. The electrochemical double-layer capacitance of yttria-stabilised zirconia. *Solid State Ionics*, 146:211–217, 2002.

[133] Pornprasertsuk R, Gheng J, Huang H, and Prinz FB. Electrochemical impedance analysis of solid oxide fuel cell electrolyte using kinetic Monte Carlo technique. *Solid State Ionics*, 178:195–205, 2002.

[134] Høgh J. *Influence of impurities on the $H_2/H_2O/Ni/YSZ$ electrode.* PhD thesis, Technical University of Denmark & Risø National Laboratory, Roskilde, 2005.

[135] Glasson WA and Tuesday CS. The atmospheric thermal oxidation of nitric oxide. *Journal of the American Chemical Society*, 85:2901–2904, 1963.

[136] Tsukahara H, Ishida T, and Mayumi M. Gas-phase oxidation of nitric oxide: Chemical kinetics and rate constant. *Nitric Oxide: Biology and Chemistry*, 3:191–197, 1999.

[137] Pattrick G, van der Lingen E, Corti CW, Holliday RJ, and Thompson DT. The potential for use of gold in automotive pollution control technologies: a short review. *Topics in Catalysis*, 30/31:273–279, 2004.

[138] Fuel Cells Private communications with scientist Kent Kammer Hansen and Technical University of Denmark Solid State Chemistry Division, Risø National Laboratory for Sustainable Energy.

[139] Zhuiykov S, Nakano T, Kunimoto A, Yamazoe N, and Miura N. Potentiometric NO_x sensor based on stabilized zirconia and $NiCr_2O_4$ sensing electrode operating at high temperatures. *Electrochemistry Communications*, 3:97–101, 2001.

[140] Stranzenbach M, Gramckow E, and Saruhan B. Planar, impedance-metric NO_x-sensor with spinel-type SE for high temperature applications. *Sensors and Actuators B*, 127:224–230, 2007.

[141] Bræstrup F and Hansen KK. $NiCr_xFe_{2-x}O_4$ as cathode materials for electrochemical reduction of NO_x. *Journal of Solid State Electrochemistry*, DOI 10.1007/s10008-009-0801-x, 2009.

[142] Miyahara S and Tsushima T. Magnetic properties of nickel and cobalt ferrite-chromite series. *Journal of the Physical Society of Japan*, 13:758–758, 1958.

[143] Kedem D and Rothem T. Internal fields in nickel ferrite. *Physical Review Letters*, 18:165–166, 1967.

[144] Bongers PF. Principles and application of crystal field theory. *Philips Technical Review*, 28:13–18, 1967.

[145] Yaresko A and Antonov V. Magnetic interactions in Cr spinels. *Journal of Magnetism and Magnetic Materials*, 310:1672–1674, 2007.

[146] Touloukian YS and Ho CY. Thermal expansion, nonmetallic solids. In *Thermophysical Properties of matter, The TPRC Data Series*, volume 13. Plenum Publishing Corporation, New York, 1977.

[147] Rais A, Gismelseed AM, and Al-Omari IA. Cation distribution and magnetic properties of nickel-chromium ferrite $NiCr_xFe_{2-x}O_4$ ($\leq x \leq 1.4$). *Physica Status Solidi B*, 242:1497–1503, 2005.

[148] Bard AJ and Faulkner LR. *Electrochemical Methods*. John Wiley & Sons, New York, 2 edition, 2001.

[149] Atkins P and de Paula J. *Atkins' Physical Chemistry*. Oxford University Press, 7 edition, 2002.

[150] Holcomb GR and Alman DE. The effect of manganese additions on the reactive evaporation of chromium in $Ni - Cr$ alloys. *Scripta Materialia*, 54:1821–1825, 2006.

[151] Machkova M, Zwetanova, Kozhukharov V, and Raicheva S. Thermodynamic treatment of chromium evaporation from steel SOFC interconnects. *Journal of the University of Chemical Technology and Metallurgy*, 43:53–58, 2008.

[152] Mikuli E, Migdal-Mikuli A, Chyży R, Grad B, and Dziembaj R. Melting and thermal decomposition of $[Ni(H_2O)_6](NO_3)_2$. *Thermochimica Acta*, 370:65–71, 2001.

[153] Lide DR. *CRC Handbook of Chemistry and Physics*. CRC Press, New York, 87 edition, 2007.

[154] Gusmano G, Montesperelli G, Nunziante P, and Traversa E. Humidity-sensitive electrical response of sintered $MgFe_2O_4$. *Journal of Material Science*, 28:6195–6198, 1993.

[155] Bræstrup F and Hansen KK. Characterization of $MgMn_xFe_{\mathbf{2}-x}O_{\mathbf{4}}$ as a possible cathode material for electrochemical reduction of NO_x. *Journal of Applied Electrochemistry*, manuscript accepted, 2009.

[156] Kulkarni JA and Darshane VS. Effect of high temperatures on cation distribution: $NiMn_2O_4 - FeMn_2O_4$ system. *Thermochimica Acta*, 93:473–476, 1985.

[157] Gillot B, Baudour JL, Bouree F, Metz R, Legros R, and Rousset A. Ionic configuration and cation distribution in cubic nickel manganite spinels $Ni_xMn_{3-x}O_4$ ($0.57 < x < 1$) in relation with thermal histories. *Solid State Ionics*, 58:155–161, 1992.

[158] www.webelements.com/manganese/atomsizes.html.

[159] Hirota K, Saruwatari K, Kato M, Nakade K, and Yoshinaga M. Low-temperature sintering of $Mg(Fe_{1-x}Mn_x)_2O_4$ ($0 \leq x \leq 0.4$) ferrite powders prepared via a citric acid route. *The Science and Engineering Review of Doshisha University*, 49:1–9, 2008.

[160] Zhang CL, Yeo S, Horibe Y, Choi YJ, Guha S, Croft M, Cheong SW, and Mori S. Coercivity and nanostructure in magnetic spinel $M(Mn, Fe)_2O_4$. *Applied Physics letters*, 90:133123/1–133123/3, 2007.

[161] Mori M, Hiei Y, Sammes NM, and Tompsett GA. Thermal-expansion behaviors and mechanisms for Ca- or Sr-doped lanthanum manganite perovskites under oxidizing atmospheres. *Journal of the Electrochemical Society*, 147:1295–1302, 2000.

[162] N. M. Tallan. *Electrical conductivity in ceramics and glass: part* A – B. New York: Dekker, 1974.

[163] Bræstrup F, Hauback BC, and Hansen KK. Temperature dependence of the cation distribution in $ZnFe_2O_4$ measured with high temperature neutron diffraction. *Journal of Solid State Chemistry*, 181:23642369, 2008.

[164] Zhuiykov S, Muta M, Ono T, Hasei M, Yamazoe N, and Miura N. Stabilized zirconia-based NO_x sensor using $ZnFe_2O_4$ sensing electrode. *Electrochemical and Solid-State Letters*, 4:H19–H21, 2001.

[165] Zhuiykov S, Ono T, Yamazoe N, and Miura N. High-temperature NO_x sensors using zirconia solid electrolyte and zinc-family oxide sensing electrode. *Solid State Ionics*, 152-153:801–807, 2002.

[166] Zhang G, Chunsheng L, Fangyi C, and Chen J. $ZnFe_2O_4$ tubes: Synthesis and application to gas sensors with high sensitivity and low-energy consumption. *Sensors and Actuators B*, 120:403–410, 2007.

[167] Arshak K and Gaidan I. Effects of NiO/TiO_2 addition in $ZnFe_2O_4$-based gas sensors in the form of polymer thick films. *Materials Science and Engineering B*, 118:44–49, 2005.

[168] M. Wen, Q. Li, and Y. Li. Magnetic, electronic and structural properties of $Zn_xFe_{3-x}O_4$. *Journal of Electron Spectroscopy and related Phenomena*, 153:65–70, 2006.

[169] Brabers VAM. The zinc-ferrite system revisited. *Journal of Physics IV France*, 7:C1233–C1236, 1997.

[170] P. W. Anderson. Antiferromagnetism. theory of superexchange interaction. *Physical Review*, 79:350–356, 1950.

[171] T. Kamiyama, K. Haneda, T. Sato, S. Ikeda, and H. Asano. Cation distribution in $ZnFe_2O_4$ fine particles studied by neutron powder diffraction. *Solid State Communications*, 81:563–566, 1992.

[172] F. K. Lotgering. The influence of the Fe^{3+} ions at tetrahedral sites on the magnetic properties of $ZnFe_2O_4$. *Journal of Physics and Chemistry of Solids*, 27:139–145, 1966.

[173] V. Šepelák, K. Tkáčová, V. V. Boldyrev, S. Wissmann, and K. D. Becker. Mechanically induced cation redistribution in $ZnFe_2O_4$ and its thermal stability. *Physica B*, 234-236:617–619, 1997.

[174] A. Hosseinpour, H. Sadeghi, and A. Morisako. Simulation of DC-hopping conduction in spinel ferrites using free electron gas model. *Journal of Magnetism and Magnetic Materials*, 316:e283–e286, 2007.

[175] Kofstad P. *Uorganisk Kjemi, En innføring i grunnstoffenes kjemi.* TANO A.S, 2 edition, 1987.

[176] V. Petříček, M. Dusek, and L. Palatinus. Jana2000, The crystallographic computing system, 2000.

[177] T. Hahn Ed. *International Tables for crystallography*, volume Vol A. John Wiley & Sons Inc, 3 edition, 1992.

[178] O. Crottaz, F. Kubel, and H. Schmid. Jumping crystals of the spinels $NiCr_2O_4$ and $CuCr_2O_4$. *Journal of Materials Chemistry*, 7:143–146, 1997.

[179] Bordeneuve H, Guillemet-Fritsch S, Rousset A, Schuurman S, and Poulain V. Structure and electrical properties of single-phase cobalt manganese oxide spinels h $Mn_{3-x}Co_xO_4$ sintered classically and spark plasma sintering (SPS). *Journal of Solid State Chemistry*, 182:396–401, 2009.

[180] Choi JJ, Ryu J, Hahn BD, Yoon WH, Lee BK, and Park DSM. Dense spinel $MnCo_2O_4$ film coating by aerosol deposition on ferritic steel alloy for protection of chromic evaporation and low-conductivity scale formation. *Journal of Materials Science*, 44:843–848, 2009.

[181] Shimizu Y and Shiotsuka M. Optoelectrochemical hydrogen-phosphate ion sensor based on electrochromism of spinel-type oxide thin-film electrode. *Japanese Journal of Applied Physics*, 41:6243–6246, 2002.

[182] Simonsen VLE. *Electrochemical Removal of Pollutants.* PhD thesis, Risø National Laboratory for Sustainable Energy, Technical University of Denmark, Fuel Cells and Solis State Chemistry Division & Syddansk Universitet, Department of Physics and Chemistry, 2008.

[183] Schmidt R and Brinkman AW. Small polaron hopping in spinel manganates. *Physical Review B*, 72:115101/1–115101/9, 2005.

[184] Lisboa-Filho PN, Bahout M, Barahona P, Moure C, and Pe na O. Oxygen stoichiometry effects in spinel-type $NiMn_2O_{4-\delta}$ samples. *Journal of Physics and Chemistry of Solids*, 66:1206–1212, 2005.

[185] Csete de Gyürgyfalva GDC and Reaney IM. Decomposition of $NiMn_2O_4$ spinels. *Journal of Materials Research*, 18:1301–1308, 2003.

[186] Safontseva N Tu and Nikiforov I Ya. On the shape of iron k absorption edges for monoferrites with a me(Mg, Mn, Ni, Zn)Fe_2O_4 spinel structure. *Physics of the Solid State*, 43:61–64, 2001.

[187] Haas O, Vogt UF, Soltmann C, Braun A, Yoon WS, Yang XQ, and Graule T. The Fe K-edge x-ray absorption characteristics of $La_{1-x}Sr_xFeO_{3-\delta}$. *Materials Research Bulletin*, 44:1397–1404, 2009.

[188] Fuel Cells Private communications with Ph.D. student Jonas Östby and Technical University of Denmark Solid State Chemistry Division, Risø National Laboratory for Sustainable Energy.

[189] Jonas Östby. *Study of the Co-Cr-Mn-O spinels: stability, electrical conductivity, XAFS, and defect chemistry.* PhD thesis, The Niels Bohr Institute, Faculty of Science, University of Copenhagen & Risø National Laboratory for Sustainable Energy, Technical University of Denmark (*in press*, 2009.

[190] Fleet ME. The structure of magnetite. *Acta Crystallographica B*, 37:917–920, 1981.

[191] Putnis A. *Introduction to Mineral Science.* Cambridge University Press, 1 edition, 2001.

[192] Calvin S, Carpenter EE, Ravel B, and Harris VG. Multiedge refinement of extended X-ray-abserption fine structure of manganese zinc ferrite nanoparticles. *Physical Review B*, 66:224405/1–224405/13, 2002.

Appendix A

List of publications

I

Bræstrup F, Hauback BC and Hansen KK, Temperature dependence of the cation distribution in $ZnFe_2O_4$ measured with high temperature neutron diffraction, *Journal of Solid State Chemistry* (2008) 181, 23642369.

II

Bræstrup F and Hansen KK, The $NiFe_2O_4 - MgFe_2O_4$ series as electrode materials for electrochemical reduction of NO_x, *Journal of Solid State Electrochemistry* (2009), DOI 10.1007/s10008-008-0653-9.

III

Bræstrup F and Hansen KK, $NiCr_xFe_{2-x}O_4$ as cathode materials for electrochemical reduction of NO_x, *Journal of Solid State Electrochemistry* (2009), DOI 10.1007/s10008-009-0801-x.

IV

Bræstrup F and Hansen KK, Characterization of $MgMn_xFe_{2-x}O_4$ as a possible cathode material for electrochemical reduction of NO_x, *Journal of Applied Electrochemistry* (2009), manuscript accepted.

I

Journal of Solid State Chemistry 181 (2008) 2364–2369

Contents lists available at ScienceDirect

Journal of Solid State Chemistry

journal homepage: www.elsevier.com/locate/jssc

Temperature dependence of the cation distribution in $ZnFe_2O_4$ measured with high temperature neutron diffraction

F. Bræstrup [a,*], B.C. Hauback [b], K.K. Hansen [a]

[a] Fuel Cells and Solid State Chemistry Department, National Laboratory for Sustainable Energy, Frederiksborgvej 399, 4000 Roskilde, Denmark
[b] Physics Department, Institute for Energy Technology, NO-2027 Kjeller, Norway

ARTICLE INFO

Article history:
Received 22 January 2008
Received in revised form
6 May 2008
Accepted 11 May 2008
Available online 24 May 2008

Keywords:
Spinel-type oxide
Conductivity
Powder diffraction

ABSTRACT

$ZnFe_2O_4$ has a spinel-type structure with Zn^{2+} ions located mainly on tetrahedral sites and Fe^{3+} ions located on octahedral sites. $ZnFe_2O_4$ was synthesized in air by a solid state reaction and characterized with X-ray diffraction, high temperature neutron diffraction, resistivity measurements and dilatometry. The distribution of cations in $ZnFe_2O_4$ was measured from 298 to 1243 K and results show that above 673 K the cations start to redistributed in the structure. $ZnFe_2O_4$ has a semi-conducting behavior at room temperature, but at temperatures above 905 K the conductivity decreases as the result of an Fe–Fe interaction between octahedral sites.

1. Introduction

Spinels are a very large class of compounds which are isotypic with the mineral spinel $MgAl_2O_4$. Spinel materials are widely used in the industry because of their usefulness as magnetic materials, semi-conductors, pigments, catalysts and refractories. Most of them are oxides but also sulphates, selenides and tellurides are know to have the spinel structure [1–3]. The spinel structure of oxides (AB_2O_4) is build up around O^{2-} ions which form a face-centered close cubic packing (CCP) sequence, with 16 tetrahedral sites and 64 octahedral sites per unit cell. The CCP layers of oxygen are stacked parallel to {111}, resulting in alternating layers of octahedral sites and tetrahedral sites. Several different cations can be introduced in the structure which leads to a variety of different charge combinations e.g. $SnMg_2O_4$, $LiCrTiO_4$ or Na_2WO_4 [4–6]. Spinels are traditionally divided into two different ideal types of structures: the *normal* spinel structure and the *inverse* spinel structure. In normal spinels, A ions are located on tetrahedral sites and B ions on octahedral sites. Inverse spinels have half the B ions located on tetrahedral sites, while the rest of the B ions and the A ions occupies the octahedral sites. The cation distribution is often quantified with the parameter γ, which corresponds to the fraction of A ions on the octahedral sites. Spinel-type materials with a normal spinel structure will have $\gamma = 0$, whereas inverse spinel structures will have a γ-value of 1.

$ZnFe_2O_4$ has an almost normal spinel structure with Zn^{2+} located on tetrahedral sites and Fe^{3+} located on octahedral sites. $ZnFe_2O_4$ is a promising electrode material in NO and NO_2 sensors [7,8] and the material has also received much interest as a possible sensor material for organic compounds such as ethanol, acetone and propanol [9,10]. Other reports also indicate that $ZnFe_2O_4$ is active toward Cl_2 gas-sensing [11].

O'Neill [12] have studied the temperature dependence of the cation distribution with X-ray diffraction by quenching the samples in water but he was not able to refine the occupancies on the tetrahedral sites. Kamiyama et al. [13] and Ligenza [14] analyzed the cation distribution by neutron diffraction but only in the temperature range of 4.2−300 K. To our knowledge no in situ high temperature neutron diffraction (HTND) have been performed on $ZnFe_2O_4$. HTND was therefore used in this study for precise determination of the distribution of the cations at different temperatures in $ZnFe_2O_4$.

2. Experimental details

2.1. Sample preparation and X-ray diffraction

$ZnFe_2O_4$ was synthesized with a solid state reaction using powder of metal oxides (ZnO 99.99% (Alfa Aesar) and α-Fe_2O_3 99.9% (Alfa Aesar)). The powder was mixed in an agate mortar and calcined at 1173 K for 30 h with a ramp rate of 373 K/h. The powder was then crushed in an agate mortar and the calcination process was repeated. The spinel powder was analyzed in air at

* Corresponding author. Fax: +45 46775858.
E-mail address: frantz.braestrup@risoe.dk (F. Bræstrup).

0022-4596/$ - see front matter © 2008 Elsevier Inc. All rights reserved.
doi:10.1016/j.jssc.2008.05.028

room temperature with X-ray diffraction on a theta–theta STOE diffractometer with a Cu anode. The powder was measured in the 2θ-range from 10° to 130° with a step width of 0.02° and an exposure time of 10 s. The powder was pressed on a CompaC PRESS at 1 ton for 30 s into an elongated rod ($4 \times 4 \times 35$ mm) which were placed in a rubber sleeve and pressed isostatically at 50 ton for 20 s using a STENHØJ 100 PRESS. The samples were then calcined at 1473 K for 6 h with a ramp rate of 373 K/h. The elongated rod was cut into two pieces: one was used for resistivity measurements ($4 \times 4 \times 18$ mm) while the other one ($4 \times 4 \times 12$ mm) was used to determine the linear thermal expansion coefficient, α.

2.2. Dilatometry

The linear thermal expansion was measured by dilatometry in air (50 ml/min) using a NETZSCH DIL 402C dilatometer with a sample load of 30 000 cN. The sample-rod was heated from room temperature up to 1273 K and back at 2 K/min. The sample remained at 1273 K for 2 h. Data were calibrated to an Al_2O_3 standard at identical conditions.

2.3. Four-point DC resistivity measurement

Platinum paste was applied to each end of the elongated rod and contacted with platinum leads. Two platinum potential probes with a fixed distance were positioned on one side of the bar. The data collection was made with an in-house data acquisition software, ELCHEMEA. The resistivity was measured every 5 min from room temperature to 1323 K and back again with a 2-h dwell at every 50 K interval and using a ramp rate of 2 K/min. In order to correct the resistivity for the porosity of the sample, the density of the elongated rod was measured by the Archimedes principle.

2.4. HTND

HTND was measured with a high-resolution powder neutron diffractometer, installed at a 2 MW JEEP II reactor at the Institute for Energy Technology in Kjeller, Norway. The powder was placed in a quartz tube inside a furnace and measured in air with a 2θ-range of 10–130°, a step width of 0.05° and a wavelength of 1.555 A using a Ge(511) monochromator. Two detector banks, each covering 20° in 2θ and containing seven ^{3}He position sensitive detectors stacked on top of each other, were used to record the neutron diffraction pattern. A more detailed description of the diffractometer can be found elsewhere [15].

Rietveld refinements were carried out using the program Jana2000 [16]. The neutron scattering lengths and the X-ray form factors were taken from the Jana2000 library. Pseudo-Voigt profile functions were used, and the background was modeled with a 10 terms Legendre polynomials.

3. Results

3.1. X-ray diffraction

X-ray powder diffraction showed that the material was a single spinel phase. The Rietveld refinement gave no satisfying result of the site occupancies because of the relatively small difference in the electron density of the cations. Therefore was only a Le Bail fit made in order to determine the unit cell parameter, $\mathbf{a} = 8.4309(2)$ A, at room temperature.

3.2. HTND

Fig. 1 shows the neutron diffraction patters of the spinel measured from 298 to 1243 K. Total 21–22 peaks were used in the refinement depending on the temperature. The neutron diffraction patterns were refined with Rietveld methods using JANA2000. All diffraction patterns were refined with the space group $Fd\bar{3}m$ (no. 227, origin choice 1) [17], but diffraction patterns measured at temperatures above 873 K were also refined with the space group $I4_1/amd$ (no. 141), which is reported for different spinel-type materials [18]. This was done in order to see if changes at the octahedral sites resulted in at change of symmetry, but refinements gave no satisfying results. Site occupancies of Zn and Fe were coupled not only between elements on the same lattice site, but also between the tetrahedral and the octahedral site. Cations on same lattice sites where assigned the same isotropic displacement parameter, U_{iso}. No impurity phases were detected as also found by X-ray diffraction. Table 1 shows an example of the refined structural parameters for $ZnFe_2O_4$ at 873 K and Fig. 2 shows the corresponding fitted neutron diffraction pattern. Refined parameters at different temperatures are shown in Table 2.

Fig. 3a shows the increase of the unit cell as a function of temperature. From 298 to 873 K, **a** increases linearly with a rate $7.3(4) \times 10^{-5}$ A K^{-1}. At 873 K the rate increases to $1.01(3) \times 10^{-4}$ A K^{-1} which is 38% faster than in the low temperature range.

Refinements show that the tetrahedrons are undistorted (not shown in Table 3) within experimental errors and change of bond distances does not seem to follow a trend through the measured temperature range. The octahedrons are on the other hand slightly distorted with increasing bond distances as a function of temperature. However, the bond distances on the octahedral sites

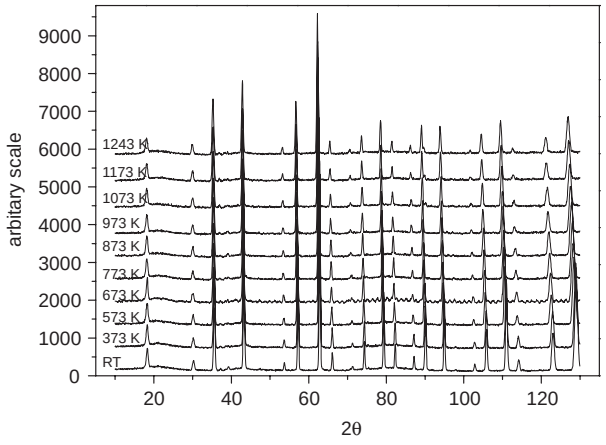

Fig. 1. HTND profiles of $ZnFe_2O_4$ at measured temperatures.

Table 1
Refined structural parameters of $ZnFe_2O_4$ at 873 K

Atom	Site	Occupancy	x	y	z	U_{iso}
Zn1	8a	0.0357(2)	0	0	0	0.0354(6)
Fe1	8a	0.0059(2)	0	0	0	0.0354(6)
Zn2	16d	0.0119(4)	0.625	0.625	0.625	0.0204(4)
Fe2	16d	0.0715(2)	0.625	0.625	0.625	0.0204(4)
O	32e	0.16667	0.3851(2)	0.3851(2)	0.3851(2)	0.0300(6)

Occupancies are given by the multiplicity of the site symmetry divided by the multiplicity of general sites.

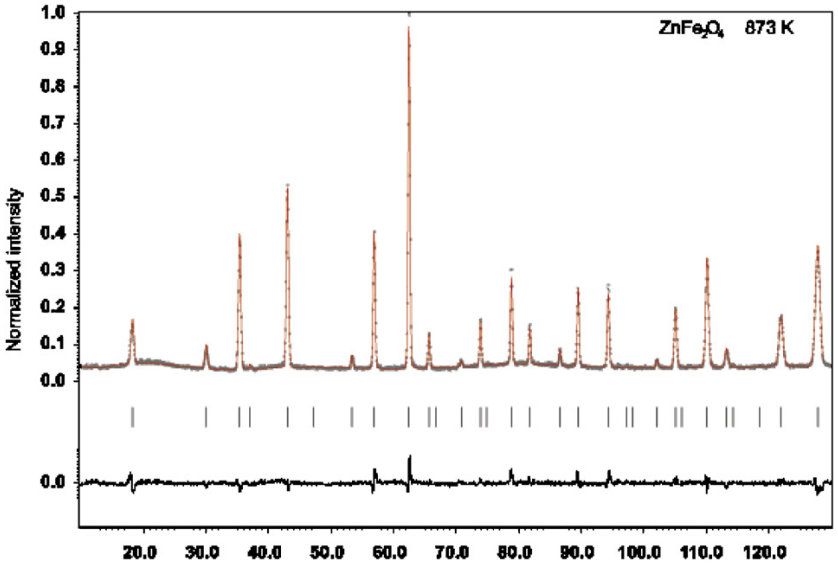

Fig. 2. Observed (gray) and calculated (red) intensities from Rietveld refinements of $ZnFe_2O_4$ at 873 K. The difference curve and the position of the Bragg reflections are shown in the lower part of the diffractogram.

Table 2

R-values, 'goodness of fit', gof, unit cell parameters, **a**, the position of oxygen, O_x, and isotropic displacement parameters, U_{iso} ($Å^2$), from the Rietveld refinements of the HTND patterns

Temp. (K)	R_p	wR_p	gof	**a** (Å)	O_x	U_{iso}, [4]	U_{iso}, [6]	U_{iso}, O_x
298	6.02	7.63	1.50	8.4371(4)	0.3849(1)	0.0164(7)	0.0124(4)	0.0175(5)
373	6.88	9.08	1.94	8.4473(6)	0.3844(2)	0.0163(7)	0.0139(8)	0.0196(9)
573	7.00	9.17	1.88	8.4573(6)	0.3852(1)	0.025(3)	0.0185(6)	0.0234(8)
673	7.05	9.18	1.96	8.4655(6)	0.3842(2)	0.026(1)	0.0231(6)	0.0303(9)
773	6.96	9.11	1.47	8.4753(3)	0.3853(2)	0.029(2)	0.0214(5)	0.0291(7)
873	6.01	7.66	1.25	8.4819(4)	0.3852(1)	0.0354(9)	0.0204(4)	0.0300(7)
973	5.89	7.38	1.20	8.4906(4)	0.3849(1)	0.0370(9)	0.0225(4)	0.0322(7)
1073	6.25	7.97	1.31	8.5025(4)	0.3846(2)	0.0394(9)	0.0251(5)	0.0345(7)
1173	6.02	7.70	1.25	8.5120(4)	0.3845(2)	0.0401(9)	0.0267(5)	0.0378(8)
1243	5.98	7.70	1.40	8.5186(4)	0.3840(2)	0.0414(9)	0.0272(5)	0.0415(8)
*373	6.52	8.27	1.34	8.4473(4)	0.3849(1)	0.0197(7)	0.0138(4)	0.0198(6)
*573	6.46	8.20	1.34	8.4573(4)	0.3850(2)	0.028(8)	0.0170(4)	0.0265(6)

Values in square brackets refer to the coordination number of the cations. Temperatures marked with, *, refer to the diffraction patterns measured during cool down. No correlation coefficients where lager than $\rho_{ij} = 0.72$. Estimated standard deviations in parentheses.

do not follow a linear trend in the whole temperature range. A sudden increase is observed at 873 K as can be seen in Fig. 3b. The bond length at 373 and 673 K is slightly higher than would be expected. Same phenomenon can also be detected in the increasement of the volume (Fig. 3c).

Figs. 4a and b show the occupancy of Zn and Fe on the tetrahedral and the octahedral sites as a function of temperature. In the temperature range of 298–673 K the site occupancies are unchanged with 91% ($\gamma = 0.09$) of the Zn at the tetrahedral lattice site. At 773 K there is a sudden change in occupancies towards a higher cation ordering ($\gamma = 0.03$), but from 773 to 1243 K the site occupancies changes almost linearly and at 1243 K only 77% ($\gamma = 0.23$) of the Zn are still located at the tetrahedral site. After cooling down the sample a new diffraction pattern was recorded at 573 and 373 K. Results show that the site occupancies are almost identical to those found while heating up the sample. The sudden change in occupancies at 773 K was tried refined by constraining the occupancies, so they followed the main trend of the graph; however, it was not possible to obtain reasible isotropic displacement parameters of any of the atoms and *R*-values and goodness of fit did not improve significantly. A few correlation coefficients also increased, $\rho_{ij} > 0.8$.

3.3. Resistivity measurement

Fig. 5a shows the four-point DC specific resistivity of $ZnFe_2O_4$ as well as the temperature profile. Data have been corrected for the open porosity (1.7%). $ZnFe_2O_4$ was a semi-conductor already at room temperature, but after heating the sample, the semi-conducting behavior disappeared at around 390 K.

Fig. 5b shows an Arrhenius plot of the specific conductivity as a function of temperature. The graph shows a semi-conducting behavior with a linear increase in conductivity but with a distinct change of slope at 905 K. The data were fitted with [19]:

$$\sigma = \sigma_0 T^{-1} \exp \frac{-E_a}{k_B T} \quad (1)$$

where σ is the specific conductivity and k_B and T are the Boltzmann constant and the temperature, respectively. The

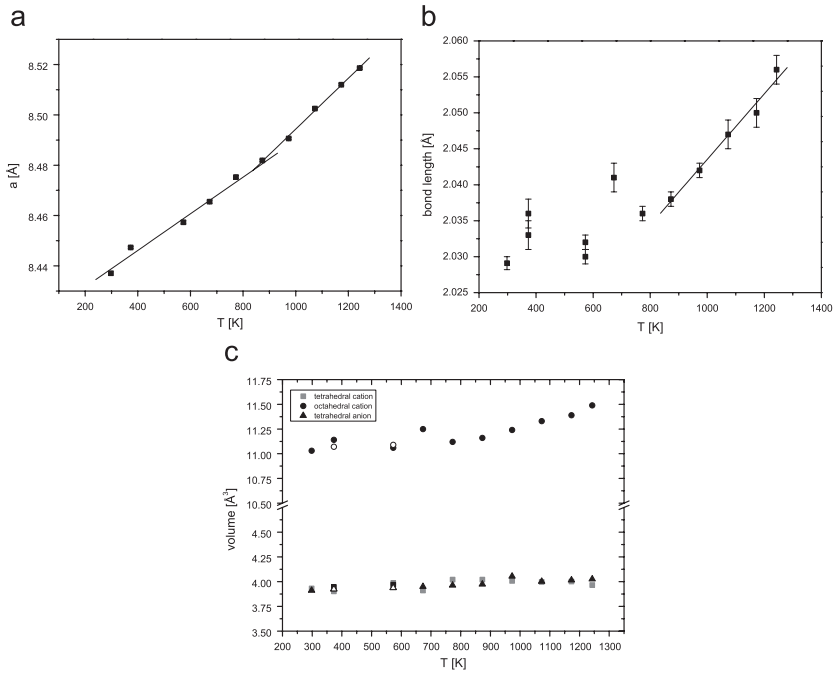

Fig. 3. (a) Unit cell parameters and (b) bond length of the octahedron as function of temperature measured with HTND. Two clear linear trends can be detected in the case of the unit cell parameter. (c) shows the volume of the polyhedrals as function of temperature. △ and ○ represent the measurements made during the cooling stage. Error bars on the unit cell parameter and the volumes are shown by the radius of the points.

Table 3
Bond lengths and bond angles from the Rietveld refinement of the HTND patterns

Temp. (K)	[4] (Å)	[6] (Å)	∠[6]$_1$ (deg)	∠[6]$_2$ (deg)	∠[6] [4] (deg)
298	1.972(1)	2.027(3)	94.82(4)	85.18(4)	121.92(4)
373	1.966(2)	2.036(2)	94.54(6)	85.46(6)	121.11(7)
573	1.982(1)	2.032(1)	94.99(4)	85.01(4)	121.80(6)
673	1.968(2)	2.041(2)	94.48(7)	85.52(7)	122.16(9)
773	1.986(2)	2.036(1)	95.00(4)	85.00(4)	121.80(7)
873	1.986(1)	2.038(1)	94.95(5)	85.05(5)	121.84(6)
973	1.984(2)	2.042(2)	94.81(3)	85.19(3)	121.93(4)
1073	1.982(2)	2.047(2)	94.66(7)	85.34(7)	122.03(8)
1173	1.983(2)	2.050(2)	94.61(7)	85.39(7)	122.07(8)
1243	1.977(2)	2.056(2)	94.35(7)	85.65(7)	122.24(8)
*373	1.972(1)	2.030(1)	94.82(4)	85.18(4)	121.92(5)
*573	1.978(2)	2.033(3)	94.87(6)	85.13(6)	121.81(6)

The [4] and [6] represent the cation–oxygen bond length of cations located on tetrahedral or octahedral coordinated lattice sites. The ∠[4] and ∠[6] represent the oxygen–cation–oxygen bond angles, whereas ∠[4] [6] represent the cation–oxygen–cation bond angles between two different coordinated cations. Bond angles show that the octahedrons are slightly disturbed, whereas the tetrahedrons are undisturbed within experimental errors. Temperatures marked with, *, refer to the diffraction patterns measured during cool down. Estimated standard deviations in parentheses.

activation energies in the lower and upper temperature range were calculated to $E_a = 0.248(1)$ and $0.126(4)$ eV, respectively.

3.4. Dilatometry

Fig. 6 shows the relative linear expansion of $ZnFe_2O_4$ as function of temperature. The curve is slightly bended toward a larger relative expansion coefficient, α, at high temperatures (~823 K) and with only a small hysteresis shown below 600 K. α, defined as $\alpha = 1/L \times \delta L/\delta T$, changes from $\alpha = 5.7 \times 10^{-7}\,K^{-1}$ at 700 K to $6.3 \times 10^{-7}\,K^{-1}$ at 900 K.

4. Discussions

The increase in unit cell parameters (Fig. 3a) consists of two linear trends. The first trend from room temperature to ~873 K is related to a simple thermal expansion due to the increase of lattice vibrations. However, the sudden increase of the unit cell parameter at ~873 K seems to be related to the increasing disorder of the cations. When the Zn ions jump from a tetrahedral lattice sites to a octahedral site, the volume of the octahedron will increase due to larger effective ion radius of Zn^{2+} ([4]: 0.60 Å, [6]: 0.74 Å) compared to Fe^{3+} ([4]: 0.63 Å, [6]: 0.65 Å) [20]. This also explains why the increase of the bond length at the octahedral site coincides with the increase of the unit cell parameter. The tetrahedral site does not seem to follow the same trend as the octahedrons, which can also be explained by the similarity of the ion radii of Zn^{2+} and Fe^{3+}. The octahedrons become less distorted at high temperatures, since the thermal energy makes the lattice expand. Refinements also indicated a decrease in atomic displacements of the oxygen position, but the uncertainties are too high to give a clear image.

It cannot be ruled out completely that a small amount of ZnO evaporates at high temperatures, leaving some of the Fe^{3+} to be chemically reduced to Fe^{2+}. The effective ion radius of Fe^{3+} and Fe^{2+} in a tetrahedral coordination are practically the same (0.63 Å), whereas the effective ion radius of Fe^{3+} (0.65 Å) and Fe^{2+} (0.78 Å) on an octahedral site differs by 20%. If any Fe^{2+} ions are found in the structure, they will mainly be located at octahedral sites [21], and therefore they will certainly contribute to the expansion of the octahedrons. Measurements of the relative linear thermal expansion also show a slightly positive deviation at 823 K, but it seems to related to the cation disorder and not the oxidation state of iron. Similar observations was observed by Brabers [22] on stoichiometrically synthesized $ZnFe_2O_4$. However, he also observed that a small surplus of Fe^{2+} incorporated into the

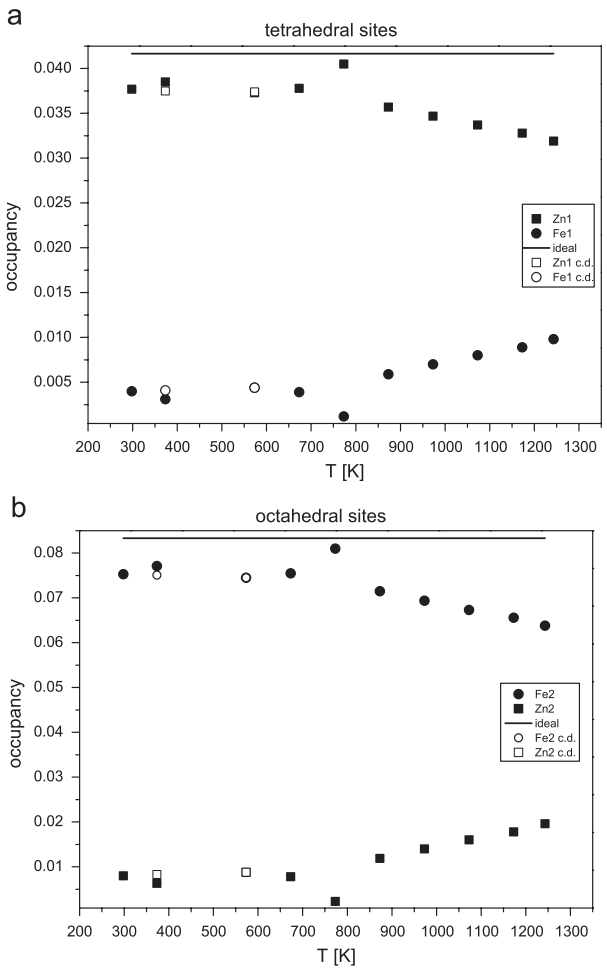

Fig. 4. Occupancies on (a) the tetrahedral and (b) the octahedral site in $ZnFe_2O_4$ as a function of temperature. ■ and ● represent Zn and Fe, respectively. □ and ○ represent the measurements made during the cooling stage. The upper horizontal line shows the ideal occupancy. Error bars are shown by the radius of the points.

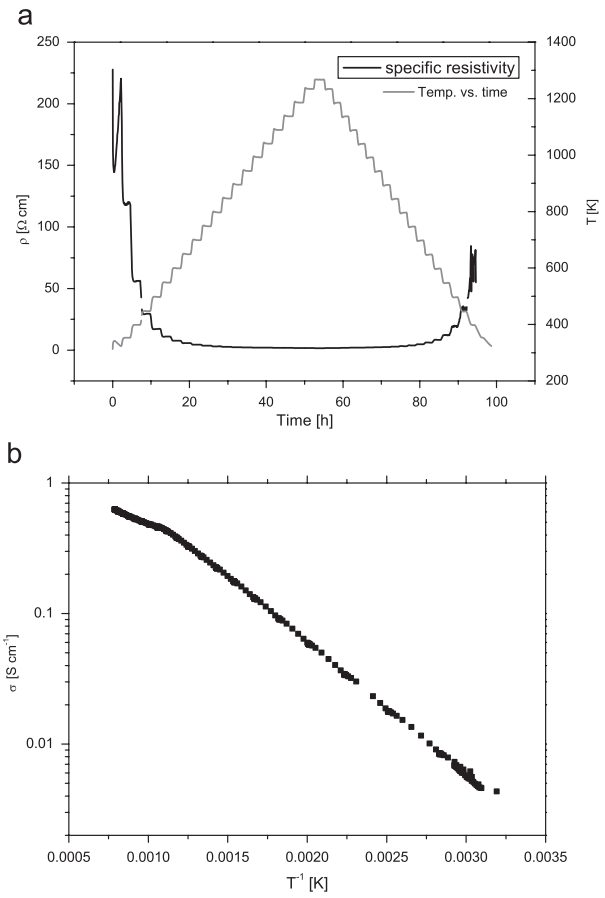

Fig. 5. (a) The specific resistivity as a function of time and temperature. (b) The specific conductivity as a function of temperature shows that $ZnFe_2O_4$ is a relatively good semi-conductor already at room temperature. At temperature above 905 K the conductivity decreases slightly.

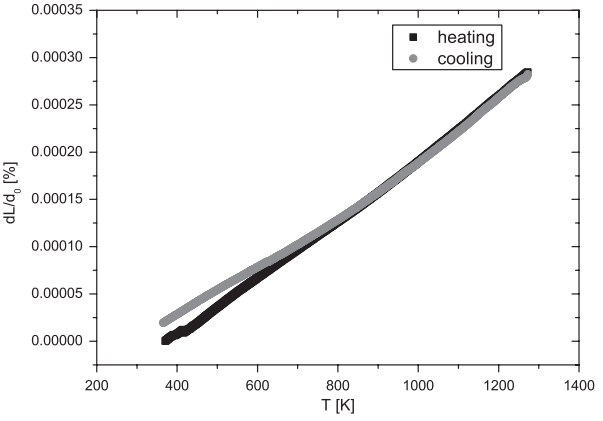

Fig. 6. The relative linear thermal expansion measured in air from room temperature to 1273 K.

structure will make the relative thermal expansion decrease at ~873 K. Therefore it is assumed that the concentration of Fe^{2+} in our sample is small since the starting material was mixed stoichiometrically and calcined at 1173 K where no substantial ZnO evaporation exists and because we do not see a negative deviation from the main trend of the relative thermal expansion.

Refinements of the occupancies show that the cations start to jump between lattice sites at 773 K. The sudden increase of ordering observed at 773 K reflects both the kinetics and the thermodynamics of the system [23]. At low temperatures the sample is not in equilibrium and the kinetic controls the cation order–disorder. At high temperatures the spinel is in equilibrium with respect to the cation order–disorder, reflecting the thermodynamic drive towards high temperature disorder. The increase in order at 773 K results from the starting value being lower than equilibrium and as soon as the temperature is high enough, the occupancies begin to converge towards the order–disorder equilibrium. The cations start to jump between lattice sites at a lower temperature compare to the sudden increase in octahedrals. This shows that the crystal structure (and with the help of the thermal lattice vibrations) can incorporate a certain amount of cation disorder without a distinct change of the unit cell volume.

The refinements of the HTND patterns also show that the cations switch back into there original lattice position when the sample is cooled down. However, the unsymmetrical behavior of the resistivity on Fig. 5a indicates that the occupancies are not

completely identical to the ones before heating the specimen. Otherwise the specific conductivity would be the same before and after heating the sample. The difference between the occupancies and the resistivity measurements is, however, most likely due to the fact that the samples used for the different measurements were exposed to different kind of temperature profile during 'cool down'.

Zn has closed atomic shells and will therefore not contribute directly to the conductivity. Only Fe can contribute to the conductivity. Anderson [24] pointed out that if the cation–anion–cation angle is 90° the domination interaction is a cation–cation interaction, whereas if the angle is 180° or as low as 120° the cation–anion–cation exchange interaction is assumed to be the dominant one. The cation–anion–cation angle between tetrahedral and octahedral sites is ~122° (Table 3), and therefore this interaction could have an influence on the conductivity, whereas the cation–anion–cation angle on tetrahedral sites (109.47°) is too low to cause a cation–anion–cation distinct interaction. It has been shown for $ZnFe_2O_4$ that Fe on a tetrahedral site and its 12 nearest Fe ions on octahedral sites form a cluster in which each of the Fe ion on the octahedral sites interact through an oxygen ion with an Fe ion on a tetrahedral site [13,25,26]. However, those experiments were preformed mainly at low temperatures. In the measured temperature range, the conductivity of $ZnFe_2O_4$ is mainly attributed to the Fe–O–Fe super exchange interactions between octahedral sites [21,27,28], where the transport property rises from hopping of localized d-electrons between cations on octahedral sites. In an ideal spinel structure cations on octahedral sties are distributed in such a way that we have a cation–anion–□–anion–cation, with □ representing an empty site. Structural defects are therefore the main key in creating the cation–anion–cation interaction in $ZnFe_2O_4$. At 905 K the conductivity decreases slightly and seems to be related to a direct cation–cation interaction between Fe atoms on octahedral sites (maximum bond length ~3 A). The activation energy, 0.126(4) eV, is very similar to the one found by Hosseinpour et al. [29] in $ZnFe_2O_4$ containing 0.5% Fe^{2+} on octahedral sites. This, however, does not support the observations of the thermal expansion as discussed earlier in this section. Similar high-temperature cation–cation interaction between octahedral sites has also been reported in Cu- and Ga-doped $ZnFe_2O_4$ [21,27,28], although it was attributed to the Cu–Cu interaction. However, these materials were only measured at a maximum temperature of 700 K which is far below our transition temperature.

5. Conclusion

$ZnFe_2O_4$ was synthesized as a solid state reaction and characterized with X-ray diffraction. HTND was preformed on a powder sample from 298 to 1243 K and refinements show that $ZnFe_2O_4$ has a almost normal spinel structure with $\gamma = 0.09$ below 673 K. Cations start to redistribute among tetrahedral and octahedral sites at temperatures above ~673 K, but they switch back to their original position when the sample is cooled down again. The expansion of the unit cell parameter and octahedrons increases rapidly at ~873 K which seems to be related to the larger Zn^{2+} ion substituting the smaller Fe^{3+} on the octahedral sites. Resistivity measurements reveal a semi-conducting behavior of $ZnFe_2O_4$ from room temperature to 905 K, which mainly arises from a Fe–O–Fe exchange interaction between octahedral sites. Above 905 K $ZnFe_2O_4$ shows a more metallic behavior which is attributed to the Fe–Fe interaction on octahedral sites.

Acknowledgment

We give our thanks to Dr. Bente Lebech for fruitful discussions concerning the structural analysis.

References

[1] O. Knop, K.I.G. Reid, R. Sutarno, Y. Nakagawa, Can. J. Chem. 46 (1968) 3463–3476.
[2] H. Duda, I. Jendrzejewska, T. Groń, S. Mazur, P. Zajdel, A. Kita, J. Phys. Chem. Solids 68 (2007) 80–86.
[3] T. Suzuyama, J. Awaka, H. Yamamotoa, S. Ebisu, M. Ito, T. Suzuki, T. Nakama, K. Yagasaki, S. Nagata, J. Solid State Chem. 179 (2006) 140–144.
[4] A.A. Al-Shahrani, J. Mater. Sci. 16 (2005) 193–196.
[5] M.A. Arillo, M.L. Lopez, M.T. Fernandez, M.L. Veiga, C. Pico, J. Solid State Chem. 125 (1996) 211–215.
[6] R.H. Busey, J.O.L. Keller, J. Chem. Phys. 41 (1964) 215–225.
[7] S. Zhuiykov, M. Muta, T. Ono, M. Hasei, N. Yamazoe, N. Miura, Electrochem. Solid-State Lett. 4 (2001) H19–H21.
[8] S. Zhuiykov, T. Ono, N. Yamazoe, N. Miura, Solid State Ionics 152–153 (2002) 801–807.
[9] G. Zhang, L. Chunsheng, C. Fangyi, J. Chen, Sensors & Actuators B 120 (2007) 403–410.
[10] K. Arshak, I. Gaidan, Mater. Sci. Eng. B 118 (2005) 44–49.
[11] J.Z. Zhang, D.H. Chen, L. Chen, Sensors Mater. 5 (2006) 227–282.
[12] H.S.C. O'Neill, Eur. J. Miner. 4 (1992) 571–580.
[13] T. Kamiyama, K. Haneda, T. Sato, S. Ikeda, H. Asano, Solid State Commun. 81 (1992) 563–566.
[14] S. Ligenza, Phys. Status Solidi B 75 (1976) 315–326.
[15] B.C. Hauback, H. Fjellvag, O. Steinsvoll, K. Johansson, O.T. Buste, J. Jorgensen, J. Neutron Res. 8 (2000) 215–232.
[16] V. Petříček, M. Dusek, L. Palatinus, Jana2000, The crystallographic computing system, Institute of Physics, Praha, Czech Republic, 2000.
[17] T. Hahn (Ed.), International Tables for Crystallography, third ed., vol. A, Wiley, New York, 1992.
[18] O. Crottaz, F. Kubel, H. Schmid, J. Mater. Chem. 7 (1997) 143–146.
[19] N.M. Tallan, Electrical Conductivity in Ceramics and Glass: Part A–B, Dekker, New York, 1974.
[20] C. Klein, C.S. Hurlbut, J.D. Dana, Manual of Mineralogy, vol. 21, Wiley, New York, 1998.
[21] M. Wen, Q. Li, Y. Li, J. Electron Spectrosc. Relat. Phenom. 153 (2006) 65–70.
[22] V.A.M. Brabers, J. Phys. IV France 7 (1997) C1233–C1236.
[23] S.A.T. Redfern, Eur. J. Miner. 14 (2002) 251–261.
[24] P.W. Anderson, Phys. Rev. 79 (1950) 350–356.
[25] F.K. Lotgering, J. Phys. Chem. Solids 27 (1966) 139–145.
[26] V. Šepelák, K. Tkáčová, V.V. Boldyrev, S. Wissmann, K.D. Becker, Physica B 234–236 (1997) 617–619.
[27] S.S. Ata-Allah, M.K. Fayek, M. Yehia, J. Magn. Magn. Mater. 279 (2004) 411–420.
[28] S.S. Ata-Allah, F.M. Sayedamed, M. Kaiser, A.M. Hashhash, J. Mater. Sci. 40 (2005) 2923–2930.
[29] A. Hosseinpour, H. Sadeghi, A. Morisako, J. Magn. Magn. Mater. 316 (2007) e283–e286.

II

J Solid State Electrochem
DOI 10.1007/s10008-008-0653-9

ORIGINAL PAPER

The $NiFe_2O_4 - MgFe_2O_4$ series as electrode materials for electrochemical reduction of NO_x

F. Bræstrup · K. K. Hansen

Received: 16 May 2008 / Revised: 12 August 2008 / Accepted: 12 August 2008

Abstract Solid solutions of spinel-type oxides with the composition $Ni_{1-x}Mg_xFe_2O_4$ ($x = 0.0, 0.3, 0.5, 0.6, 1.0$) were prepared with the glycine-nitrate combustion synthesis ($x = 0.0, 0.3, 0.5, 0.6$) and the citric-acid combustion synthesis ($x = 1.0$). The oxides were used as electrode materials in a pseudo-three-electrode setup in the temperature range of 400–600 °*C*. Cyclic voltammetry and electrochemical impedance spectroscopy were used to characterize the electrochemical behavior in 1% NO and 10% O_2. Measurements show that $NiFe_2O_4$ has relatively high cathodic activity in both NO and O_2, whereas $MgFe_2O_4$ shows much higher activity in NO compared to O_2. $MgFe_2O_4$ was also measured with cyclic voltammetry in 1% NO_2 and different gas mixtures of NO and O_2 at 300 and 400 °C. Results show that the cathodic activities (−0.6 V) are relatively high with current ratios, $I_{NO_x+O_2}/I_{O_2}$, ranging from 10.1–167.7 and with a maximum at 400 °C. Dilatometry measurements were performed on the materials in air up to 1,000 °C, and they showed that the Curie temperature could be detected for all samples. Four-point DC resistivity measurements at elevated temperatures show that $Ni_{0.4}Mg_{0.6}Fe_2O_4$ has the highest conductivity, whereas $Ni_{0.7}Mg_{0.3}Fe_2O_4$ and $NiFe_2O_4$ have the highest conductivity at lower temperatures.

Keywords Spinel-type oxide · Conductivity · Powder diffraction · NO_x · O_2

F. Bræstrup (✉) · K. K. Hansen
Fuel Cells and Solid State Chemistry Department,
Risø National Laboratory for Sustainable Energy,
Technical University of Denmark, Copenhagen, Denmark
e-mail: frantz.braestrup@risoe.dk

Introduction

One of the main polluting agents from internal combustion processes in diesel-fired engines is NO_x (NO and NO_2) gases. Presently, the three-way catalytic converter (TWCC) is employed for treating gasoline engine emissions; however, the TWCC requires stoichiometric conditions to simultaneously catalyze oxidizing and reducing reactions. This makes it unsuitable in lean burn and diesel engine applications. Several attempts have been made to solve the problem with NO_x emission, and the one that has gained the most attention is the system based on the selective catalytic reduction process (SCR). In SCR, the reduction of NO_x is performed by injecting a reducing agent, such as ammonia, urea, or a hydrocarbon into the exhaust gas upstream of the SCR catalyst. Although the SCR technology has been shown to reduce NO_x by 65–99% [1] over a range of diesel operating conditions, one of the disadvantages with mobile SCR technology is that the reduction agent must be carried onboard in a tank, which places some requirements on packing the substance. It also has to be durable and function-effective in a diverse range of a truck engines. Moreover, systems must be designed to prevent unreacted reducing agents to escape out of the tailpipe of the vehicle, as well as N_2O formation.

An alternative route is to reduce NO_x electrochemically in an all solid-state reactors [2]. The NO_x gases are reduced at the cathode following the overall Eqs. 1 and 2:

$$4e^- + 2NO \rightarrow N_2 + 2O^{2-} \quad (1)$$

$$4e^- + NO_2 \rightarrow 0.5N_2 + 2O^{2-}. \quad (2)$$

A drawback is that O_2 can also be reduced at the cathode (Eq. 3), which will lead to a high consumption of current.

$$4e^- + O_2 \rightarrow 2O^{2-}. \quad (3)$$

A good electrode material therefore has to be selective towards reduction of NO and NO_2, as well as a good electronic conductor and/or a good ion conductor. Since NO and NO_2 are less stable than O_2, the energy level of the antibonding orbitals of NO_x is located at a lower energy level than the corresponding antibonding orbitals of O_2. By adjusting the potential in such a way that the valence electrons of the electrode material are placed at an energy level in between that of the antibonding orbitals of NO (or NO_2) and O_2, it will be possible to reduce only the NO_x [3].

Previous reports using metal electrodes such as Pd, Pt, Au, Ag, Ir, and NiO [2, 4–9] on an yttrium stabilized zirconia (YSZ) oxygen ion conductor have shown some interesting results; however, most of the metals are relatively expensive, which has intensified the research for low-cost ceramics to be used as electrode materials. RuO_2 has also been suggested as a candidate for electrochemical NO_x removal [5]; however, Ru is highly poisonous and forms higher volatile oxides, such as RuO_3 and RuO_4. Catalytic NO_x decomposition on spinel-type oxides [10–14] has been reported; however, only a few observations on electrochemical decomposition on spinel-type electrode materials [15, 16] have been presented in literature to our knowledge. In this study, the electrochemical reduction of NO_x and O_2 has been investigated on point electrodes of spinel-type oxides, $Ni_{1-x}Mg_xFe_2O_4$ ($x = 0.0, 0.3, 0.5, 0.6, 1.0$), with the purpose of finding cheap electrode materials, of nonprecious metals, to be used in electrochemical filters placed on diesel-fired vehicles.

Experimental details

Sample preparation and X-ray diffraction

$Ni_{1-x}Mg_xFe_2O_4$ ($x = 0.0, 0.3, 0.5, 0.6, 1.0$) were prepared from aqueous metal nitrates ($Ni(NO_3)_2 \cdot 2.6\ H_2O$, $Mg(NO_3)_2 \cdot 2.6\ H_2O$, and $Fe(NO_3)_2 \cdot 3.9\ H_2O$) using the glycine-nitrate combustion synthesis [17] ($x = 0.0, 0.3, 0.5, 0.6$) and the citric-acid combustion synthesis [18] ($x = 1.0$). After synthesis, the powder was ball-milled for 24 h and then calcined in air at 1,000 °C for 6 h. All samples were analyzed by X-ray diffraction using a STOE theta-theta diffractometer. Scans were conducted over the 2θ-range of $15° - 80°$, with a step width of 0.05°. Le Bail fits were carried out using the program Jana2000 [19] in order to determine the unit cell parameter, **a**. Pseudo-Voigt profile functions were used, and the background was modeled with 10-term Legendre polynomials.

The powder was pressed uniaxially at 1 ton into elongated pellets, followed by isostatic pressing at 50 tons to make the pellets more dense and to increase their mechanical strength. The samples were then sintered in air at 1,000 °C for 6 h. The pellets were then mechanically tooled into cone-shaped electrodes as described by others [20, 21].

Cyclic voltammetry and impedance spectroscopy

Cyclic voltammetry (CV) and electrochemical impedance spectroscopy (EIS) were recorded with a Gamry Femtostate in a pseudo-three-electrode setup [22] suggested by Fabry [23]. The cone, acting as a point electrode, was arranged with the tip placed downwards on a polished one-end closed YSZ-tube electrolyte containing air as reference gas and a silver electrode used as the counter/reference electrode. CV and EIS were recorded at 400, 500, and 600 °C in 10% O_2 in Ar or 1% NO in Ar (Air Liquide) with a flow rate of 20 ml/min. Additional measurements were performed on the $MgFe_2O_4$-electrode in 1 % NO_2 in Ar and gas mixtures of 0.5% NO + 5% O_2, 0.5% NO + 10% O_2, and 0.5% NO_2 + 10% O_2. Measurements containing NO_2 gas (Air Liquide) were performed only at 300 and 400 °C. A 1-h equilibrium time was used to record the open current voltage (OCV) before recording the voltammograms in the potentional range of -0.6 V $-$ 0.5 V with a sweep rate of 1.0 and 10 mV s^{-1}. EIS were recorded from 177,793(1) to 0.050(1) Hz with 10 points/decade and an amplitude of 24 mV (rms). In order to compare the electrodes directly, the currents in the voltammograms were converted to current densities by dividing with the contact area, which was determined by EIS using Newman's formula [24], Eq. 4,

$$r = \frac{1}{4\sigma R_e}. \quad (4)$$

Newmann's formula assumes that the contact area is circular, with r being the radius of the contact area, σ is the specific conductivity of the electrolyte material and R_e is the electrolyte resistance. σ can be determined from Eq. 5 [25].

$$\sigma = \frac{1.51 \cdot 10^6}{T} \cdot e^{\frac{-0.94[eV]}{Tk_B}} \quad (5)$$

where T and k_B are the temperature and the Boltzman's constant, respectively.

Dilatometry and thermogravimetry

The linear thermal expansion was measured by dilatometry in air (flow rate: 50 ml/min) using a NETZSCH DIL 402C dilatometer with a sample load of 30.000 cN. The sample-rod was heated from room temperature up to 1,000 °C and back at 2 °C/min. The sample remained at 1,000 °C for 2 h. Data were calibrated to an Al_2O_3 standard at identical conditions. Thermogravimetry (TG) measurements on (~ 46 mg) $MgFe_2O_4$ were performed on a NETZSCH TG 439 thermo microbalance in air (flow rate: 50 ml/min). The measurement was run with the same temperature profile as used in the dilatometry measurements.

Four-point DC resistivity measurements

Platinum paste was applied to each end of the elongated rod and contacted with platinum leads. Two platinum potential probes with a fixed distance were positioned on one side of the bar. The data collection was made with an in-house data acquisition software, ELCHEMEA. The resistivity was measured every 5 min from room temperature to 1,000 °C and back again with a ramp rate of 2 °C/min and a 2-h dwell at every 50-°C interval. The resistivities of the samples were corrected for the porosity using the Bruggerman asymmetric model [26]. The densities of the elongated rods were measured by the Archimedes principle. Measurements showing signs of sintering were repeated in order to minimize its effects.

Results and discussions

Almost all materials were single-phase spinel-type oxides. However, a small impurity phase of NiO (approx. 1%) was observed in $Ni_{0.5}Mg_{0.5}Fe_2O_4$. X-ray diffraction measured at room temperature showed an increase in unit cell parameters with increasing Mg content (Fig. 1). $NiFe_2O_4$ has an inverse spinel-type structure with Ni^{2+} located primarily on the octahedral sites and Fe^{3+} located on both the tetrahedral and the octahedral sites. The ionic radii of Ni^{2+} on a tetrahedral and an octahedral site are 0.55 Å and 0.69 Å respectively, whereas Fe^{3+} has an ionic radius of 0.63 Å (tetrahedral sites) or 0.65 Å(octahedral sites) [27]. When Mg^{2+}, having an ionic radius of 0.57 Å (tetrahedral sites) or 0.72 Å (octahedral sites) is introduced in the structure in favor of Ni^{2+}, it will enter the tetrahedral lattice site, therefore forcing Fe^{3+} on the tetrahedral site to move into an octahedral site. That would, in principle, not increase the volume of the unit cell. However, although

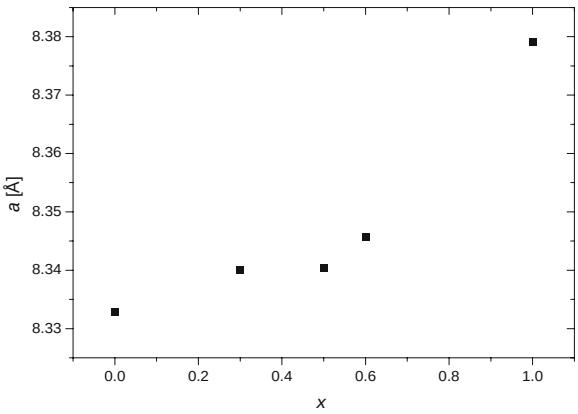

Fig. 1 Unit cell parameters, *a*, at different spinel compositions. A small increase in *a* is observed from $0.0 \leq x \leq 0.6$, whereas the unit cell is significantly higher at $x = 1.0$. *Error bars* are at the same magnitude as the dimension of the points

the increase in unit cell is very small in the range of $0 \leq x \leq 0.6$, some of the Mg^{2+} must be located on the octahedral sites, otherwise, there will be no expansion of the unit cell. This is due to the fact that Mg^{2+} is 11% bigger than Fe^{3+} on an octahedral site. The relatively large unit cell expansion of $MgFe_2O_4$ is a result of the structure now favoring a pseudoinverse spinel-type structure [28] with Mg^{2+} located mainly on octahedral sites and Fe^{3+} on tetrahedral and octahedral sites. The solid solution of $NiFe_2O_4$ and $MgFe_2O_4$ therefore covers the change from an inverse spinel-type structure towards a more normal spinel-type structure and back to a pseudoinverse spinel-type structure.

Conductivity measurements

Figure 2 shows the specific conductivity of the spinels as a function of temperature. A large hysteresis is only observed for $Ni_{0.7}Mg_{0.3}Fe_2O_4$. At high temperatures (above ~ 700 °C), the conductivity increases as more Mg is substituted with Ni (maximum at $x = 0.5$). At higher Mg content, the conductivity decreases again, as also described in earlier reports [29, 30]. However, they found a maximum conductivity for $Ni_{0.4}Mg_{0.6}Fe_2O_4$. The conductivity is mainly attributed to the cation–anion–cation super exchange interactions between octahedral sites, where the transport property rises from hopping of localized *d* electrons between cations on octahedral sites [31, 32]. Mg^{2+} will, as discussed in the "Results and discussions" section, enter the tetrahedral sites, resulting in a migration of Fe^{3+} ions into the octahedral sites. The increase in concentration of

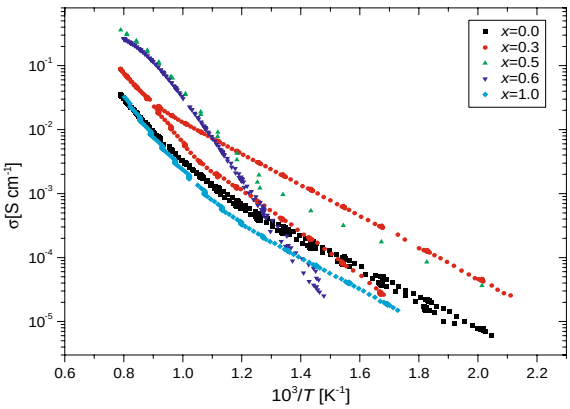

Fig. 2 Four-point DC conductivity measurements of the spinels measured from room temperature to 1,000 °C in air

Fe^{3+} on the octahedral sites will increase the hopping rate of the electrons. Increasing the Mg^{2+} content will eventually force the Mg^{2+} ions to occupy the octahedral sites, leaving the Fe^{3+} ions to migrate back onto the tetrahedral sites. This will lower the concentration of Fe^{3+} ions on the octahedral sites and, therefore, also the hopping rate of the electrons. The data were fitted with an Arrhenius Eq. 6,

$$\sigma = \sigma_0 \exp \frac{-E_a}{k_B T}, \tag{6}$$

where σ is the specific conductivity and E_a is the activation energy.

The conductivities of $NiFe_2O_4$ and $MgFe_2O_4$ behave in a similar way. Both show a slightly curved behavior starting at 607 °C ($NiFe_2O_4$) and 574 °C ($MgFe_2O_4$). $NiFe_2O_4$ has a Curie point in the range of 585–590 °C [33, 34], which could explain some of the changes in conductivity. However, the change in conductivity of $NiFe_2O_4$ and $MgFe_2O_4$ is more likely a result of reordering of the cations (see the "Dilatometry" section). Activation energies (Table 1) are very similar for $NiFe_2O_4$ and $MgFe_2O_4$. At lower temperatures, activation energies are in the range of 0.415–0.536 eV, with $MgFe_2O_4$ having the highest activation energies. At high temperatures, activation energies decrease to 0.177–0.214 eV.

The conductivity of $Ni_{1-x}Mg_xFe_2O_4$, $(x = 0.5, 0.6)$ shows a more different behavior. The conductivity increases quite rapidly from 500 to 800 °C compared to the other samples. Above 800 °C, the conductivity changes slope towards a lower activation energy. This more metallic behavior is a result of a direct cation–cation interaction on octahedral sites also observed in Cu-containing ferrite with a spinel-type structure [31, 32]. $Ni_{0.5}Mg_{0.5}Fe_2O_4$ shows a significant change in conductivity at 495 °C, which might be related to the Curie temperature.

During heating, $Ni_{0.7}Mg_{0.3}Fe_2O_4$ follows the same trend as both $NiFe_2O_4$ and $MgFe_2O_4$, but the conductivity during cooling is significantly higher. The large hysteresis of $Ni_{0.7}Mg_{0.3}Fe_2O_4$ must be a result of the changes in the cation distribution. The upward curvature of the conductivity takes place at higher temperatures than that of both $NiFe_2O_4$ and $MgFe_2O_4$. When the sample is cooled below the critical temperature (blocking temperature), a relatively large amount of Mg^{2+} is trapped in the tetrahedral sites. This will leave the Fe^{3+} and the Ni^{2+} on the octahedral sites and thereby increase the conductivity relative to the heating stage.

Dilatometry

Earlier reports show that spinels in general are bad oxygen ion conductors. A composite electrode of spinel and $Ce_{0.9}Gd_{0.1}O_{1.95}$ (CGO10) (an oxygen ion conductor, which has a higher ionic conductivity than YSZ at low temperatures) are therefore needed in order to have a proper current running. It is therefore important to know the thermal expansion coefficient of the spinels when it is mixed with other materials.

Measurements with dilatometry show, with an exception of $MgFe_2O_4$, a single discontinuity of the relative linear expansion (see Fig. 3). This is observed during both the heating and cooling stages and is

Table 1 Activation energies, E_a, calculated from the conductivity measurements

Compound	E_a, high T, H	E_a, high T, C	E_a, low T, H	E_a, low T, C
$NiFe_2O_4$	0.211(1) eV	0.207(1) eV	0.415(1) eV	0.449(1) eV
$Ni_{0.7}Mg_{0.3}Fe_2O_4$	0.286(1) eV	0.209(1) eV	0.471(2) eV	0.416(2) eV
$Ni_{0.5}Mg_{0.5}Fe_2O_4$	–	0.179(4) eV	0.489(2) eV	0.448(6) eV
$Ni_{0.4}Mg_{0.6}Fe_2O_4$	–	–	0.287(1) eV	0.298(2) eV
$MgFe_2O_4$	0.177(1) eV	0.214(1) eV	0.536(4) eV	0.477(3) eV

H and C represent the heating and the cooling stages. T is the temperature. Estimated standard deviations are in parentheses.

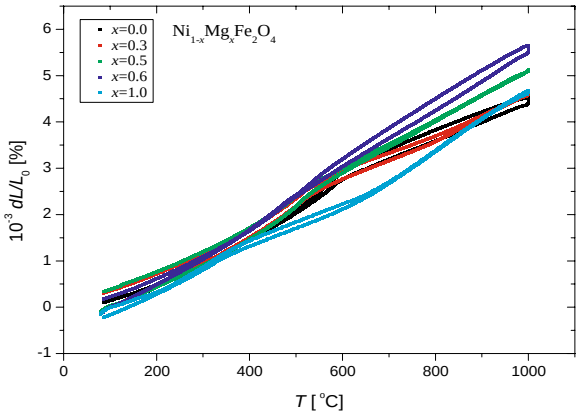

Fig. 3 Linear expansion of the different spinels measured in the temperature range of 80 to 1,000 °C. The Curie point is detectable for all of the spinels

related to the Curie temperature, T_c [33]. The thermal expansion coefficient, α, defined as $\alpha = \frac{1}{L}\frac{\delta L}{\delta T}$, does not change much before or after T_c, although it reaches a slightly lower value after T_c (see Table 2).

In general, T_c measured during cool down is located at slightly lower temperatures compared to the heating stage (see Table 2). T_c also decreases with increasing Mg content of the Ni-containing spinels. Figure 4 shows the dilatometry measurements of $MgFe_2O_4$. The relative linear expansion reveals two discontinuities at 327 and 800 °C, both appearing during the heating and the cooling stages. α shows a sharp peak at 325 °C as in the case of the Ni-containing materials, whereas the peak at 800 °C is much more broad (starts appearing at 620 °C (heating) or 570 °C (cooling)). The first discontinuity is related to the magnetic ordering of the Fe electrons, although there seem to be some disagreements on the type of magnetic ordering [35–37]. The T_c peak was not observed by Carter [38] and Weil [39], who concluded that the magnetic exchange interaction energy is independent of the Fe–O–Fe spacing. Our results, however, show that this is not the case. In $MgFe_2O_4$, T_c is highly sensible to the cation distribution [35], which again is very sensible to the thermal history of the spinel. The reason for the different results must be found in the difference in sample preparation (more Fe^{3+} on octahedral sites will increase the number of super exchange interactions and make the Curie point more pronounced) or the number of collected data points. Carter narrowed his data set down to ~ 20 data points, which makes it difficult to detect a relatively narrow peak if present.

The second discontinuity, starting at 620 °C, is more difficult to explain but seems to be related to some sort of structural expansion superimposed onto the thermal expansion. Carter also detected the same kind of upward curvature of the expansion of $MgFe_2O_4$ but was not able to explain the phenomena. One origin of the structural expansion would be a change of stoichiometry (loss of oxygen). This would result in a structural expansion as also reported for different oxides [40, 41]. However, TG measurements show no sign of oxygen loss at the specific temperature. Another explanation would be to relate the upward curvature of the expansion to the order–disorder transition between cations on tetrahedral and octahedral sites. Discussed in the "Results and discussions" section is the ionic radius of the cations responsible for the change of the lattice parameters. In most cases, the compounds are not in equilibrium at low temperatures, where the orderings of the cations are controlled by the kinetics [42]. At high temperatures, the spinels are in equilibrium with respect to the cation order–disorder, reflecting the thermodynamic drive towards high-temperature disorder. The increase of the relative linear expansion at 620 °C results from the starting value of the ordering parameter being lower than the equilibrium value. When the interaction between kinetics and thermodynamics allows it, Mg^{2+} will start to jump to an octahedral site and thereby force the unit cell to expand faster than the thermal vibrations allow. At around 800 °C, the cation order–disorder has reached an equilibrium leading the thermal expansion to take over the main process and thereby decreasing the relative linear expansion. Earlier reports [35, 43] show that the ordering of the cations at equilibrium temperatures starts somewhere between 400 and 650 °C, which is in good

Table 2 Curie temperatures, T_c, and expansion coefficients, α

Compound	T_c (heating)	T_c (cooling)	$\alpha_{400\ °C}$	$\alpha_{800\ °C}$
$NiFe_2O_4$	584 °C	581 °C	$1.13 \cdot 10^{-5}$	$8.08 \cdot 10^{-6}$
$Ni_{0.7}Mg_{0.3}Fe_2O_4$	516 °C	510 °C	$1.30 \cdot 10^{-5}$	$1.26 \cdot 10^{-5}$
$Ni_{0.5}Mg_{0.5}Fe_2O_4$	510 °C	499 °C	$1.20 \cdot 10^{-5}$	$1.10 \cdot 10^{-5}$
$Ni_{0.4}Mg_{0.6}Fe_2O_4$	468 °C	466 °C	$1.16 \cdot 10^{-5}$	$7.75 \cdot 10^{-6}$
$MgFe_2O_4$	327 °C	325 °C	$*6.17 \cdot 10^{-5}$	$7.38 \cdot 10^{-4}$

The α value, marked with *, is measured at 500 °C.

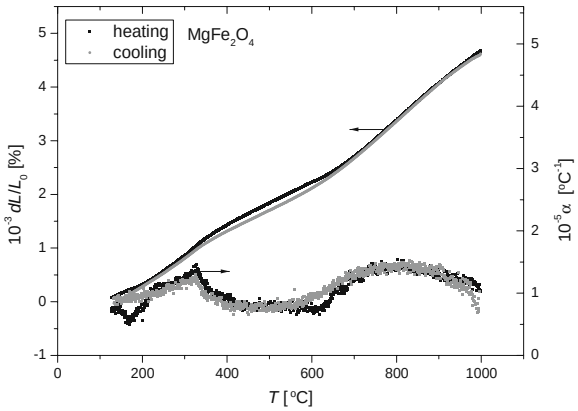

Fig. 4 Linear expansion and expansion coefficients of $MgFe_2O_4$. The peak at ∼ 325 °C is the Curie temperature, T_c and the broad peak at 800 °C is due to cation ordering

agreement with our results. The structural expansion takes place over a range of ∼ 180 °C, which is also similar to what is reported by Harrison. Antao [44] measured the cation ordering in $MgFe_2O_4$ using in situ, high-temperature synchrotron X-ray powder diffraction. They found that, when heating the sample, the cations start to jump between lattice sites at 581 °C (more Mg^{2+} on octahedral sites), and during cooling, the cations jump back to their original position until the blocking temperature is reached at 543 °C. This will explain not only the change of conductivity in the same temperature range but also the behavior of the linear expansion in our experiments.

A small uptake of oxygen at 985 °C was detected with TG. Thermodynamic calculations (FactSage [45]) show that $MgFe_2O_4$ will decompose to MgO and a more Fe-rich spinel at 980 °C. $MgFe_2O_4$ have been found to be slightly over-stoichiometric with respect to the metal ions [46], which will explain the small uptake of oxygen following reaction 7:

$$\delta O_2 + MgFe_2O_{4-\delta} \rightarrow \delta MgO + Mg_{1-\delta}Fe_2O_4. \quad (7)$$

The phase change was not observed in the dilatometry measurements because of slow kinetics [47]. However, a small amount of the material has decomposed during the experiment, which was confirmed in the TG measurement. The expansion coefficients of the spinels ($\alpha = 10 \cdot 10^{-6} - 15 \cdot 10^{-6}$ °C^{-1}) are very similar to the expansion coefficient of CGO10 ($\alpha = 11.9 \cdot 10^{-6}$ °C^{-1} [48]), so a composite electrode of our spinels and CGO10 seems possible.

Cyclic voltammetry

Figure 5 shows the voltammogram recorded at 400 °C. Similar voltammograms were also recorded at 500 and 600 °C; however, they look very similar to those recorded at 400 °C and are therefore not shown for all of the spinels. Part of the voltammograms recorded on $NiFe_2O_4$ and $MgFe_2O_4$ are shown in Fig. 6 since they show a more interesting behavior than that of the rest of the spinels. $NiFe_2O_4$ has the highest cathodic activity in NO and O_2 at 500 and 600 °C. However, at 400 °C, $MgFe_2O_4$ shows higher activity in NO than $NiFe_2O_4$ does. The activity in O_2 differs significantly between the two electrode materials, with $NiFe_2O_4$ showing the highest activity. Figure 7 shows the current densities in NO and O_2 as a function of the Mg^{2+} content. As more Mg^{2+} is substituted into the $NiFe_2O_4$ compound, the activity in NO and O_2 decreases significant until a minimum is reached at the $Ni_{0.5}Mg_{0.5}Fe_2O_4$ electrode. The activity on $Ni_{0.4}Mg_{0.6}Fe_2O_4$ increases slightly again, but on the $MgFe_2O_4$, electrode the picture looks more blurry. Figure 8 shows the current ratios of NO with respect to O_2. Ni-containing electrode materials all show current ratios in the range of 0.4–2.4 but without any systematic trends. It was not possible for us to reproduce the measurements from Simonsen [15], who got some very interesting results on $NiFe_2O_4$ (potential range −1.0–0.5 V). However, theoretically, electrochemical calculations [45] show that $NiFe_2O_4$ is reduced to Ni + Fe_3O_4 at potentials lower than −0.86 V (600 °C). In our measurements, we did not go below −0.6 V at any temperature, which might explain why our measurements did not match

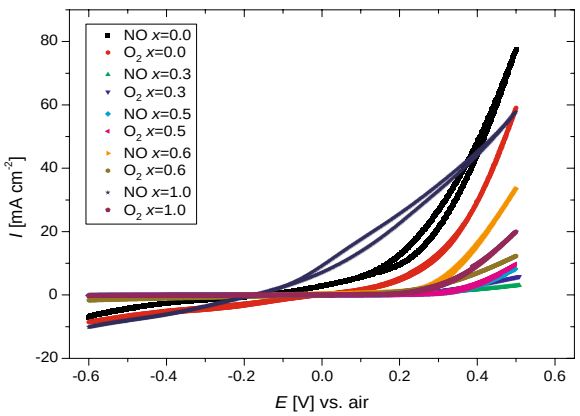

Fig. 5 Cyclic voltammograms on the different spinels at 400 °C. Data were recorded in 1% NO and in 10% O_2 with air as reference gas (sweep rate: 1 mV/s)

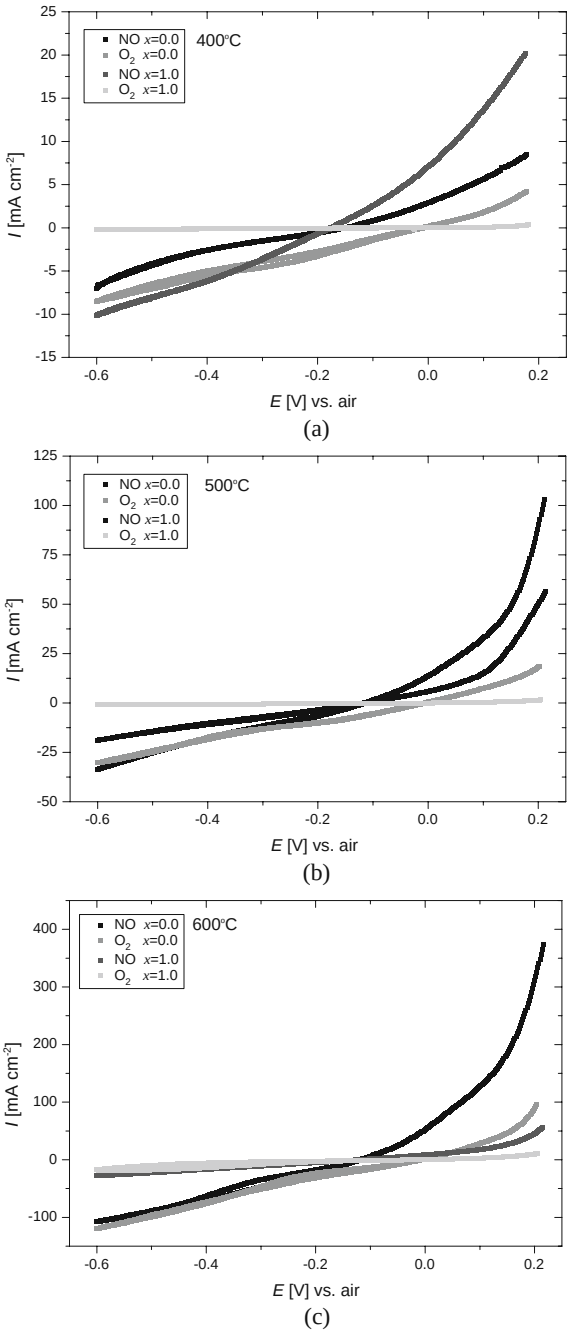

Fig. 6 Cyclic voltammogram on $NiFe_2O_4$ and $MgFe_2O_4$. **a**, **b**, and **c** show a part of the voltammograms (−0.6–0.2 V) at 400, 500, and 600 °C, respectively. The voltammograms were recorded in 1% NO and in 10% O_2 with air as reference gas (sweep rate: 1 mV/s)

theirs. A comparison of our results with Hansen [16] is more difficult. Their data have not been normalized to current densities and the NO concentration used

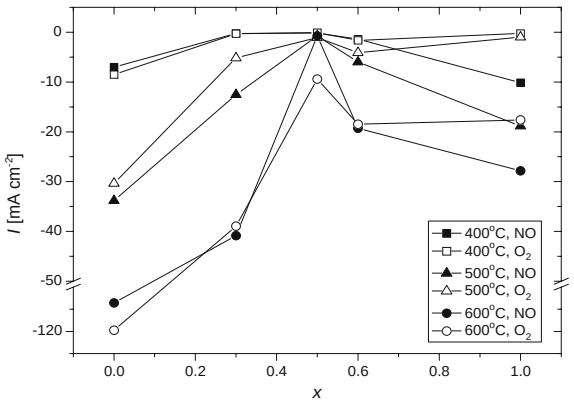

Fig. 7 Current densities in NO and O_2 using the different electrode materials ($Ni_{1-x}Mg_xFe_2O_4$). Data are shown for 400, 500, and 600 °C. x refers to the Mg content

is twice as high as in our measurements. However, estimated values of the current ratios are much smaller ($(I_{NO}/I_{O_2} \leq 1)$ than we find, which makes our materials more interesting.

The activities of the spinels seem to be correlated to the distribution of Fe^{3+} on different lattice sites. The more Fe^{3+} is located on the tetrahedral sites, the more active is the spinel. $NiFe_2O_4$ has the highest content of Fe^{3+} on tetrahedral sites among the spinels, and it also has the highest activity. As more Mg^{2+} is incorporated into the lattice, the more Fe^{3+} will be located on octahedral sites, causing an increase in conductivity (in air) and a decrease in activity. When the Mg^{2+} content reaches a critical value ($x = 0.5$), the structure now

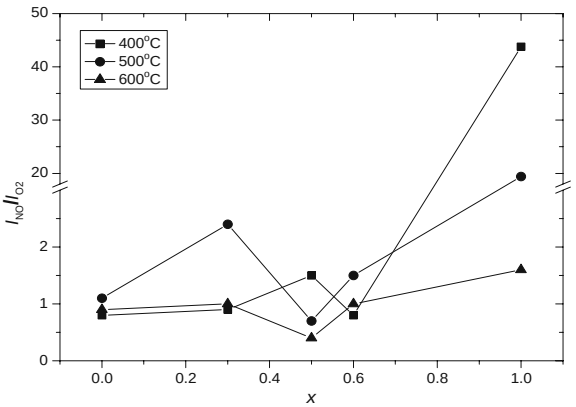

Fig. 8 Current ratios between NO and O_2 for the different spinels ($Ni_{1-x}Mg_xFe_2O_4$). $MgFe_2O_4$ shows significantly higher current ratios at 400 and 500 °C compared to the other spinels. x refers to the Mg content

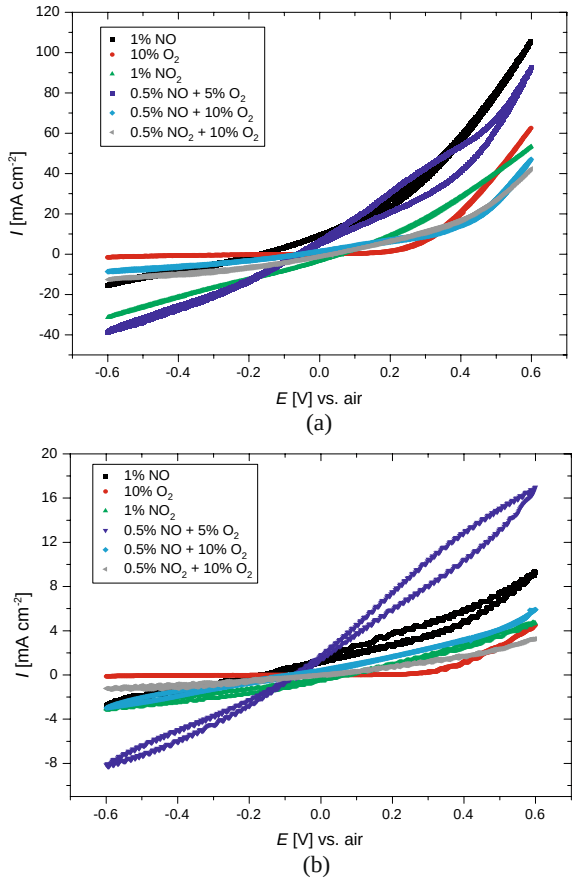

Fig. 9 Cyclic voltammograms on $MgFe_2O_4$ in different gas mixtures at 400 °C (**a**) and 300 °C (**b**). Air was used as reference gas and data were collected with a sweep rate of 1 mV/s. The electronic noise at 300 °C is notable

favors Mg^{2+} to move to octahedral sites and Fe^{3+} to tetrahedral sites. This causes a decrease in conductivity and an increase in activity. If Ni^{2+} had the dominant effect on the activity, we would expect a decrease in activity with increasing Ni^{2+} content, but we will be left to explain the high activity on $MgFe_2O_4$. If Mg^{2+}, on the other hand, had the dominant effect on the activity, we would expect an increase in activity with increasing Mg^{2+} content.

In general, $MgFe_2O_4$ shows higher activity in NO than in O_2 at all temperatures, with a maximum current ratio at 400 °C. Additional measurements in 1% NO_2 and different gas mixtures (0.5% NO_2 + 5% O_2, 0.5% NO_2 + 10% O_2, 0.5% NO + 10% O_2) were therefore performed on the $MgFe_2O_4$ electrode material in the temperature range of 300–600 °C. Figure 9a and b show the voltammogram at 400 and 300 °C, respectively. Measurements at 300 °C show that activity in NO at −0.6 V is higher than in O_2. The activity in NO_2 and 0.5 % NO + 5 % O_2 is higher than both NO and O_2. The much higher activity in 0.5 % NO + 5 % O_2 is presumably influenced by the fact that a small concentration of NO_2 is formed in the gas mixture; however, other reaction mechanisms/processes not identified seem to dominate the system. The presence of 5% O_2 together with NO does not seem to block the active sites, otherwise the activity would has been somewhere lower. Higher oxygen partial pressure seems to inhibit the reduction of NO quite substantially.

Figure 10 shows the current ratios with respect to O_2 at −0.6 V as a function of temperature. In the case of NO and NO + O_2, the current ratios peak at 400 °C with maximums of 43.8 and 167.7, respectively. Measurements in NO_2 and NO_2 + O_2 at 300 and 400 °C show maximum current ratios of 135.9 and 54.8, respectively. No measurements were made at lower temperatures because of the relatively low electronic conductivity of $MgFe_2O_4$. The ratios of the current densities peak at 400 °C and then fall off almost symmetrically around the peak. Measurements in O_2 + NO_2 and in NO_2 were only made at two different temperatures, so we can therefore not verify a similar kind of current density peak at 400 °C. No voltammograms were recorded above 400 °C because of the thermal decomposition of NO_2 at higher temperatures [45]. Measurements on a portable flue gas analyzer (TESTO 350-S) show that ∼ 20% of the NO_2 have reacted into NO and O_2 at 400 °C, which has to be considered when the data are evaluated.

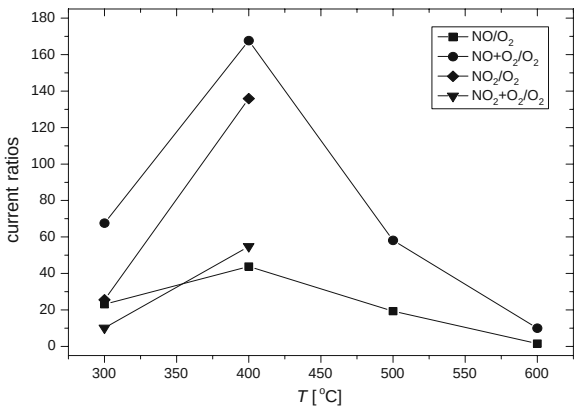

Fig. 10 Current ratios for the $MgFe_2O_4$ electrode measured as a function of temperature at −0.6 V

Figure 11 shows the theoretical calculations on the molar reaction as a function of OCV at 400 °C using Nernst Eq. 8:

$$E = \frac{-\Delta G^{\ominus}}{nF} + \frac{RT}{nF} \ln K, \tag{8}$$

where $\Delta G^{\ominus}$ is the standard potential, n is the number of transferred electrons, F is the Faraday constant, R is gas constant, T is the temperature, and K is the molar reaction constant. An example of K for the reduction of NO to N_2 (Eq. 1) is shown in Eq. 9:

$$K = \frac{(1-\chi)^2}{\chi \cdot p_{O_2}/p^{\theta}}, \tag{9}$$

where χ is the molar reaction and p_{O_2}/p^{θ} is the partial pressure of oxygen in air divided with the standard pressure. The graphs show that the reduction of NO to N_2 lies at relatively high potentials, whereas the reduction of O_2 or NO_2 lies at potentials around −0.1 V. A suitable electrode material should therefore be able to reduce NO (or NO_2) without reducing O_2. Reactions involving N_2O are also shown; however, they are meant as a demonstration of how many processes can occur in the potential range.

The OCV of the different gas mixtures are shown in Fig. 12. The OCV of NO has much lower potentials compared to the thermodynamic calculations (Fig. 11) and it changes only very little as a function of temperature. The concentration gradient of O_2 over the electrolyte could increase the local oxygen partial pressure at the point electrode, which opens up for reactions

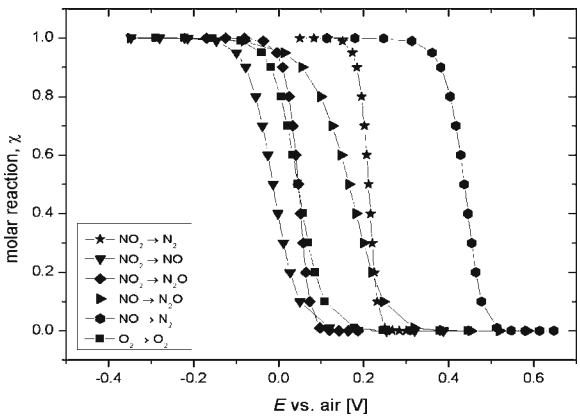

Fig. 11 Theoretical calculations on the molar reaction as function of OCV at 400 °C

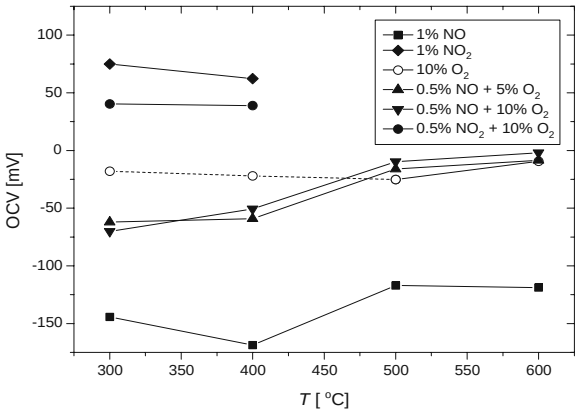

Fig. 12 OCV of $MgFe_2O_4$ in different gas mixtures as a function of temperatures. The *dotted line* of 10% O_2 from 300–400 °C shows the theoretical values of the standard potential

Eqs. 3 and 10 to occur. This and reaction kinetics will explain the lowering of the OCV.

$$O^{2-} + NO \rightarrow NO_2 + 2e^{-}. \tag{10}$$

The OCV of O_2 shows that the potentials at 500 and 600 °C are around −0.02 V, which is close to the standard potential calculated with FactSage 5.5. At 300 and 400 °C, OCV could not be measured with trustworthy accuracy. This is essentially a consequence of the shape of the CV curve, which has a wide region where the current is close to zero. This makes it difficult to measure the OCV since small fluctuations will have a great influence on recorded value. The presence of O_2 together with NO causes OCV to coincide with the OCV of O_2, suggesting that NO does not react at these potentials. The OCV of NO_2 and $NO_2 + O_2$ fall fairly close to each other, with $NO_2 + O_2$ at slightly lower potentials. The presence of O_2 and possible NO should decrease the OCV of $NO_2 + O_2$ according the measurements. However, OCV of $NO_2 + O_2$ still lies fairly close to the OCV of NO_2, suggesting a reaction involving NO_2 to be the dominant one.

Unfortunately, no direct gas conversion can be measured with the cone setup because of the low contact area of the point electrode and the relatively high flow rate. Therefore, we cannot supply a direct answer of the selectivity of the electrode material. However, it does supply information of the activity, which can be used as a relative tool to do further tests on those materials that exhibit high activity in different gases of interest. $MgFe_2O_4$ is considered a highly interesting candidate as a cathode material in electrochemical filters

for direct decomposition of NO_x gases. However, the recorded OCV implies that a relatively large over potential is needed in order to reduce NO on a $MgFe_2O_4$ electrode.

Conclusion

The electrochemical studies of Ni/Mg containing ferries with a spinel-type structure show that the two end members of the $NiFe_2O_4$–$MgFe_2O_4$ series have a relative high activity in NO in the measured temperature range. However, the activity in O_2 differs significantly from the two end members, with the $NiFe_2O_4$ electrode showing the largest activity. Recorded measurements on the $MgFe_2O_4$ electrode show that the current ratios of NO/O_2, $(NO + O_2)/O_2$, NO_2/O_2, and $(NO_2 + O_2)/O_2$ are much higher compared to the other spinels, with the exception of NO/O_2 at 600 °C. As more Fe^{3+} is incorporated on the octahedral site, the higher the conductivity is but the lower the activity in NO and O_2 is. Recordings of OCV suggest that the reduction of NO is inhibited by the presence of O_2, whereas the reduction of NO_2 seems to dominate in the presence of O_2. Four-point DC resistivity measurements show that $Ni_{0.5}Mg_{0.5}Fe_2O_4$ and $Ni_{0.4}Mg_{0.6}Fe_2O_4$ have the highest conductivity at elevated temperatures, whereas the spinels with low Mg content ($Ni_{0.7}Mg_{0.3}Fe_2O_4$ and $NiFe_2O_4$) have the highest conductivity at lower temperatures. An order–disorder of the cations could also be detected from the conductivity measurements in most of the samples. Measurement on thermal expansion show that the temperature of the magnetic order is detectable in all samples, but an additional wide peak is also detected in $MgFe_2O_4$ at 800 °C, which seems to be related to a cation reordering. Thermal expansion coefficients are comparable with CGO10, which is important since a composite electrode of spinel and CGO10 is needed in order to construct a usable electrode.

References

1. DieselNet (2008) www.dieselNet.com, Technical report
2. Pancharatnam S, Huggins RA, Mason DM (1975) J Electrochem Soc 122:869
3. Kammer K (2005) Appl Catal B 58:33
4. Gür T, Huggins R (1979) J Electrochem Soc 19:1067
5. Iwayama K, Wang X (1998) Appl Catal B 19:137
6. Hibino T (1995) J Appl Electrochem 25:203
7. Hibino T, Ushiki K, Kuwahara Y (1995) J Chem Soc Faraday Trans 91:1955
8. Hamamoto K, Fujishiro Y, Awano M (2007) J Electrochem Soc 154:F172
9. Hamamoto K, Fujishiro Y, Awano M (2006) J Electrochem Soc 153:D167
10. Changguan WF, Teraoka Y, Kagawa S (1996) Appl Catal B 8:217
11. Changguan WF, Teraoka Y, Kagawa S (1997) Appl Catal B 12:237
12. Shangguan WF, Teraoka Y, Kagawa S (1998) Appl Catal B 16:149
13. Haneda M, Kintaichi Y, Hamada H (2005) Appl Catal B 55:169–175
14. Drouet C, Alphonse P, Rousset A (2001) Appl Catal B 33:35
15. Simonsen VLE, Find D, Lilliedal M, Petersen R, Hansen KK (2007) Top Catal 45:143
16. Hansen KK, Christensen H, Skou EM (2000) Ionics 6:340
17. Chick LA, Pederson LR, Maupin GD, Bates JL, Thomas LE, Exarhos GJ (1990) Mater Lett 10:6
18. Koteswara Rao K, Banu T, Vithal M, Swamy GYSK, Ravi Kumar K (2002) Mater Lett 54:205
19. Petříček V, Dusek M, Palatinus L (2000) Jana2000, The crystallographic computing system. Institute of Physics, Praha
20. Hansen KK, Vels Hansen K (2007) Solid State Ionics 178:1379
21. Hansen KK (2007) Electrochem Commun 9:2721
22. Hansen KK, Christensen H, Skou EM, Skaarup SV (2000) J Appl Electrochem 30:193
23. Fabry P, Kleitz M, Deportes C (1972) J Solid State Chem 5:1
24. Newman J (1966) J Electrochem Soc 113:501
25. Appel CC, Bonanos N, Horsewell A, Linderoth S (2001) J Mater Sci 36:4493
26. Bruggerman DAG (1935) Ann Phys 24:636
27. Klein C, Hurlbut CS, Dana JD (1998) Manual of mineralogy, 21th edn. Wiley, New York
28. West AR (1987) Solid state chemistry and its applications, 2nd edn. Wiley, New York
29. Berchmans LJ, Kalai Selvan R, Selva Kumar PN, Augustin CO (2004) J Magn Magn Mater 279:103
30. Berchmans LJ, Kalai Selvan R, Augustin CO (2004) Mater Lett 58:1928
31. Ata-Allah SS, Fayek MK, Yehia M (2004) J Magn Magn Mater 279:411
32. Ata-Allah SS, Sayedamed FM, Kaiser M, Hashhash AM (2005) J Mater Sci 40:2923
33. Ziemniak SE, Anovitz LM, Castelli RA, Porter WD (2007) J Phys Chem Solids 68:10
34. Bozorth RM (1951) Ferromagnetism, 5th edn. D. Van Nostrand, New York
35. Harrison RJ, Putnis A (1999) Phys Chem Mineral 26:322
36. Turkin AI, Drebushchak VA (2004) J Cryst Growth 265: 165
37. Modi KB, Joshi HH, Kulkarni RG (1996) J Mater Sci 31:1311
38. Carter RE (1959) J Am Ceram Soc 42:324
39. Weil L (1951) J Phys Rad 12:260
40. Fagg DP, Kharton VV, Shaula A, Marozau IP, Frade JR (2005) Solid State Ionics 176:1723
41. Søgaard M, Hendriksen PV, Mogensen M (2007) J Solid State Chem 180:1489
42. Redfern SAT (2002) Eur J Mineral 14:251
43. Levy D, Diella V, Dapiaggi M, Sani A, Gemmi M, Pavese A (2004) Phys Chem Miner 31:122
44. Antao SM, Hassan I, Parise JB (2005) Am Mineral 90:219
45. ThermFact (2007) FactSage version 5.5. www.factsage.com
46. Bevan DJM, Shelton JP, Anderson JS (1948) J Chem Soc NOV:1729
47. Brabers VAM, Klerk J (1977) J Phys 38:207–209
48. Corbel G, Mestiri S, Lacorre P (2005) Solid State Sci 7:1216

III

J Solid State Electrochem
DOI 10.1007/s10008-009-0801-x

ORIGINAL PAPER

$NiCr_xFe_{2-x}O_4$ as cathode materials for electrochemical reduction of NO_x

F. Bræstrup · K. K. Hansen

Received: 5 November 2008 / Revised: 28 January 2009 / Accepted: 28 January 2009

Abstract Solid solutions of spinel-type oxides with the composition $NiCr_xFe_{2-x}O_4$ ($x = 0.0, 0.5, 1.0, 1.5, 2.0$) were prepared with the glycine–nitrate combustion synthesis. Four-point DC resistivity measurements show an increase in the conductivity as more Cr is introduced into the structure, whereas dilatometer measurements show that the linear thermal expansion decreases with increasing Cr content. The oxides were used as electrode materials in a pseudo-three-electrode setup in the temperature range of 300–600 °C. Cyclic voltammetry and electrochemical impedance spectroscopy were used to characterize the electrochemical behavior in 1% NO, 1% NO_2, and 10% O_2. $NiCr_2O_4$ shows high activity in NO and NO_2 relative to O_2 and can therefore be considered as a possible electrode material. Peaks were detected in the voltammograms recorded on $NiCr_2O_4$ in 1% NO. The origin of the peaks seems to be related to the oxidation of Cr or the formation of nitrogen-containing species formed on the surface of the electrode.

Keywords Spinel-type oxide · Conductivity · Powder diffraction · NO_x · O_2

F. Bræstrup (✉) · K. K. Hansen
Fuel Cells and Solid State Chemistry Division,
Risø National Laboratory for Sustainable Energy,
Technical University of Denmark,
Copenhagen, Denmark
e-mail: frantz.braestrup@risoe.dk

Introduction

The formation of NO and NO_2 gases is one of the main polluting agents from internal combustion processes in diesel fired engines. In addition to being harmful to human health [1], NO_x also contributes to the formation of acid rain [2]. Over the years, scientists have been working on solving the problem with NO_x emission, and so far, the selective catalytic reduction process (SCR) has gained the most attention for diesel exhaust. In SCR, the reduction of NO_x is performed by injecting a reducing agent, such as ammonia, urea, or a hydrocarbon, into the exhaust gas upstream of the SCR catalyst.

An alternative way of solving the problem with NO_x emission is an electrochemical reduction of NO_x over a solid state cell [3]. In such a cell, NO_x gases are reduced at the cathode while O_2 is formed at the anode. However, since O_2 is also present in relatively high concentrations in the exhaust gas from a diesel fired engine, it can also be reduced at the cathode, which will lead to a high consumption of current. A good electrode material therefore has to be selective towards reduction of NO_x.

Pd, Pt, Au, Ag, and Ir have previously been tested [3–7] as possible electrode materials, and a few of them have also shown some interesting results; however, most of the metals are relatively expensive, which has intensified the research for low-cost ceramics to be used as electrode materials. NiO and RuO_2 have also been suggested as candidates for electrochemical NO_x removal [5, 8, 9]; however, in the case of RuO_2, Ru is highly poisonous and forms volatile higher oxides such as RuO_3 and RuO_4. In the case of NiO, operation temperatures have been shown to be too high compared with the temperature of the exhaust gas from a

Published online: 25 February 2009

diesel engine. Different perovskites [10–13] and individual members of the Ruddleston–Popper phases [14] have also been reported as possible electrode materials; however, current densities are relatively low and the activity in O_2 is high compared to the activity in NO. Catalytic NO_x decomposition on spinel-type oxides [15–21] has been reported; however, only a few observations on electrochemical decomposition on spinel-type electrode materials [22–24] have been presented in literature to our knowledge.

$NiCr_2O_4$ has been analyzed as a possible sensor material [25–27] to detect NO_x gases in the presence of O_2. It has shown high selectivity towards detection of NO_x and no cross selectivity towards CO_2. In this study, the electrochemical reduction of NO_x and O_2 has been investigated on spinel-type oxides, $NiCr_xFe_{2-x}O_4$ ($x = 0.0, 0.5, 1.0, 1.5, 2.0$), with the purpose of finding cheap electrode materials, of nonprecious metals, to be used in electrochemical filters.

The spinel-type oxides were measured in a pseudo-three-electrode setup [28] suggested by Fabry [29]. The advantage with this setup is to suppress the effect of microstructures such as porosity, grain size, and grain shape. Recorded data will therefore reflect the true electro-catalytic properties of the material. However, using a cone-shaped point electrode will not make it possible to measure any gas conversion because of the small contact area (compared to the flow rate).

Experimental details

Sample preparation and X-ray diffraction

$NiCr_xFe_{2-x}O_4$ ($x = 0.0, 0.5, 1.0, 1.5, 2.0$) were prepared from aqueous metal-nitrates ($Ni(NO_3)_2$, $Cr(NO_3)_3$ and $Fe(NO_3)_3$) using the glycine–nitrate combustion synthesis [30]. After synthesis, the powder was ball milled for 24 h and then calcined in air at 1,000 °C for 6 h. All samples were analyzed by X-ray diffraction using a STOE theta-theta diffractometer. Scans were conducted over the 2θ-range of 15°–80°, with a step width of 0.05°. Le Bail fits were carried out using the program Jana2000 [31] in order to determine the unit cell parameter, a. Pseudo-Voigt profile functions were used, and the background was modeled with a 10 terms Legendre polynomials.

The powder was pressed uniaxially at 1 ton into pellets, followed by isostatic pressing at 50 tons. This was done in order to make the pellets more dense and to increase their mechanical strength. The samples were then sintered in air at 1,000 °C for 6 h. The pellets were then mechanically tooled into identical cone-shaped electrodes [11, 32] and bares of $4 \times 4 \times 16$ mm. The densities of the samples were measured by the Archimedes principle (see Table 1).

Dilatometry

The linear thermal expansion was measured by dilatometry in air (flow rate: 50 ml/min) using a NETZSCH DIL 402C dilatometer with a sample load of 30,000 cN. The sample-rod was heated from room temperature up to 1,000 °C and back at 2 °C/min. The sample remained at 1,000 °C for 2 h. Data were calibrated to an Al_2O_3 standard at identical conditions.

Four-point DC resistivity measurements

Four-point DC resistivity measurements were conducted on sintered elongated bars. Two Pt wires were attached onto the bars with Pt paste and data were recorded with an in-house data acquisition software, ELCHEMEA. The resistivity was measured every 5 min from room temperature to 1,000 °C and back again with a ramp rate of 2 °C/min and a 2-h dwell at every 50 °C interval. The densities of the elongated rods were measured by the Archimedes principle, and the resistivities of the samples were then corrected for the porosity using the Bruggeman asymmetric model [33].

Cyclic voltammetry and impedance spectroscopy

Cyclic voltammetry (CV) and electrochemical impedance spectroscopy (EIS) were recorded with a

Table 1 Electrode porosities; Curie temperatures, T_c; and expansion coefficients, α

Compound	Porosities	T_c	α
$NiFe_2O_4$	12.5 %	584 °C	$8.0(2) \cdot 10^{-6}$ °C^{-1}
$NiCr_{0.5}Fe_{1.5}O_4$	5.8 %	423 °C	$4.6(1) \cdot 10^{-6}$ °C^{-1}
$NiCrFeO_4$	13.7 %	284 °C	$2.3(1) \cdot 10^{-6}$ °C^{-1}
$NiCr_{1.5}Fe_{0.5}O_4$	8.4 %	~130 °C	$4.1(1) \cdot 10^{-6}$ °C^{-1}
$NiCr_2O_4$	3.6 %	–	$5.6(3) \cdot 10^{-7}$ °C^{-1}

The expansion coefficients are mean values calculated from 600–800 °C. Curie temperatures were read of the graphs and, therefore, statistical errors are given

Gamry Femtostate in a pseudo-three-electrode setup. The cone, acting as a point electrode, was arranged with the tip placed downwards on a polished one-end closed yttrium-stabilized-zirconia-tube electrolyte containing air as reference gas and a silver electrode used as the counter/reference electrode. CV and EIS were recorded in the temperature range from 300 to 600 °C, with a 100 °C step. Data were recorded in 10% O_2 in Ar, 1% NO in Ar, or 1% NO_2 in Ar (Air Liquide) with a flow rate of 20 ml/min. Measurements containing NO_2 gas were performed only at 300 and 400 °C. A 1-h equilibrium time was used to record the open circuit voltage before recording the voltammograms in the potential range of −0.6–0.6 V with different sweep rates (1.0, 10, 100, 200, 400, and 600 mVs^{-1}). EIS were recorded from 177,793(1) to 0.050(1) Hz with 10 points/decade and an amplitude of 24 mV (rms). In order to compare the electrodes directly, the current recorded in the voltammograms (typically in the order of 10^{-8}–10^{-7} A at 500 °C, −0.6 V) were converted into current densities by dividing with the contact area, which was determined by EIS using Newman's formula [34], Eq. 1,

$$r = \frac{1}{4\sigma R_e}, \tag{1}$$

where r is the radius of the circular contact area, σ is the specific conductivity of the electrolyte material, and R_e is the electrolyte resistance. σ can be determined from Eq. 2 [35].

$$\sigma = \frac{1.51 \cdot 10^6}{T} \cdot e^{\frac{-0.94[\mathrm{eV}]}{Tk_B}}, \tag{2}$$

where T and k_B are the temperature and the Boltzman's constant, respectively. Uncertainties on the contact areas were less than 6%. No corrections were made for the IR drop since calculations showed that the corrections were less than 0.2% at all temperatures.

Results and discussions

X-ray diffraction

Almost all materials were single-phase cubic spinel-type oxides. However, a small impurity phase of tetragonal $NiCr_2O_4$ (approx. 5%) was detected together with the cubic $NiCr_2O_4$. $NiFe_2O_4$ has an inverse spinel-type structure with Ni^{2+} located primarily on the octahedral sites and Fe^{3+} located on both the tetrahedral and the octahedral sites. The ionic radii of Ni^{2+} on tetrahedral and octahedral sites are 0.55 and 0.69 Å, respectively, whereas Fe^{3+} has an ionic radius of 0.63 Å (tetrahedral coordinations) or 0.65 Å (octahedral coordinations) [36]. When Cr^{3+}, having an ionic radius of 0.62 Å (octahedral coordinations), is introduced in the structure in favor of Fe^{3+}, it will enter the octahedral lattice site [37], keeping the structure inverse as long as $x \leq 1$. When $x > 1$, Ni is forced to leave the octahedral sites and move to a tetrahedral site, which causes a shrinkage of the unit cell because of the different ionic radii of Fe and Ni. Replacing more Fe with Cr, the structure will now change towards a normal spinel structure [38]. X-ray diffraction measured at room temperature show an decrease in unit cell parameters with increasing Cr content (Fig. 1). A relatively large change of the unit cell parameter is observed when half of the Fe has been replaced by Cr. We would have expected a larger unit cell in the case of $NiCrFeO_4$; however, one explanation would be that a relatively large amount of the Ni^{2+} is located on the tetrahedral sites where its ionic radius is smaller relative to Fe^{3+}.

Conductivity measurements

Figure 2 shows the specific conductivity of the spinels as a function of temperature. Below ~ 650 °C, the conductivity decreases slightly when Cr^{3+} is introduced in the lattice. The conductivity then increases as more Cr^{3+} is incorporated into the lattice, with $NiCr_2O_4$ having the highest conductivity. The conductivity of $NiFe_2O_4$ is mainly attributed to the cation–anion–cation indirect interactions between octahedral sites, where the transport property rises from hopping of localized d electrons between cations [39, 40]. When Cr^{3+} is introduced into the structure, it tends to shield this interac-

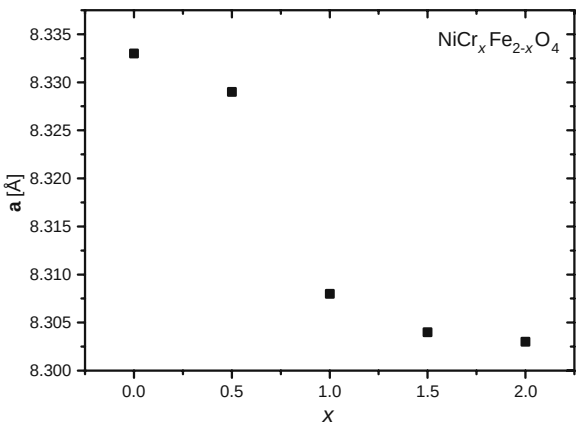

Fig. 1 Unit cell parameters, a, measured at different spinel compositions. A small decrease in a is observed. *Error bars* are at the same magnitude as the dimension of the points

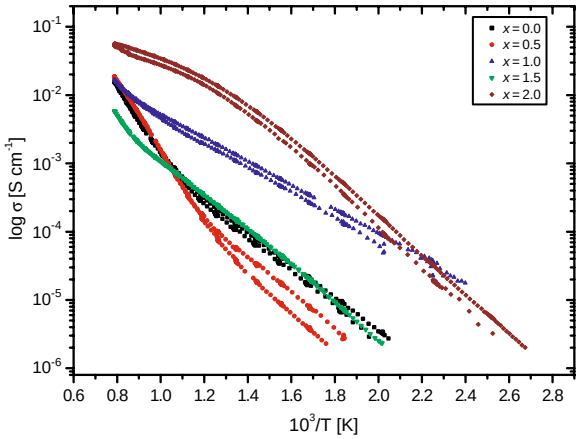

Fig. 2 Four-point DC conductivity measurements of the spinels measured from room temperature to 1,000 °C in air. x refers to the Cr content

tion mechanism and thereby decrease the conductivity. However, as more Cr^{3+} is introduced into the structure, the unit cell decreases, and so does the Cr^{3+}–Cr^{3+} distance. This will strengthen the direct interaction between the Cr^{3+} ions and eventually be the dominating interaction mechanism in the spinel [41]. This interaction will cause an increase in the conductivity at high temperatures, as also observed in Fig. 2.

Dilatometry

Measurements with dilatometry show a gradual decrease in the relative linear expansion (see Fig. 3) as more Cr is incorporated into the structure. The thermal expansion coefficients, α, defined as $\alpha = \frac{1}{L}\frac{\delta L}{\delta T}$, for the different compounds are shown in Table 1. For most of the samples, the Curie temperature, T_c, can be detected as a relatively narrow and asymmetrical peak in the graph of thermal expansion coefficients [42]. T_c decreases with increasing Cr content (see Table 1), which was also reported by Rais [43].

For most of the spinels, the relative linear expansion reveals an almost reversible discontinuity (see Fig. 4) at around 700–900 °C, all appearing during the heating and the cooling stage. This suggests a redistribution between cations on tetrahedral and octahedral sites. In most cases, the compounds are not in equilibrium at low temperatures where the ordering of the cations is controlled by the kinetics [44]. At high temperatures, the spinels are in equilibrium with respect to the cation order–disorder, reflecting the thermodynamic drive towards high-temperature disorder. When the cation rearrangement has reached equilibrium, the thermal expansion takes over the main process, which causes a decrease of the relative linear expansion. Similar observations have been reported on other ferric-spinels [24].

The oxygen ion conductivity of spinels is very low [45, 46]. Therefore, in order to measure any gas conversion, the number of three-phase boundaries must be increased. A mixed electrode of spinel and, for instance, $Ce_{0.9}Gd_{0.1}O_{1.95}$ (CGO10) (an oxygen ion conductor) is therefore needed. Results show that the thermal expansion coefficient of the spinels is, in general, smaller than the thermal expansion coefficient of CGO10 ($\alpha = 11.9 \cdot 10^{-6}$ °C^{-1} [47]). A mixed electrode manufactured with one of our spinels and CGO10 would therefore be a disadvantage because of the large difference in expansion

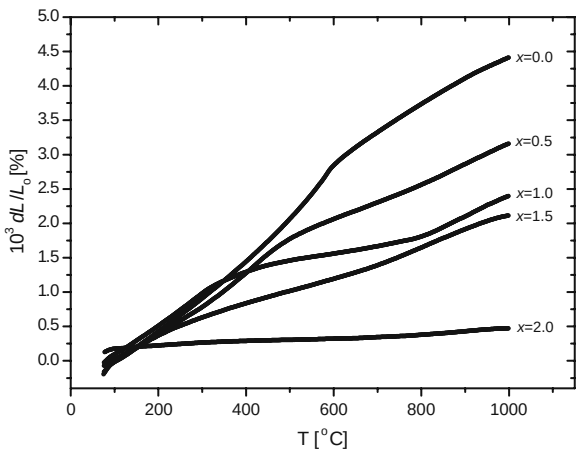

Fig. 3 Linear expansion of the different spinels measured in the temperature range of 80 to 1,000 °C. x refers to the Cr content

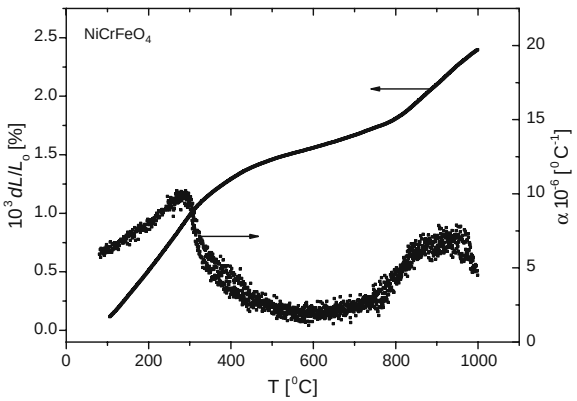

Fig. 4 Linear expansion and the expansion coefficient recorded on the $NiCrFeO_4$ electrode. The Curie temperature can easily be detected at ~ 284 °C

coefficients. A small particle size and a high porosity could maybe reduce tensions in the microstructure, but experiments must be made in order to verify this.

Cyclic voltammetry

Part of the voltammograms recorded at 300, 400, and 500 °C in 1% NO are shown in Fig. 5. The highest activity is recorded for $NiFe_2O_4$, but when Cr^{3+} is introduced into the structure, a gradual decrease of the activity is detected. A small increase in activity is seen when all Fe^{3+} have been substituted by Cr^{3+}, and it suggests that Fe^{3+} is more electrocatalytically active than Cr^{3+} in NO.

Figure 6 shows three voltammograms recorded on $NiCr_2O_4$ in 1% NO_2 at 400 °C. At high sweep rates, the voltammograms appear as straight lines in the potential range, and only at 1 or 10 mV s^{-1}, a small curvature is observed at maximum and minimum applied potential. Voltammograms recorded at 300 °C are similar to the one recorded at 400 °C, although the I/E curves are linear at all sweep rates. The linearity seems to be caused by limitations of the ionic conductivity in the electrolyte. It is not clear why the activity of the $NiCr_{1.5}Fe_{0.5}O_4$ electrode is much lower than the other materials. Measurements were repeated several times but with the same result. Analyzing the current densities of the spinels shows that the activities in O_2 and NO (see Fig. 7) change only little (not including $NiFe_2O_4$); however, current densities in NO_2 seem to vary in a nonsystematic way at 300 °C as a function of the Cr content. At 400 °C, current densities in NO_2 seem more stable through the series until no more Fe is left in the structure. Then, the current density on the $NiCr_2O_4$ electrode changes significantly. The same picture is seen in NO and O_2; however, this time, it is the second end member of the series, $NiFe_2O_4$, that shows the largest activities, whereas the Cr-containing spinels show lower activities. The cathodic activity in O_2 is, in general, quite low at all temperatures, which is an advantage since it will minimize the extra consumption of current caused by the reduction of O_2 in the exhaust gas from a diesel engine (see "Introduction"). The porosities of the electrodes were, in general, low and relatively similar in values. They were therefore not taken further into account.

Because of the small contact area and the relatively high flow rate, no direct gas conversion could be measured. Therefore, in order to evaluate the compounds as possible electrode materials, current ratios between NO_x and O_2 were used as a relative tool to give information of which spinels there should be tested further.

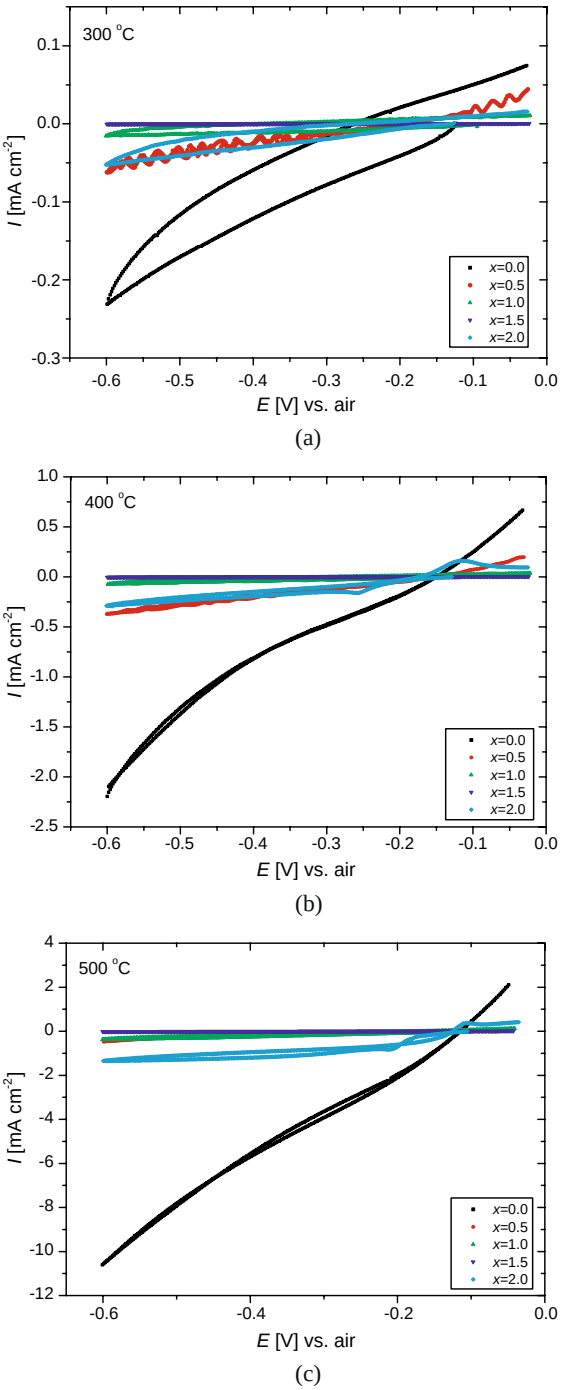

Fig. 5 Cyclic voltammograms on $NiCr_xFe_{2-x}O_4$. **a–c** Part of the voltammograms (−0.6–0 V) recorded at 300, 400, and 500 °C, respectively. The voltammograms were recorded in 1% NO with air as reference gas (sweep rate: 1 mV s^{-1}). The more "wave-shaped" curve of $NiCr_{0.5}Fe_{1.5}O_4$ recorded at 300 °C is due to noise, which reflects a small measured current that again originates from a very small contact area between the cone-shaped electrode and the electrolyte

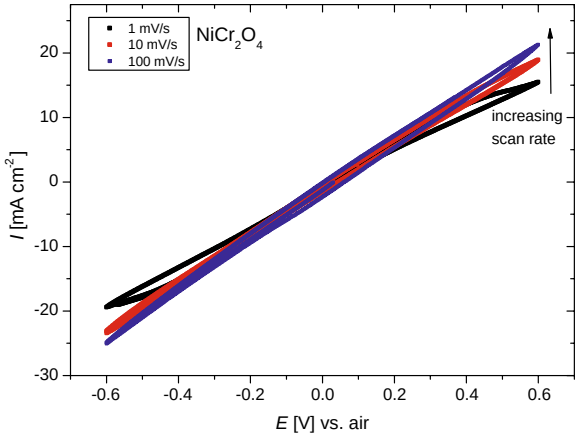

Fig. 6 CV on $NiCr_2O_4$ at 400 °C. Data were recorded in 1% NO_2. Only voltammograms recorded with sweep rates of 1, 10, and 100 mV s^{-1} are shown

Figure 8 shows the ratio of the current densities with respect to O_2 (I_{NO}/I_{O_2}). $NiCr_2O_4$ has the highest ratio, which decreases with increasing temperature. $NiFe_2O_4$ and $NiCr_{0.5}Fe_{1.5}O_4$ also show relatively high current ratios; however, this is only at 300 °C, and in the case of $NiCr_{0.5}Fe_{1.5}O_4$, also at 400 °C. The much lower current ratio of $NiFe_2O_4$ at 400 °C seems to be the result of the relatively high activity in O_2 at temperatures above 300 °C (see Fig. 7).

Figure 9 shows the current ratios, I_{NO_2}/I_{O_2}, of NO_2 with respect to O_2 at −0.6 V. All electrode materials, except for $NiCr_{1.5}Fe_{0.5}O_4$, show much higher activity in NO_2 compared to NO and O_2. $NiCr_2O_4$ shows significantly higher current ratios from 600 to 700, which seems to be a result of the relatively low activity in O_2.

A general problem when working with cone-shaped electrodes is the ohmic drop across the electrode. If the conductivity of the electrode is very low compared to the ionic conductivity of the electrolyte, Newman's formula (Eq. 1) will give inaccurate contact areas. In our case, the high-frequency interception with the real axis in the impedance plot will be given by Eq. 3:

$$R_s = R_e + R_c, \tag{3}$$

where R_c is the ohmic resistivity of the cone-shaped electrode. If $R_e \gg R_c$, R_e can be taken as equal to R_s, which is then used in Newman's formula to calculate the contact areas. Knowing the specific conductivity of the electrode material, finite-element calculations, using the software program COMSOL 3.4 Multiphysics [48], can be applied to calculate the resistance of the cone. However, results show that the area correction is less than 5% at 600 °C, and therefore, a correction of R_s is not needed.

Peaks in voltammograms

Peaks were detected on the voltammograms recorded in the NO atmosphere using the $NiCr_2O_4$-electrode (see Table 2). Peaks were not detected in O_2 and NO_2, however, since the activity in NO_2 is 10 times higher compared to NO, which might explain why no peaks are detected on the $NiCr_2O_4$ electrode. Figure 10 shows the cyclic voltammograms recorded on $NiCr_2O_4$ at 500 °C with increasing sweep rates. Voltammograms recorded at 400 °C and 600 °C look similar to the one recorded at 500 °C and are therefore not presented. Voltammograms recorded at 300 °C are smeared out when sweep rates exceed 10 mV s^{-1}. This is caused by limitations of the electronic conductivity in the electrode and the ionic conductivity in the electrolyte.

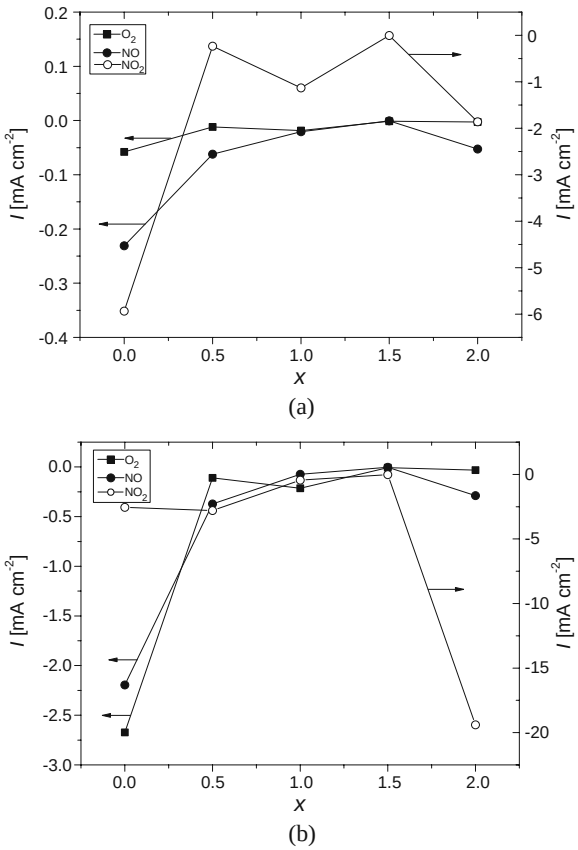

Fig. 7 Current densities recorded on $NiCr_xFe_{2-x}O_4$ at **a** 300 °C and **b** 400 °C with an applied potential of −0.6 V. *x* refers to the Cr content

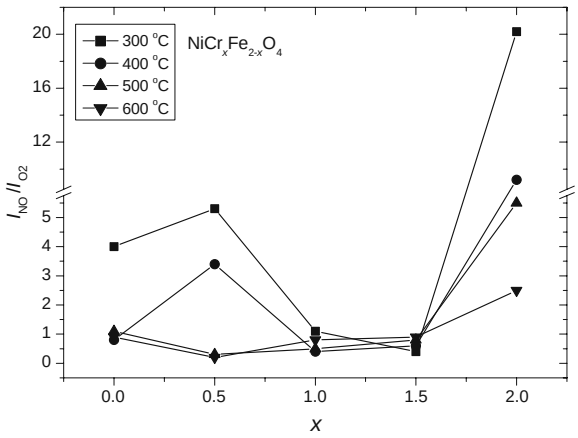

Fig. 8 Current ratios between NO and O_2 for the different spinels ($NiCr_xFe_{2-x}O_4$). $NiCr_2O_4$ shows higher current ratios compared to the other spinels. x refers to the Cr content

Two oxidation (and reduction) peaks positioned very close to each other are observed at high sweep rates (200–600 mV s^{-1}) at 500 and 600 °C. The smaller oxidation peak is most detectable after the second cycle. The larger reduction/oxidation peaks shift (see Fig. 11) approximately 20 mV towards lower potentials after the second cycle. The peaks does not reflect a complete reversible reaction because $|I_{red}/I_{ox}| \neq 1$. The origin of the peaks is not understood completely; however, speculations can be made: Since no peaks were observed in O_2 or in NO_2, an obvious conclusion would be to assign at least one set of peaks to the reduction/oxidation of NO as shown in Eqs. 4 and 5,

$$4e^- + 2NO \rightarrow N_2 + 2O^{2-}, \tag{4}$$

$$2O^{2-} + 2NO \rightarrow 2NO_2 + 4e^-. \tag{5}$$

We would not expect the reverse reaction of Eq. 4 because of the high electrochemical stability of N_2. In order to verify that the peaks are related to the reduction/oxidation of NO, the peak heights of the larger oxidation peak were plotted vs the square root of the sweep rate (see Fig. 12). A linear trend line is observed at 400, 500, and 600 °C; however, at high sweep rates at 600 °C, a deviation from the linear trend is observed. This is caused by the interference with the peak at slightly lower potential. Using Eq. 6 [49]:

$$\frac{i_p}{A} = 0.4463F\sqrt{\frac{F}{RT}}c^*\sqrt{\nu}\sqrt{D_a}, \tag{6}$$

where i_p is the peak height, A is the contact area, F is the Faraday constant, c^* is the initial concentration of the active species, ν is the sweep rate, and D_a is the apparent diffusion constant. The diffusion constant calculated in 1% NO at 500 °C is equal to $2.3 \cdot 10^{-13}$ m^2 s^{-1}. The diffusion constant of a perfect gas (kinetic theory of a perfect gas [50]) is equal to

$$D = \frac{1}{3}\lambda\bar{c}, \tag{7}$$

where λ is the mean free path, given as:

$$\lambda = \frac{K_B T}{\sqrt{2}\sigma p}, \tag{8}$$

and $\bar{c}$ is the mean speed, given as:

$$\bar{c} = \sqrt{\frac{8RT}{\pi M}}. \tag{9}$$

σ is the collision cross-section, p is the pressure, R is the gas constant, and M is molar mass. Calculations show that, for a perfect gas (1% NO), $D = 4.1 \cdot 10^{-4}$ m^2 s^{-1} (500 °C), which is much larger than the measured value. This suggests that the origin of the peak or peaks might be coupled to a bulk diffusion.

Within the potential range, two electrochemical reactions can occur, as shown in Eqs. 10 and 11:

$$\frac{1}{2}O_2 + NiCr_2O_4 \rightarrow NiO + 2CrO_2 \quad E = -0.14\,V, \tag{10}$$

$$\frac{3}{2}O_2 + NiCr_2O_4 \rightarrow NiO + 2CrO_3 \quad E = -0.28\,V. \tag{11}$$

The equilibrium potentials are calculated at 500 °C using FactSage 5.5 [51]. The position of the reduction and oxidation peaks at 400 and 500 °C (1 mV s^{-1})

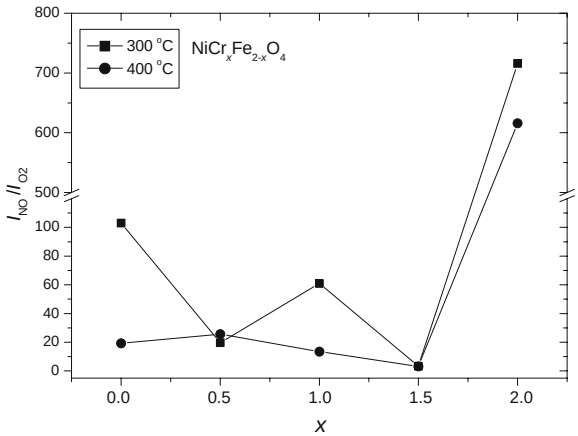

Fig. 9 Current ratios between NO_2 and O_2 for the different spinels ($NiCr_xFe_{2-x}O_4$). $NiCr_2O_4$ shows higher current ratios compared to the other spinels. x refers to the Cr content

Table 2 Positions of the oxidation (Ox) and reduction (Re) peaks found for $NiCr_2O_4$

Sweep rate	400 °C		500 °C		600 °C	
–	Ox	Re	Ox	Re	Ox	Re
1 mVs^{-1}	−111 mV	−261 mV	−102 mV	−212 mV	−80 mV	−194 mV
10 mVs^{-1}	−55 mV	−306 mV	−85 mV	−242 mV	−68 mV	−224 mV
100 mVs^{-1}	34 mV	–	−15 mV	−304 mV	−37 mV	−264 mV
200 mVs^{-1}	64 mV	–	15 mV	−324 mV	−18 mV	−284 mV
400 mVs^{-1}	91 mV	–	42 mV	−422 mV	3 mV	−318 mV
600 mVs^{-1}	114 mV	–	65 mV	−455 mV	18 mV	−361 mV

The position of the reduction peak could not be determined for all sweep rates at 400 °C. All positions were read of the graphs and therefore no statistical errors are given

matches quite well with the equilibrium potential of Eq. 10; however, the position of the peaks at 600 °C does not coincide well with the equilibrium potential of Eq. 10. The oxidation peak seems to be shifted and approximately 50 mV more towards high potentials than expected. Formation of CrO_3 seems, however, not to be present due to the position of the peaks. Considering the charge transfer and assuming a perfect cone shows that the reaction 10 proceeded approximately 19 μm up in the cone electrode (500 °C, 1 mV s^{-1}). If the oxidation/reduction of Cr is in fact the explanation of the peaks, we are still left with the questions of why no peaks are observed in O_2 or NO_2, why no voltammograms of the other Cr-containing spinels appear to show peaks in any of the gases, what causes the second reduction/oxidation peak, and finally why we start by seeing a reduction peak when no CrO_2 could be detected by X-ray diffraction before starting the experiment.

Since no peaks were detected in the O_2-containing atmosphere for $NiCr_2O_4$, it suggests that the origin of the peaks is not due to the formation of Cr oxides but must be found in the formation of other unknown nitrogen-containing species on the surface. Similar observations were reported by Simonsen [22], and peak formations were also attributed to the formation of nitrogen-containing species on the surface. Earlier reports show that Cr species evaporate relatively easy at elevated temperatures [52, 53], and it is possible that some of the Cr in the outermost atomic layers of the particles has evaporated during sintering. This would lead to a depletion of Cr at the surface of the materials and would explain the absence of peaks in the Fe-containing materials since it has been shielded from contact with any of the reaction gases. The second set of peaks is very difficult to ascribe a certain process, but it may be due to reduction/oxidation processes of the NO gas. Therefore, giving the missing peaks in O_2 on the $NiCr_2O_4$ electrode suggests the formation of other (unknown) stable or metastable nitrogen-containing species on the surface of the electrode. However, it cannot be $Ni(NO_3)_2$ or $Cr(NO_3)_3$ since they will decompose above 300 °C [54, 55]. The position of the peaks

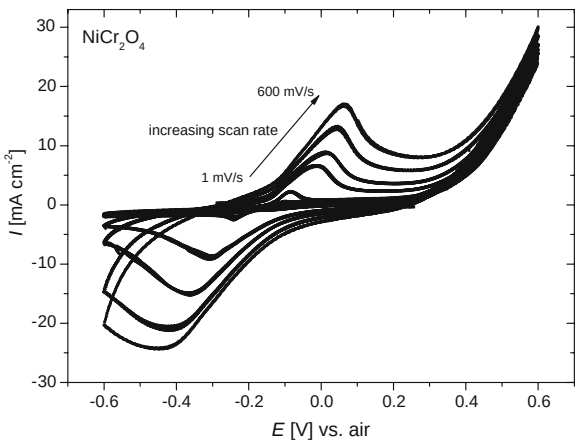

Fig. 10 CV on $NiCr_2O_4$ at 500 °C. Data were recorded in 1% NO using different sweep rates

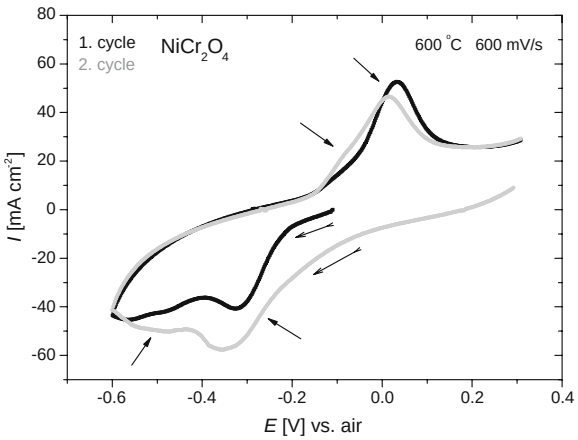

Fig. 11 Part of the cyclic voltammogram recorded at 600 °C (sweep rate: 600 mV s^{-1}). *Bold arrows* show the reduction/oxidation peaks, whereas the *thin peaks* show the direction of the scan

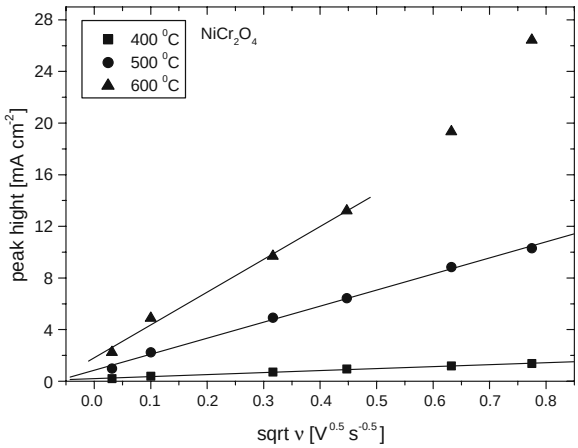

Fig. 12 Peak height plotted vs the square root of the sweep rate. A linear trend can be detected at 400 and 500 °C; however, at 600 °C, the linearity is disturbed at high sweep rates

fits, on the other hand, quite well with the oxidation of Cr, and it cannot be ruled out that it contributes to the peak formation.

Conclusion

Substitution of Fe^{3+} with Cr^{3+} in the spinel-type oxides; $NiCr_xFe_{2-x}O_4$ show a decrease of unit cell parameters and an increase of the conductivity. Dilatometry measurements show a decrease in the linear expansion in the measured temperature range and, in most samples, the Curie temperature and a cation redistribution could also be detected. CV and EIS were recorded on the spinels in 1% NO, 1% NO_2, and 10% O_2. Results show that the activity of $NiFe_2O_4$ is relatively high in NO and NO_2. However, it also has a high activity in O_2. The activity of $NiCr_2O_4$ is, although lower than for $NiFe_2O_4$, also relatively high. However, the activity in O_2 is low, which makes it a candidate for a possible electrode material in an electrochemical cell for the reduction of NO_x gases from a diesel fired engine. Formation of peaks in the voltammograms on the $NiCr_2O_4$ electrode suggests the formation of nitrogen-containing species on the surface or, alternatively, oxidation of Cr in the electrode.

References

1. Butler AR, Williams DLH (1993) Chem Soc Rev 22:233
2. Manahan SE (1994) Enviromental chemistry, 6th edn. CRC, London
3. Pancharatnam S, Huggins RA, Mason DM (1975) J Electrochem Soc 122:869
4. Gür T, Huggins R (1979) J Electrochem Soc 19:1067
5. Iwayama K, Wang X (1998) Appl Catal B 19:137
6. Hibino T (1995) J Appl Electrochem 25:203
7. Hibino T, Ushiki K, Kuwahara Y (1995) J Chem Soc Faraday Trans 91:1955
8. Hamamoto K, Fujishiro Y, Awano M (2007) J Electrochem Soc 154:F172
9. Hamamoto K, Fujishiro Y, Awano M (2006) J Electrochem Soc 153:D167
10. Simonsen VLE, Johnsen MM, Hansen KK (2007) Top Catal 45:131
11. Hansen KK (2007) Electrochem Commun 9:2721
12. Kammer Hansen K, Skou EM, Christensen H (2000) J Electrochem Soc 147:2007
13. Kammer Hansen K, Skou EM, Christensen H (2005) Solid State Ionics 176:915
14. Simonsen VLE, Nørskov L, Kammer Hansen K (2008) J Solid State Electrochem 12:1573
15. Changguan WF, Teraoka Y, Kagawa S (1996) Appl Catal B 8:217
16. Changguan WF, Teraoka Y, Kagawa S (1997) Appl Catal B 12:237
17. Shangguan WF, Teraoka Y, Kagawa S (1998) Appl Catal B 16:149
18. Haneda M, Kintaichi Y, Hamada H (2005) Appl Catal B 55:169-175
19. Drouet C, Alphonse P, Rousset A (2001) Appl Catal B 33:35
20. Chen L, Horiuchi T, Mori T (1999) Catal Lett 60:237
21. Fino D, Russo N, Saracco G, Specchia V (2006) J Catal 242:38
22. Simonsen VLE, Find D, Lilliedal M, Petersen R, Hansen KK, (2007) Top Catal 45:143
23. Hansen KK, Christensen H, Skou EM (2000) Ionics 6:340
24. Bræstrup F, Hansen KK (2008) J Solid State Electrochem. doi:10.1007/s1000800806539
25. Zhuiykov S, Nakano T, Kunimoto A, Yamazoe N, Miura N (2001) Electrochem Commun 3:97
26. West DL, Montgomery FC, Armstrong TR (2005) J Electrochem Soc 152:H74
27. Stranzenbach M, Gramckow E, Saruhan B (2007) Sens Actuators B 127:224
28. Hansen KK, Christensen H, Skou EM, Skaarup SV (2000) J Appl Electrochem 30:193
29. Fabry P, Kleitz M, Deportes C (1972) J Solid State Chem 5:1
30. Chick LA, Pederson LR, Maupin GD, Bates JL, Thomas LE, Exarhos GJ (1990) Mater Lett 10:6
31. Petříček V, Dusek M, Palatinus L (2000) Jana2000, The crystallographic computing system. Institute of Physics, Praha
32. Hansen KK, Vels Hansen K (2007) Solid State Ionics 178:1379
33. Bruggeman DAG (1935) Ann Phys 24:636
34. Newman J (1966) J Electrochem Soc 113:501
35. Wang WG, Barfod R, Larsen PH, Kammer K, Bentzen JJ, Hendriksen PV, Mogensen M (2003) In: Singhal SC, Dokiya M (ed) Solid oxide fuel cells VIII, vol 7. Electrochemical Society, Pennington
36. Klein C, Hurlbut CS, Dana JD (1998) Manual of mineralogy, 21th edn. Wiley, New York
37. Kedem D, Rothem T (1967) Phys Rev Lett 18:165
38. Bongers PF, Philips (1967) Tech Rev 28:13
39. Ata-Allah SS, Fayek MK, Yehia M (2004) J Magn Magn Mater 279:411

40. Ata-Allah SS, Sayedamed FM, Kaiser M, Hashhash AM (2005) J Mater Sci 40:2923
41. Yaresko A, Antonov V (2007) J Magn Magn Mater 310: 1672
42. Touloukian YS, Ho CY (1977) Thermophysical properties of matter. The TPRC data series vol 13. Plenum, New York
43. Rais A, Gismelseed AM, Al-Omari IA (2005) Phys Stat Sol B 242:1497
44. Redfern SAT (2002) Eur J Mineral 14:251
45. O'Bryan HM, DiMarcello FV (1970) J Am Ceram Soc 53:413
46. Dieckmann R, (1984) Solid State Ionics 12:1
47. Corbel G, Mestiri S, Lacorre P (2005) Solid State Sci 7:1216
48. COMSOL (2007) COMSOL version 3.4. www.comsol.com
49. Bard AJ, Faulkner LR (2001) Electrochemical methods, 2nd edn. Wiley, New York
50. Atkins P, de Paula J (2002) Atkins' physical chemistry, 7th edn. Oxford, Oxford
51. ThermFact (2007) FactSage version 5.5. www.factsage.com
52. Holcomb GR, Alman DE (2006) Scr Mater 54:1821
53. Machkova M, Zwetanova A, Kozhukharov V, Raicheva S (2008) J Uni Chem Tech Metall 43:53
54. Mikuli E, Migdał-Mikuli A, Chyży B, Grad B, Dziembaj R (2001) Thermochim Acta 370:65
55. Lide DR (2007) CRC Handbook of chemistry and physics, 87th edn. CRC, New York

VI

J Appl Electrochem
DOI 10.1007/s10800-009-9923-1

ORIGINAL PAPER

Characterization of $MgMn_xFe_{2-x}O_4$ as a possible cathode material for electrochemical reduction of NO_x

F. Bræstrup · K. K. Hansen

Received: 16 February 2009 / Accepted: 29 April 2009

Abstract *Spinel-type oxides of* $MgMn_xFe_{2-x}O_4$, $x = 0.0$, 0.2, 0.4, 0.6, 0.8, 1.0, were synthesized as a solid state reaction and characterized with dilatometry and resistivity measurements up to 1000 °C. Results showed a general decrease of the linear expansion and an increase in conductivity as a function of the Mn content. Point electrodes were analyzed from 300 to 600 °C in a pseudo-three-electrode setup in 1% NO, 1% NO_2, and 10% O_2 using cyclic voltammetry. The activities in O_2 were in general very low whereas the activities in NO were slightly higher. The activities in NO_2 were for all materials much higher than the activities in O_2. Even though Mn tends to decrease the activity of the materials, current ratios of I_{NO_x}/I_{O_2} have relatively high values in both NO and NO_2.

Keywords Spinel · Cone-electrodes · NO_x · O_2

1 Introduction

Spinel-type oxides (AB_2O_4, A = tetrahedral sites, B = octahedral sites) are in general poor electron conductors [1] and very bad oxygen ion conductors due to the almost perfect stoichiometric oxygen lattice [2]. Cations on the other hand tend to diffuse much easily through the structure [3]. Despite these properties spinel-type oxides are widely used in the industry because of their usefulness as magnetic materials, semi-conductors, pigments, catalysts, and refractories.

F. Bræstrup (✉) · K. K. Hansen
Fuel Cells and Solid State Chemistry Division, Risø National Laboratory for Sustainable Energy, Technical University of Denmark, Lyngby, Copenhagen, Denmark
e-mail: frantz.braestrup@risoe.dk

In search of a better fuel efficiency in the transportation sector, vehicles with a diesel-fired engine have increased their market share quite significantly over the years [4]. However, diesel-fired engines run with an excess of oxygen (lean conditions) which eliminates the use of the three-way converter which requires stoichiometric conditions to simultaneously catalyze oxidizing and reducing reactions. One of the main polluting agents from internal combustion processes in diesel- fired engines is the formation of NO_x (NO and NO_2) gases. So far the selective catalytic reduction process (SCR), where a reducing agent is injected into the exhaust gas upstream of the SCR catalyst, seems to be the only existing technology that can minimize the problem with NO_x gases from the diesel exhaust. However, SCR is most suitable for buses and trucks. But even in these cases there are problems with storage and escape of the reducing agent through the tailpipe of the vehicle. This shows that no perfect working technologies exist in this field [5].

Pancharatnam [6] suggested that NO_x could be removed over a solid state cell where NO_x gases are reduced at the cathode while O_2 is formed at the anode. However, since O_2 is also present in relatively high concentrations in the exhaust gas from a diesel-fired engine, it can also be reduced at the cathode which will lead to a high consumption of current. A good electrode material therefore has to be selective toward reduction of NO_x. Several attempts have been made to find cheap electrode materials of non-precious metals that can be used in such a cell. However, so far the materials, such as NiO, different perovskites, and individual members of the Ruddleston-Popper phases [7–11], have shown inadequate performance at the working conditions in a diesel-fired vehicle. The activity in O_2 is also in most cases too high compared to the activity in NO. RuO_2 [12] has also been suggested as possible electrode material; however, it is highly poisonous

Published online: 26 May 2009

and forms volatile of higher order oxides. Catalytic NO_x decomposition on spinel-type oxides [13–19] has been reported; however, to our knowledge only few observations on electrochemical decomposition on spinel-type electrode materials [20–22] have been presented in literature.

$MgFe_2O_4$ is a promising electrode material in NO and NO_2 sensors [22] and it has also received some interest as a possible humidity sensor material [23]. However, $MgFe_2O_4$ is a poor electronic conductor which will limit the current passing through the cell. The purpose of this article is therefore to investigate the effects of substituting Mn into the $MgFe_2O_4$ structure and to determine the conductivity with respect to the electro-catalytic activity. Since spinels act as isolators with respect to oxygen ion diffusion, it is most likely that in case of cell manufacturing, they have to be mixed with a solid state oxygen ion conductor. Therefore measurements on thermal expansion were also conducted on the different samples.

The spinel-type oxides were measured in a pseudo-three-electrode setup [24] suggested by Fabry et al. [25]. The advantage with this setup is that it suppresses the effect of geometry and morphology on the electrode behavior. Recorded data will therefore reflect the true electro-catalytic properties of the material. However, it is not possible to measure any gas conversion using a cone-shaped point electrode because of the small contact area. Instead, current ratios of I_{NO_x}/I_{O_2} are used as indicators of the apparent selectivity of the reduction of NO_x gases.

2 Experimental details

2.1 Sample preparation and X-ray diffraction

$MgMn_xFe_{2-x}O_4$, $x = 0.0$, 0.2, 0.4, 0.6, 0.8, 1.0, was synthesized as a solid state reaction using powder of metal oxides [MgO 99.99%, MnO_2 99.6%, and α-Fe_2O_3 99.9% (Alfa Aesar)]. The powder was mixed in an agate mortar and calcined at 900 °C for 30 h with a ramp rate of 120 °C/h. The powder was then crushed and the calcination process was repeated at 1050 °C. Relatively low sintering temperatures were used to avoid evaporation of Mn oxides. All samples were analyzed by X-ray diffraction using a STOE theta–theta diffractometer with a Cu anode. X-ray diffractograms were collected at $15° \leq 2\theta \leq 80°$ with a step width of 0.05°. Le Bail fits were carried out using the program Jana2000 [26] to determine the unit cell parameter a. Pseudo-Voigt profile functions were used, and the background was modeled with a 10 terms Legendre polynomials.

The powder was uniaxially pressed at 1 ton for 30 s into elongated bars and pellets which were placed in a rubber sleeve and pressed isostatically at 50 tons for 20 s. The samples were then calcined at 1100 °C for 10 h with a ramp rate of 50 °C/h. The elongated rods was cut into pieces of $4 \times 4 \times 18$ mm^3 and $4 \times 4 \times 12$ mm^3 to be used for resistivity and dilatometry measurements, respectively. The elongated pellets were mechanically tooled into identical cone-shaped electrodes, all having a diameter of 7.5 mm and with a cone side in an angle of 45° with the base.

2.2 Dilatometry

The linear thermal expansion was recorded using a NETZSCH DIL 402C dilatometer with a sample load of 30000 cN. Data were recorded in air with a flow rate of 50 mL/min. The samples were heated from room temperature up to 1000 °C and back at 2 °C/min. The sample remained at 1000 °C for 2 h. Data were calibrated to an Al_2O_3 standard at identical conditions.

2.3 Four-point DC resistivity measurement

The elongated bars ($4 \times 4 \times 18$ mm^3) were contacted with platinum leads and painted with Pt paste at each end of the bar. Two Pt potential probes with a fixed distance were positioned on one side of the bar. The data collection was made with an in-house data acquisition software, ELCHEMEA. The resistivity was measured every 5 min from room temperature to 1000 °C and back again with a 2-h dwell at every 50 °C interval and using a ramp rate of 2 °C/min. The porosity of the samples were measured with a Micromeritics AutoPore IV Mercury Porosimeter to correct the resistivities using Bruggeman formula [27].

2.4 Cyclic voltammetry and impedance spectroscopy

Cyclic voltammetry and impedance spectroscopy were recorded with a Gamry Femtostate in a pseudo-three-electrode setup on the cone-shaped electrodes. The base of the cone was painted with Au paste which acted as current collector. The cone, acting as the working electrode, was arranged with the tip placed downward on a polished one-end closed YSZ-tube (Yttrium-stabilized Zirconia) electrolyte containing air as reference gas. The thickness of the electrolyte was approximately 2 mm. The inside of the tube was painted with Ag paste and fired at 600 °C to get a good electrical contact. The Ag electrode was then used as the counter/reference electrode. The much smaller contact area of the cone electrode (point electrode), compared to the counter electrode, suppressed a polarization of the counter electrode as it was at the same time constantly exposed to a reference gas. A reference electrode could therefore be placed together with the counter electrode (a pseudo-three-electrode setup).

Data were recorded in 10% O_2 in Ar, 1% NO in Ar (Air Liquide) at 300, 400, 500, and 600 °C, and in 1% NO_2 in Ar (Air Liquide) at 300 and 400 °C. A flow rate of 20 mL/min was applied during all measurements. A 1 h equilibrium time was used to record the open circuit voltage (OCV) before recording the voltammograms in the potential range of −0.6 to 0.6 V with different sweep rates (1.0 and 10 mVs^{-1}). In order to compare the different electrode materials directly, the recorded current was converted into current densities by dividing with the contact area between the electrode and the electrolyte. The contact area was determined by using Newman's formula [28], Eq. 1,

$$r = \frac{1}{4\sigma R_e}, \tag{1}$$

where r is the radius of the circular contact area, σ is the specific conductivity of the electrolyte material, and R_e is the electrolyte resistance. σ can be determined from Eq. 2 [29].

$$\sigma = \frac{1.51 \cdot 10^6}{T} \cdot e^{\frac{-90.7[\mathrm{kJmol}^{-1}]}{RT}}, \tag{2}$$

where T and R are the temperature and the gas constant, respectively. R_e (see Table 1) was determined with impedance spectroscopy recorded from 177793(1) to 0.050(1) Hz with 10 points/decade and an amplitude of 24 mV (rms). Uncertainties on the contact areas were less than 10%. No corrections were made for the *IR* drop since calculations showed that the corrections were less than 1% at all temperatures.

3 Results and discussions

3.1 X-ray diffraction

All samples were analyzed as single phase cubic spinel-type oxides. Plotting the unit cell parameter a as a function of the Mn content shows that a only changes a little when Fe is substituted by Mn. Mg^{2+} ions have a strong preference to occupy the B sites and partially occupy the A sites [30]. Fe^{3+} on the other hand occupies both A and B sites with no preference, since their ionic radii are very similar [31]. Mn^{3+} tends to occupy B sites instead of A sites [32]. However, the ionic radius of Mn^{3+} is slightly bigger than that of Fe^{3+},[1] which will explain the small increase of the unit cell as more Mn is incorporated into the structure. Earlier reports [33] show similar increase in unit cell, but they state that the Mn content could not exceed $x = 0.4$ in order to synthesize a single phase powder. However, magnetic measurements on [34] $MgMn_xFe_{2-x}O_4, x \geq 1$ show that the material could be synthesized as a single phase with a solid state reaction (Fig. 1).

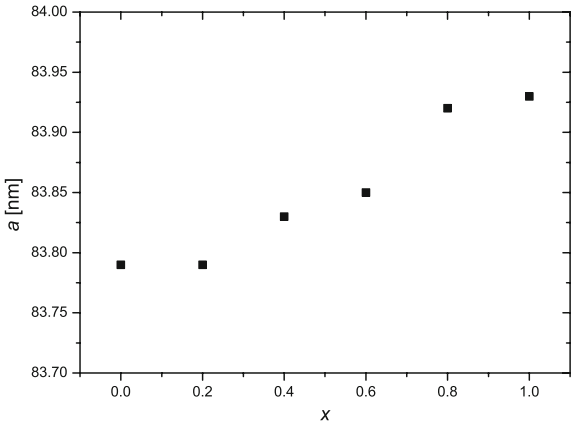

Fig. 1 Unit cell parameters, a, measured at different spinel compositions. A small increase in a is observed. x refers to the Mn content. Error bars are at the same magnitude as the dimension of the points

Table 1 Electrode porosities, Curie temperatures, T_c, expansion coefficients, α, and mean values of the electrolyte resistance, $\langle R_e \rangle$

Compound	Porosities (%)	T_c (°C)	α ($°C^{-1}$)	$\langle R_e \rangle$ (MΩ)
$MgFe_2O_4$	27.18	322	$1.25(1) \cdot 10^{-5}$	2.5(2)
$MgMn_{0.2}Fe_{1.8}O_4$	29.92	304	$1.40(1) \cdot 10^{-5}$	7.4(3)
$MgMn_{0.4}Fe_{1.6}O_4$	33.16	251	$1.27(1) \cdot 10^{-5}$	12(4)
$MgMn_{0.6}Fe_{1.4}O_4$	33.78	163	$1.195(5) \cdot 10^{-5}$	7.1(2)
$MgMn_{0.8}Fe_{1.2}O_4$	37.92	141	$1.05(1) \cdot 10^{-5}$	13(3)
$MgMnFeO_4$	32.04	138	$1.010(9) \cdot 10^{-5}$	4.7(4)

The expansion coefficients are mean values calculated from 600 to 800 °C

3.2 Dilatometry and resistivity measurements

Figure 2 shows the dilatometry measurements of the samples. It shows, with the exception of $MgFe_2O_4$, a gradual decrease of the linear thermal expansion as more Mn is incorporated into the structure. The graphs (not shown for all materials) of the expansion coefficient show for all samples a peak positioned around 150−325 °C. The shape and position of the peaks agrees with the expected Curie temperature, T_c [35–37]. Figure 3 shows an example of the thermal expansion and expansion coefficient in the case of $MgMn_{0.2}Fe_{1.8}O_4$. Table 1 shows the decreasing Curie temperatures and the mean expansion coefficient in the temperature range of 600 to 800 °C. As discussed in the Introduction, spinels are in general bad oxygen ion

[1] http://www.webelements.com.

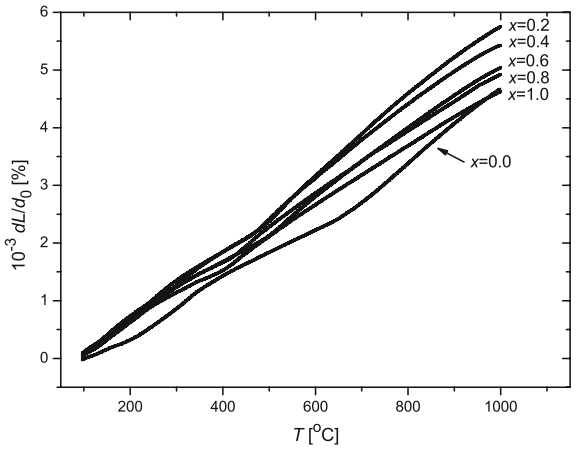

Fig. 2 Linear expansion of the different electrode materials measured in the temperature range of 80 to 1000 °C. *x* refers to the Mn content

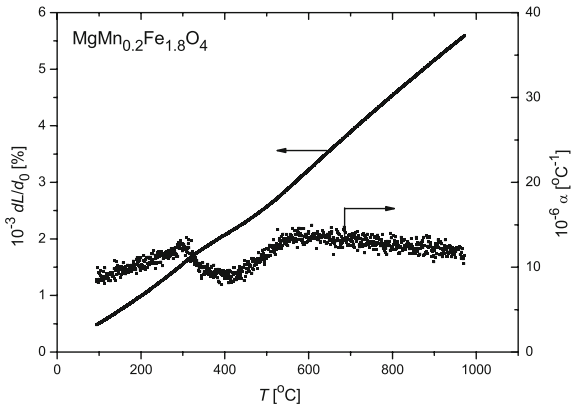

Fig. 3 Linear expansion and the expansion coefficient recorded on the $MgMn_{0.2}Fe_{1.8}O_4$ electrode. The Curie temperature can easily be detected at ~304 °C

conductors. Therefore, an oxygen ion material, such as $Ce_{0.9}Gd_{0.1}O_{1.95}$ (CGO10), must be mixed with the spinel material when more advanced cells need to be produced. Results show that the thermal expansion coefficient of the spinels is in general smaller than the thermal expansion coefficient of CGO10 ($\alpha = 11.9 \cdot 10^{-6}$ °C^{-1}); however, it should be possible to manufacture a suitable microstructure based on similar expansion coefficients in solid oxide fuel cells [38, 39]. Experiments however must be made to verify this.

Figure 4 shows the resistivities of the samples converted into Bruggeman-corrected specific conductivities. Results show that the conductivity increases when Fe is substituted with Mn. The conductivity is mainly caused by exchange interaction between B sites ($B-O^{2-}-B$) with hopping of localized *d*-electrons between cations [40, 41]. Substituting

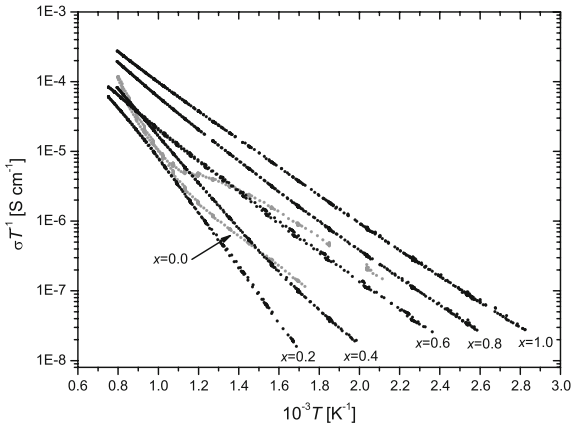

Fig. 4 Four-point DC conductivity measurements of the spinels measured from room temperature to 1000 °C in air. *x* refers to the Mn content

Mn into the structure will increase the conductivity as Mn can exist in more than one valence state (2+, 3+, and 4+) with Mn^{2+} primarily occupying the A sites and Mn^{3+} and Mn^{4+} occupying the B sites [32]. It is however believed that the oxidation state on Mn found in the samples is primarily 3+.

3.3 Cyclic voltammetry

The activity in 10% O_2 is for all materials very low ($\ll$1 mA cm^{-2}, −0.6 V), and within the uncertainties of the recorded data and contact areas (10%) it was not possible to determine a general trend with respect to activities and the Mn content.

The cathodic activities recorded in 1% NO at 400, 500 and 600 °C are low, and therefore, differences between the Mn-containing materials are small. Therefore only the results for some of the electrodes are shown in the figures. $MgMn_{0.4}Fe_{1.6}O_4$ has a slightly higher cathodic activity (−0.6 V) at 400 and 500 °C than the other Mn-containing samples. At all temperatures, the cathodic activity on $MgFe_2O_4$ was significantly higher (see Fig. 5). It is not known why $MgMn_{0.4}Fe_{1.6}O_4$ has higher activities but porosity measurements show no distinct differences compared to the other electrodes.

Data recorded in 1% NO_2 show a higher activity of the electrodes compared with the recorded data in NO and O_2. Earlier reports show similar trend on ferrite spinel-type electrodes [22, 42] and perovskites [8]. However, the cathodic activities of the Mn-containing electrodes are significantly lower compared to those of $MgFe_2O_4$ as also observed in NO. The activity of $MgMn_{0.2}Fe_{1.8}O_4$ is slightly higher than that of the other electrodes at 400 °C, whereas $MgMn_{0.8}Fe_{1.2}O_4$ shows higher activity at 300 °C (not shown) (Fig. 6).

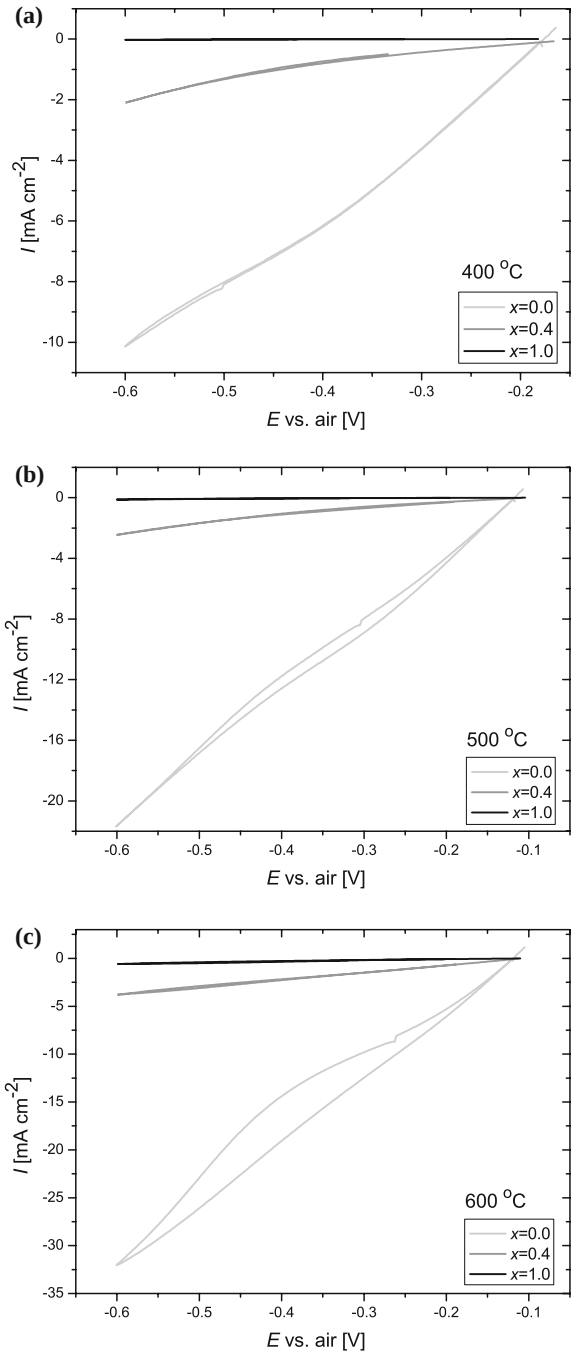

Fig. 5 Cyclic voltammograms on $MgMn_xFe_{2-x}O_4$. (**a**), (**b**), and (**c**) show a part of the voltammograms recorded at 400, 500, and 600 °C, respectively. The voltammograms were recorded in 1% NO with air as reference gas (sweep rate: 1 mVs^{-1}). Voltammograms recorded at 10 mVs^{-1} looked similar

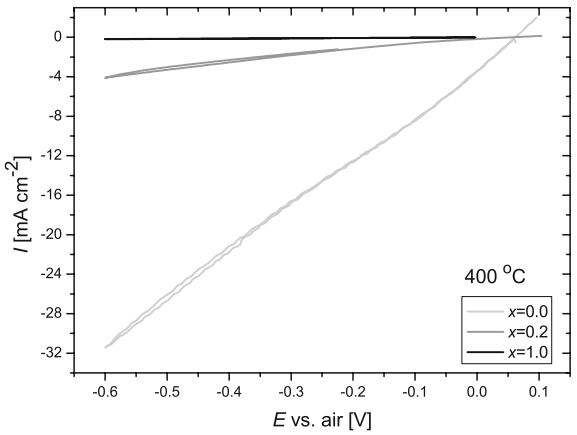

Fig. 6 Part of the cyclic voltammograms recorded at 400 °C in 1% NO_2 with a sweep rate of 1 mVs^{-1}. Voltammograms recorded at 10 mVs^{-1} looked similar

As previously discussed (see Introduction), current ratios of I_{NO_x}/I_{O_2} can be used as a tool to evaluate the electrode materials. Figure 7 shows the current ratios of I_{NO}/I_{O_2} and I_{NO_2}/I_{O_2} . At 400 °C, current ratios of I_{NO_2}/I_{O_2} show ratios of 25−30, with the exception of $MgMn_{0.4}Fe_{1.6}O_4$ which has a much higher current ratio of ∼65. Measurements were repeated with the same result, so it was not possible to explain the one-point jump on the curve. At 300 °C, current ratios increase with $MgFe_2O_4$ having the highest value of ∼135. It then drops to 40−50 for the Mn-containing electrodes.

Current ratios of I_{NO}/I_{O_2}. show in general much lower values compared to I_{NO_2}/I_{O_2}. At 600 °C current ratios are low and in the range of 1 to 3. At 500 °C, the highest current ratio is observed for $MgFe_2O_4$; however, the curves show a small broad peak at $0.4 \leq x \leq 0.6$. Still ratios only range from 1 to 5 for the Mn-containing electrodes. At 400 °C we see a large peak at $0.2 \leq x \leq 0.8$ with a maximum current ratio of ∼46. We were not able to explain the sudden drop at $x = 0.2$, and again porosity measurements did not help answer it either. We therefore believe that the porosity of the electrode materials have very little effect on the recorded data from a cone setup.

4 Conclusion

We have successfully synthesized single phase spinel-type oxides with a composition of $MgMn_xFe_{2-x}O_4$, $x = 0.0, 0.2,$

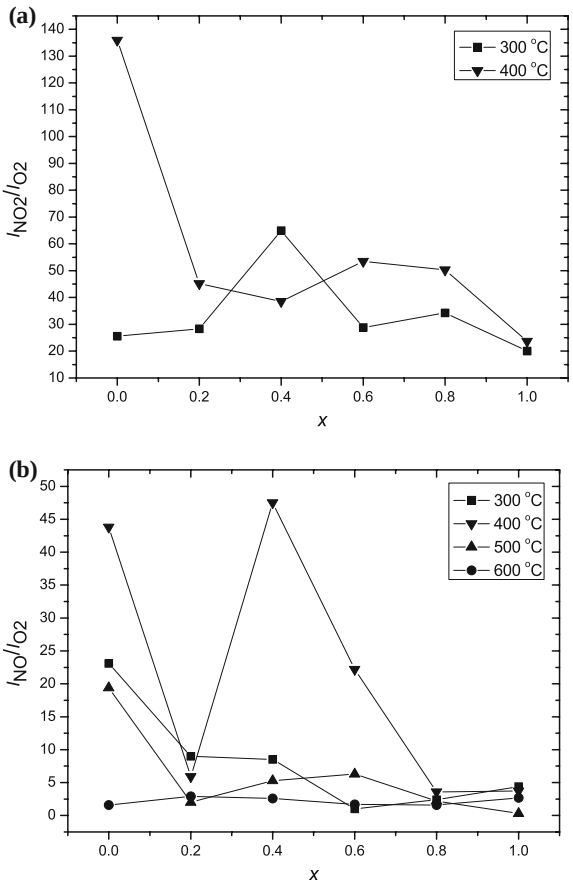

Fig. 7 Current ratios of (**a**) I_{NO_2}/I_{O_2}. and (**b**) I_{NO}/I_{O2} recorded on $MgMn_xFe_{2-x}O_4$ with an applied potential of −0.6 V. *x* refers to the Mn content

0.4, 0.6, 0.8, 1.0, using the solid state reactions. Dilatometry measurements showed a decreasing linear thermal expansion for the Mn-containing materials. Conductivity measurements show an increase in the electric conductivity when more Mn is incorporated into the structure. Data recorded with cyclic voltammetry in 1% NO, 1% NO_2 and 10% O_2 showed a decreasing activity when Mn was incorporated into the structure; however, current ratios are still relatively high compared to those of $MgFe_2O_4$.

Acknowledgments The Danish Council for Strategic Research (project no: 2194-05-0067) is thanked for the financial support. We would also like to thank the colleagues of the Fuel Cells and Solid State Chemistry Division for fruitful discussions.

References

1. Petric A, Ling H (2007) J Am Ceram Soc 90:1515
2. O'Bryan HM, DiMarcello FV (1970) J Am Ceram Soc 53:413
3. Dieckmann R (1984) Solid State Ionics 12:1
4. Seguin C (2006) Diesel car sales set to overtake petrol in Europe. http://www.pwc.com
5. http://www.dieselNet.com/news/2007/02delphi.php, Delpi announces ammonia sensor for SCR systems
6. Pancharatnam S, Huggins RA, Mason DM (1975) J Electrochem Soc 122:869
7. Simonsen VLE, Johnsen MM, Hansen KK (2007) Top Catal 45:131
8. Hansen KK (2007) Electrochem Commun 9:2721
9. Hansen KK, Skou EM, Christensen H (2000) J Electrochem Soc 147:2007
10. Hansen KK, Skou EM, Christensen H (2005) Solid State Ionics 176:915
11. Simonsen VLE, Nørskov L, Hansen KK (2008) J Solid State Electrochem 12:1573
12. Iwayama K, Wang X (1998) Appl Catal B 19:137
13. Shangguan WF, Teraoka Y, Kagawa S (1996) Appl Catal B 8:217
14. Shangguan WF, Teraoka Y, Kagawa S (1997) Appl Catal B 12:237
15. Shangguan WF, Teraoka Y, Kagawa S (1998) Appl Catal B 16:149
16. Haneda M, Kintaichi Y, Hamada H (2005) Appl Catal B 55:169–175
17. Drouet C, Alphonse P, Rousset A (2001) Appl Catal B 33:35
18. Chen L, Horiuchi T, Mori T (1999) Catal Lett 60:237
19. Fino D, Russo N, Saracco G, Specchia V (2006) J Catal 242:38
20. Simonsen VLE, Find D, Lilliedal M, Petersen R, Hansen KK, (2007) Top Catal 45:143
21. Hansen KK, Christensen H, Skou EM (2000) Ionics 6:340
22. Bræstrup F, Hansen KK (2008) The $NiFe_2O_4$–$MgFe_2O_4$ series as electrode materials for electrochemical reduction of NO_x. J Solid State Electrochem. doi:10.1007/s1000800806539
23. Gusmano G (1993) J Mater Sci 28:6195
24. Hansen KK, Christensen H, Skou EM, Skaarup SV (2000) J Appl Electrochem 30:193
25. Fabry P, Kleitz M, Deportes C (1972) J Solid State Chem 5:1
26. Petříček V, Dusek M, Palatinus L (2000) Jana2000. The crystallographic computing system. Institute of Physics, Praha, Czech Republic
27. Bruggeman DAG (1935) Ann Phys 24:636
28. Newman J (1966) J Electrochem Soc 113:501
29. Singhal SC, Dokiya M (2003) In Proceedings of the solid oxide fuel cells VIII, vol 7. Electrochem Soc Inc., New York, p 400
30. Kulkarni R, Joshi H (1985) Solid State Commun 53:1005
31. Klein C, Hurlbut CS, Dana JD (1998) Manual of mineralogy, 21st edn. Wiley, New York
32. Gillot B, Baudour JL, Bouree F, Metz R, Legros R, Rousset A (1992) Solid State Ionics 58:155
33. Hirota K, Saruwatari K, Kato M, Nakade K (2008) Sci Eng Rev Doshisha Univ 49:1
34. Zhang CL, Yeo S, Horibe Y, Choi YJ, Guha S, Croft M, Cheong SW (2007) Appl Phys Lett 90:133123
35. Touloukian YS, Ho CY (1977) Thermophysical properties of matter. The TPRC data series, vol 13. Plenum Pub Co., New York
36. Harrison RJ, Putnis A (1999) Phys Chem Mineral 26:322
37. Turkin AI, Drebushchak VA (2004) J Cryst Growth 265:165
38. Corbel G, Mestiri S, Lacorre P (2005) Solid State Sci 7:1216
39. Mori M, Hiei Y, Sammes NM, Tompsett GA (2000) J Electrochem Soc 147:1295
40. Ata-Allah SS, Fayek MK, Yehia M (2004) J Magn Magn Mater 279:411
41. Ata-Allah SS, Sayedamed FM, Kaiser M, Hashhash AM (2005) J Mater Sci 40:2923
42. Bræstrup F, Hansen KK (2009) $NiCr_xFe_{2-x}O_4$ as cathode materials for electrochemical reduction of NO_x. J Solid State Electrochem. doi:10.1007/s10008-009-0801-x